8-2012

# PROGNOSTIC AND HEALTH-MANAGEMENT ORIENTED FUEL CELL MODELING AND ON-LINE SUPERVISORY SYSTEM DEVELOPMENT

Xian Zhang
*Clemson University*, xianz@g.clemson.edu

# PROGNOSTIC AND HEALTH-MANAGEMENT ORIENTED FUEL CELL MODELING AND ON-LINE SUPERVISORY SYSTEM DEVELOPMENT

---

A Dissertation
Presented to
the Graduate School of
Clemson University

---

In Partial Fulfillment
of the Requirements for the Degree
Doctor of Philosophy
Automotive Engineering

---

by
Xian Zhang
August 2012

---

Accepted by:
Dr. Pierluigi Pisu, Committee Chair
Dr. Mohammad Omar
Dr. Robert Prucka
Dr. Ardalan Vahidi

## ABSTRACT

Of the fuel cells being studied, the proton exchange membrane fuel cell (PEMFC) is viewed as the most promising for transportation. Yet until today, the commercialization of the PEMFC has not been widespread in spite of its large expectation. Poor long term performances or durability, and high production and maintenance costs are the main reasons. For the final commercialization of fuel cells in the transportation field, durability issues must be addressed, while costs should be further brought down. At the same time, health-monitoring and prognosis techniques are of great significance in terms of scheduling condition-based maintenance (CBM) to minimize repair and maintenance costs, the associated operational disruptions, and also the risk of unscheduled downtime for the fuel cell systems.

This dissertation presents a comprehensive on-line supervisory system to address the important issues related to the PEMFC durability, including: 1) diagnosis of critical operating conditions, 2) optimization of the operating conditions, and 3) health monitoring (or damage tracking) and remaining useful life (RUL) prediction. In order to design and implement this supervisory system, a comprehensive fuel cell model is developed that integrates a control/diagnostic oriented dynamic fuel cell model and a prognostic oriented fuel cell degradation model, due to a lack of such models in the existing literature.

To address the first issue, a model-based on-line diagnostics system is developed for fuel cell flooding and drying diagnosis, thanks to the incorporation of the diagnostic feature in the dynamic fuel cell model. The channel flooding diagnostic problem is

decoupled from the gas diffusion layer (GDL) flooding and membrane drying diagnostic problem. Simultaneous state and parameter estimation problems are formulated for both cases. Dual extended Kalman filter (EKF) and dual unscented Kalman filter (UKF) techniques are applied respectively to solve the problems. The second issue is addressed by a diagnostic based control design for the air supply of the fuel cell system. The design concept allows selection of the most suitable controller in a controller bank that delivers the best performance under specific operating conditions and that mitigates the faulty condition based on the feedback of the diagnosis results. The control problem is reformulated as an H-infinity robust control problem, the objective of which is to minimize the difference between the desired and actual excess $O_2$ ratio, thus preventing and minimizing oxidant starvation at the cathode. Finally, an UKF-based health-monitoring and prognostic scheme is proposed and applied to the damage tracking and RUL prediction for the fuel cell. The developed aging model is employed as the kernel for this scheme, which utilizes the fuel cell output voltage as the only feature for the prognostic and health management task.

## TABLE OF CONTENTS

Page

## LIST OF TABLES

## LIST OF FIGURES

List of Figures (Continued)

Figure Page

# CHAPTER ONE

# BACKGROUND AND INTRODUCTION

## 1.1 RESEARCH MOTIVATION

Polymer electrolyte membrane fuel cells (PEMFCs) are very efficient electrochemical energy conversion devices that convert the chemical energy of supplied reactants to electrical energy and produce electricity. Due to many of its advantages, PEM fuel cell is the most promising candidate, among various types of fuel cells, for use in transportation applications. However, the relatively short life of PEM fuel cells has undoubtedly become a significant barrier to their commercialization in stationary and mobile applications. The life time target of the Department of Energy (DOE) for 2010 – 2015 requires PEM fuel cells to achieve 5000h for mobile and 40,000h for stationary applications[1]. In the last decade, great progress has been achieved in PEM fuel cell with respect to the performance and durability but, for transportation application, more work needs to be done to address the durability issue of PEM fuel cell, since the lifetime targets can only be met under ideal laboratory conditions in the present.

The durability of the PEM fuel cell is largely determined by its essential component, namely the membrane-electrode-assembly (MEA), which contains the polymer electrolyte membrane and two electrodes and is usually manufactured as an integrated unit. Most PEM fuel cells today employ Nafion as the polymer electrolyte membrane, and Pt/C or PtM/C (PtM represents Pt alloy) as the catalyst coated electrode. While these materials present excellent properties and enable the PEM fuel cells to achieve satisfactory performance at their initial fresh states, their inevitable deterioration

during the long time operation of the fuel cell cause gradual performance degradation and can finally lead to a complete failure of the fuel cell system, which is defined as the end-of-life (EOL) of the fuel cell.

Operating conditions (OCs) are the main factors that affect the fuel cell's degradation processes after its manufacture and assembly. Some operating conditions such as flooding, membrane drying, and reactants starvation are considered detrimental to the fuel cell health because the degradation of the fuel cell components can be greatly exacerbated under these OCs. Thus to elongate the fuel cell life, it is extremely important to optimize the fuel cell's OCs at any time, which demands the development of the control system that maintain the optimal OCs and the diagnostic system that is able to detect and estimate/evaluate the faulty conditions.

On the other hand, the poor durability of the fuel cell also requires the design of a health monitoring and prognostic system as the basis for the condition-based maintenance (CBM). By tracking the health state and predicting the remaining useful life (RUL) of the fuel cell, maintenances can be scheduled based on the system damage condition to minimize repair and maintenance costs and associated operational disruptions, while also minimizing the risk of unscheduled downtime [2].

Therefore, to deal with the durability issue of the fuel cells, a comprehensive on-line supervisory system incorporating the features of control/diagnostic, health monitoring and prognostic is highly demanded.

## 1.2 INTRODUCTION TO PEM FUEL CELL AND ITS AGING PROCESS

### *1.2.1 PEM Fuel Cell*

A typical PEM fuel cell unit is mainly composed of the following functioning components (see Figure 1-1): 1) Polymer electrolyte membrane, for conducting proton; 2) Catalyst layers, the site for the two half reactions to take place; 3) Gas diffusion layers (GDL), porous material to distribute the reactants and products and to conduct the electricity; 4) Bipolar plates, to form the gas channels and collect electricity.

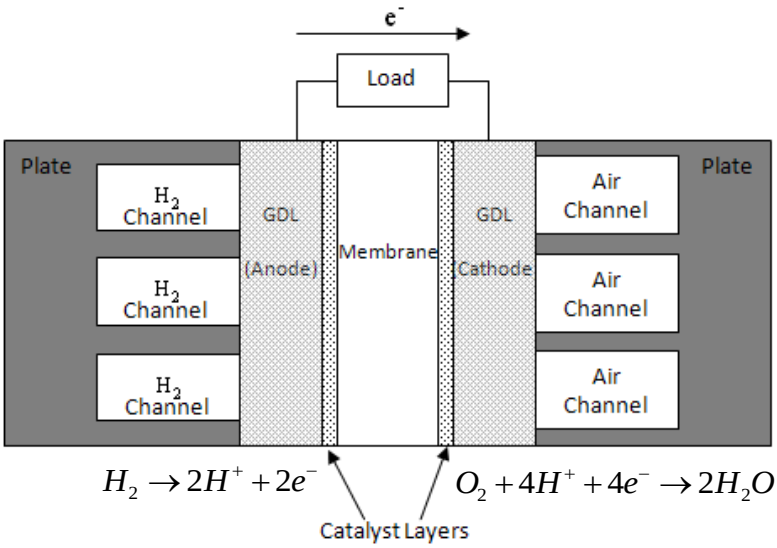


Figure 1-1 Main Components of a PEM FC unit

Usually onto each side of the membrane is bonded a catalyzed porous electrode, the anode-electrolyte-cathode assembly is thus one item, and is referred to as 'membrane electrode assembly' (MEA) [3]. The operation of the PEM fuel cell can be summarized as [4]: reactant gases are supplied to both electrodes of the fuel cell via channels, the GDL facilitates their even distribution to the catalyst-coated membrane, and the catalyst

accelerate the oxidation and reduction of the reactants, which are the primary reaction desired for fuel cell operation. In the case of a $H_2$-Air type fuel cell, the hydrogen oxidization reaction (HOR: $H_2 \rightarrow 2H^+ + 2e^-$) occurs at the anode and the oxygen reduction reaction (ORR: $O_2 + 4H^+ + 4e^- \rightarrow 2H_2O$) occurs at the cathode.

### *1.2.2 The Aging Process of PEM Fuel Cell*

To date long-term performance and durability of the fuel cells are difficult to quantify because not all degradation mechanisms of the various fuel cell components are completely understood. The fuel cell's performance degrades irreversibly throughout its lifetime mainly due to the following components' degradations: (1) catalyst degradation (catalyst particle coarsening); (2) carbon support degradation (carbon corrosion); and (3) membrane degradation (chemical deterioration and dehydration) [5], [6]. Factors affecting these degradation processes would be: temperature, high potentials, heat cycle but most of all by water management, contaminants, and impurities. Thus, depending on the power load and the long-term operating conditions of the fuel cell, the extent of performance and durability degradation varies. In general, the longer the fuel cell stack is operated in transient or cycling conditions, or detrimental operating conditions such as flooding, the stronger is the corrosion and therefore the degradation.

In the following, the degradation mechanisms of the fuel cell components are introduced, with the focus on the catalyst and catalyst support, and membrane. More comprehensive reviews on the durability and degradation issues of the PEM fuel cell can be found in [5], [7–11].

#### 1.2.2.1 CATALYST DEGRADATION

Among the various degradation mechanisms, corrosion of the catalyst is frequently addressed in the literature and is better understood. It means the loss and change in structure and distribution of the platinum on the carbon support accompanied by a decrease in electrochemical active surface area (ECSA) of the electrode. The loss of ECSA can be explained by two phenomena, namely the catalyst particle agglomeration or coarsening, and the absolute mass loss of the effective catalyst.

The catalyst agglomeration/coarsening is a process characterized by the redistribution of initially small narrow and uniformly dispersed Pt-particles to form larger particles which are then distributed more widely [5]. The order of the particle-size growth is in the range of nanometers. In a typical scenario for a PEM fuel cell, for example, the mean radius of the Pt-particles can grow from an initial 2.5nm to a final 10nm at the end of the fuel cell's life.

The following three mechanisms are usually responsible for the Pt redistribution in the fuel cell electrode [11]:

i. *Quasi-Ostwald ripening* that occurs when small particles dissolve, diffuse, and redeposit onto larger particles, resulting in reduced Pt particle surface area via a minimization in surface energy;

ii. *Reprecipitation* that occurs when Pt dissolves into the ionomer phase within the cathode and then precipitates out again as newly formed Pt particles;

iii. *Particle coalescence* that occurs when Pt particles are in close proximity and sinter together to form a larger particle.

Cell potential cycling is one of the most important factors contributing to platinum agglomeration and/or oxidation. It is believed that platinum-solubility is a function of the potential and that there exists a particular equilibrium voltage. When the cell is cycled above the equilibrium voltage the surface of some Pt particles dissolves to produce an ion state and the Pt-ions are driven into the solution (water) [5]. When decreasing the cycling potential again below the equilibrium, the platinum is forced back out of the solution and then deposits on either a previously existing platinum particle (mechanism i), or a particle or defect that did not previously serve as a platinum site (mechanism ii). Step changes in the cell voltage may also help this process.

The effect of $O_2$ partial pressure on cathode degradation was found to be insignificant, while higher RH, or even flooding in the catalyst layer facilitates the Pt ion transport and thus accelerate the catalyst degradation via Ostawald ripening mechanism. [12]

The role of particle migration and coalescence (mechanism iii) in the Pt surface area loss at low-temperature fuel cells is still uncertain, and there still lacks unique experiment evidence in support of crystal migration and coalescence. But the mechanism cannot be ruled out from a theoretical standpoint[13].

Among the three mechanisms, mechanism i and iii account for the overall catalyst particle growth.

The absolute mass loss of the effective catalyst occurs when the dissolved Pt ions transports into the membrane and gets chemically reduced by hydrogen that permeates through the membrane from the anode, forming a Pt "band"[14]. The Pt band can actually be observed by electron probe microanalysis (EPMA) inside the electrolyte membrane of the used MEA at a location near the cathode catalyst layer [15]. The catalyst loss can also be facilitated by the corrosion of the catalyst support, which is discussed next.

#### 1.2.2.2 CARBON CORROSION

Carbon material at the cathode can be oxidized to $CO_2$ following the reaction formula as given in (1.1). The thermodynamic potential at standard conditions for this reaction is only 0.207V ([9], [16]), meaning that the electrochemical oxidation of the carbon is thermodynamically possible during the normal operation of the fuel cells.

$$C + 2H_2O \rightarrow CO_2 + 4H^+ + 4e^- \tag{1.1}$$

Although thermodynamically unstable, the carbon corrosion rate at PEMFC's typical operating temperature (< 90˚C) is very slow, even in the presence of catalyst and water. In fact, stable performance after prolonged operation suggests that the rates of carbon loss are so low as to be largely negligible over the required lifetimes of fuel cell power plants, provided that the local cathode potential does not exceed about 1 V[17]. However, during some special conditions, such as localized fuel starvation and start/stop, this aging process can be greatly accelerated and irreversible damage caused to the carbon even if the fuel cell is only operated under these conditions for a short time interval.

Local fuel starvation is caused by flow maldistribution or blockages that restrict hydrogen flow to certain regions of the cell; while during start/stop, either hydrogen is introduced to the anode of a cell that is filled with air or nitrogen, or air or nitrogen is introduced to the anode that is filled with hydrogen. Under both conditions, the cell can be equivalently divided into two sections: one with a fuel-rich region and one with a fuel-starved region connected electrically in parallel by the highly conductive bipolar plates that distribute reactants and collect current. The section of the cell that contains hydrogen operates normally as a power source, which establishes a potential difference ( $\Delta\varphi = \varphi_c - \varphi_a$, with $\varphi_c$ and $\varphi_a$ being the potential at the cathode and anode) across the cell that can be harnessed to drive external loads. The section with the fuel-starved region, however, operates in a driven mode, where the proton current flows in the opposite direction as in the fuel-rich region, i.e., from the cathode to the anode. To sustain the cathodic current at the anode, ORR ( $O_2 + 4H^+ + 4e^- \rightarrow 2H_2O$ ) takes place and results in a negative potential difference across the anode / electrolyte interface, i.e., $\Delta\varphi_{\mathrm{ae}}^{\mathrm{starve}} = \varphi_{\mathrm{e}}^{\mathrm{starve}} - \varphi_{\mathrm{a}} < 0$, where $\varphi_{\mathrm{e}}^{\mathrm{starve}}$ is the electrolyte potential in the fuel-starved region. Since $\Delta\varphi = \Delta\varphi_{\mathrm{ec}}^{\mathrm{starve}} + \Delta\varphi_{\mathrm{ae}}^{\mathrm{starve}}$ (neglecting the potential difference across the membrane), the cathode potential becomes much more positive in the fuel-starved region (almost doubled compared to that in the fuel-rich region). At these more positive potentials, both oxygen evolution and carbon corrosion can occur at the cathode [17].

While during localized fuel starvation and start/stop the elevated cathode potential cause damage to the cathode carbon, gross fuel starvation can be detrimental for the

carbon support in the anode [11]. In the case of gross fuel starvation, cell voltages can become negative, as the anode is elevated to positive potentials and the carbon is consumed instead of the absent fuel. For multiple cells in a stack, fuel maldistributions can lead to some cells having insufficient fuel to carry the current that is being pushed through them by adjacent cells. In the absence of a sufficient anodic current source from hydrogen, the cell potential climbs higher until oxidation occurs — in this case, the oxidation of the carbon support of the catalyst layer.

The carbon corrosion would increase with operating temperature and decreases with relative humidity.

#### 1.2.2.3 MEMBRANE DEGRADATION

The most widely used PEM in the PEM fuel cell today is still Nafion, a perfluorinated sulfonic acid (PFSA) membrane developed by DuPont. It is based on an aliphatic perfluorocarbon sulfonic acid, and it exhibited excellent physical properties and oxidative stability in both wet and dry states[11]. However, during the long term operation of the PEM fuel cell, especially under some harsh operating conditions, the PEM in the fuel cell gradually lose these great properties at its fresh state and can eventually fail completely with its essential property be compromised: separation of the fuel and oxidant. The degradation of the membrane is typically characterized by the reduced thickness, weakened mechanical strength, loss of proton conductivity, and the formation and propagation of micro-crack in it. The membrane degradation mechanisms are generally categorized as chemical degradation and mechanical degradation in the literature.

Chemical degradation is a major cause of failure of PFSA membrane. It is thought that hydroxyl (-OH) or peroxy (-OOH) radicals attack polymer end groups that still contain residual terminal H-groups. Characterization by X-ray photoelectron spectroscopy (XPS) revealed that during fuel cell operation the interactions between carbon, fluorine and oxygen are changing [10]. An example given by Curtin et al. [18] is the attack of hydroxyl radicals on carboxylic end groups:

$$R_f - CF_2COOH + \bullet OH \rightarrow R_f - CF_2\bullet + CO_2 + H_2O \quad (1.2)$$

$$R_f - CF_2\bullet + \bullet OH \rightarrow R_f - CF_2OH + R_f - COF + HF \quad (1.3)$$

$$R_f - COF + H_2O \rightarrow R_f - COOH + HF \quad (1.4)$$

Studies on chemical degradation have shown that the conditions leading to increased radical attack in PFSAs include higher temperature (especially above 90 ℃), low humidification, high gas pressure, use of pure hydrogen and pure oxygen, and high cell voltages. Some of these conditions are consistent with a higher concentration of $H_2$ and $O_2$. The role of relative humidity, potential and also of membrane thickness is still a subject of study. Recent results suggest that the state of the catalyst surface may play an important role [10].

The decomposition of the membrane directly leads to membrane thinning and loss of proton conductivity. It also has effect on the mechanical weakening. The strain-to-failure, an indicator of the membrane mechanical strength, is reduced during the chemical degradation process.

Even without induced chemical reaction, pure mechanical factors can result in the degradation of the membranes. Variations in temperature and humidity inevitably occur

during PEM fuel cell operation. Due to the large hygrothermal expansion coefficient of ionomer membrane, stresses and equivalent strains can be induced in the membrane or MEA. Relative humidity (RH) cycling can cause cyclic stress in the membrane of MEA. This has been found to be particularly detrimental to the mechanical integrity of the membrane, similar to the fatigue process observed in many structural materials under cyclic stresses. Interestingly, evidence has also shown that defects generated and propagated during the RH cycling condition do not contribute much to the gas crossover before the occurrence of the final mechanical breach, even though the strain-to-failure index is found to be constantly decreasing during the mechanical degradation process [19].

#### 1.2.2.4 SUMMARY OF THE FUEL CELL DEGRADATION

The impact of the operating conditions and component degradation mechanism of the fuel cell are now summarized in Table 1-1 and Table 1-2, respectively.

Table 1-1 Summary of the primary adverse operating conditions of fuel cells

| Code | Operating Condition | Primary effect | Secondary effect | Affected components |
|---|---|---|---|---|
| OC ① | Flooding | Aggravate the corrosion of electrode, catalyst layer, GDL, even membrane | a) Impurities deposit on catalyst<br>b) Impurities transported into membrane, replacing $H^+$<br>c) Reactant starvation | i) Catalyst layer (Pt-C)<br>ii) Carbon support<br>iii) Bipolar Plates<br>iv) membrane |
| OC ② | Drying (more likely anode | a) Facilitate chemical attack to | Form the following destructive cycle of | Membrane |

| | | | | |
|---|---|---|---|---|
| | side) | membrane<br>b) Change membrane's mechanical properties (membrane becomes brittle, and develops crack) | increasing gas crossover rate:<br>Gas Crossover→ Hotspot → Pinhole formation → Gas Crossover | |
| OC ③ | Reactant Starvation | Cell reversal | Carbon corrosion | i) Carbon support<br>ii) Membrane |
| OC ④ | Potential Cycling / High potential | a) Facilitate Ostwald ripening mechanism<br>b) Facilitate carbon corrosion<br>c) Facilitate chemical attack to membrane | a) ECSA decrease<br>b) Membrane thinning, and following destructive cycle | i) Catalyst layer (Pt-C)<br>ii) Carbon support<br>iii) membrane |
| OC ⑤ | High Temperature | Accelerate various side reactions, e.g., formation of $H_2O_2$ in membrane | a) electrode corrosion<br>b) Higher $H_2$ crossover | i) Catalyst layer (Pt-C)<br>ii) Carbon support<br>iii) membrane |

Table 1-2 Summary of the primary aging mechanisms of various components in fuel cell

| Component | Primary Aging Mechanism | Operating Conditions that Exacerbate the Aging Mechanism | Aging Effect |
|---|---|---|---|
| I. Membrane | a) Chemical attack by OH, OOH radicals to | Drying (a, c); High Temperature (a) | a) Chemical properties of the membrane change |

| | | | |
|---|---|---|---|
| | polymer end groups<br>b) Fatigue stresses due to temperature and humidity cycling<br>c) Mechanical degradation led by chemical attack and mechanical stress (destructive cycle of increasing gas crossover rate)<br>d) $H^+$ replaced by contaminations | High potential (a);<br>High gas pressure / High reactant concentration (a);<br>temperature cycling (b);<br>humidity cycling (b);<br>pressure difference of the two electrodes | (F…)<br>b) Membrane thinning (due to chemical attack by radicals)<br>c) Develop crack, which can lead to catastrophic fuel cell failure<br>d) Lower conductivity (Water, and $H^+$ as well) |
| II. Electrode / Electro catalyst | Pt catalyst nano-particles sintering / oxidized / aggregation due to high potential and potential cycling | Potential Cycling / High potential<br>Flooding<br>High / Low Temperature | Decrease of active ECSA |
| III. GDL | Carbon corrosion | Potential Cycling / High potential<br>Start-up<br>Reactant Starvation | a) Loss of Pt<br>b) change the micro structure of the GDL, and decrease its hydrophobicity |
| IV. Bipolar Plate | Material corrosion (especially metal bipolar plate) | Flooding | a) lead to membrane contamination<br>b) formation of resistive surface layer which gives rise to higher Ohmic resistance |

## 1.3 PROBLEM STATEMENT

This dissertation deals with the durability issue of the fuel cells by proposing a comprehensive on-line supervisory system with the capability of control/diagnostic, health monitoring and prognostic. The design and implementation problem of such a supervisory system can then be decomposed to the following main problems:

1. Control/diagnostics and prognostics oriented fuel cell modeling;

One of the challenges to build the supervisory system comes from developing an integrated model that describes both the fast and slow dynamics of the fuel cell, which is still in lack in the literature. This dissertation aims at developing a control oriented model that explicitly incorporates the fault vector $f$ and aging parameter vector $\vartheta$, and a prognostic-oriented aging model that can characterize and predict the degradation process. The model complexity of these models needs to be kept minimal to server their purpose.

A general model in state space form that can be applied to any dynamical system with possible fault set and aging parameters is given below ([20])

$$\begin{aligned} \dot{x} &= \mathrm{f}\left(x, \vartheta, u, f\right) \\ \dot{\vartheta} &= \varepsilon \cdot \mathrm{g}\left(x, \vartheta, u, f\right) \\ y &= \mathrm{h}\left(x, \vartheta, u, f\right) \end{aligned} \tag{1.5}$$

where $x \in R^n$ is the set of state variables associated with the fast dynamic behavior of the system, $\vartheta \in R^m$ is the set of the underlying system aging parameters (slowly varying with the system degradation), $u \in R^l$ is the input vector, $f \in R^q$ is the fault vector, $\varepsilon$ $(0 < \varepsilon << 1)$ is an extremely small parameter indicating the slow degradation

behavior of the variable $\vartheta$, and defining the time-scale separation between the fast dynamics and the slow drift; $p \in R^k$ is the set of aging factors that have an effect on the aging of the system and it is often a function of states, inputs and external parameters; $y \in R^p$ is the output vector.

2. Diagnosis and optimization of the operating conditions;

The most common faults – or detrimental operating conditions – in a fuel cell need to be detected and evaluated. Mitigation strategies are also needed to optimize the fuel cell operating condition at any time. In this dissertation, we focus on fuel cell channel flooding, GDL flooding, membrane drying, and reactant starvation.

3. Health monitoring and prognostics for the fuel cell components.

Damage variables that best characterize the health state of the fuel cell need to identified, validated experimentally, and then tracked throughout the fuel cell life. Based on the health monitoring result, prognostic scheme needs to be developed for prediction of the remaining useful life (RUL) of the fuel cell.

## 1.4 LITERATURE REVIEW

Corresponding to the proposed problems in the last section, research work in three relatively independent areas is reviewed in this section. The three areas are: 1) fuel cell modeling for the control/diagnostic purpose and for characterization of its aging process; 2) diagnostic approach applied to the fuel cell system; and 3) general health monitoring and prognostic methods, with focus on the electro-chemical systems.

### *1.4.1 Fuel cell modeling*

The research areas of FC system dynamics and the aging process of the fuel cells are relatively independent with each other and a unified study of the fast and slow dynamics as given in model (1.5) is still missing in the literature. Although extensive researches have been carried out to date on establishing control oriented dynamic models for fuel cell and fuel cell system ([21–25]), these models focus only on the fast dynamics (with time constant $10^{-3} \sim 10^{2}$ sec) of the FC system, such as the gas supplying dynamics, and heat transfer dynamics, and ignore the slow dynamics of fuel cell deterioration by considering $\varepsilon = 0$. The impact of aging parameters on the performance of the system is usually implicitly included in the model and empirically determined, and assumed to be constant over the infinite time interval. Very few of the existing control-oriented fuel cell system models found in the literature incorporate the aging parameters explicitly. In [26], apparent catalytic rate constant is incorporated in the electrochemical model of a PEM fuel cell. The considered parameter accounts for the effect of more than one aging parameter, including rate constants for the electrode reaction, as well as properties such as effective catalyst surface area.

On the other hand, modeling work addressing PEMFC degradation has been much less reported. Many of these models have little physical basis, and thus have no predictive capability [27]. Franco et al. [28–31] have done a series of leading work on developing a multi-scale mechanistic model of the electrochemical aging processes in a PEMFC to describe, in particular, the carbon corrosion at the cathode, the cathodic oxidation/dissolution of platinum and the carbon supported platinum electrochemical

ripening. The model takes into account the details such as the coupling with intermediate reaction species of the oxygen reduction reaction (ORR) and the parasite water adsorption on the catalyst surface, expected in realistic PEFC environments. The model is powerful in terms of establishing nano/microstructure-performance relationships, elucidating MEA degradation and failure mechanisms, and helping improve both PEMFC electrochemical performance and durability. However, its CFD modeling approach makes it unsuitable for the on-line prognostic purpose due to the computation burden involved. Also, the model needs too many parameters that are hard to obtain.

Darling and Meyers [32] proposed a spatially lumped model that treats a single, porous platinum electrode and the ionomeric solution that fills the pores of the electrode. The model includes spherical platinum particles that can grow and shrink as platinum plates and dissolves; a platinum oxide layer; and an ionic platinum species in solution ($Pt^{2+}$). The kinetic expressions for platinum oxidation and dissolution developed in this work is incorporated by the same authors [33] in a transient, one-dimensional mathematical model of the cross section of a PEM fuel cell. In this model, each electrode contains two platinum particle sizes, enabling a description of electrochemically driven transfer of platinum between particles of different sizes. That is, platinum can be exchanged between particles by dissolution and crystallization, capturing the underlying principles of the quasi-Ostwald ripening. Simulation results, however, didn't quite capture the curvature of the ECSA evolution with time as seen in the durability tests, and show that the ECSA decreases linearly. The authors presumed that this may have been caused by short simulation time.

Bi and Fuller [14] modified the model in [32], [33] by considering the diffusion of Pt ions in the membrane electrode assembly (MEA), while still adopted the two particle groups model structure. The authors concluded that the model is not adequate to predict well the catalyst degradation rates including Pt nanoparticle growth, catalyst surface area loss and cathode Pt mass loss, and suggest other degradation mechanisms such as new Pt cluster formation on carbon support and neighboring Pt clusters coarsening be investigated.

Holby et al. [34] investigated the influence of particle size distribution (PSD) and crossover hydrogen on the Pt nanoparticle stability in PEM fuel cells by extending the previous degradation model of Darling and Meyers[32], [33] to include PSD effects, more complete interfacial thermodynamics, and hydrogen crossover effects. With the PSD sampled non-uniformly at 700 distinct radii (with 200 radii concentrated in the small particle region of the final distribution for accuracy), the model successfully captured the evolution trend of the PSD and the ECSA of the catalyst with aging. However, the computational efficiency of the model is also compromised by considering so many particle groups.

A first order rate kinetic model was proposed by Debe et al. [35] and applied to the normalized surface area changes as a function of number of cycles and temperature to fit the experimental data. The same model is employed by Holby et al. [36] to study the temperature effect on the Pt surface area loss. This model is oversimplified and lacks a physical basis.

Little research work on the modeling of the membrane degradation has been found in the literature. This may be partly due to the still unclear many degradation mechanism of the membrane aging process. In [19], a so-called progressive degradation model is presented as an example to demonstrate the modeling approach for damage accumulation model that combines multiple degradation effects (chemical and mechanical). Strain-to-failure of the membrane is chosen as the mechanical strength indicator. The model is based on the experimental data fitting, and lacks a physical basis. Also, since there is no connection between the damage variable (strain-to-failure) and the cell's instantaneous performance, there is no model output for feedback purpose.

### *1.4.2 Fuel cell diagnostics*

The fuel cell diagnostic methods in the literature can be roughly grouped into two categories, namely the intrusive method, and the non-intrusive method (Figure 1-2). The intrusive diagnostic method usually requires special modification to the fuel cell that affects its integrity (e.g., fuel cell with transparent bipolar plates for channel flooding observation), or alters the fuel cell's operating conditions (e.g., EIS method that imposes a perturbation current or voltage on the fuel cell). The non-intrusive diagnostic method, on the other hand, utilizes only the easy to obtain information from the plant sensors while keeping the fuel cell's integrity and does not change the system's normal operating conditions.

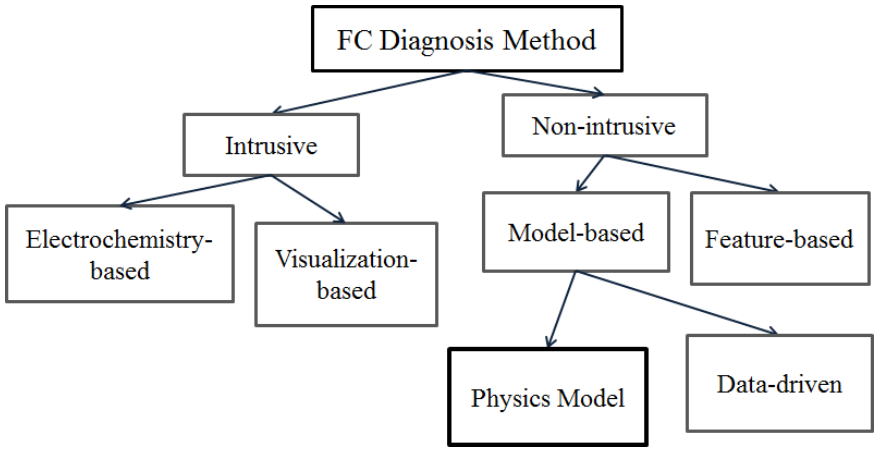


Figure 1-2 A classification of FC diagnosis method

In the intrusive method category, two subcategories are usually seen, one is the so-called visualization-based method such as neutron imaging techniques and the aforementioned transparent fuel cell; the other is the electrochemistry-based method such as the Electrochemical Impedance Spectroscopy (EIS) techniques and cyclic voltammetry.

The most widely applied electrochemical-based diagnostics tool is the EIS technique, which is used to measure the fuel cell's AC impedance around some steady state operating point as a function of frequency ([37–45]). The basic idea of the EIS-based diagnosis is to exploit the different impacts of different faults (e.g., water flooding and membrane drying) on the measured impedance (in terms of magnitude and phase) to detect and differentiate the faults. Equivalent circuit models of the fuel cell are often built for data fitting of the measured fuel cell impedance, and the fitted parameters that are sensitive to some faults can then be used as indicators of the faults (e.g., [39]).

An extension of the EIS method called the nonlinear frequency response analysis (NFRA) applies a sinusoidal perturbation of high amplitude to the fuel cell current and analyzes the resulting voltage using the concept of higher order frequency response

functions. Kadyk et al. [46] employed this method for the diagnosis of membrane dehydration, fuel cell flooding and anode catalyst poisoning in a single polymer electrolyte fuel cell. It is shown that the linear part of the system response corresponds to the classical EIS, which are not sufficient to clearly distinguish between different fuel cell faults, while with the second order frequency response function it is possible to achieve the task. However, since the magnitude of the perturbation current is comparable to the operating current with this method, it is considered inapplicable as a non-intrusive on-line diagnosis tool.

Although the EIS technique (and the same with NFRA technique) provides resourceful information about the operating conditions of the fuel cell, the measurement of the AC impedance usually requires maintained steady state operating conditions (steady voltage or current) during the whole frequency sweep session, which is quite stringent especially for the fuel cell with automotive application. Also, the use of an AC spectrometer is not a very convenient solution for on-board integration due to the complexity and cost of the equipment. Therefore, in this dissertation, this electrochemical based diagnostic tool is not considered for our on-line diagnostic scheme. For a more comprehensive review of the electrochemical techniques applied to the fuel cell system, the interested readers could refer to the review paper [47][48].

Non-intrusive method can be further divided into two subcategories, namely the model based diagnostic method and the feature based diagnostic method. The feature based method does not rely on any form of models, rather, it extracts features that are sensitive to certain faults from the external measurable variables such as voltage and

pressure drop across the fuel cell channel, and analyzes the "symptom" in the feature, which is usually acquired as a prior knowledge from experimental data, for the fault detection and isolation. Steiner et al. [49] proposed a wavelet analysis method that, utilizing only the stack voltage signal, allows the detection of the flooding based on the patterns obtained from the wavelet packet coefficients. Similarly, Niroumand et al. [50] used cell voltage oscillation to isolate cathode flooding.

Pressure drop is a feature, or physical indicator that has been widely used for the channel flooding. Chen and Zhou [51] describes an approach to utilize frequency of pressure drop signal as a diagnostic tool for PEM fuel cell stack dynamic behaviors. Barbir et al. [52] diagnose flooding and drying conditions inside a stack by monitoring pressure drop and cell resistance respectively in an operational fuel cell stack. Note the cell resistance is measured directly by an Agilent 4338B Milliohmmeter. General Motors patented a method and apparatus that was based on pressure drop monitoring for detecting and correcting water flooding in an air-breathing PEM fuel cell [53] by comparing the measured pressure drop across flow field of a fuel cell stack to acceptable pressure drops (in a lookup table) determined empirically from a substantially identical, unflooded stack at various electrical discharge rates

The feature-based method provides little to none physical insight into the fault nature. And due to the limited available features and the fact that one feature (e.g. the voltage) can usually be affected by multiple possible faults (e.g. flooding, drying, catalyst poisoning), the faults that can be detected and identified by the chosen feature are also

limited. To achieve the fault detection and identification at the same time, model information of the fuel cell needs to be exploited.

Data driven models, such as fuzzy logic and neural network models, have found their application in the fuel cell diagnostics. For example, in [54] a fuzzy diagnostic-oriented static fuel cell model with the voltage and current as the model input is proposed. In [55], Steiner et al. presented a flooding diagnosis procedure based on black-box model, The flooding diagnosis procedure is based on the analysis of a residual obtained from the comparison between an experimental and an estimated pressure drop. The estimation of this latter is ensured by an artificial Neural Network that has been trained with flooding-free data.

### *1.4.3 Health Monitoring and Prognostics*

Health monitoring and prognostics of complex systems is a basic requirement for condition-based maintenance in many application domains where safety, reliability, and availability of the systems are considered mission critical.

Unlike health monitoring technology, prognostics technology is still in its infancy although some research work on developing the technology has been done over the recent years. Most of the relevant work in the field of prognostics comes from the structural engineering community, where failure due to structural fatigue can lead to catastrophic consequences (e.g., in aeronautical and marine applications). Many such systems use vibration sensors to monitor the health of rotating machinery such as helicopter gearboxes or jet engines [56].

The challenges in developing model-based prognostics approaches are well summarized in [20]. First, it is necessary to identify and experimentally validate damage variables – not always an easy and generalizable process, as it usually involves very lengthy experiments under controlled conditions, which do not necessarily reflect actual aging in real life. Second, once a damage variable is identified, there remains the challenge of reliably extracting features or estimating parameters from experimental data that closely correlate with the damage variable. Third, damage evolution is invariably a nonlinear phenomenon, making the modeling of it more difficult, and is also dependent on initial conditions (e.g. structural or material defect distribution).

Orchard et al. [57–59] proposed a novel particle filtering based prognostic framework. This approach employs a state dynamic model and a measurement model to predict the posterior probability density function of the state, that is, to predict the time evolution of a fault or fatigue damage. It avoids the linearity and Gaussian noise assumption of Kalman filtering and provides a robust framework for long-term prognosis while accounting effectively for uncertainties. Correction terms are estimated in a learning paradigm to improve the accuracy and precision of the algorithm for long-term prediction. The approach is applied to a crack fault, and the results support its robustness and superiority.

Many publications can be found that deal with battery prognosis in the literature [60–74]. Most methods for state-of-charge or state-of-health prognostics are impedance based.[75].

## 1.5 CONTRIBUTIONS

The durability issue of the PEM fuel cells constitutes a grave barrier to their commercialization in stationary and mobile applications. Within the current limitations of the fuel cell's state-of-the-art manufacturing technology, a comprehensive on-line supervisory system for control/diagnostic, health monitoring and prognostic purpose has become indispensable in extending the effective life of the fuel cell system, monitoring its health or damage state and predicting the system's remaining useful life in application domains where safety, reliability, and availability of the systems are considered mission critical.

While the control problem for the fuel cell system has received a lot of attention and has been analyzed in many publications during the last decade, literature that focused on the on-line real-time diagnostics and prognostics of the fuel cell is still scarce at present. On one hand, most diagnostic approaches for the fuel cell are intrusive and unsuitable for the on-line diagnostic purpose (e.g., the EIS method); and the existing control-oriented fuel cell models considered no effect of the faulty conditions or component degradation on the fuel cell performance, and needs to be modified for model-based diagnostic schemes. On the other hand, little work has been done for the prognostic and health management of fuel cells, and we are not aware of any prior publication presenting a prognostic-oriented fuel cell aging model. Literature search result shows that models addressing PEMFC degradation either have little physical basis and thus no predictive capability, or involve too much details and are computationally inefficient.

In this dissertation, we develop an integrated fuel cell model that is suitable for control, diagnostics, and health monitoring and prognostics (CDHMP) design and simulation validation as well. Based on this unified model, an on-line supervisory system for CDHMP is proposed. The main contributions of the dissertation are summarized as follows:

1) A comprehensive fuel cell dynamic model incorporating fault effects and aging effects (damage variables) is established to be used as the platform for algorithm validation of the control, diagnostic and health monitoring systems. Major improvements of this model compared to the existing fuel cell models are: (1) Gas dynamics in the fuel cell channel is modeled to include channel water flooding effect on the inlet pressure of the flow field; (2) Channel water dynamic model is incorporated that is capable of describing the accumulation and removal of the liquid water in the fuel cell channel; (3) The dynamics of reactants transportation in the GDL is considered as a function of the liquid water present in the GDL; (4) The effect of the effective catalyst surface area (ECSA) and the gas crossover of the membrane is incorporated in the electro-chemical module of the fuel cell model.
2) A model-based on-line diagnostics system is developed for fuel cell flooding and drying diagnosis thanks to the incorporation of the diagnostic feature in the dynamic fuel cell model. The channel flooding diagnostic problem is decoupled from the GDL flooding and membrane drying

diagnostic problem. Both problems are formed as simultaneous state and parameter estimation problem. Extended Kalman Filter and Unscented Kalman Filter techniques are applied respectively to solve the problems.

3) A diagnostic based control design for the air supply of the fuel cell system is proposed. While few publications in the literature have discussed the feedback of the diagnostic output signal to the controller, this concept allows selection of the most suitable controller in a controller bank that delivers the best performance under specific operating conditions and that mitigates the faulty condition based on the feedback of the diagnosis results. The control problem is reformulated as an H-infinity robust control problem, the objective of which is to minimize the difference between the desired and actual excess $O_2$ ratio, thus preventing and minimizing the oxidant starvation at the cathode.

4) Prognostic-oriented aging models are created to describe the slowly-varying dynamics in the fuel cell that characterize the degradation processes of the MEA of the fuel cell. The aging parameters, i.e. the states of the aging models, are chosen based on the experiment results such that they not only exhibit pronounced degradation trend but also distinguishably affect the fuel cell's instantaneous performances. Physics principles based modeling approach is employed to build a first-step detailed model with hundreds of state variables, which is then analyzed and further simplified to a second order lumped model for prognostic

application. The connection between the operating condition, especially the load profile, and the degradation rate is established.

5) An UKF-based health-monitoring and prognostic scheme is proposed and applied to the damage tracking and remaining useful life (RUL) prediction for the fuel cell. The developed aging model is employed as the kernel for this scheme, which utilizes the fuel cell output voltage as the only feature for the prognostic and health management task.

## 1.6 DISSERTATION OVERVIEW

The rest of this dissertation is organized as follows:

In Chapter 2, a comprehensive control-oriented fuel cell model is developed to incorporate the effect of faulty conditions and components degradation on the system performance. System identification and simulation is then carried out for model validation and performance analysis.

Chapter 3 presents a diagnostic-based control scheme for the air supply subsystem of the FCS. $O_2$ excess ratio control problem to minimize the oxidant starvation and channel flooding diagnosis problem are discussed. The air supply control is formulated as a robust control problem and two H-infinity controllers with different feedback selections are designed and compared. The controller with better performance is then implemented with the full model developed in Chapter 2 for simulation validation. The channel flooding diagnosis problem is formulated as a simultaneous state and parameter estimation problem and EKF technique is applied to solve the problem.

In Chapter 4, aging process of the PEM fuel cell is studied experimentally as a preliminary step for building the demanded prognostic-oriented degradation model for health monitoring and prognostic purpose. Various in-situ diagnostic tools are explored for the damage tracking for the health state of the fuel cell during its durability test. We discuss the criteria for choosing valid aging indicator for the fuel cell and compare several candidate damage variables. Experimental results of the evolution of these damage variables are presented and analyzed.

In Chapter 5, based on the damage variables selected in Chapter 4, physics-based, prognostic-oriented fuel cell degradation models are developed with the focus on the catalyst degradation model, which establishes the relationship between the operating conditions and the degradation rate of the ECSA. The model complexity is kept minimal for on-line prognostic purpose. A simple degradation model to describe the membrane micro-crack propagation is also briefly discussed.

Chapter 6 presents an integrated diagnostic and prognostic scheme since both diagnostic and prognostic problems are based on the electro-chemical module of the fuel cell and share the same output feature, i.e., the cell voltage. Cathode GDL flooding and membrane drying diagnosis problem is considered and formulated as simultaneous state and parameter estimation problem similar to that of channel flooding. The health monitoring and prognostic scheme employs the degradation model developed in Chapter 5 and an UKF framework for damage tracking and life prediction of the fuel cell.

Finally, Chapter 7 summarizes the research work and presents concluding remarks, possible future directions are discussed.

# CHAPTER TWO

# CONTROL AND DIAGNOSTIC ORIENTED FCS DYNAMIC MODELING

In order to study the on-line diagnostic and control systems for monitoring and optimizing the fuel cell's operating conditions, a comprehensive control/diagnostic oriented fuel cell model is demanded. Current existing control oriented fuel cell system models, however, do not take into account the impact of the fuel cell's faulty conditions and long term components' degradation on the fuel cell instantaneous performance, and are limited to control design under nominal operating conditions only.

In this chapter, a comprehensive fuel cell dynamic model incorporating fault effects and aging effects (damage variables) is established and presented with detailed description. For the faulty conditions, we are mainly interested in channel flooding, GDL flooding, membrane drying and reactants starvation; the electro-chemical catalyst surface area (ECSA) and $H_2$ crossover equivalent leak current density are chosen as the damage variables, which are determined from the experimental analysis presented later in Chapter Four. System identification is performed on the developed model with experimental data obtained from a laboratory fuel cell test stand, and simulation results are also presented.

## 2.1 MODEL ASSUMPTIONS

The fuel cell system dynamical model in this dissertation is established in accordance with a real in-lab experimental platform, consisting of a fuel cell test stand and a unit test fuel cell, the detail of which is presented in Chapter Four. Figure 3-2 depicts the simplified and generalized diagram of a fuel cell system. Since identical gas

supplying pipelines are employed at both sides in the fuel cell test stand, only the gas supplying system at the cathode side is depicted.

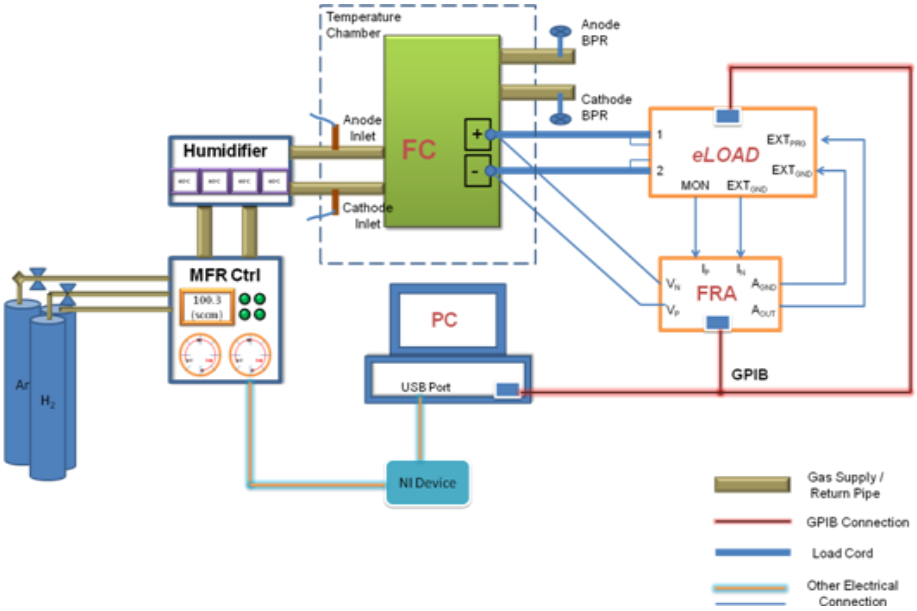


Figure 2-1Schematic of the Experimental Setup

The operation of the system can be briefly described as follows: the mass flow controller (MFC) controls the mass flow rate of the reactant gases, which are supplied by the supplying pipelines (or supply manifold in fuel cell stack system) to the humidifier (generalized as water injection), after which the reactant gases are supplied to the electrodes of the fuel cell via channels. The GDL facilitates even distribution to the catalyst-coated membrane, and the catalyst accelerates the oxidation and reduction of the reactants, which are the primary reaction desired for fuel cell operation. The unconsumed reactants and product (water in vapor or liquid form) finally exit the fuel cell and are released into the environment through exhaust pipelines (or return manifold in fuel cell stack system).

The main assumptions made for the model developed in this dissertation are the following:

1) Both cathode and anode sides of the fuel cell are open-ended;
2) All the gases obey the ideal gas law;
3) The water produced at the cathode catalytic site is in the form of vapor;
4) Membrane transports only water vapor between two electrodes, though liquid water may be present at the electrodes;
5) There is no liquid water flowing into the fuel cell flow channel, i.e., flooding before fuel cell is not considered;
6) The fuel cell is largely operating under constant temperature in isothermal condition.

Assumption 1) is based on the lab test equipment structure in reality for the convenience of experimental study; assumptions 2) ~ 4) are common assumptions made for PEM fuel cells [76]; assumption 5) is valid when appropriate preheating of the inlet reactants is employed in the fuel cell auxiliary system. Faults related to preheating could happen, resulting in pre-flooding issue in the system, however, for analysis simplicity, this specific case is not considered, thus assumption 5); assumption 6) is justified because the heat management in this research is achieved by an environmental chamber capable of maintaining the temperature of everything contained in it ideally within a very small range around the set point.

## 2.2 GENERAL PIPE/DUCT MODEL

In a fuel cell system, reactants are replenished and product removed from the fuel cell continuously with the help of gas supplying system. The electrochemical process in the fuel cell is very fast (time constant $10^{-19}$ sec), therefore can always be neglected in the analysis of dynamics, while the heat conduction process is typically very slow (time constant $10^{3}$ sec) and therefore can be treated as quasi-static. For control and diagnostic design purposes, the most important process to be considered is the reactant / product mass transport process dynamics.

In this section, a general model for generic pipe gas flow is presented based on the fluid dynamics principles, with the focus on the relationship between the mass flow rates and the pressures at the inlet and outlet of a pipe. It is shown that the supplying / exhaust pipe models can be obtained through simplification to the general model according to their particular geometric property. With some modification, the fuel cell flow channel model is obtained in the next section by taking into account the mass exchange occurring across the channel/GDL interface.

Figure 2-2 shows a general pipe with length $L$ (in 1D), in which a fluid is flowing from left to right under the driven force of pressure drop across the channel. We denote mass flow rates and the pressures at the inlet and outlet as $W_{in}, W_{out}, p_0, p_N$ respectively, the distance from the channel inlet as $x$, and the density of the fluid at $x$ as $\rho$.

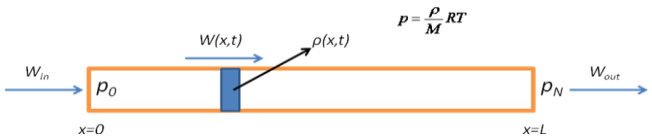


Figure 2-2 Pressure drop of a general pipe

For a general pipe filling with flowing fluid, the frictional pressure drop at steady state can be represented as[77]

$$\frac{dp}{dx} = \frac{2\chi \cdot \bar{u} \cdot \mu}{D_h^2} \tag{2.1}$$

where $p$ is the pressure at $x$, $\chi$ is a dimensionless constant depending on the geometry of the pipe cross section (for circular channels $\chi = 16$), $D_h$ is the hydraulic diameter of the fuel cell flow channel (m), $\mu$ is the fluid viscosity (kg/m s), $\bar{u}$ is the mean flow velocity of the fluid (m/s). In terms of mass flow rate $W$ (kg/s), $\bar{u} = \frac{W}{A \cdot \rho}$, where $A$ is the cross sectional area of the channel ($m^2$), and $\rho$ is the fluid density ($kg/m^3$) at ($x$,$t$), the partial derivative of which w.r.t. time is

$$\frac{\partial \rho}{\partial t} = -\frac{1}{A}\frac{\partial W}{\partial x} \tag{2.2}$$

For ideal gas, $p = \frac{\rho}{M}RT$, with $M$ being the molar mass of the flowing gas (kg/mol), $R$ being the universal gas constant (J/mol K) and $T$ being the absolute temperature (K). Substituting the ideal gas law in (2.1) and (2.2) results in

$$\begin{cases} \dfrac{\partial p}{\partial t}\left(\dfrac{AM}{RT}\right) = -\dfrac{\partial W}{\partial x} \\ -\dfrac{\partial p}{\partial x} = kW(x) \end{cases} \tag{2.3}$$

where $k$ can be calculated as $k = \frac{2\chi \cdot \mu(T)}{D_h^2 \cdot A \cdot \rho} = \frac{2\chi \cdot \mu(T) \cdot R \cdot T}{D_h^2 \cdot A \cdot M \cdot p}$, here $\mu$ is explicitly expressed as a function of the temperature. As in fuel cell flow gas streams are almost always gas mixture (e.g. in cathode side of PEMFC, the gas mixture is composed of

oxygen, nitrogen and water vapor) instead of pure gas, the viscosity of the gas mixture would then dependent on the components of the mixture, as well as the mixture's absolute temperature.

In this model, we use the following equation (by Sutherland's law) for viscosity calculation of a single gas species

$$\frac{\mu_j}{\mu_{j0}} \approx \left( \frac{T}{T_{0j}} \right)^{1.5} \frac{T_{0j} + S_j}{T + S_j} \tag{2.4}$$

where $\mu_{j0}, T_{0j}, S_j$ can be obtained from experiments or kinetic theory. Table 2-1 gives the parameter values for relevant fluid species ([77]).

Table 2-1 Parameter for viscosity calculation

| Substance | $\mu_0$ ($10^{-6}$ kg/m s) | $T_0$ (K) | $S_j$ |
|---|---|---|---|
| $H_2$ | 8.411 | 273 | 97 |
| $O_2$ | 19.19 | 273 | 139 |
| $N_2$ | 16.63 | 273 | 107 |
| Air | 17.16 | 273 | 111 |
| $H_2O$ (vapor) | 11.2 | 350 | 1064 |

We then calculate the viscosity of a gas mixture using the following equation,

$$\mu_{mix} = \sum_{i=1}^{n} \frac{y_i \mu_i}{\sum_{j=1}^{n} y_j \Phi_{ij}} \tag{2.5}$$

where $n$ is the total number of species in the mixture, $y_i$ is the mole fraction of species $i$, and $\Phi_{ij}$ is a dimensionless number given by

$$\Phi_{ij} = \frac{1}{\sqrt{8}}\left(1+\frac{M_i}{M_j}\right)^{-1/2}\left[1+\left(\frac{\mu_i}{\mu_j}\right)^{1/2}\left(\frac{M_i}{M_j}\right)^{1/4}\right]^2.$$

In equation(2.3), $k$ depends on many factors including the properties of the gas species, the channel geometry, the gas temperature and also the absolute gas pressure. For simplicity, we assume constant $k$ value in the following calculations. In actual fact, for a general pipe, the first three factors affecting $k$ are indeed fixed, and using the mean value of the inlet and outlet pressures in the calculation of $k$ results in very good approximation.

Even with the assumption that $k$ is constant, the PDEs in equation(2.3) can be hard to solve due to varying boundary conditions; and also, since the model is developed for control and diagnostics purpose, we aimed at obtaining a lumped model instead of a distributed one, for that the solution to the PDEs, i.e. detailed mass flow rate or pressure profile along the channel length, incurs only unnecessary computation complexity for control and diagnostic scheme design. The only variables of interest in this general pipe model are the mass flow rates and the pressures at the inlet and outlet $W_{in}, W_{out}, p_0, p_N$. We sought to convert the PDEs in (2.3) to ODEs, with $W_{in}, p_N$ as the model inputs and $W_{out}, p_0$ as the outputs.

By dividing the pipe in discussion into $N$ equal sections, and manipulating the resulted system of ODEs, we can finally manage to approximate the $N$-th order linear

time invariant (LTI) system with the following two first order transfer functions as $N$ goes to infinity (detailed in Appendix section).

$$\begin{cases} p_0 = \dfrac{kL}{T_1 s+1} W_{in} + \dfrac{1}{T_1 s+1} p_N \\ W_{out} = \dfrac{1}{T_1 s+1} W_{in} - \dfrac{2}{kL}\left(1 - \dfrac{1}{T_1 s+1}\right) p_N \end{cases} \tag{2.6}$$

where $T1$ is the time constant of the simplified first order system, given by $T_1 = \frac{1}{2} k \cdot L^2 \cdot \frac{A \cdot M}{R \cdot T}$.

For the simplicity of illustration and to gain further physical insight to the gas supplying system, we put the general pipe model (2.6) in analogy to an electrical ciruit [25] of second order as shown in Figure 2-3, with pressures compared to voltages and mass flow rates to currents. It then became clear that $k\,L$ constitutes the whole frictional resistance to the flowing gas stream, and that the volume to be filled leads to the gas filling dynamics, whose time constant is determined by the friction resistance along the channel ($k\,L$) and the volume of the channel ($L\,A$) combined.

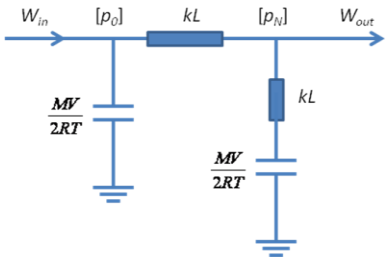


Figure 2-3 *RC* second-order electrical circuit analogy of general pipe model

The relation between pressure drops at junctions of pipes or nozzles and the local mass flow rates could be approximated linearly by introducing a frictional nozzle

constant $k_j$ ($j$ = *in* for inlet nozzle constant, and $j$ = *out* for outlet nozzle constant), i.e. $\Delta p = k_j W$, when the pressure drop is relatively small. The diagram in Figure 2-3 can thus be expanded by including the nozzle constants at both inlet and outlet of a pipe, as shown in Figure 2-4.

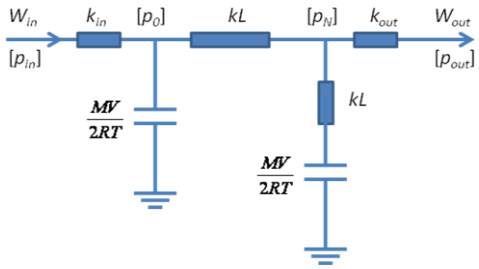


Figure 2-4 Electrical circuit analogy of general pipe model with inlet and outlet frictional nozzle constant

Figure 2-5 presents the test data obtained by feeding a fuel cell with step-profile gas streams, $H_2$ at anode side and air at cathode side, and measuring the pressures at the channel inlets. The pressure reading is seen to hold a strong linear relation with the mass flow rate, justifying the linear approximation of the frictional nozzle constants. Also, note that under higher pressures, the slopes of the fitted lines are lower, indicating a smaller friction loss. This can be explained by the formula $k = \frac{2\chi \cdot \mu(T) \cdot R \cdot T}{D_h^2 \cdot A \cdot M \cdot p}$ given before, which predicts lower friction coefficient at higher pressure.

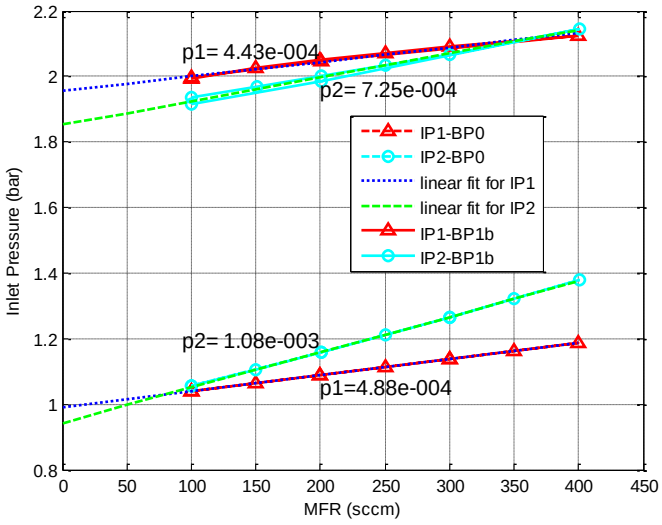


Figure 2-5 Inlet pressure w.r.t. steady-state MFR at different back pressures

By defining $\alpha_k = \frac{kL}{k_{out}}$, it can be shown that when $\alpha_k \ll 1$, the model represented by Figure 2-4 can be further simplified to a first-order model as depicted in Figure 2-6, which actually corresponds to gas supplying pipelines, or lumped manifolds, whose channel cross section areas are relatively large, resulting in small friction loss; and when $\alpha_k$ is comparable to 1 or even greater than 1, model in Figure 2-4 can be simplified to that in Figure 2-7, where the model dynamics is negligible, examples may include a unit fuel cell flow channel, due to its very small cross section area.

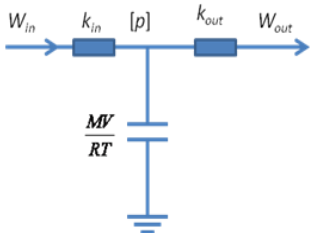


Figure 2-6 First order simplification of Figure 2-4 without channel friction resistance when $\alpha_k \ll 1$

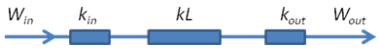


Figure 2-7 Static pipe model with channel friction resistance when $\alpha_k$ is comparable to or greater than 1

## 2.3 GAS DYNAMICS IN FC FLOW CHANNELS

Fuel cell flow channels differ from a general flow field, or pipe, in that one side of the channel is not closed but open to gas diffusion media. Therefore, in addition to convective flow inside the flow channel, there is also diffusive flow across the open side of the channel, driven by the concentration gradient across the open area. Also different from the gas stream flowing in a general pipe, composition in the gas mixture along a fuel cell flow field varies due to the mentioned mass exchange, thus dynamics of each component need to be considered separately. Equation (2.7) describes the gas dynamics at the fuel cell cathode.

$$\begin{cases} -\dfrac{\partial p}{\partial x} = kW(x) \\ p = p^{O_2} + p^{N_2} + p^{v} \\ \dfrac{\partial p^{s}}{\partial t} = \dfrac{RT}{AM^{s}} \cdot \left( -\dfrac{\partial W^{s}}{\partial x} - w_{\mathrm{c2g}}^{s} \right) \\ W = W^{O_2} + W^{N_2} + W^{v} \\ W^{s} = W \cdot \dfrac{p^{s} M^{s}}{p^{O_2} M^{O_2} + p^{N_2} M^{N_2} + p^{v} M^{v}} \end{cases} \tag{2.7}$$

In the above equations, the superscript $s=O_2$, $N_2$, $v$, representing respectively oxygen, nitrogen and vapor component in the gas mixture at cathode side; $w_{\mathrm{c2g}}^{s}$ (kg/s·m) is the diffusive mass flow rate in unit length along the channel across the open area interfacing flow channel and GDL for species $s$ (O2 or vapor), where c2g stands for

"channel to GDL". The total diffusive mass flow rate for species *s* along the channel, denoted as $W_{\mathrm{c2g}}^{s}$, can then be represented as

$$W_{\mathrm{c2g}}^{s} = \int_{x=0}^{L} w_{\mathrm{c2g}}^{s} dx = \int_{x=0}^{L} \bar{h}^{s} \frac{dp^{s}}{dz} dx \tag{2.8}$$

where $\frac{dp^{s}}{dz}$ is proportional to the concentration gradient across the open interfacial area (*z* is the coordinate axis perpendicular to the MEA area), and $\bar{h}^{s}$ depends on the diffusivity at the interface and the width of the open area.

Discretizing (2.7) and then reducing the model order turns out to be too complicated and the approach is not adopted here. Simulation results show that, by discretizing the channel to only a small number of sections ($n = 5$), good approximations can usually be attained. However, it should be noted that, minimum discretization is desired because each section to be added would introduce 3 (actually more, if considering liquid phase water) state variables and thus incur more computation burden especially for control and diagnostic applications. In this dissertation, the channel is divided into two sections only (Figure 2-8) for simplicity.

Figure 2-8 illustrates the convective flow, as well as the diffusive flow of the gas mixture in the cathode channel of a fuel cell, divided into two parts. The lumped pressures $p_1$, $p_2$ are assumed to occur at $x = L/4$, and $x = \frac{3}{4} \cdot L$, i.e., the middle of the corresponding section. $p_{\mathrm{GDL}}^{O_2}$, $p_{\mathrm{GDL}}^{v}$ are the partial pressures of O2 and vapor in the GDL, and $W_{\mathrm{c2g}}^{(1)}, W_{\mathrm{c2g}}^{(2)}$ are the mass flow rates of gas mixture (including O2 and vapor, while N2 is not considered in the mass exchange between channel and GDL) into the GDL from

the former and latter part of the channel, respectively. $W_{ch}$ is the mass flow rate at $x = L/2$ .In the following model derivation, only gas dynamics of the mixture components are considered, while liquid phase water is discussed in the next section.

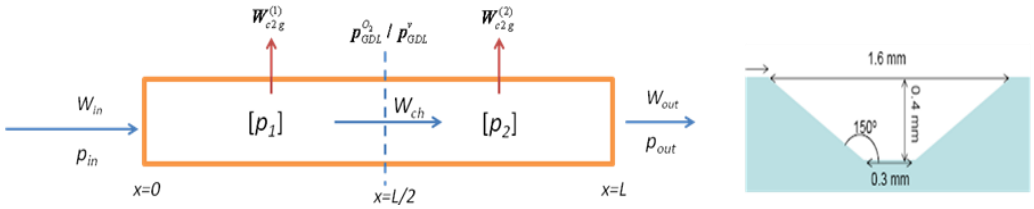


Figure 2-8 Diagram of convective and diffusive flow of gas mixture in cathode channel (perpendicular / cross sectional view)

In Figure 2-8, we have for the friction loss along the channel that

$$\begin{aligned} p_1 - p_2 &= \frac{kL}{2} \cdot W_{\text{ch}} \\ p_i &= p_{(i)}^{O_2} + p_{(i)}^{N_2} + p_{(i)}^{v} \qquad (i = 1, 2) \end{aligned} \tag{2.9}$$

and according to mass conservative law, the dynamics of the gas component is given by

$$\begin{aligned} \frac{dp_{(1)}^{s}}{dt} &= \frac{2RT}{M^{s} V_{\text{ch}}} \left( W_{\text{in}}^{s} + W_{src(1)}^{s} - W_{\text{c2g(1)}}^{s} - W_{\text{ch}}^{s} \right) \\ \frac{dp_{(2)}^{s}}{dt} &= \frac{2RT}{M^{s} V_{\text{ch}}} \left( W_{\text{ch}}^{s} + W_{src(2)}^{s} - W_{\text{c2g(2)}}^{s} - W_{\text{out}}^{s} \right) \end{aligned} \tag{2.10}$$

where $s$=$O_2$, $N_2$, $v$, and the diffusive mass flow rate from the flow channel to the GDL for species $s$ are

$$\begin{aligned} W_{\text{c2g(i)}}^{O_2} &= h_{(i)}^{O_2} \left( p_{(i)}^{O_2} - p_{GDL}^{O_2} \right) \\ W_{\text{c2g(i)}}^{N_2} &= 0 \\ W_{\text{c2g(i)}}^{v} &= h_{(i)}^{v} \left( p_{(i)}^{v} - p_{GDL}^{v} \right) \end{aligned}$$

Also in the above equations, source terms $W^s_{src(i)}$ describe the mass production or mass vanishing due to phase transformation, e.g., vapor produced by water transformation from liquid to gas phase (evaporation process). In fuel cells, evaporation rate and condensation rate of water in different phases are the only source terms needed to be considered in the mass conservation equations. Thus for $s$=$O_2$, $N_2$, $W^s_{src(i)} = 0$, while for vapor we have

$$W^v_{src(i)} = W^{(i)}_{\text{evap}} = M^v \cdot R^{(i)}_{\text{evap}} \left[ V_{\text{ch}}/2 - V^{(i)}_{\text{l,ch}} \right] \tag{2.11}$$

where $M^v = M_{H_2O}$ is the molar mass (kg/mol) of water, $V^{(i)}_{\text{l,ch}}$ the liquid water volume ($m^3$) in the $i$-th section of the channel, $R^{(i)}_{\text{evap}}$ the volumetric evaporation rate [mol/($m^3$ s)] in that section, and is given by the following equation

$$R^{(i)}_{\text{evap}} = \begin{cases} \gamma_{\text{evap}} \dfrac{p^{v,sat}_{(i)} - p^v_{(i)}}{RT} & \text{if} \quad V^{(i)}_{\text{l,ch}} > 0 \\ \min\left\{ 0, \gamma_{\text{evap}} \dfrac{p^{v,sat}_{(i)} - p^v_{(i)}}{RT} \right\} & \text{if} \quad V^{(i)}_{\text{l,ch}} = 0 \end{cases} \tag{2.12}$$

where $\gamma_{\text{evap}}$ is the volumetric evaporation coefficient ($s^{-1}$), which is a positive constant. From the above equation, $R^{(i)}_{\text{evap}}$ is seen to be proportional to the difference between the saturation pressure of vapor and the actual vapor partial pressure at a certain location. When the vapor partial pressure exceeds the saturation pressure, condensation results and $R^{(i)}_{\text{evap}} < 0$. Note that when there is no liquid water present in the channel ($V^{(i)}_{\text{l,ch}} = 0$), evaporation could not happen; this is incorporated in the model by imposing the constraint $R^{(i)}_{\text{evap}} \le 0$ under such condition.

The volumetric evaporation coefficient $\gamma_{\text{evap}}$ being constant all the time is normally based on the homogeneity assumption requiring, in the evaporation case, that a certain amount of liquid water is present and uniformly distributed in the discussed space. To address the loss of this homogeneity when the volume of the liquid water is extremely small, a correction factor $o_{evap}\left(V_l\right)$ can be included to modify the volumetric evaporation coefficient when the evaporation rate $R_{\text{evap}} > 0$ . $o_{evap}\left(V_l\right)$ is plotted in Figure 2-9, where $V_{l,\varepsilon}$ is a very small number that is arbitrarily chosen here.

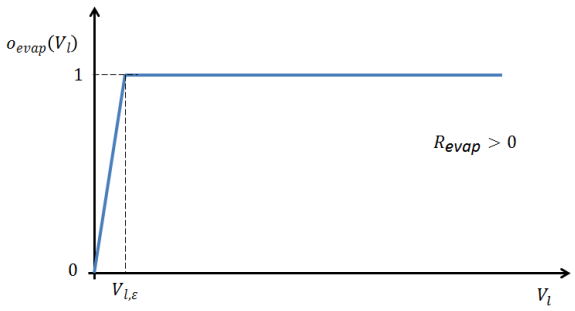


Figure 2-9 Evaporation correction factor when $R_{\text{evap}} > 0$

The composition of the gas mixture flowing out of a section of channel is considered to be the same as the one inside the section, under the lumped parameter assumption. In(2.10), the mass flow rate of species *s* at the outlet of the former and the latter sections of the channel can then be written as

$$W_{\text{ch}}^{s} = W_{ch} \cdot \frac{p_{(1)}^{s} M^{s}}{p_{(1)}^{O_2} M^{O_2} + p_{(1)}^{N_2} M^{N_2} + p_{(1)}^{v} M^{v}}$$
$$W_{\text{out}}^{s} = W_{out} \cdot \frac{p_{(2)}^{s} M^{s}}{p_{(2)}^{O_2} M^{O_2} + p_{(2)}^{N_2} M^{N_2} + p_{(2)}^{v} M^{v}} \tag{2.13}$$

Utilizing the electrical circuit analogy as in Figure 2-4, we can represent the above equations ((2.9),(2.10),(2.13)) by the electrical circuit in Figure 2-10.

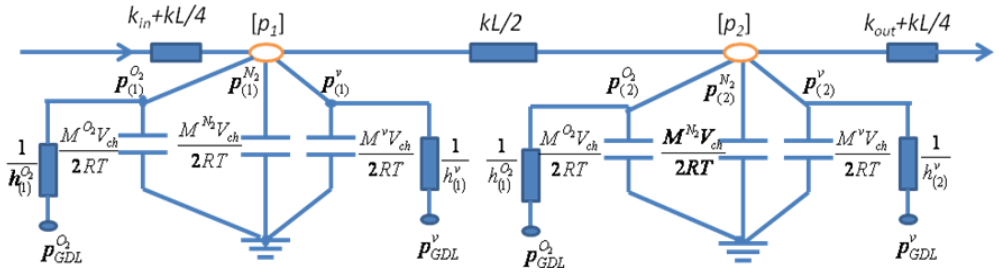


Figure 2-10 Electrical circuit analogy of fuel cell channel with inlet and outlet nozzle constants

## 2.4 LIQUID WATER IN FC FLOW CHANNELS

Humidity management is a critical, and also delicate, issue in fuel cell system, while a well humidified membrane is always desired for good ionic conductivity, excess liquid water accumulation at other locations inside the fuel cell leads to flooding, which also compromises the performance of the fuel cell. As pointed out in the work from Kumbur et al. ([78]), according to different locations of water accumulation, three types of flooding can be identified in PEM fuel cells, namely i) catalyst layer flooding, ii) GDL flooding, and iii) flow field flooding. Since the reactant flows carry no liquid water entering the flow field, flooding in flow field is usually caused by water transported through GDL to flow channel under capillary pressure gradient. The liquid water thus entering the channel can reside on the surface of the GDL and also on the other walls of the channel in the form of droplets or water slugs (formed by coalesced droplets) with different sizes. Water accumulated in the channel (especially at the interface of the GDL and the channel, along with that inside the GDL) may hinder the reactant transport to the

catalyst layers where the reaction takes place and results in a higher mass concentration loss. In addition, the cross sectional area of the channel is effectively reduced due to the flow field volume occupation by liquid water, higher flow resistance results and leads to an increased parasitic pressure loss. This can be clearly seen in(2.9), where the flow resistance is proportional to the parameter $k = \frac{2\chi \cdot \mu(T)}{D_h^2 \cdot A \cdot \rho}$, which in turn is inversely proportional to the square of the cross sectional area ( $D_h^2 \sim A$).

Two phase flow of water is considered in this dissertation to capture such phenomena as flooding in the GDL and the flow channel, as well as their effects on the fuel cell performance. Vapor dynamics in the fuel cell channel has been addressed along with other reactant gas in the last section, where the liquid water volume $V_{\text{l,ch}}^{(i)}$ is used as a constraint condition on the water evaporation rate. Also, as mentioned above, $V_{\text{l,ch}}^{(i)}$ is used to modify the effective cross sectional area of the flow field, as shown in(2.14) , based on the simplified assumption that the liquid water inside the channel is evenly spread along the length of the flow field.

$$A_{\text{ch,eff}}^{(i)} = A_{\text{ch}}^{(i)} - \frac{2}{L} \cdot V_{\text{l,ch}}^{(i)} \tag{2.14}$$

The dynamics of the liquid water volume can be modeled by employing the mass conservation law:

$$\frac{dV_{\text{l,ch}}^{(i)}}{dt} = \frac{1}{\rho_{H_2O}} \left( W_{\text{l,ch,in}}^{(i)} + W_{\text{l,g2c}}^{(i)} - W_{\text{evap}}^{(i)} - W_{\text{l,ch,out}}^{(i)} \right) \tag{2.15}$$

where $\rho_{H_2O}$ is the density of liquid water (kg/m$^3$), $W_{\text{l,ch,in}}^{(i)}$ and $W_{\text{l,ch,out}}^{(i)}$ are the liquid water mass flow rate at the inlet and outlet of the *i*-th section of the channel respectively, $W_{\text{evap}}^{(i)}$ the evaporation rate as in(2.11), and $W_{\text{l,g2c}}^{(i)}$ is the liquid water mass flow rate from GDL to flow channel, and is computed as the output of the GDL model presented in the next section.

According to our model assumptions, the mass flow rate of liquid water entering the fuel cell, or the first section of fuel cell channel, is zero, i.e., $W_{\text{l,ch,in}}^{(1)} = 0$, meaning no pre-fuel-cell flooding occurs in the reactants supplying systems. While $W_{\text{l,ch,in}}^{(2)} = W_{\text{l,ch,out}}^{(1)}$, and $W_{\text{evap}}^{(i)}$ calculated using(2.11), the only terms in (2.15) remained to be computed are $W_{\text{l,g2c}}^{(i)}$ and $W_{\text{l,ch,out}}^{(i)}$. The liquid water mass flow rates from GDL to channel (*i*-th section) $W_{\text{l,g2c}}^{(i)}$ depend on the gas diffusion media material and also the level of water saturation inside the GDL, and is thus determined in the GDL model presented in the next section. The mass flow rate of the liquid water flowing out of the *i*-th section of channel $W_{\text{l,ch,out}}^{(i)}$ is discussed in this section.

### *2.4.1 Typical assumptions for liquid water removal in control-oriented FC model*

The process of the liquid water being removed from a flow-through channel is actually very difficult to describe in the mathematical sense, due to the complexity of liquid water transport mechanism on different material surfaces (i.e., GDL surface, which is hydrophobic; and channel wall surface, which is hydrophilic), and also the uncertainties involved in this process, such as the forms and sizes of local water droplets,

and their emerging locations on the GDL surface, etc. Two extreme assumptions for simplification of this problem are typically seen in the literature of control-oriented fuel cell dynamic modeling:

1) No water exits channel in liquid form

2) All liquid water is purged instantly after formation

In reference [79], it is assumed that "The liquid water does not leave the stack and will either evaporate when the humidity drops below 100% or accumulate in the cathode". According to this assumption, the mass flow rate of liquid water exiting the fuel cell is zero.

For flow-through cathode channel, it is assumed in reference [23] that "almost all the liquid water condensed inside the cathode channel is dragged by the water exhaust". According to this assumption, the varying rate of liquid water mass inside the fuel cell channel is zero (or, without loss of generality, the mass of liquid water inside the fuel cell channel is zero).

Both assumptions above oversimplify the problem by generalizing special cases under certain specific operating conditions, thus avoiding the derivation of a global dynamic relationship between the liquid water flow along, and out of, the channel and the pneumatic operating conditions inside the fuel cell flow field. Essentially, the first assumption is valid only under low reactant mass flow rate with low liquid water production rate, and would overestimate the amount of liquid water present in the channel in most cases; the second assumption, on the contrary, requires very high reactant mass flow rate for the instant purging, thus underestimating the liquid water volume at normal

operating conditions. In order to study the effect of the liquid water inside the channel on the temporal performance of a fuel cell, the developed fuel cell dynamic model should allow the liquid water to accumulate in, and also be removed out of, the channel, necessitating the relaxation of the assumption on the channel liquid water and incorporation of a module that describe the liquid water removal process.

### *2.4.2 Water droplet removal from GDL surface*

Optical diagnostic approaches are capable of directly visualizing the liquid water behavior in fuel cell flow channels, and have higher spatial, temporal resolutions than indirect visualizing techniques like Neutron imaging, therefore are employed by many researchers to study the in-channel liquid water dynamics, qualitatively and quantitatively. Using experimental setup composed of transparent fuel cell (fuel cell equipped with transparent endplates), imaging system (video camera), and auxiliary controllable reactant supplying system ([78], [80], [81]), researchers are able to observe the characteristic steps in the channel liquid water buildup and removal process, such as droplets emergence on the GDL surface, droplet coalescence, droplet detachment by the gas core flow, and droplet wicking onto hydrophilic channel walls, also various flow pattern of connected capillary flow along the channel when more liquid water has accumulated inside the channel, including corner flow, annular flow, and slug flow with transient channel clogging. We discuss water droplet removal from GDL surface in this section, and connected capillary flow along channel in the next section.

Due to the GDL's hydrophobic nature, liquid water emerges and grows on the GDL surface in the form of droplets before swept away by the core gas flow, or

contacting the hydrophilic channel wall and then spreading onto it via capillary wicking. In [78], Kumbur et al. studied the influence of various factors, such as channel geometry, droplet size, surface tension, hydrophobicity of the diffusion media material and air flow rate, on the droplet behavior on the surface of the GDL, without considering the contact and interaction of the droplet with the channel walls. Force balance model is established for a single droplet resting on the GDL surface, taking into account adhesion force (surface tension force) and drag force, which is composed of pressure force created by the pressure gradient in the flow field and shear force. The model is used to predict the effect of operating conditions and material properties (e.g., PTFE treatment) on the contact angle hysteresis (measure of droplet instability, defined as the difference of advancing and receding contact angles), and is validated with experimental data obtained by employing visualization of a water droplet under an imposed shear flow. In[81], force balance model with only the shear force as the drag force is employed to analyze the detachment droplet diameter, assuming constant droplet contact angle (or equivalently, constant hydrophobicity of the diffusion media material), and constant hysteresis angle. Since both adhesion force and drag force are functions of the droplet diameter, linear and quadratic respectively, there exists a detachment droplet diameter $d_{dd}$, for constant gas stream, beyond which the drag force would exceed the adhesion force, detaching the droplet from the surface. Reversely, for a certain droplet diameter, there corresponds a critical gas velocity $\overline{u}_c$.

The relationship between the detachment droplet diameter $d_{dd}$ and the critical gas velocity $\overline{u}_c$, given in[81], is as follows,

$$3+\log_{10} d_{dd} = -2.59\log_{10} \bar{u}_c + K_{\text{cf}} - 1.59\log_{10}\left(1+5.2\,\text{Re}_{dc}^{-0.63}\right) \tag{2.16}$$

where $\text{Re}_{dc} = \dfrac{\rho_g \cdot \bar{u}_c \cdot d_d}{\mu_g}$ is the critical Reynolds number for droplet, $\rho_g, \mu_g$ are the density and viscosity of the gas flowing in the channel. $K_{\text{cf}}$ is a correction factor close to 1, which varies for different GDL materials and must be experimentally determined. In this dissertation, $K_{\text{cf}} = 1$ is assumed.

By numerically solving(2.16), the critical Reynolds number as a function of the droplet diameter in the anode / cathode channel are plotted in Figure 2-11. Note that equation (2.16) only applies when the water droplet stays clear of the channel walls and detaches from the GDL surface through the shear force exerted by the gas core flow. For channel geometry of the fuel cell used in this research, the maximum droplet diameter before the droplet touches and interacts with the channel bottom wall is calculated as 4.2mm, thus the span of the droplet diameter axis.

Under low or middle flow rate (with lower Reynolds number than the critical Reynolds number), droplet/wall interactions could occur before the droplet reaches its point of instability (defined as when the drag force exerted on the droplet starts to overcome the adhesion force), in this case, capillary wicking of the liquid water onto the hydrophilic channel walls is a principal mechanism for liquid water removal from the GDL surface. Indeed, the results of the studies above provide no direct method for calculating the flow rate of the liquid water draining out of the channel, for that deformation and removal of a water droplet from the GDL surface can only be considered as, in most cases, the beginning of a dynamic removal process of the liquid water out of

the channel. After the droplet reaches its point of instability and detaches from the GDL surface, two different consequences could follow, 1) the droplet contacts the channel wall and attaches to it, or 2) the droplet rolls over the GDL surface. In either case, the droplet may merge with other droplets downstream in further movement before it finally leaves the channel, leading to other mechanisms of water removal from the channel, and making the analytic results from the force balance model on a GDL surface inapplicable.

Therefore, the interaction of the liquid water with the channel wall, which is hydrophilic, needs to be taken into account for effective calculation of the liquid water mass flow rate exiting the channel.

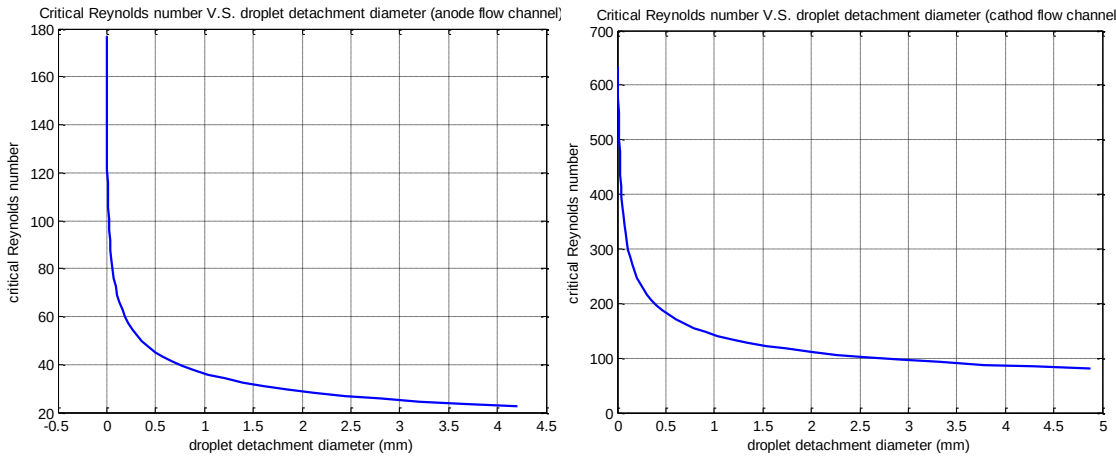


Figure 2-11 Critical Reynolds number with respect to the droplet detachment diameter in the anode channel (left) and in the cathode channel (right) respectively

### *2.4.3 Liquid water removal from channel – capillary flow along channel*

Under the low reactant flow rate and strongly wetting channel surface conditions typical in the PEM FC application, a principal mode of liquid water removal is by connected capillary flow when more water has accumulated inside the channel.

The capillary flow has long been studied in various research areas, such as oil trapping, due to its importance in fluid transport. It was found that in noncircular capillaries, characteristic of underground porous media, most of the wetting liquid flow occurs in the comer regions. In [82], the problem of low Reynolds number wetting liquid flow in a noncircular capillary occupied predominantly by a non-wetting gas phase is separated into individual corner flow problems. The two-dimensional hydrodynamic problem of wetting liquid flow along the corners has been solved numerically using a Galerkin finite elements technique. The solution to this problem is quantitatively expressed in terms of a dimensionless flow resistance, as given in [82], and rearranged here in(2.17).

$$W_{\mathrm{l,ch}} = \rho_l \frac{R_{gl}{}^2 \cdot \left(-\nabla p_l\right) \cdot S}{\beta_f \cdot \mu_l} \tag{2.17}$$

In the expression above, $\rho_l, \mu_l$ are the density and viscosity of the liquid water, $\nabla p_l$ the liquid pressure gradient that drives the flow, $R_{gl}$ is the mean radius of the gas-liquid interfacial curvature residing in the corner (annotated in Figure 2-12), $S$ the cross-sectional area of liquid flow, and $\beta_f$ is a dimensionless flow resistance, function of channel comer geometry (half angle $\alpha_h$ , and degree of roundness $Ro$), surface viscosity $\mu_s$, and contact angle $\theta_c$, as expressed below

$$\beta_f = \mathrm{f_{fr}}\left(\mu_s, \theta_c, \alpha_h, Ro\right) \tag{2.18}$$

The geometry of the channel corner is depicted in Figure 2-12, the roundness *Ro* is taken as zero here, indicating the corner is perfectly sharp, i.e., with zero roundness. The results for $\beta_f$ are presented in [82] in both graphic and tabular form.

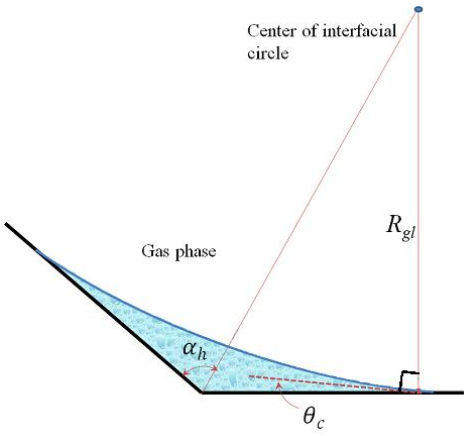


Figure 2-12 The geometry of the channel corner

The low Bond number assumption used in the capillary flow study restricts the analysis to pores of dimension less than ~1 mm, which is a condition met by typical channel geometry in the PEM fuel cell application. Also, due to the material properties distinction between GDL and channel walls, the liquid water tends to imbibe into the interior corners, which has been experimentally verified by visual study in [81], forming the corner flow as that in a general noncircular capillary occupied predominantly by a non-wetting gas phase. Thus the expression (2.17) for corner flow in the capillary is employed for the calculation of the mass flow rate of liquid water flow along the fuel cell channel in this dissertation.

It should be noted that, in the study above, given the environment in which the capillary is set, it is assumed that "a local depletion of surfactants at the interface will be healed more quickly by transfer of surfactant molecules to the interface from the bulk

solution than by tension-driven flow along the surface" because abundant liquid source is present at one end of the capillary. In contrast, liquid water in the fuel cell enters the channel by first emerging from the GDL surface and then imbibing into the corners formed by the channel side wall and top wall; when liquid water flows out of the channel by capillary flow and there is not enough water produced to replenish it, the connected flow may be separated, stopping the corner flow. Therefore in this dissertation, the capillary flow is assumed only when the amount of water present in the channel exceeds a certain threshold.

Theoretically, the minimum water volume to form connected capillary flow along the fuel cell channel depends solely on the channel geometry, based on the assumption that the liquid water accumulated in the flow field is evenly distributed along the channel. In the real fuel cell application, however, uneven liquid water production rate occurs along the flow field, and could even cause local clogging before a connected flow is formed.

### *2.4.4 Summary for channel liquid water removal*

The key steps in the channel liquid water buildup and removal process are recapped here:

1) Water droplet emerges and grows on GDL surface (Figure 2-13 (a));

2) Water droplet detaches from GDL surface, by two mechanisms;

   i. Under high gas flow rate, small droplets can be swept away from the GDL surface by the core gas flow, resulting in a mist flow in the gas channel.

ii. Under low to middle gas flow rate, the droplet could grow until its diameter becomes comparable with the channel dimension, followed then by capillary wicking from the hydrophobic GDL onto the hydrophilic channel walls.

3) Capillary flow of the liquid water along and out of the channel;

a. Corner flow

When enough water imbibes into the corner of the channel, connected capillary flow may form in the corner regions and drain the liquid water out. The corner flow is illustrated in Figure 2-13 (b). It can be seen that, due to the specific channel geometry (short width of the channel top wall), only a small amount of water can flow in corner flow mode.

b. Annular film flow

When more liquid water accumulates in the flow field, the channel top wall may also be covered by liquid water, forming the annular film flow, draining out of the liquid water. The annular flow is illustrated in Figure 2-13 (c).

The annular film flow of liquid water can sometimes turn into a water lens due to the instability of thick films, and then followed by channel clogging, which completely cuts off the reactant gas flow. The pressure on the upstream side of the water lens then builds up rapidly to break the lens and flushes the majority of water inside the channel out.

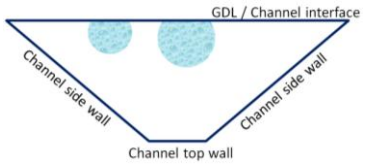


(a) Droplets emerge / grow on GDL surface

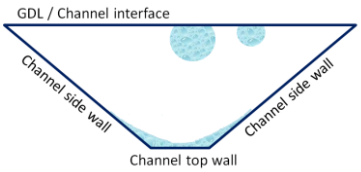


(b) Corner flow (Droplets on GDL surface)

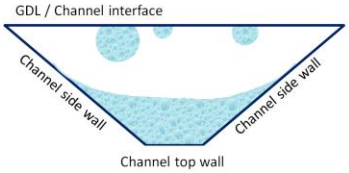


(c) Annular flow (Droplets on GDL surface)

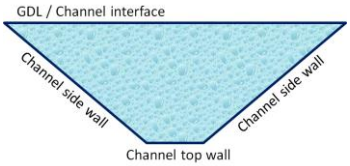


(d) Water slug – complete channel obstruction

Figure 2-13 Various patterns of liquid water distribution inside the channel (cross-sectional view)

Based on the liquid water behavior in the flow channel, the following assumptions are made:

- When only a small amount of water is present in the flow field (defined by a certain threshold), the mass flow rate of liquid water out of channel is zero under low to medium gas velocity, and proportional to the mean gas velocity when high reactant flow rate is applied;
- When the amount of water present in the channel exceeds a certain threshold (e.g., 20% of the flow channel volume), liquid water would be drained out via capillary flow, which would stop after the water volume dropped below another threshold (e.g., 5% of the flow channel volume);
- The stress exerted by the non-wetting gas phase on the interface is neglected;

- The liquid water inside the flow field is evenly distributed along the channel, the variation of the gas-liquid interfacial curvature with respect to axial position is assumed to be small;
- The effect of gradients in surface tension on the flow field is neglected;
- The ratio of gravity forces to interfacial forces is small, i.e., low *Bo* (explain) number assumption;
- The liquid pressure gradient in(2.17) is the same as the gas pressure gradient;

The mass flow rate of the liquid water flowing out of the *i*-th section of channel $W_{\mathrm{l,ch,out}}^{(i)}$ is finally given in the following equation

$$W_{\mathrm{l,ch,out}}^{(i)} = \begin{cases} 0 & \text{when } \mathrm{H}\left(V_l^{(i)}\right) = 0, \text{ and } \mathrm{Re}^{(i)} \le \mathrm{Re}_{\mathrm{th}}^{(i)} \\ \rho_l \dfrac{V_l^{(i)}}{V_{ch}/2} \cdot \bar{u}_c^{(i)} \cdot A_{ch} & \text{when } \mathrm{H}\left(V_l^{(i)}\right) = 0, \text{ and } \mathrm{Re}^{(i)} \ge \mathrm{Re}_{\mathrm{th}}^{(i)} \\ \rho_l \dfrac{{R_{gl}}^2 \cdot \Delta p^{(i)} \cdot S^{(i)}}{\beta_f \cdot \mu_l} & \text{when } \mathrm{H}\left(V_l^{(i)}\right) = 1 \end{cases} \tag{2.19}$$

For gas stream flowing inside the *i-th* section of the channel, the Reynolds number is defined as

$$\mathrm{Re}^{(i)} = \frac{\rho^{(i)} \cdot \bar{u}^{(i)} \cdot D_h^{(i)}}{\mu^{(i)}} = \frac{\rho^{(i)} \cdot D_h^{(i)}}{\mu^{(i)}} \frac{W^{(i)}}{A_{\mathrm{ch,eff}}^{(i)} \cdot \rho^{(i)}} = \frac{D_h^{(i)} \cdot W^{(i)}}{A_{\mathrm{ch,eff}}^{(i)} \cdot \mu^{(i)}} = \frac{4 \cdot W^{(i)}}{P_{\mathrm{ch,eff}}^{(i)} \cdot \mu^{(i)}}$$

$\mathrm{H}(\bullet)$ is a sharp (square) hysteresis function for the liquid water volume in the channel, with $V_{l,th1}^{(i)}$ and $V_{l,th2}^{(i)}$ as the thresholds, 1 and 0 as the outputs.

## 2.5 GDL MODEL

The GDL model used in this dissertation is a modified version of the one built by McKay et al. in [83] and [84], with the same three volume discretization. Two modifications are made here. The first difference lies in the nominal diffusivity for species *i* diffusing through species *j*. The binary gas diffusion coefficient, while taken as constants in [83],[84], is typically a strong function of temperature, pressure and molar mass of both species *i* and *j*, and can be explicitly described in the following equation base on the kinetic theory of gases:

$$D_{ij} = \frac{\left(p_{ci}p_{cj}\right)^{1/3}}{p}\sqrt{\frac{1}{M_i}+\frac{1}{M_j}}\,a_D\left(\frac{T}{\sqrt{T_{ci}T_{cj}}}\right)^{b_D}\left(T_{ci}T_{cj}\right)^{5/12} \tag{2.20}$$

The subscript *c* stands for critical, and $T_{ci}$, $T_{cj}$, $p_{ci}$, $p_{cj}$ are the critical temperatures and pressures of species *i* and *j*. *p* is the total pressure (atm). The critical properties of gases of interest in hydrogen PEMFC are given in the following table.

| Substance | $T_c$ (K) | $p_c$ (atm) |
|---|---|---|
| $H_2$ | 33.3 | 12.8 |
| $O_2$ | 154.4 | 49.7 |
| $N_2$ | 126.2 | 33.5 |
| $H_2O$ | 647.3 | 217.5 |

The second modification is with the discretized liquid water flow through GDL. In this dissertation, we have

$$W_{l,GDL}(k) = \frac{A_{fc}\rho_l K\left[K_{rl}(k)+K_{rl}(k+1)\right]}{2\mu_l}\,\frac{p_c(k)-p_c(k+1)}{\delta_{GDL}/3} \tag{2.21}$$

where $W_{l,GDL}(k)$ is the liquid water flow from the $k$ th GDL layer to the ($k$+1) th GDL layer, $p_c$ is capillary pressure, $\rho_l$ is the liquid water density, $K$ is the absolute permeability, $\mu_l$ is the viscosity of liquid water, $K_{rl}$ is the relative permeability of liquid water. Since the GDL is divided into three layers, for the variables with index number greater than 3, we have $p_c$ (4) = 0 and $K_{rl}$ (4) = 0.

For the details of the GDL model, interested readers could refer to the mentioned papers above.

## 2.6 MEA MODEL

In the MEA module, two fuel cell phenomena are modeled: the water transport through membrane captured by the membrane hydration model; and the reactant consumption and product generation at the catalyst sites captured by the catalyst layer model. We briefly describe the two models in the following respectively.

### *2.6.1 Membrane hydration model*

The membrane hydration model, or water transport model, can be widely found in the literature, as in[22]. The membrane is considered to be homogeneous and of lumped parameter. The flux of water vapor through the membrane, $N_{v,mem}$, accounts for the effects of both back-diffusion and electro-osmotic drag,

$$N_{v,mem} = n_d\left(\lambda_m\right)\frac{i}{F} - \alpha_w D_w\left(\lambda_m\right)\frac{\left(c_{v,ca} - c_{v,an}\right)}{t_m} \tag{2.22}$$

where $i$ is the current density, $F$ the Faraday constant, $n$d the electro-osmotic drag coefficient, $D$w the membrane water vapor diffusion coefficient, $\alpha_w$ is a correction factor

for $D$w, $\lambda_m$ the membrane water constant, $c_{v,ca}, c_{v,an}$ are the water vapor concentration at cathode and anode sides of the membrane, and $t$m the membrane thickness. Since discretized GDL model is adopted in this dissertation, $c_{v,ca}, c_{v,an}$ would be the vapor concentration at the closest GDL layer (three layers in total) to the membrane at cathode and anode sides.

More details on membrane hydration model can be found in literature such as [84].

### *2.6.2 Catalyst layer model*

The catalyst layer model bridges the gap between mass transportation module (GDL model) and electro-chemical module (cell V-I model) of the fuel cell system model. On one hand, catalyst layer model serves as the boundary conditions to the GDL model equations as to provide the rate of reactant consumption and product generation; on the other hand, the catalyst layer model is also supposed to output to the electro-chemical module the reactant / product concentrations at the catalyst sites where the two half electrode reaction processes take place.

The reactant consumption rate and product generation rate (kg/s) are given in the following equations, which constitute the first part of the catalyst layer model.

$$W_{\text{rct}}^{H_2} = M^{H_2} \frac{I}{2F} \tag{2.23}$$

$$W_{\text{rct}}^{O_2} = M^{O_2} \frac{I}{4F} \tag{2.24}$$

$$W_{\text{gen}}^{H_2O} = M^{H_2O} \frac{I}{2F} \tag{2.25}$$

where $I$ is the current given by $I = i \cdot A_{fc}$.

The second part of the catalyst layer model is omitted in this dissertation for simplification purpose. Specifically, the concentration of H2 and O2 at the catalyst sites are approximated by that in the inner most layer of the GDL, and the concentration of $H^+$ is assumed constant and its effect on the electrode reaction neglected. More precisely speaking, the proton concentration in the catalyst layer depends on the hydration at the same location and could vary as the current and/or the humidification level of the inlet reactant gases fluctuate. A simple proton dynamic model is considered in [85], but only empirical and current dependent, thus it is not incorporated in the fuel cell model here.

## 2.7 CELL VOLTAGE MODEL

In this section, we describe a physics-based model of unit cell voltage. While still following the simplicity principle to develop only 0-D model, more first principle laws are explored and advantages of incorporating the GDL model made use of. Compared to the fuel cell stack voltage model in [22], which is more empirical-prone, the model in this dissertation provides more insights in issues such as how the operating conditions and aging parameters can affect the cell performance.

The cell voltage under operation is the difference of the ideal voltage and various kinds of overpotentials, as described in the following equation

$$V_{\text{cell}} = E - \eta_{act} - \eta_{ohm} \tag{2.26}$$

where $E$ is the reversible cell voltage, which is the ideal voltage a fuel cell can produce by thermodynamic theory; $\eta_{act}$ is the overpotential due to activation loss; $\eta_{ohm}$ is the overpotential due to Ohmic loss.

Generally, in form, the overpotentials for electrochemical systems like fuel cells also include overpotential due to mass transport loss (or concentration loss overpotential $\eta_{conc}$) in addition to that of the activation loss and Ohmic loss, as seen in most literature. The inclusion of this term accounts for the concentration loss during mass transport when using operating conditions in the flow field instead of that at catalyst sites in cell voltage calculation. However, when mass transport component model (mainly GDL module) is incorporated in the fuel cell model to account for the concentration loss and the operating conditions at the reaction sites can be directly obtained and used, the term $\eta_{conc}$ should be left out of the cell voltage equation to avoid double counting. We explain this idea in more details as we describe each component part of the cell voltage individually in the following.

### *2.7.1 Reversible Cell Voltage*

For hydrogen fuel cell, the reversible cell voltage is given by

$$E = 1.229 - 0.85\times10^{-3}\left(T_{fc} - 298.15\right) + \frac{RT_{fc}}{2F}\ln\left[\frac{p^*_{H_2}\left(p^*_{O_2}\right)^{\frac{1}{2}}}{p_{H_2O}}\right] \tag{2.27}$$

where $p^*_{H_2}$ and $p^*_{O_2}$ are reactant partial pressures at catalyst layer, expressed in atm. Note in [22] and other literature where concentration loss overpotential is included, the

pressures in (2.27) are those at flow field instead of reaction sites. We use "*" to denote variables at catalyst layer in the following for emphasis.

### *2.7.2 Activation Loss*

Activation loss occurs at both electrodes in fuel cells, with its principle rooted in activation energy found in general chemical reactions. Under open circuit condition when no current is drawn and reactants concentration is maintained at a certain level, equilibrium electrical potential difference is established (after a transient $\ll$ 1ms) between each electrode and electrolyte, comprising the ideal reversible voltage between two electrodes ($E$), as represented by the following equation

$$E = \Delta\varphi_{\mathrm{c}}^{\mathrm{e}} + \Delta\varphi_{\mathrm{a}}^{\mathrm{e}} \tag{2.28}$$

where $\Delta\varphi_{\mathrm{c}}^{\mathrm{e}}$ is the equilibrium electrical potential difference between cathode and electrolyte and $\Delta\varphi_{\mathrm{a}}^{\mathrm{e}}$ is the equilibrium electrical potential difference between electrolyte and anode.

For an electrode at equilibrium state, cathodic (reductive) and anodic (oxidative) current with the same magnitude is flowing in opposite direction, at any time instant, to or from the electrode, resulting in zero net current. The magnitude of this current density (cathodic or anodic) is called exchange current density ($j_0$), and can be illustrated using the following simple electrode reaction, with $O$ representing some oxidant and $R$ the reductant.

$$R \underset{\text{backward}}{\overset{\text{forward}}{\rightleftharpoons}} O + ne^{-} \tag{2.29}$$

In the above redox reaction, $n$ moles of electrons would be transferred simultaneously (ideal assumption) between the chemical reactant and the electrode for every mole of $O$ being reduced or $R$ being oxidized. If the forward reaction rate is $v_{\mathrm{f}}$ (mol/cm$^2$/s) and the backward one is $v_{\mathrm{b}}$ (mol/cm$^2$/s), then the forward and backward current density (A/cm$^2$) are given in the following equations

$$\begin{aligned} j_{\mathrm{f}} &= nFv_{\mathrm{f}} \\ j_{\mathrm{b}} &= nFv_{\mathrm{b}} \end{aligned} \tag{2.30}$$

At equilibrium, we have

$$j_0 = j_{\mathrm{f}} = j_{\mathrm{b}} \tag{2.31}$$

i.e., the net current density $j = j_{\mathrm{f}} - j_{\mathrm{b}} = 0$.

In order for the net current to flow in a certain direction, the established equilibrium electrical potential difference across the electrode/electrolyte interface has to be altered to break the dynamic equilibrium, i.e., part of the equilibrium potential difference has to be sacrificed (fuel cell operation), or overpotential be added (electrolysis).

The term overpotential has been generalized to be used in both fuel cell and electrolysis modes for Galvanic cell, and is defined as the absolute value of the difference between the actual and equilibrium electrical potential difference, $\eta = \left|\Delta\varphi^{\mathrm{e}} - \Delta\varphi\right|$. In fuel cell mode, the overpotential due to activation ($\eta_{act} = \Delta\varphi^{\mathrm{e}} - \Delta\varphi$) is related to the current density by Butler-Volmer equation as in(2.32).

$$j = j_0 \left( e^{\alpha nF\eta_{act}/(RT)} - e^{-(1-\alpha)nF\eta_{act}/(RT)} \right) \tag{2.32}$$

where $\alpha$ is the transfer coefficient and depends on the shape of the potential energy diagram for the formation and decomposition of the activated state (explained later).

In the B-V equation, exchange current density ($j_0$) is seen to be crucial to the performance of the fuel cell electrode, and is usually determined by fitting experiment data at certain operation conditions. However, the dependence of the exchange current density on operation conditions at the electrode surface (temperature, reactant / product concentration) is not explicitly shown in the above B-V equation and needs to be exploited in more detail for modeling purpose by studying the kinetics of electrode process. As the activation loss at anode side is much smaller than that at cathode side for hydrogen PEMFC used in this research, only the latter is considered here.

The electrode reaction at cathode of the PEM fuel cell is as follows

$$O_2 + 4H^+ + 4e^- \underset{\text{backward}}{\overset{\text{forward}}{\rightleftharpoons}} 2H_2O \tag{2.33}$$

The actual electrode process is much more complex than that described above and usually involves many steps.

For simplicity, we assume the one step electron transfer reaction at cathode in this dissertation, with the activated surface complex represented by $C^{\ddagger}$, as shown in the following electrode formula

$$O_2 + 4H^+ + 4e^- \rightleftharpoons C^{\ddagger} \rightleftharpoons 2H_2O \tag{2.34}$$

By applying the theory of absolute reaction rates, and considering the double layer structure effect, the forward current density can be obtained as follows

$$j_{\mathrm{f}} = 4F\chi_1 \frac{k_B}{h_P} \exp\left(-\Delta\vec{G}_{\mathrm{f}}^{a0}/RT\right) p_{O_2}^{*} \left(c_{H^+}^{*} e^{-4F\varphi'/RT}\right)^4 \tag{2.35}$$

where $\chi_1$ is a constant coefficient, $k_B$ the Boltzmann's constant, $h_P$ the Planck's constant; $p_{O_2}^{*}$ and $c_{H^+}^{*}$ are reactant concentrations (pressure is equivalent to concentration) at electrode surface, $\varphi'$ is the potential difference across the diffuse double layer when taking into account the double layer structure and is used to modify the actual concentration of the ionic reactants (in this case $H^+$) that participate in the electron transfer reaction; $\Delta\vec{G}_{\mathrm{f}}^{a0}$ represents the electrochemical normal free energy of activation for the forward reaction, which is composed of two parts: the chemical normal free energy of activation ($\Delta G_{\mathrm{f}}^{a0}$) and the electric potential energy change from the reactant state to the activated complex state. If the electric potential at the location of the activated complex is $\varphi^a$, then $\Delta\vec{G}_{\mathrm{f}}^{a0}$ can be written as

$$\Delta\vec{G}_{\mathrm{f}}^{a0} = \Delta G_{\mathrm{f}}^{a0} + nF\left(\varphi^a - \varphi'\right) = \Delta G_{\mathrm{f}}^{a0} + nF\beta\left(\Delta\varphi_{\mathrm{c}} - \varphi'\right) \tag{2.36}$$

where $\beta$ is a factor that is essentially identical to $(1-\alpha)$, with $\alpha$ being the transfer coefficient introduced before.

Substitute (2.36) into(2.35), we then get

$$j_{\mathrm{f}} = 4F\chi_1 \frac{k_B}{h_P} \exp\left(-\Delta G_{\mathrm{f}}^{a0}/RT\right) p_{O_2}^{*} \left(c_{H^+}^{*} e^{-4F\varphi'/RT}\right)^4 \exp\left[-4F\beta\left(\Delta\varphi_{\mathrm{c}} - \varphi'\right)/RT\right] \tag{2.37}$$

Though by considering the double layer structure, the electrode process can be better described, the correction for the reactants concentration and electric potential using the double layer structure is uncertain and difficult to characterize. Also, under certain conditions, $\varphi'$ changes only slightly with the electrode potential, thus in this dissertation,

$\varphi'$ is treated as constant, i.e., independent of the reactant concentration and the overpotential at the electrode. By including all the $\varphi'$ terms into the constant coefficient $\chi_1$ (or alternatively neglecting the double layer structure and regarding $\varphi'=0$), (2.37)becomes

$$j_{\mathrm{f}} = 4F\tilde{\chi}_1 \frac{k_B}{h_P} \exp\left(-\Delta G_{\mathrm{f}}^{a0}/RT\right) p_{O_2}^{*} \left(c_{H^+}^{*}\right)^4 \exp\left(-4F\beta\Delta\varphi_{\mathrm{c}}/RT\right) \tag{2.38}$$

Substituting $\Delta\varphi_{\mathrm{c}} = \Delta\varphi_{\mathrm{c}}^{\mathrm{e}} - \eta_{act}$, and $\beta = (1-\alpha)$, we get

$$j_{\mathrm{f}} = 4F\tilde{\chi}_1 \frac{k_B}{h_P} \exp\left(\frac{-\Delta G_{\mathrm{f}}^{a0}}{RT}\right) p_{O_2}^{*} \left(c_{H^+}^{*}\right)^4 \exp\left[-4F(1-\alpha)\frac{\Delta\varphi_{\mathrm{c}}^{\mathrm{e}}}{RT}\right] \exp\left[4F(1-\alpha)\frac{\eta_{act}}{RT}\right] \tag{2.39}$$

At electrode equilibrium, $\Delta\varphi_{\mathrm{c}} = \Delta\varphi_{\mathrm{c}}^{\mathrm{e}}$, i.e., $\eta_{act} = 0$, and the forward current density becomes equal to the exchange current density

$$j_{\mathrm{f0}} = 4F\tilde{\chi}_1 \frac{k_B}{h_P} \exp\left(-\Delta G_{\mathrm{f}}^{a0}/RT\right) p_{O_2}^{*} \left(c_{H^+}^{*}\right)^4 \exp\left[-4F(1-\alpha)\Delta\varphi_{\mathrm{c}}^{\mathrm{e}}/RT\right] \tag{2.40}$$

The exchange current density is usually determined experimentally at some reference operation conditions. Suppose the temperature is maintained at a fixed level during the actual operation and is the same as the reference temperature, the exchange current density then depends only on the reactant concentration, with its value at reference concentration given as follows

$$j_{\mathrm{f0}}^{\mathrm{ref}} = 4F\tilde{\chi}_1 \frac{k_B}{h_P} \exp\left(-\Delta G_{\mathrm{f}}^{a0}/RT\right) p_{O_2}^{*\mathrm{ref}} \left(c_{H^+}^{*\mathrm{ref}}\right)^4 \exp\left[-4F(1-\alpha)\Delta\varphi_{\mathrm{c}}^{\mathrm{e[ref]}}/RT\right] \tag{2.41}$$

Note that in(2.40) the equilibrium electric potential $\Delta\varphi_{\mathrm{c}}^{\mathrm{e}}$ also depends on the reactant concentration by Nernst equation

$$\Delta\varphi_{\mathrm{c}}^{\mathrm{e}} = \Delta\varphi_{\mathrm{c}}^{\mathrm{e[ref]}} + \frac{RT}{4F}\ln\left[\frac{p_{O_2}^{*}\left(c_{H^+}^{*}\right)^4}{p_{O_2}^{*\mathrm{ref}}\left(c_{H^+}^{*\mathrm{ref}}\right)^4}\right] \tag{2.42}$$

By combining (2.40)(2.41)(2.42), and recognizing that $j_{f0} = j_0$, the dependence of the exchange current density on operation conditions at the electrode surface (reactant concentration) can be explicitly expressed as in the following equation

$$j_0 = j_0^{\text{ref}} \left[ \frac{p_{O_2}^*}{p_{O_2}^{*\text{ref}}} \left( \frac{c_{H^+}^*}{c_{H^+}^{*\text{ref}}} \right)^4 \right]^{\alpha} \tag{2.43}$$

In a similar way, backward current density at cathode can also be obtained, and we have the net current density as

$$\begin{aligned} j &= j_{\text{f}} - j_{\text{b}} \\ &= j_{\text{f0}} \exp\left[ 4F(1-\alpha)\eta_{act}/RT \right] - j_{\text{r0}} \exp\left[ -4F\alpha\eta_{act}/RT \right] \\ &= j_0^{\text{ref}} \left\{ \left[ \frac{p_{O_2}^*}{p_{O_2}^{*\text{ref}}} \left( \frac{c_{H^+}^*}{c_{H^+}^{*\text{ref}}} \right)^4 \right]^{\alpha} e^{4F(1-\alpha)\eta_{act}/RT} - e^{-4F\alpha\eta_{act}/RT} \right\} \end{aligned} \tag{2.44}$$

which is the B-V equation with explicit dependence on reactant concentration at the electrode surface.

When $\eta_{act}$ is not too small (greater than 30 mV), the second exponential term in the equation above (B-V equation) is negligible, and B-V equation can be approximated by

$$j = j_0^{\text{ref}} \left[ \frac{p_{O_2}^*}{p_{O_2}^{*\text{ref}}} \left( \frac{c_{H^+}^*}{c_{H^+}^{*\text{ref}}} \right)^4 \right]^{\alpha} e^{4F(1-\alpha)\eta_{act}/RT} \tag{2.45}$$

It should be noted that the current densities discussed above are all with respect to the actual catalyst surface area ( $A_{\text{cat}}$ ) instead of the nominal fuel cell active area ( $A_{\text{fc}}$ ), or

the electrode geometric area. The following conversion needs to be performed to get the current density with respect to electrode geometric area

$$j \times A_{\text{cat}} = i \times A_{\text{fc}} \Rightarrow i = j \frac{A_{\text{cat}}}{A_{\text{fc}}} = j \frac{A_{\text{cat}}^0}{A_{\text{fc}}} \frac{A_{\text{cat}}}{A_{\text{cat}}^0} = j \frac{A_{\text{cat}}^0}{A_{\text{fc}}} \xi_{\text{cat}} \tag{2.46}$$

where $A_{\text{cat}}^0$ is the catalyst surface area at the beginning of the fuel cell life, or $A_{\text{cat}}^0 = A_{\text{cat}}\big|_{t=0}$ , $\xi_{\text{cat}}$ is the electro-chemical active surface area degradation factor, representing the ratio of actual catalyst surface area over the original catalyst surface area. Substituting(2.45) into(2.46), the expression for the current density (with respect to $A_{\text{fc}}$ ) can be obtained

$$\begin{aligned} i &= j_0^{\text{ref}}\big|_{t=0} \times \frac{A_{\text{cat}}^0}{A_{\text{fc}}} \cdot \xi_{\text{cat}} \times \left[ \frac{p_{O_2}^*}{p_{O_2}^{*\text{ref}}} \left( \frac{c_{H^+}^*}{c_{H^+}^{*\text{ref}}} \right)^4 \right]^\alpha e^{4F(1-\alpha)\eta_{act}/RT} \\ &= i_0^{\text{ref}}\big|_{t=0} \times \xi_{\text{cat}} \times \left[ \frac{p_{O_2}^*}{p_{O_2}^{*\text{ref}}} \left( \frac{c_{H^+}^*}{c_{H^+}^{*\text{ref}}} \right)^4 \right]^\alpha e^{4F(1-\alpha)\eta_{act}/RT} \end{aligned} \tag{2.47}$$

In the above equation, $i_0^{\text{ref}}\big|_{t=0}$ represents the reference exchange current density determined at the beginning of the fuel cell life.

By assuming the concentration of $H^+$ only varies slightly around the reference level and neglecting its effect on the exchange current density, the above equation can be rewritten with overpotential as the function of the current density

$$\eta_{act} = \frac{RT}{4(1-\alpha)F} \ln \left[ \frac{i}{i_0^{\text{ref}}\big|_{t=0}} \times \frac{1}{\xi_{\text{cat}}} \times \left( \frac{p_{O_2}^{\text{ref}*}}{p_{O_2}^*} \right)^\alpha \right] \tag{2.48}$$

### *2.7.3 Ohmic Loss*

The overpotential due to Ohmic loss is simply based on the Ohmic law as follows

$$\eta_{ohm} = i \cdot A_{\text{fc}} \cdot R_{ohm} \tag{2.49}$$

where $R_{ohm}$ is the total Ohmic resistance ( $\Omega$ ) composed of the resistance of various fuel cell parts and can be written as

$$R_{ohm} = R_{ohm}^{mem} + R_{ohm}^{GDL} + R_{ohm}^{plate} + R_{ohm}^{contact} \tag{2.50}$$

where $R_{ohm}^{mem}$ is the Ohmic resistance of the polymer membrane to proton transfer; $R_{ohm}^{GDL}$ is the Ohmic resistance of the GDL, and $R_{ohm}^{plate}$ that of the bipolar plates, both to electron conducting; $R_{ohm}^{contact}$ represents the contact resistance between adjacent components, e.g., contact resistance between MEA and GDL.

While $R_{ohm}^{GDL}$ , $R_{ohm}^{plate}$ and $R_{ohm}^{contact}$ relies mainly on the structures and materials employed for the relevant components and can generally be considered as constants during fuel cell operation (though may be subject to change from corrosion during aging process on a much longer time scale), $R_{ohm}^{mem}$ depends strongly on the water content contained in the membrane, and in a relatively short time window (order of minute) can vary within a wide range due to membrane humidity cycling. A general expression of membrane resistance is given below

$$R_{ohm}^{mem} = \frac{t_m}{A_{\text{fc}} \cdot \sigma_m} = \frac{t_m}{A_{\text{fc}} \cdot \left(b_{11}\lambda_m - b_{12}\right) e^{b_2\left(\frac{1}{303} - \frac{1}{T_{fc}}\right)}} \tag{2.51}$$

In the above equation, $\sigma_m$ is called membrane conductivity and is a linear function of membrane water content $\lambda_m$ at fixed temperature, $\sigma_m$ is also seen as an increasing function of the membrane temperature (or the cell temperature for isothermal fuel cell model); $b_{11}$, $b_{12}$, $b_2$ are constants usually determined empirically.

### *2.7.4 The effect of leak current density on FC performance*

Even under open circuit with zero current, there is always an offset observed between the actual cell voltage and the theoretical reversible cell voltage. This can largely be attributed to the fuel crossover and internal currents across the membrane, the effects of which are essentially equivalent and can be combined by introducing internal current density or leak current density $i_{leak}$ into the activation loss overpotential expression, which modify (2.48) slightly into(2.52).

$$\eta_{act} = \frac{RT}{4(1-\alpha)F} \ln \left[ \frac{\left[ i + i_{leak}^{\text{ref}} \left( \frac{p_{H_2}^{*}}{p_{H_2}^{\text{ref}*}} \right) \right]}{i_0^{\text{ref}}\big|_{t=0}} \times \frac{1}{\xi_{\text{cat}}} \times \left( \frac{p_{O_2}^{\text{ref}*}}{p_{O_2}^{*}} \right)^{\alpha} \right] \tag{2.52}$$

The leak current density $i_{leak}$, though very small at MEA's fresh state, slowly but constantly grows during the aging of the fuel cell as the MEA deteriorate, and could lead to a catastrophic failure when the fuel cell meets its end-of-life.

### *2.7.5 Operating cell voltage*

By combining the reversible cell voltage and various irreversible losses (overpotentials), the fuel cell terminal voltage under operation as a function of current density can be written as follows

$$\begin{aligned} V_{\text{cell}} &= E - \eta_{act} - \eta_{ohm} \\ &= 1.229 - 0.85\times10^{-3}\left(T_{fc} - 298.15\right) + \frac{RT_{fc}}{2F}\ln\left[\frac{p_{H_2}^{*}\left(p_{O_2}^{*}\right)^{\frac{1}{2}}}{p_{H_2O}}\right] \\ &\quad - \frac{RT}{4\left(1-\alpha\right)F}\ln\left[\frac{\left[i + i_{leak}^{\text{ref}}\left(\frac{p_{H_2}^{*}}{p_{H_2}^{\text{ref}*}}\right)\right]}{i_0^{\text{ref}}\big|_{t=0}} \times \frac{1}{\xi_{\text{cat}}} \times \left(\frac{p_{O_2}^{\text{ref}*}}{p_{O_2}^{*}}\right)^{\alpha}\right] \\ &\quad - i\cdot A_{\text{fc}}\cdot\left[\left(\frac{t_m}{A_{\text{fc}}\cdot\left(b_{11}\lambda_m - b_{12}\right)e^{b_2\left(\frac{1}{303}-\frac{1}{T_{fc}}\right)}}\right) + R_{ohm}^{GDL} + R_{ohm}^{plate} + R_{ohm}^{contact}\right] \end{aligned} \tag{2.53}$$

### *2.7.6 Cell current calculation under voltage mode*

Most fuel cell models take load current as the model input and cell or stack voltage as output, as given in(2.53), with the assumption that the fuel cell is operated under current mode that dictates the cell current. A safer way to operate fuel cell in reality, however, is under voltage mode that dictates the cell terminal voltage instead, which is also the cycling mode adopted in the fuel cell test in this dissertation. A closed form solution to the current as function of the load voltage cannot be obtained by directly inverting(2.53). Thus to implement the voltage mode in Simulink or any other simulation software, an auxiliary electrical inductor is imagined to be added in the electrical circuit

between one terminal of the fuel cell and one terminal of the electronic load, as depicted in Figure 2-14.

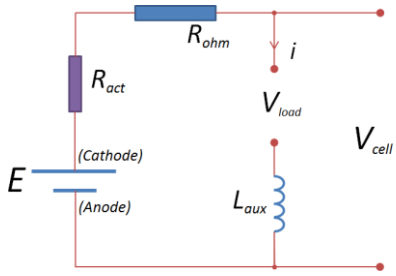


Figure 2-14 Simplified circuit diagram for the fuel cell electro-chemical module

With the imagined auxiliary inductor added into the circuit, the current density can now be treated as a state variable described by the following ordinary differential equation.

$$L_{aux}\frac{di}{dt} = V_{cell} - V_{load} \tag{2.54}$$

where *V*cell is given by(2.53). Equation (2.54) can then be implemented in Simulink to calculate fuel cell current with the load voltage as the model input.

When the inductance in the circuit diagram in Figure 2-14 is extremely small (*L*-aux = $10^{-5}$ is assumed here), the fast dynamics of the current can be neglected, and (2.54) degenerates into an algebraic equation (singular perturbation problem), the solution of which, called $\bar{i}$, is exactly the implicit solution of (2.53).

When *L*aux is small, the difference of $i$ and $\bar{i}$ is of the order of *L*aux itself, i.e. $i - \bar{i} = O(L_{aux})$ [86], thus can be ignored.

## 2.8 SYSTEM IDENTIFICATION

In this section, system parameters in the model are identified using real experimental data by essentially minimizing the differences between the model outputs and the actual system outputs. Due to the complexity and sensor limitation of the fuel cell system (including the balance of the plant, which here is the integrated fuel cell test stand), as well as a lack of dedicated *in-situ* diagnostic tool for measuring the water content inside the fuel cell (e.g., neutron imaging), model parameters in membrane/GDL hydration module (such as the membrane water vapor diffusion coefficient correction factor) assume the values of those in similar fuel cells found in literature ([84], [87]). Nominal geometries of the unit fuel cell, e.g., fuel cell active area, are employed in the model, while the equivalent electrical circuit parameter, the total Ohmic resistance, is obtained by fitting the EIS curves recorded by frequency response analyzer.

The system identification is carried out in two parts. First, the reactant gas supplying sub-model is identified with the pneumatic subsystem input/output data. The mass flow rate of the reactant gases at the mass flow controller (on both anode and cathode sides as shown in Figure 2-15) is taken as the subsystem's inputs, and channel inlet pressures as the system outputs, while the current drawn by the electric load is treated as a known disturbance. Second, utilizing the identified gas supplying system parameters, cell voltage model parameters, mainly in the activation loss module, are identified using cell voltage as the input and current the output.

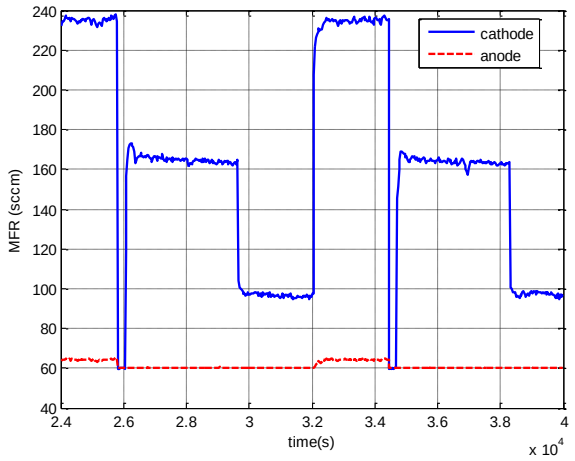


Figure 2-15 Mass flow rate of hydrogen (anode side) and air (cathode side) as pneumatic subsystem's inputs

The operating conditions controlled by the test stand are summarized in Table 2-2 with their setting values.

Table 2-2 Controlled operating conditions in the fuel cell test stand

| Controlled Variable | Control Method | Controlled value during durability test |
|---|---|---|
| Hydrogen Mass Flow (Anode) | MFC | 1.3 stoichiometry (min: 60 sccm[1]) |
| Air Mass Flow (Cathode) | MFC | 2 stoichiometry (min: 60 sccm) |
| Back Pressure(anode/cathode) | Back Pressure Regulator | 25/20 psi (approximate setting values, relative to 1 atm) |
| FC temperature | Environmental chamber | 80 ℃ |
| Humidifier Dew Point Temperature (DPT) | Dew Point Humidifier | 78 ℃ (Both sides) |

The system parameters that remain to be identified are: pipes' inlet/outlet frictional nozzle constants in the gas supplying system, pipe volumes, and activation loss model parameters (Table 2-4). Also, since the back pressures are regulated by manually

[1] Standard cubic centimeters per minute

adjustable back pressure regulators with inaccurate gauge reading, they need to be identified as well. The model parameters with known values are given in Table 2-3.

Table 2-3 Parameter values for fuel cell systems

| Symbol | Parameter Definition | Parameter Value for simulation |
|---|---|---|
| $\alpha_w$ | Correction factor for membrane water vapor diffusion coefficient $D_w$ | 20 |
| $\varepsilon_{pore}$ | GDL porosity | 0.5 |
| $\theta_c$ | Contact angle of the water droplet w.r.t. GDL material | 60˚ |
| $\gamma_{\text{evap}}$ | Volumetric evaporation coefficient | 900 ($s^{-1}$) |
| $\sigma_c$ | Surface tension between water and air | 0.0644 (N/m) |
| $\mu_{H_2O}$ | Liquid water viscosity | $4.05\times10^{-4}$ (kg/m/s) |
| $\rho_{mb,dry}$ | Membrane dry density | 1900 ($kg/m^3$) |
| $A_{ch}$ | Channel geometric area | $3.8\times10^{-7}$ ($m^2$) |
| $A_{fc}$ | Fuel cell active area | 15 ($cm^2$) |
| $P_{ch}$ | Perimeter of the channel sectional area | $3.5\times10^{-3}$ (m) |
| $L$ | Channel length | 0.5 (m) |
| $M_{mb,dry}$ | Membrane dry equivalent weight | 1.0 (kg/mol) |
| $d_{GDL}$ | GDL thickness | $3.8\times10^{-4}$ (m) |
| $R_{ohm}^{GDL}+R_{ohm}^{plate}+R_{ohm}^{contact}$ | Total ohmic resistance components except membrane resistance | 22.9 (mΩ) |
| $t_m$ | Membrane thickness | $5.08\times10^{-5}$ (m) |

The results of the system identification are presented in Figure 2-16 (part 1), and Figure 2-17, Figure 2-18 (part 2). The identified system parameter values are given in Table 2-4.

For the first part of system identification, since fully humidified reactant gases are used, and the fuel cell is operated under medium current density (0.2 ~ 0.47 A/cm$^2$) for the majority of time, the channel is almost always flooded with incessant water accumulation and removal, constituting a very unstable and stochastic process. The amount of liquid water in the channel can thus be perceived as an unknown noisy disturbance and set to zero during the system identification, while parameters to be identified are optimized such that the modeled inlet pressure matches the lowest peak of the actual pressure sensor reading.

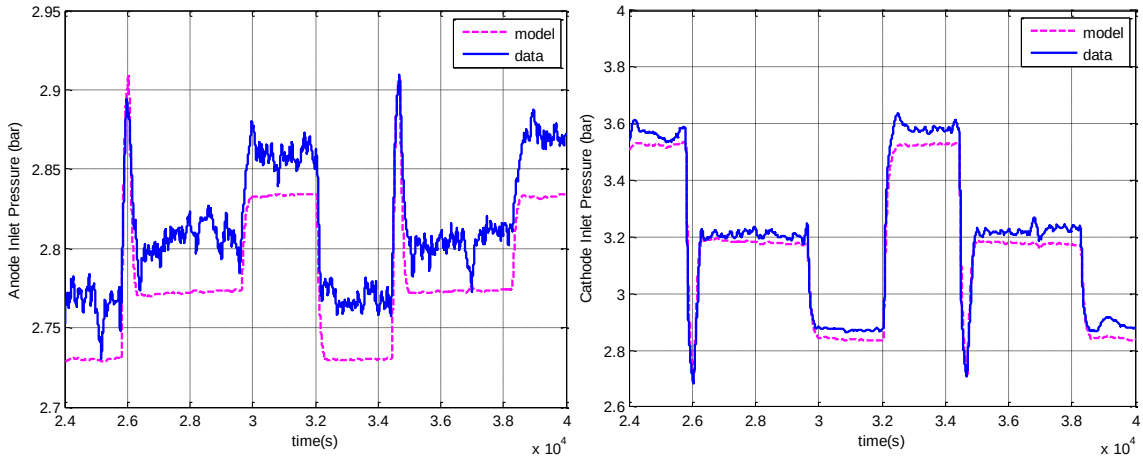


Figure 2-16 Anode (left) and Cathode (right) inlet pressure (model assumption: no liquid water in channel)

As mentioned before, the fluctuation of the measured inlet pressures on both sides seen in Figure 2-16 can be attributed to the varying amount of liquid water inside the anode and cathode channels. The cathode side gas stream, with a much higher mass flow rate than that at the anode (Figure 2-15), removes the channel water more efficiently and expels the liquid water out of channel before it accumulates to occupy a large portion of the channel volume, diminishing its impact on the inlet pressure. The liquid water in

anode channel, under a much weaker flowing gas stream, can accumulate to an extent that most channel volume is occupied before it gets expelled, resulting in fluctuation with a wider range (around 0.05bar). With the finalized parameter values, the model eventually manage to capture the pneumatic dynamics in the gas supplying systems, and the steady-state outputs match the lowest value of the pressure profile, which supposedly corresponds to the pressure with no liquid water present in the channel.

For the second part of system identification, since the fuel cell is operated under constant voltage mode, the model takes the voltage as input and the current the output.

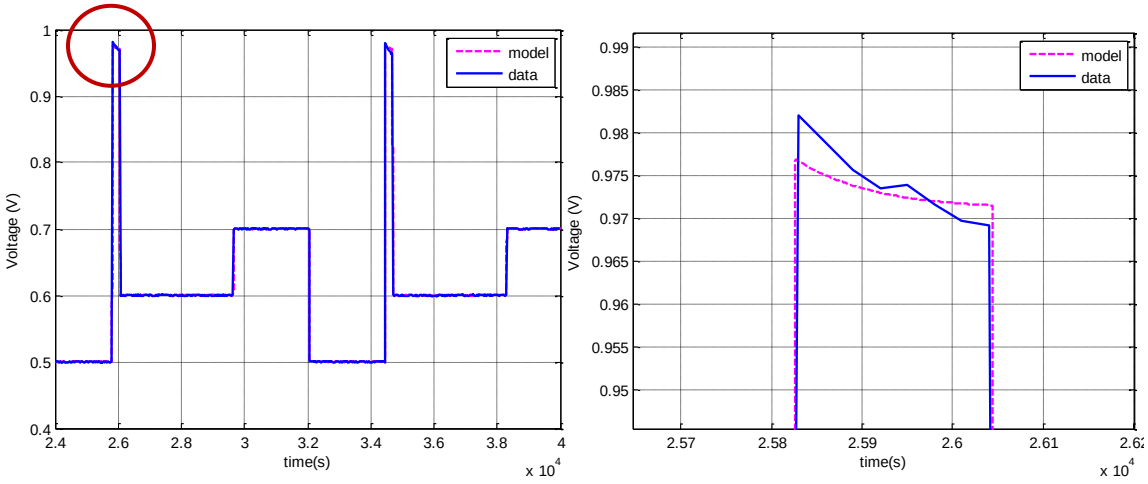


Figure 2-17 Voltage profile of the fuel cell w.r.t. time under CV mode (a) and zoom in of the circled area in subplot (left): OCV section of the voltage profile (right)

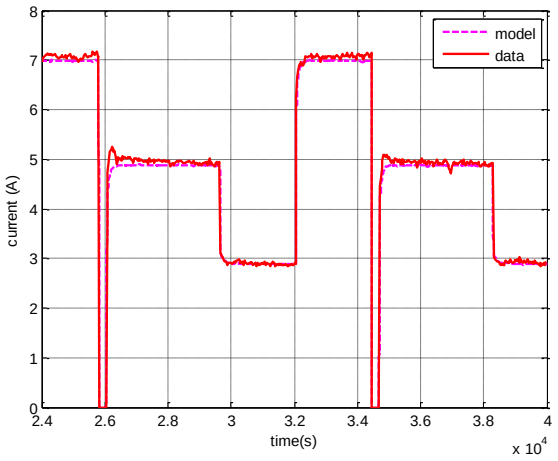


Figure 2-18 Current profile of the fuel cell under CV mode

As can be seen in Figure 2-17 and Figure 2-18, with the identified system parameters, the model output matches the data very well. Note that since no liquid water is assumed in the channel, the reactants' concentrations (partial pressures) inside the channels are underestimated.

Table 2-4 Identified system parameters

| | Symbol | Parameter Definition | Parameter Value for simulation |
|---|---|---|---|
| Pipe frictional nozzle constants | $k_{in,ch,ca}$ | Cathode channel inlet constant | $7\times10^{9}$ (Pa s/kg) |
| | $k_{out,ch,ca} + k_{in,rm,ca}$ | Sum of cathode channel outlet constant and return pipe inlet constant | $1.4\times10^{10}$ (Pa s/kg) |
| | $k_{in,ch,an}$ | Anode channel inlet constant | $2.2\times10^{10}$ (Pa s/kg) |
| | $k_{out,ch,an} + k_{in,rm,an}$ | Sum of anode channel outlet constant and return manifold constant | $9.5\times10^{10}$ (Pa s/kg) |
| | $k_{out,sm,ca}$ | Cathode supply pipe out constant | $1\times10^{6}$ (Pa s/kg) |
| | $k_{out,sm,an}$ | Anode supply pipe out constant | $8\times10^{6}$ (Pa s/kg) |
| | $k_{out,rm,ca}$ | Cathode return pipe out | $1\times10^{9}$ (Pa s/kg) |

| | | | |
|---|---|---|---|
| | | constant | |
| Pipe Volumes | $k_{out,rm,an}$ | Anode return pipe out constant | $9\times10^{9}$ (Pa s/kg) |
| | $V_{sm,ca}$ | Cathode supply pipe volume | $3\times10^{-4}$ ($m^3$) |
| | $V_{sm,an}$ | Anode supply pipe volume | $4\times10^{-4}$ ($m^3$) |
| | $V_{rm,ca}$ | Cathode return pipe volume | $1\times10^{-4}$ ($m^3$) |
| | $V_{rm,an}$ | Anode return pipe volume | $2\times10^{-4}$ ($m^3$) |
| Back Pressures (w.r.t the atmosphere) | $BP_{ca}$ | Anode back pressure | 23 (psi) |
| | $BP_{an}$ | Cathode back pressure | 19.2 (psi) |
| Activation loss model parameters | $i_0^{ref}$ | Reference exchange current density | $5\times10^{-6}$ ($A/cm^2$) |
| | $\alpha$ | transfer coefficient | 0.78 |

## 2.9 SIMULATION

With the system parameters identified in last section, simulation validation is conducted on the developed fuel cell dynamic model in this section. Constant voltage mode is used in the simulation, similar to the operating load employed in the experiment. The voltage and current profiles are plotted in the figure below.

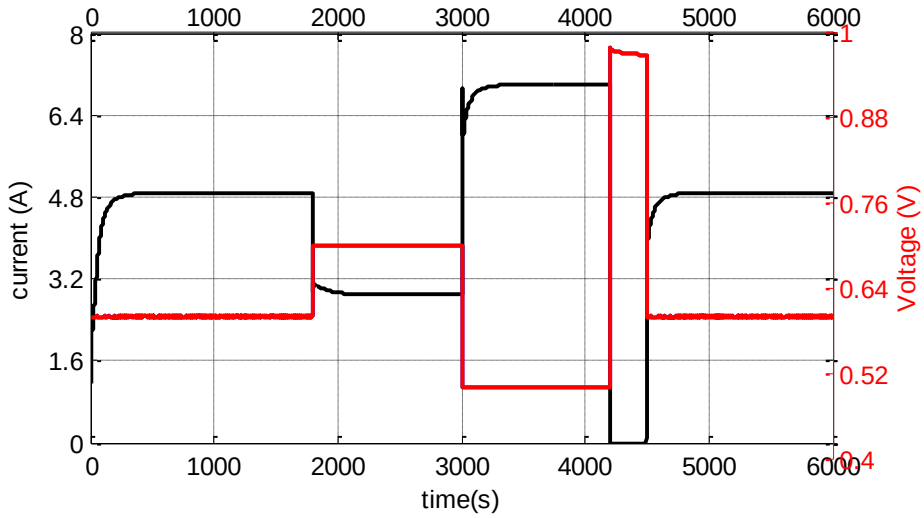


Figure 2-19 Voltage profile as system input and current profile

As seen in Figure 2-19, the fuel cell is put under four different levels of voltage load during a total 6000s simulation time, including 0.6V for the first 30 minutes, 0.7V for 20 minutes, 0.5V for 20 minutes, OCV for five minute, and 0.6V for the rest of the simulation. An operating temperature of 80˚C and fully humidification of the inlet reactant gases on both sides are assumed. The stoichiometry for supplying the $H_2$ / the air is 1.3/2.5. Simulation results are given in Figure 2-20 ~ Figure 2-22.

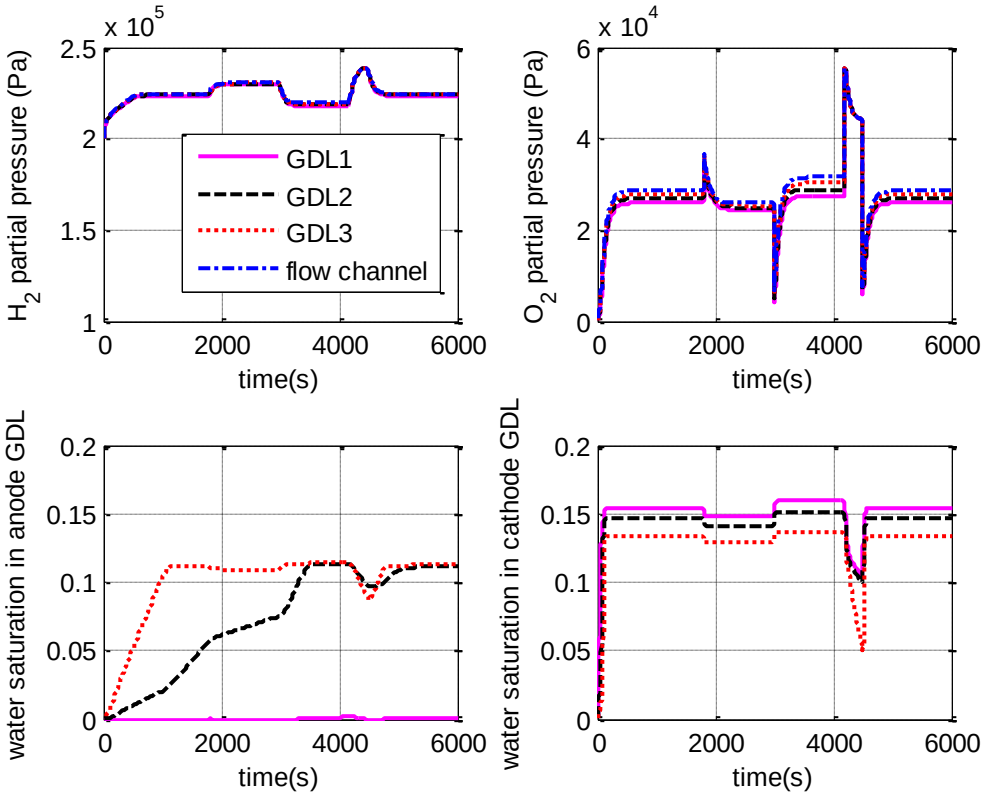


Figure 2-20 Reactants and product concentration in the fuel cell

In Figure 2-20, the reactants concentrations (in the form of partial pressures) and the liquid water content in different locations inside the fuel cell (GDL, or flow channel) are plotted with respect to time. Recall that a discretized 3-layer GDL model is adopted in our dynamic fuel cell model, thus the variables of interest in each layer are respectively

plotted in the figure. From the two top subplots, it can be seen that, under the same condition (no flooding in the channel), the mass transportation loss at the cathode side is greater than that at the anode side, since the relative difference between the reactant concentration in the channel and in GDL1 (the closet layer of the GDL to the membrane) is larger at cathode than at anode. Another notable difference between the two electrodes is observed in the two subplots at the bottom of the figure, where the water content decrease at cathode in the order of GDL1, GDL2, and GDL3, while the trend appears to be reverse at anode. This is caused by inadequate back diffusion of water from cathode to anode. Note that, by modifying the coefficient of the membrane, larger amount of water back diffusion can be achieved in the simulation, leading to higher water content in GDL1 at anode and transportation direction from GDL1 to GDL3.

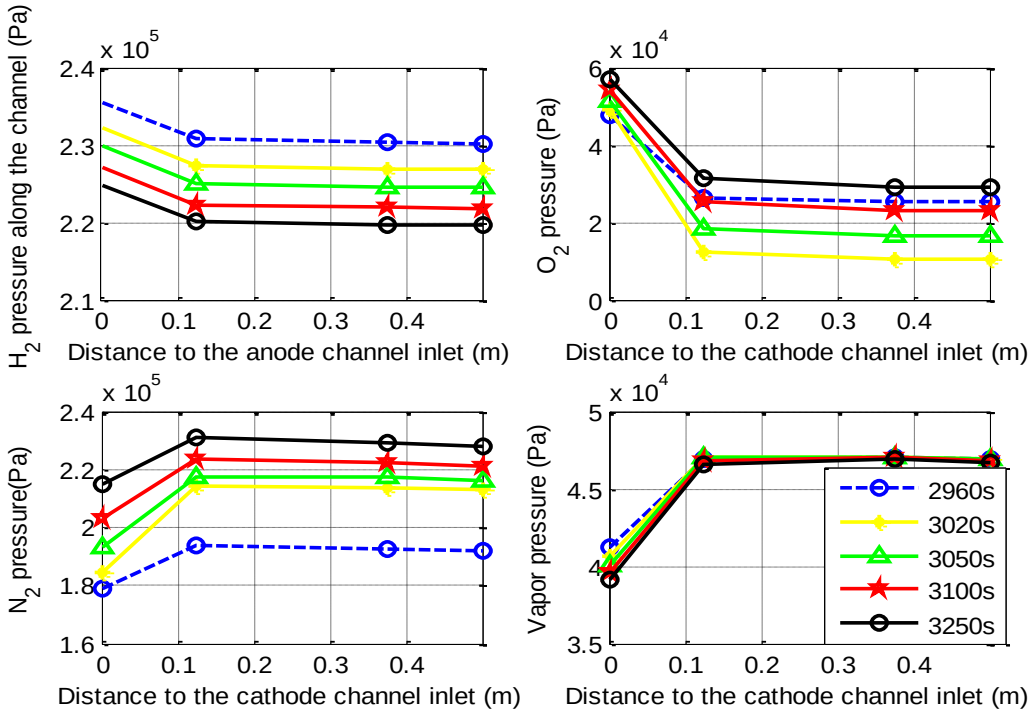


Figure 2-21 Reactants and vapor distribution along the channel length in transient (both sides)

Figure 2-21 depicts the reactants and vapor distribution along the channel length in transient condition. It can be seen that the biggest concentration drop happens immediately after the supplied gas enters the inlet of the flow field. The concentration of the component gas then experiences a mild drop through the flow channel.

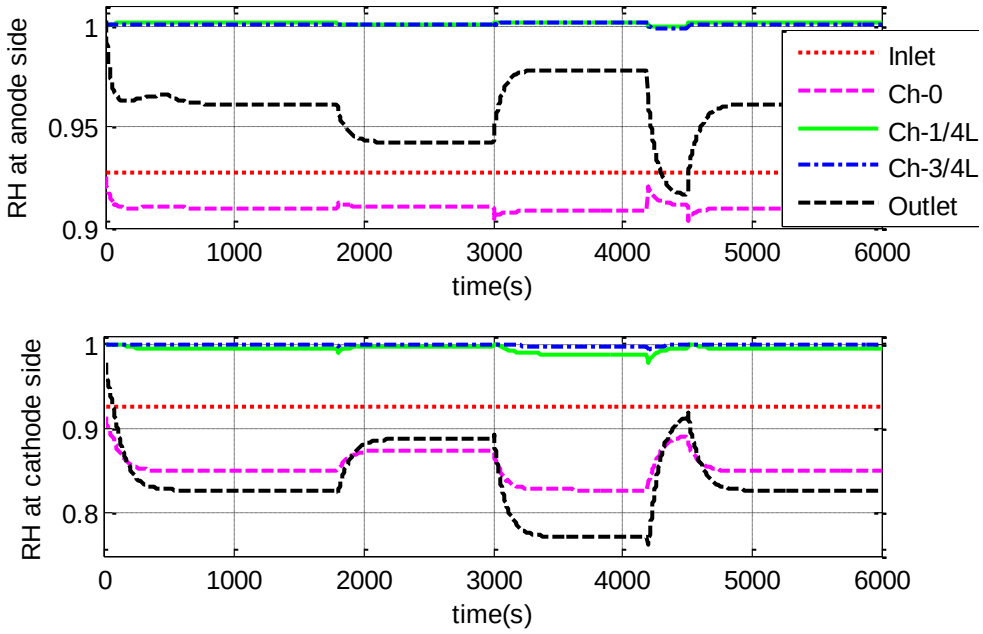


Figure 2-22 Relative humidity along the channel (both sides)

Figure 2-22 depicts the relative humidity at given locations along the channel w.r.t. time. It is noted that the inlet RH is well below 1 (about 0.93) despite the fact that fully humidified reactant gases are supplied. This is caused by the pressure drop at the inlet nozzle, which also brings down the partial pressure level of the vapor, hence a smaller RH. Also note that, the outlet RH is below 1, too, in spite of the saturated condition achieved in the flow channel. This, again, can be attributed to the pressure drop at the nozzle of the outlet.

## 2.10 CHAPTER SUMMARY

A comprehensive fuel cell dynamic model incorporating fault effects and aging effects is developed in this chapter. Major improvements of this model compared to the existing fuel cell models are: (1) Gas dynamics in the fuel cell channel is modeled to include channel water flooding effect on the inlet pressure of the flow field; (2) Channel water dynamic model is incorporated that is capable of describing the accumulation and removal of the liquid water in the fuel cell channel; (3) The dynamics of reactants transportation in the GDL is considered as a function of the liquid water present in the GDL; (4) The effect of the effective catalyst surface area (ECSA) and the gas crossover of the membrane is incorporated in the electro-chemical module of the fuel cell model.

The fuel cell system model is implemented in Simulink as a platform for algorithm validation of the control, diagnostic and health monitoring systems. System identification is then performed on the developed model with experimental data. The results show that the model can accurately capture the system dynamics with the identified system parameter values. More simulations are conducted in different operating conditions.

The developed model can be easily adapted to model any real fuel cell system with fuel cell stacks.

# CHAPTER THREE

# ROBUST CONTROL DESIGN FOR FUEL CELL SYSTEM

After the fuel cell system components are designed and manufactured and the fuel cell stack fully assembled, the main factor that affects the fuel cell system's performance and long term durability is the fuel cell's operating conditions. Control system that optimizes the operating conditions while satisfying the power demand of the system is therefore highly desirable. As some operating conditions, such as the membrane water content, cannot be easily obtained by direct measurement, on-line diagnostic system that detects and estimates/evaluates the faulty conditions is also required.

There are three major control subsystem in the FCS, namely the reactants supply system, the water management system, and the heat management system ([76]), as summarized in the following table.

Table 3-1 Major control subsystem in a FCS

| Control subsystem | Control Variable | Control Objective | Actuator |
|---|---|---|---|
| Air/fuel supply system | MFR (mass flow rate) | Maintain a reasonable level of reactant excess ratio<br>Net output power tracking | MFC (mass flow controller)<br>or Compressor |
| | Reactant pressure | Maintain the reactant pressure at the electrodes | Back pressure regulator |
| Water management system | Water content inside fuel cell | Maintain a reasonable water content | Humidifier |
| Heat management system | Operating temperature | Maintain the desired operating temperature | Cooler (heat tape or temperature chamber in lab) |

Based on the fuel cell system structure adopted in the previously developed model (as presented in Chapter Two), the heat management is achieved by temperature chamber and can be assumed ideal; while in the water management control subsystem, the actuator (i.e., the humidifier) is insufficiently fast for effective feedback control and thus only set reference is used. Therefore, here we only focus on the control problem of the reactant supplying system which aims at maintaining the desired $O_2$ excess ratio and preventing oxidant starvation.

In this chapter, we propose a diagnostic-based control scheme for the air supply system. A general framework for this problem is shown in Figure 3-1. H-infinity technique is employed for the controller design to minimize the difference between the desired and actual oxygen excess ratio. Diagnosis of the faulty condition in the air supply system, i.e., channel flooding, is formulated as a simultaneous state and parameter estimation problem. An extended kalman filter (EKF) is then developed to solve the problem.

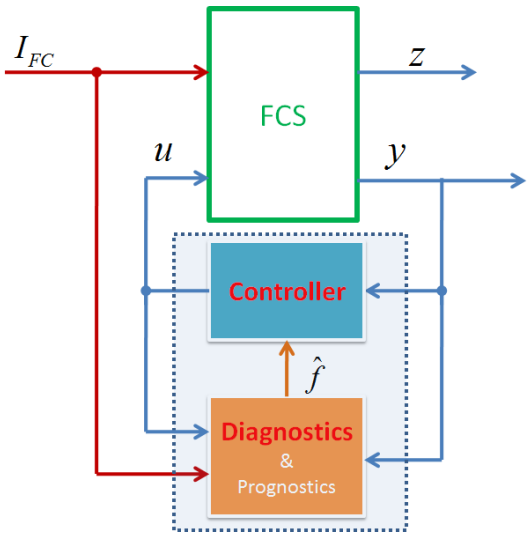


Figure 3-1 General framework for diagnostic-based control scheme

## 3.1 PROBLEM FORMULATION

A simplified diagram of the fuel cell to be controlled is shown in Figure 3-2, with the air supply system accentuated that supplies air to the fuel cell cathode flow channel to replenish the oxygen being consumed and maintains the reactant gas pressure at the electrode at some desired level. The structure of the air supply system is based on a laboratory fuel cell test stand, which is to be described in the next chapter. This air supply subsystem is composed of a mass flow controller (MFC), a gas supplying pipeline (supply manifold in the case of a commercial FCS), a humidifier (water injection in the diagram), fuel cell flow channel(s), a return pipeline and a back pressure regulator.

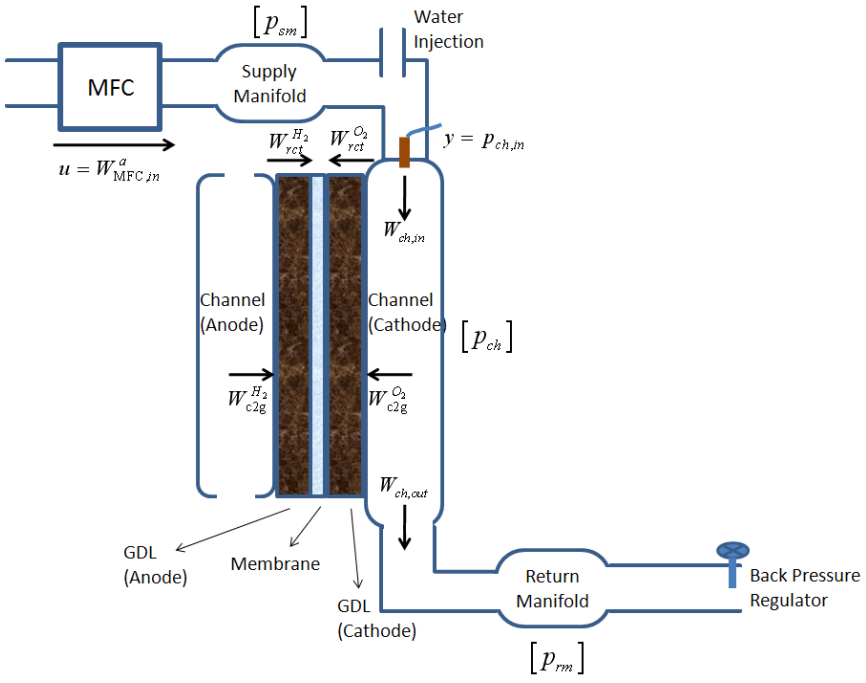


Figure 3-2 Simplified diagram of the fuel cell system

As depicted in the above picture, the mass flow controller (MFC) acts as the subsystem's actuator and controls the mass flow rate of the inlet air ($W^{a}_{\mathrm{MFC,in}}$) entering the air supply system. The incoming air is conducted by the supplying pipeline to the humidifier to receive humidification before entering the fuel cell channel, where part of the oxygen is diffused into and distributed by the GDL (with a mass flow rate of $W^{O_2}_{\mathrm{c2g}}$) to the catalyst site for reaction (with a reaction rate of $W^{O_2}_{\mathrm{rct}}$). The remainder of the air and produced water vapor then exits the fuel cell channel and is conducted by the returning pipeline to leave the air supplying system and enter the atmosphere. The manually adjustable back pressure regulator is located at the end of the return pipeline to operate the fuel cell at the specified pressure. And the fuel cell channel inlet pressure is measured by the pressure sensor installed immediately before the fuel cell inlet.

In this dissertation, two problems related to the air supply system presented before are considered: 1) Control of the oxygen excess ratio ( $\lambda_{O_2} = W_{\mathrm{ch,in}} \big/ W^{O_2}_{\mathrm{c2g}}$ ), with the objective to maintain $\lambda_{O_2}$ at a desired level $\lambda^{\mathrm{des}}_{O_2}$ , and 2) Diagnostics of the channel flooding, with the objective to detect the water flooding in the fuel cell flow field and estimate the fault magnitude, i.e., the water volume accumulated in the channel.

In order to solve the problems, we investigated the design of $H_\infty$ controllers (theoretically a bank of $H_\infty$ controllers are needed to deal with different operating conditions) for $O_2$ excess ratio control, and an observer-based diagnostic scheme for channel flooding diagnostics. The framework of the integrated control and diagnostics scheme is presented below in Figure 3-3.

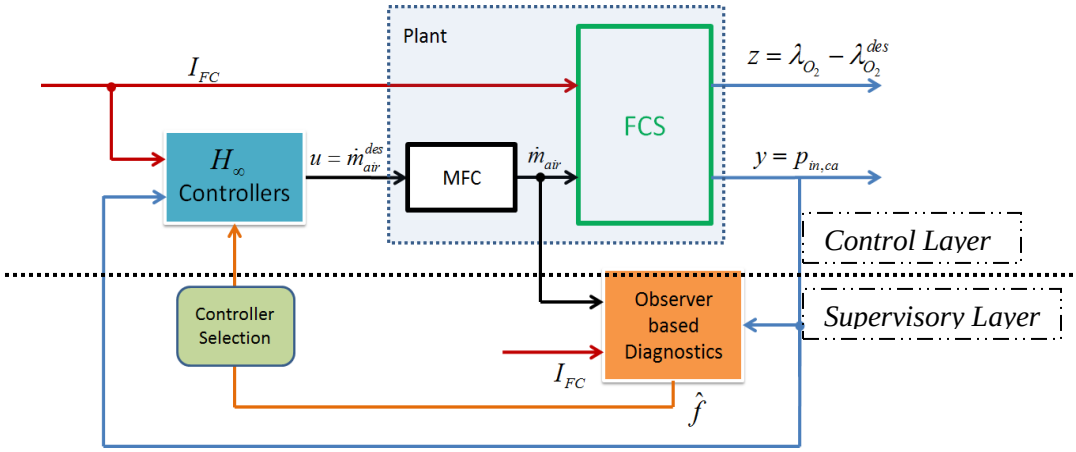


Figure 3-3 Framework for the proposed control and diagnostics scheme (with a MFC as the actuator)

There are two layers in the above framework. The control layer includes a bank of $H_\infty$ controllers and the controlled plant; and the supervisory layer is composed of the diagnostic module and a controller selection module.

In the control layer, the controller command $\dot{m}_{air}^{des}$ is taken as the plant's input, and the current load $I_{FC}$ is considered as a known disturbance to the plant. For oxygen excess ratio control purpose, only the cathode inlet pressure is taken as the measured output to be fed back to the controller. The performance index is chosen to be the difference of the actual and the desired $O_2$ excess ratio. The diagnostic module in the supervisory layer performs the fault detection and estimation for the channel flooding fault. Based on the estimated fault information and the current system operating conditions, the controller selection module would determine which $H_\infty$ controller in the controller bank has to be selected.

In the framework in Figure 3-3, a mass flow controller (MFC) is employed as the actuator for the plant. In practice, gas supplying devices such as a compressor are more

often integrated in the commercial fuel cell systems. While a compressor model can be highly nonlinear, its linearization during controller design can cause large uncertainties and may require more linearization points and controllers to deal with the problem. Nevertheless, the presented framework can be applied to the practical fuel cell systems with some slight modification. As shown in Figure 3-4, an inverse model of the compressor is integrated in the plant to counteract the nonlinearity in the compressor. With the main nonlinearities eliminated by the inverse model, the overall dynamics of the combined inverse model and the actual compressor combined can be considered as almost linear. Therefore, in this dissertation, we only study the framework presented in Figure 3-3.

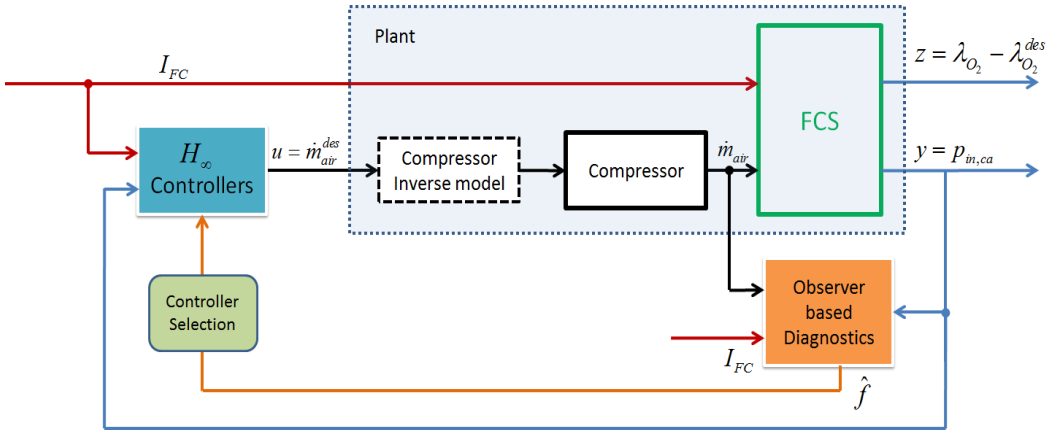


Figure 3-4 Framework for the control and diagnostics scheme with a compressor as the actuator

It should be noted that, though we only focused on developing the control and diagnostic schemes for the air supplying system in this dissertation, due to the symmetric structure of the reactant supplying systems, the developed algorithms for the cathode side can also be applied to the anode side of the fuel cell system.

## 3.2 ROBUST CONTROL DESIGN

### *3.2.1 Air Supplying System Model Simplification and Linearization*

The air supplying subsystem model has been presented in Chapter 2 (refer to equations(2.9),(2.10),(2.13)), where details such as the gas dynamics of the mixture components and the two phase flow of the water in the channel are considered during the modeling. Also the flow field is discretized into two sections. While the modeling approach provides more accuracy in capturing the real dynamics of the fuel cell system – which is useful for the simulation study – the complexity involved also brings difficulty when it comes to the controller design. For $H_\infty$ control design in this dissertation, further simplification of the complex model, including model order reduction, is desired. Linearization is then performed on the simplified, yet still nonlinear model.

By lumping the supply manifold, the fuel cell flow channel and the return manifold respectively into three volumes, and neglecting the gas transport dynamics in the GDL, a simple air supply system model can be derived based on the mass conservation law and the fluid mechanics principles, with its state space equations given in (3.1) and (3.2). The model can be better illustrated by making an analogy to an electrical circuit, with the mass flow rate analogous to the current, and the pressure analogous to the voltage, as shown in Figure 3-5.

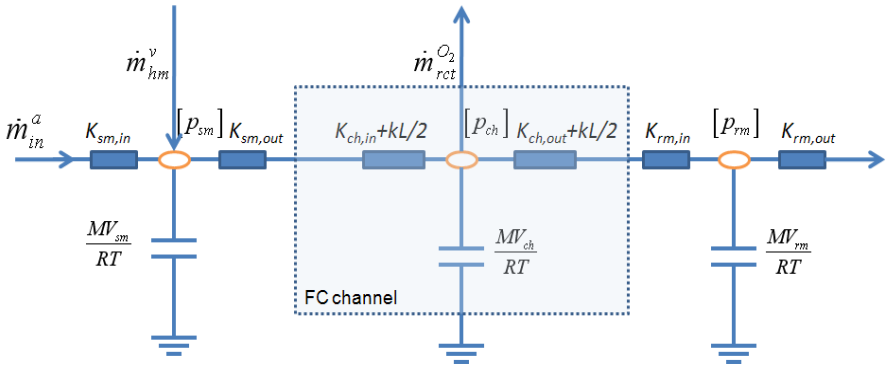


Figure 3-5 A simplified electrical circuit model for air supplying system

A resistor in Figure 3-5 represents the frictional resistance of the pipe to the flowing gas, and a capacitor is used to capture the gas filling dynamics. $\dot{m}^{v}_{hm}$ is the mass flow rate of the water vapour added to the inlet air stream by the humidifier, and $\dot{m}^{O_2}_{rct}$ is the consumption rate of the oxygen at the electrode.

$$\begin{cases} \dfrac{MV_{sm}}{RT}\dot{p}_{sm} = \left(\dot{m}^{a}_{in} + \dot{m}^{v}_{hm}\right) - \dfrac{p_{sm} - p_{ch}}{K_{sm,out} + K_{ch,in} + \dfrac{k_{ch}L}{2}} \\ \dfrac{MV_{ch}}{RT}\dot{p}_{ch} = \dfrac{p_{sm} - p_{ch}}{K_{sm,out} + K_{ch,in} + \dfrac{k_{ch}L}{2}} - \dot{m}^{O_2}_{rct} - \dfrac{p_{ch} - p_{rm}}{\dfrac{k_{ch}L}{2} + K_{ch,out} + K_{rm,in}} \\ \dfrac{MV_{rm}}{RT}\dot{p}_{rm} = \dfrac{p_{ch} - p_{rm}}{\dfrac{k_{ch}L}{2} + K_{ch,out} + K_{rm,in}} - \dfrac{p_{rm} - p_{bpr}}{K_{rm,out}} \end{cases} \tag{3.1}$$

$$\begin{cases} p_{ch,in} = p_{ch} + \left( \dfrac{p_{sm} - p_{ch}}{K_{sm,out} + K_{ch,in} + \dfrac{k_{ch}L}{2}} - \dot{m}^{O_2}_{rct} \right) \times \left( K_{ch,in} + \dfrac{k_{ch}L}{2} \right) \\ \lambda_{O_2} = \dfrac{p_{sm} - p_{ch}}{K_{sm,out} + K_{ch,in} + \dfrac{k_{ch}L}{2}} \bar{x}^{a} x^{O_2}_{a} \Big/ \dot{m}^{O_2}_{rct} \end{cases} \tag{3.2}$$

In (3.1) and(3.2), all the $K_{i,j}$ (e.g. $K_{sm,out}$) are treated as constants independent of pressures and temperature. $k_{ch} = \dfrac{32\mu(T)RT}{D_h^2 \cdot A \cdot M \cdot p_{ch}}$, where $D_h$ is the hydraulic diameter of the fuel cell flow channel, and $A$ is the cross sectional area of the channel. $\mu$ is the viscosity of the gas mixture (oxygen, nitrogen and water vapor), and is dependent on the mixture's absolute temperature, pressure, as well as the components of the mixture. $\overline{x}^a$ is the dry air mass fraction of the inlet humidified air. $x_a^{O_2}$ is the oxygen mass fraction in the environment air, which is given by $x_a^{O_2} = \dfrac{M_{O_2} \cdot 0.21}{M_{O_2} \cdot 0.21 + M_{N_2} \cdot 0.79}$.

For simplicity, a static perfect humidifier is assumed, which humidifies the incoming air to the fully saturated state, i.e. 100% relative humidity. Thus the total inlet air

$$\begin{aligned} \dot{m}_{in}^a + \dot{m}_{hm}^v &= \dot{m}_{in}^a \left(1 - x_{amb}^v\right)\left[1 + \frac{p_{sat}^v(T) M_{H2O}}{\left[p_{sm} - p_{sat}^v(T)\right] M_a}\right] \\ &= \dot{m}_{in}^a \left(1 - x_{amb}^v\right)\frac{1}{\overline{x}^a} \end{aligned}$$

where $x_{amb}^v$ is the vapor mass fraction in the ambient air.

The model given in (3.1) and (3.2)is nonlinear since the state variables appear in the denominators of some terms. For linear control techniques such as $H_\infty$ control to be applied, the model needs to be first linearized around some operating conditions. Figure 3-6 illustrates two control configurations with the plant to be linearized included in a dashed box.

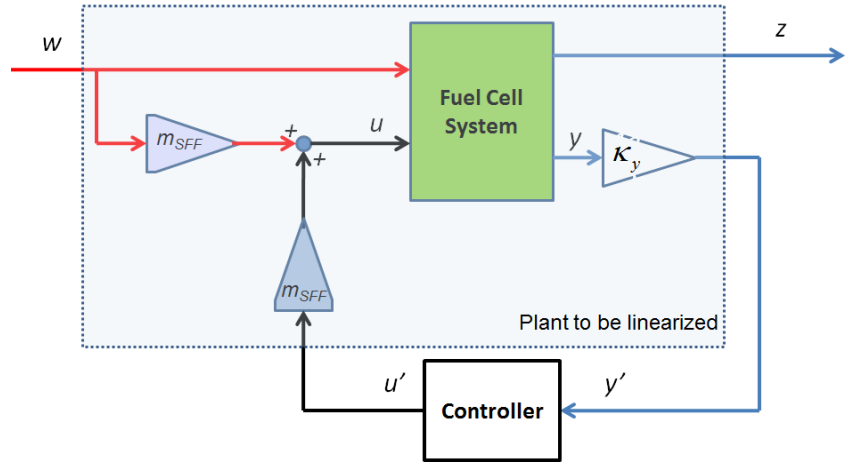


(a)

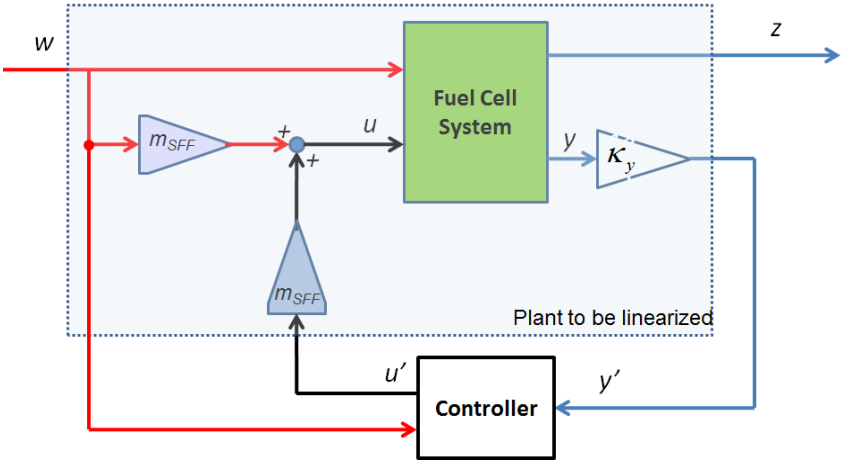


(b)

Figure 3-6. Two control configurations for the air supply system control problem

In both control configurations, a static feed forward (with a constant scaling parameter of $m_{SFF}$) loop is added to the feedback loop to produce the control signal, i.e., $u = m_{SFF}\left(w + u'\right)$. The input to the plant to be linearized now becomes $\begin{bmatrix} w \\ u' \end{bmatrix}$, where $w$ is the known disturbance, and $u$' is the controller's output. Note that to make performance

weight design more straightforward, the controller's output and the measured plant output are scaled by $m_{SFF}$ and $\kappa_y$ ($\kappa_y$ =$10^{-5}$) respectively.

The plant is then linearized around $\begin{bmatrix} w_0 \\ u_0' \end{bmatrix} = \begin{bmatrix} 10 \\ 0 \end{bmatrix}$. The linearized state equations are given in(3.3).

$$\begin{aligned}
\alpha_1 \delta \dot{x}_1 &= \left(1 - x_{amb}^{v}\right) \frac{1}{\bar{x}^a} m_{SFF} \left(\delta w + \delta u'\right) - \frac{\delta x_1 - \delta x_2}{K_{n1} + \beta / x_{20}} \\
\alpha_2 \delta \dot{x}_2 &= \frac{\delta x_1 - \delta x_2}{K_{n1} + \beta / x_{20}} - \frac{\delta x_2 - \delta x_3}{K_{n2} + \beta / x_{20}} - m \cdot \delta w \\
\alpha_3 \delta \dot{x}_3 &= \frac{\delta x_2 - \delta x_3}{K_{n2} + \beta / x_{20}} - \frac{\delta x_3}{K_{n3}}
\end{aligned} \tag{3.3}$$

where $\begin{bmatrix} \delta x_1 & \delta x_2 & \delta x_3 \end{bmatrix}^T = \begin{bmatrix} \delta p_{sm} & \delta p_{ch} & \delta p_{rm} \end{bmatrix}^T$, $K_{n1} = K_{sm,out} + K_{ch,in}$, $K_{n3} = K_{rm,out}$, and $K_{n2} = K_{ch,out} + K_{rm,in}$; $x_{20}$ is the equilibrium state value of the total pressure inside the channel ($p_{ch}$).

To make the linearization of the output equations easier, the original performance index $z$ ($\lambda_{O_2} - \lambda_{O_2}^{des}$) is slightly modified to be $z = \left(\lambda_{O_2} - \lambda_{O_2}^{des}\right) \frac{\dot{m}_{rct}^{O_2}}{m_{SFF}}$

$$= \left( \frac{p_{sm} - p_{ch}}{k_{sm,out} + k_{ch,in} + \frac{k_{ch} L}{2}} \bar{x}^a x_a^{O_2} - \lambda_{O_2}^{des} \dot{m}_{rct}^{O_2} \right) \Big/ m_{SFF} .$$

The linearized output equations are given in(3.4).

$$\begin{cases} \delta z = \dfrac{\delta x_1 - \delta x_2}{k_1 + \beta / x_{20}} \bar{x}^a x_a^{O_2} \Big/ m - \lambda_{O_2}^{des} \delta w \\ \dfrac{\delta y}{\kappa_y} = \delta x_2 + \left( \dfrac{\delta x_1 - \delta x_2}{k_1 + \beta / x_{20}} - m \cdot \delta w \right) \left( k_{ch,in} + \beta / x_{20} \right) \end{cases} \tag{3.4}$$

A simulation is then carried out to compare the nonlinear and linearized models. The current load used for the simulation and the simulation results are presented in Figure 3-7 and Figure 3-8 respectively.

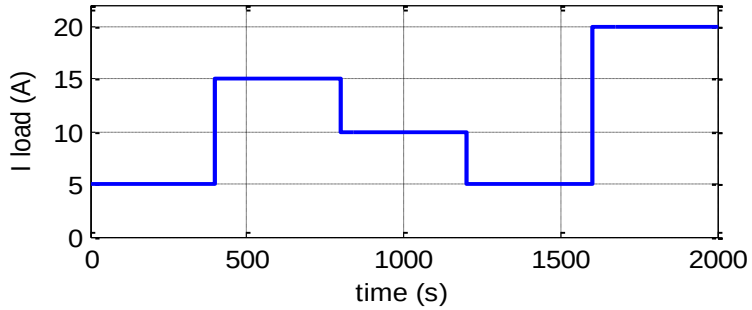


Figure 3-7 Simulation input.

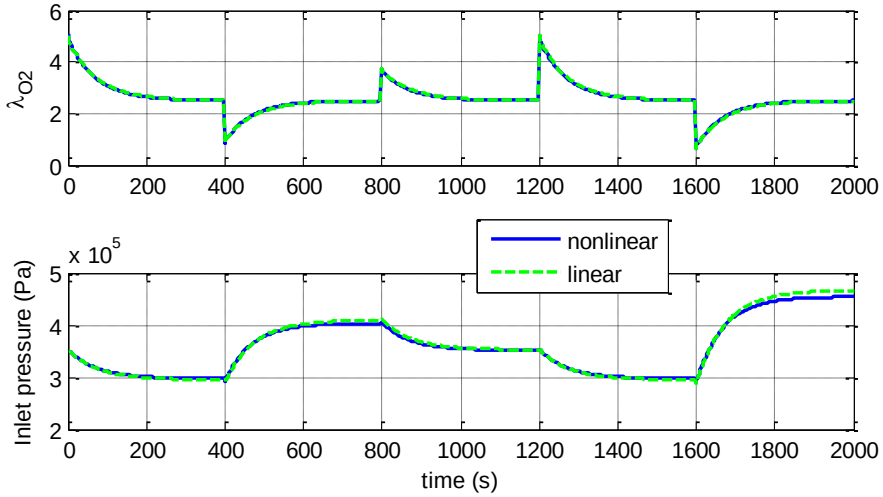


Figure 3-8 Simulation outputs .

The results show a good match between the nonlinear and linearized model outputs. One can also observe from the simulation result that, at a sudden rise of the current demand, the oxygen excess ratio drops below 1, and takes a very long time (about three minutes) to recover to the steady state value (2.5). This can be seen more clearly in the following close-up.

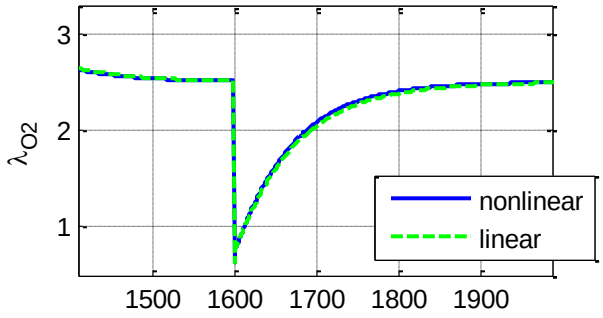


Figure 3-9 A close-up of Figure 3-8

### *3.2.2 $H_\infty$ Control Design for the Nominal Plant (Air Supply System)*

Based on the control configurations presented in Figure 3-6 and the linearized system equations (3.3) and (3.4), the control problem can now be formulized as the standard LFT form as shown in Figure 3-10. Our control objective is then to minimize the performance index $z$ (the error between the actual $O_2$ excess ratio and the desired one) and, at the same time, minimize the control effort $u'$ to prevent large actuator action – which is especially meaningful when a compressor is employed as the actuator in a fuel cell system. Some sources of uncertainties of the system are also considered, and the robust stability of the closed-loop system with the designed controller is examined afterwards.

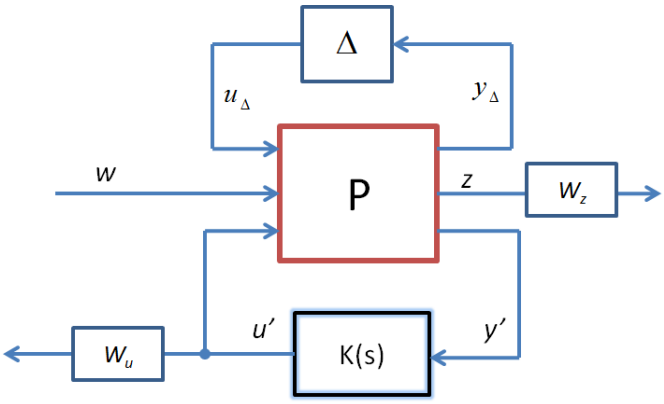


Figure 3-10 Standard LFT form for the control problem formulation

The trade-off between the system performance and the control energy used is achieved by choosing appropriate performance weights $W_z$ and $W_u$ for the two selected system outputs.

For the system performance, the minimization of the performance index $z$ at low frequencies is most desirable, thus a low pass filter is chosen as $W_z$ to penalize the system's low frequency gain, i.e., $W_z(s) = \dfrac{r_{0,z}}{T_z \cdot s + 1}$.

On the other hand, to avoid the sudden rises and falls of the controller's output $u'$ that mainly consists of high frequency signals during the transition states, a high pass filter is chosen as $W_u$, i.e., $W_u(s) = \dfrac{\tau_u s + r_{0,u}}{(\tau_u / r_{\infty,u})s + 1}$, where $r_{0,u}$ is the steady state gain of the weight, $r_{\infty,u}$ is the magnitude of the weight at higher frequencies, and $1/\tau_u$ is approximately the frequency where the magnitude of the weight reaches 100% of $r_{\infty,u}$.

The $H_\infty$ control problem can now be stated as: *find a controller K(s) in Figure 3-10 (neglecting the uncertainty loop) that minimizes the transfer function between the disturbance and the weighted system outputs, i.e.,* $\min_{w\neq 0} \dfrac{\left\| \begin{bmatrix} W_z \cdot z \\ W_u \cdot u' \end{bmatrix} \right\|_2}{\|w\|_2}$.

The problem can be solved with the help of the robust control toolbox in Matlab. In this dissertation, two control configurations, as given in Figure 3-6, are compared. In the first configuration, the controller utilizes only the measured inlet pressure as its input, while the controller in the second configuration utilizes the current load feedback as well.

For the controllers design and comparison, the performance weights are selected to be $W_u = \dfrac{0.05s+0.01}{0.1s+1}$, $W_z = \dfrac{10}{100s+1}$, the bode plot of which are shown in Figure 3-11.

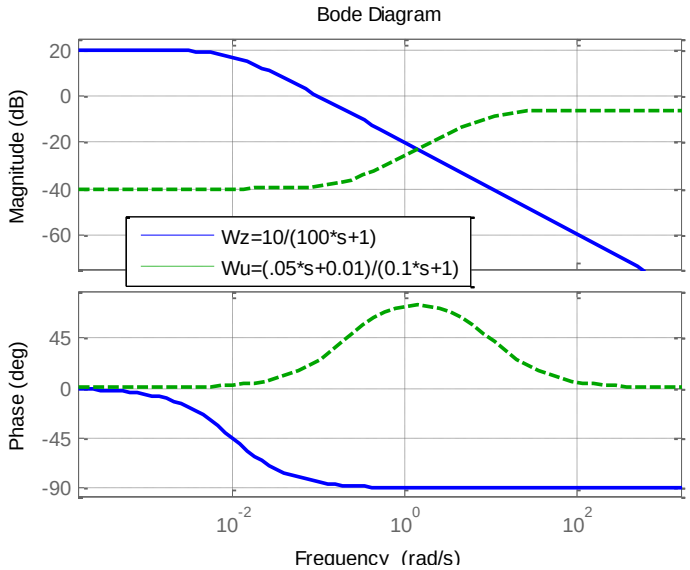


Figure 3-11 The bode plot of $W_z$ and $W_u$

The $H_\infty$ optimal controllers (strictly speaking, only suboptimal) thus designed are given below in the form of transfer functions (the numeric values of the coefficients of the TFs are approximated with two digits precision).

*Controller a* (without current feedback):

$$K_a(s) = \frac{-2.79\times10^2 s^4 + 1.02\times10^5 s^3 + 1.6\times10^6 s^2 + 5.46\times10^6 s - 5.7\times10^3}{s^4 + 1.8\times10^2 s^3 + 1.3\times10^3 s^2 + 3.94\times10^3 s + 9.74\times10^3}$$
$$= -279\frac{(s-0.001)(s+5.12)(s+10)(s-381)}{(s+5.13)(s+172.6)(s^2+2.24s+11)}$$

The optimal gain ( $H_\infty$ norm for the closed loop system) for the first control configurations is $G_{opt1}$=1.615.

*Controller b* (with current feedback):

$$K_b(s) = \frac{\begin{bmatrix} -4.88\times10^8 s^4 - 8.48\times10^{10} s^3 - 3.61\times10^{11} s^2 + 1.18\times10^{11} s - 9.49\times10^{11} \\ -3\times10^6 s^4 - 3.1\times10^8 s^3 + 2.11\times10^9 s^2 + 3.9\times10^{10} s + 1.05\times10^{11} \end{bmatrix}}{s^5 + 4.53\times10^5 s^4 + 8.77\times10^7 s^3 + 1.78\times10^9 s^2 + 8.13\times10^9 s + 6.27\times10^9}$$
$$= \frac{\begin{bmatrix} -4.88\times10^8 (s+5.11)(s+169.37)(s^2-0.73s+2.25) \\ -3\times10^6 (s+4.3)(s+5.08)(s-14.76)(s+108.2) \end{bmatrix}}{(s+0.97)(s+5.13)(s+16.3)(s+171.3)(s+4.53\times10^5)}$$

The optimal gain with the second control configuration is $G_{opt2}$=0.83.

Simulations are then conducted with the designed controller $K_i(s)$ ($i=a,b$) implemented in the control loop. The current load as given in Figure 3-7 is used, and the simulation results with different controllers are presented in Figure 3-12.

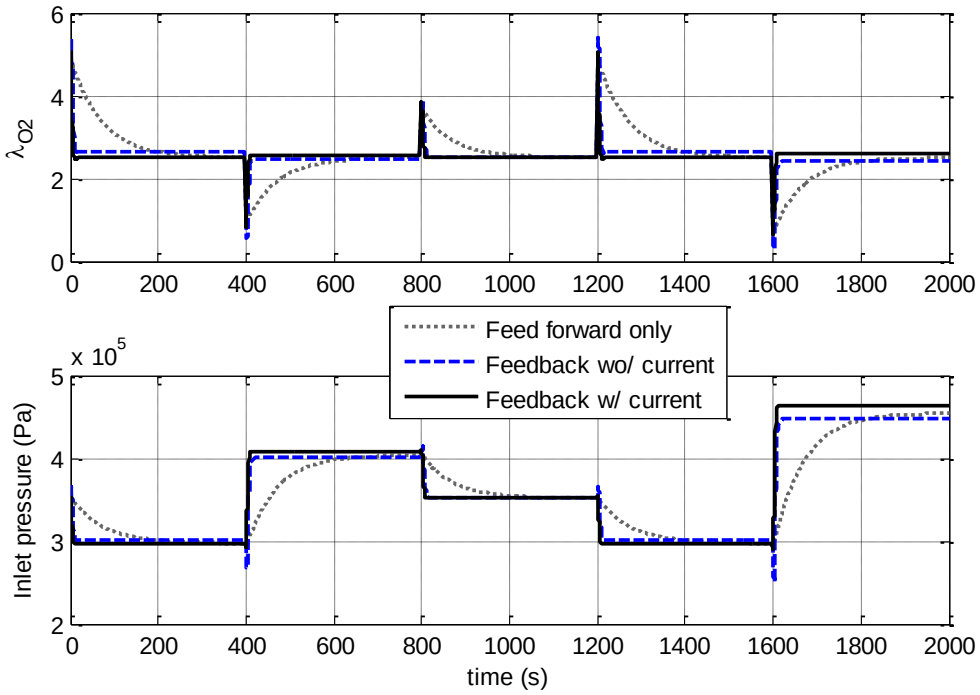


Figure 3-12 Simulation result with different control configurations

It can be seen that for both configurations with feedback control, the designed controllers manage to bring the $O_2$ excess ratio back to the desired value much faster than when only the feed forward control is used. While it takes about 200s for $\lambda_{O_2}$ to reach the steady state without feedback control, a close-up of Figure 3-12 below shows that the $O_2$ excess ratio recovered from the sudden drop to the steady state in less 10s when feedback control is applied.

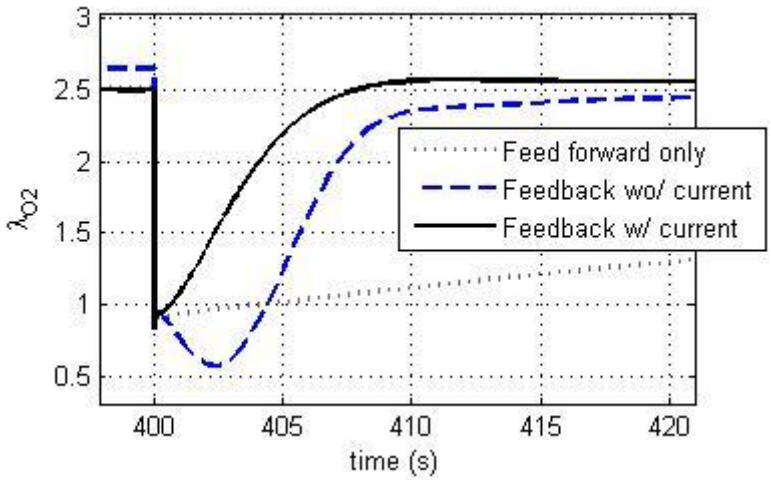


Figure 3-13 A close-up of Figure 3-12

It can also be seen from the above figure that, with the same weighting functions, the feedback controller with the current utilization performs even better than that without the current utilization in terms of both response speed and the static error (especially at low current load, i.e., before 400s in the above figure). Also, the further drop (400~404s) of the performance index in the system response following the current step with Controller (a) is undesirable. Therefore, control configuration (b) in Figure 3-6 is employed for the later discussion in this chapter.

The selection of the weighting functions, i.e., $W_z$ and $W_u$, also plays a very important role in the controller design. Generally, by weighting more heavily on the performance index (larger $W_z$) relative to the controller's output, a faster response and a smaller performance index static error can be achieved. However, the control effort might also be too large to be practical for actual control. On the contrary, a larger $W_u$ would put more limitations on the control effort but result in a slower system response. This is

demonstrated below by comparing two controller designs with different weighting function $W_u$ (the same $W_z = \frac{10}{100s+1}$).

The two weights on the controller output are chosen to be: 1) $W_{u1} = \frac{0.05s+0.01}{0.1s+1}$, (with $G_{opt}$=0.83), and 2) $W_{u2} = \frac{s+0.01}{s+1}$, (with $G_{opt}$=1.8). The bode plots of the two weights are shown below.

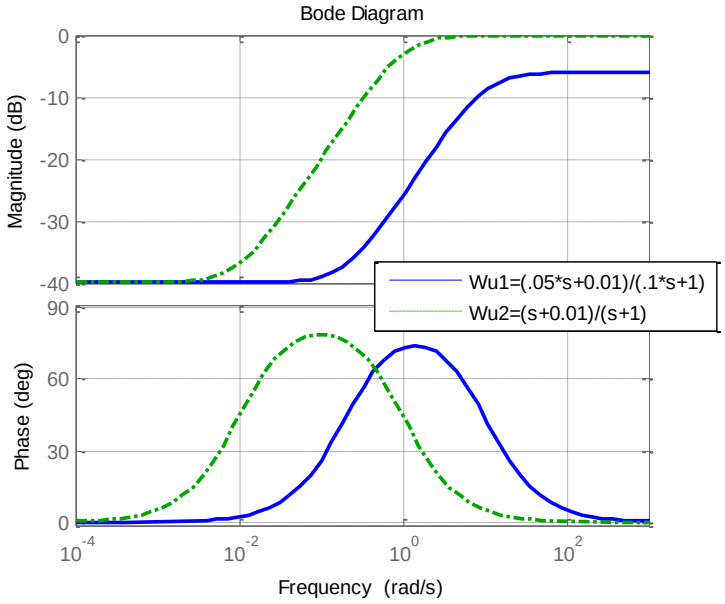


Figure 3-14 Comparison of two weighting functions on the control effort

Both weights have the same steady state gain (0.01). $W_{u1}$ has a high frequency gain of 0.5, and reaches it around 20 rad/s, while $W_{u2}$ has a high frequency gain of 1, and reaches it around 1 rad/s, thus $W_{u2}$ is greater in the magnitude than $W_{u1}$ over the whole frequency range, indicating a heavier weight and more limitation on the controller output,

especially at the higher frequencies. The simulation results using the controllers designed with different $W_u$ are presented in the following figure.

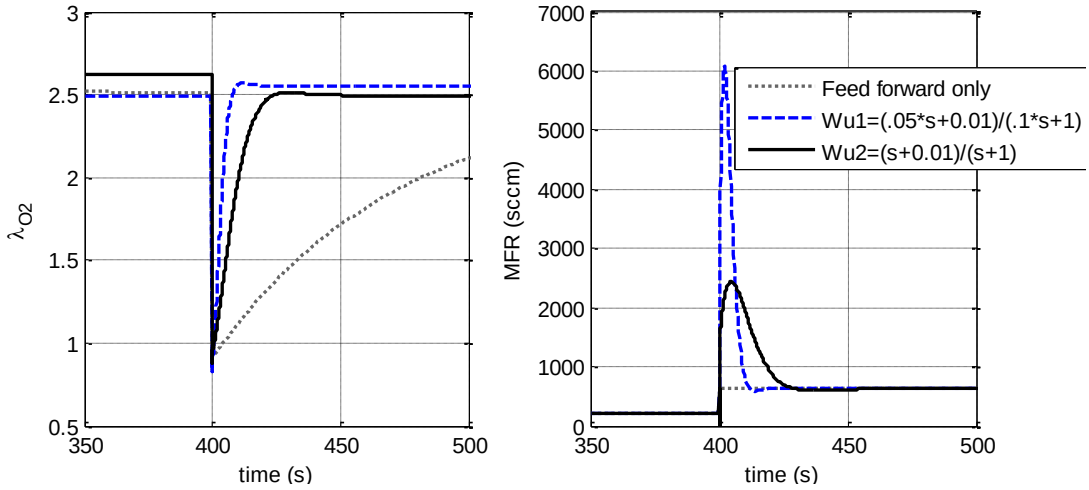


Figure 3-15 Simulation result using H∞ controller with different $W_u$

While the designed controller with $W_{u1}$ has a slightly better performance, its corresponding controller output (the mass flow rate at the mass flow controller) is too high (maximum 6000 sccm), and can cause unnecessary extra energy consumption of the controller and accelerate its aging. By weighting more heavily on the controller output with weight $W_{u2}$, a much more conservative control command is achieved (maximum 2300 sccm), with sacrificing only some slight performance.

### *3.2.3 Simulation with $H_\infty$ Control Integrated in the Full Fuel Cell System Model*

The controller designed in the last section (Section 3.2.2) is based on the simplified air supply system model expressed as (3.1) and (3.2). In this section, the designed $H_\infty$ controller is integrated in the full fuel cell system model for validation. For

simplicity, the channel water flooding is not considered here. The performance weights are selected as follows:

$$W_z = \frac{10}{100s+1}, \text{ and } W_u = \frac{s+0.01}{s+1} \text{ (conservative limitation on the controller output)}$$

Using the robust control toolbox in Matlab, the controller can be optimized and is given below in the form of transfer functions.

*Controller 1*:

$$K_1(s) = \frac{\begin{bmatrix} 8.13\times10^5 s^4 + 3.56\times10^8 s^3 - 3.2\times10^9 s^2 - 6.24\times10^9 s - 2.6\times10^9 \\ -2.75\times10^5 s^4 + 2.7\times10^7 s^3 + 5.13\times10^8 s^2 + 9.86\times10^8 s + 5\times10^8 \end{bmatrix}}{s^5 + 1.65\times10^5 s^4 + 2.03\times10^7 s^3 + 3.1\times10^8 s^2 + 3.7\times10^8 s + 7\times10^7}$$

$$= \frac{\begin{bmatrix} 8.13\times10^5 (s+0.64)(s+1.0639)(s-10.5)(s+446.6) \\ -2.75\times10^5 (s+1.03)(s+1.0653)(s+14.5)(s-114.6) \end{bmatrix}}{(s+0.23)(s+1.0637)(s+16.3)(s+105.2)(s+1.65\times10^5)}$$

The optimal gain with controller 1 is $G_{opt2}$=1.77.

The simulation is carried out using the current load profile given in Figure 3-16 (a), with the results presented in Figure 3-16 (b) ~ Figure 3-21. The system responses in the case of feedforward open-loop control are also plotted for the purpose of comparison.

In Figure 3-16 (a), the current demand is seen to step up at 400s from 5A to 15A, and then step down to 10A at 850s, with the corresponding voltage response first stepping down and then up. It can be seen more clearly from Figure 3-17 that, with the designed $H_\infty$ controller, both the current and the voltage recover from the sudden drop to the steady state much faster than the case of feedforward control only.

For the open-loop control case, the current demand after stepping up to 15A is not instantaneously met. The simulation result shows that the actual current drawn by the

external load immediately drops down to about 12.6A after the demand rise and then creeps up slowly to the steady state value 15A for a steady current output. The voltage is zero during this time interval (10s), meaning completely no power delivery. This can be explained by zero oxygen partial pressure at the cathode reaction site, or reactant starvation at the cathode, when the sudden large current demand consumes all the oxygen near the catalyst site and the maximum current that can be drawn is limited by the diffusion rate of the oxygen in the GDL, which in turn is limited by the partial pressure of the oxygen in the channel. This process can be illustrated by the evolution of the $O_2$ partial pressure in the GDL and in the channel plotted in Figure 3-18.

On the other hand, the simulation results with the designed $H\infty$ feedback controller demonstrate a much shorter reactant starvation interval of about 2s (the sudden drop in the GDL $O_2$ partial pressure after the current demand rise is inevitable) — a great improvement on the fuel cell operating conditions.

Figure 3-19 compares the oxygen excess ratio $\lambda_{O_2}$ and the cathode inlet pressure in the two control cases (open-loop and feedback). As expected, a much faster system response is achieved by employing the feedback controller with the optimal $H\infty$ design, while the performance index ( $\lambda_{O_2}$ ) is kept minimum at the steady state as well. Also, with the chosen performance weights, the control input (the mass flow rate at the mass flow controller) is bounded to a maximum of 2400sccm, as seen in Figure 3-20.

Finally, the hydrogen partial pressures near the catalyst layer and in the flow channel are plotted in Figure 3-21, with only the open-loop stoichiometric flow control. It is observed that, even without any feedback control, there is only a slight drop in the

hydrogen partial pressure near the catalyst layer (less than 5%, in contrast, the $O_2$ partial pressure has a 100% drop) following the sudden current demand rise, implying that there is actually no need for implementing a feedback controller for $H_2$ flow control.

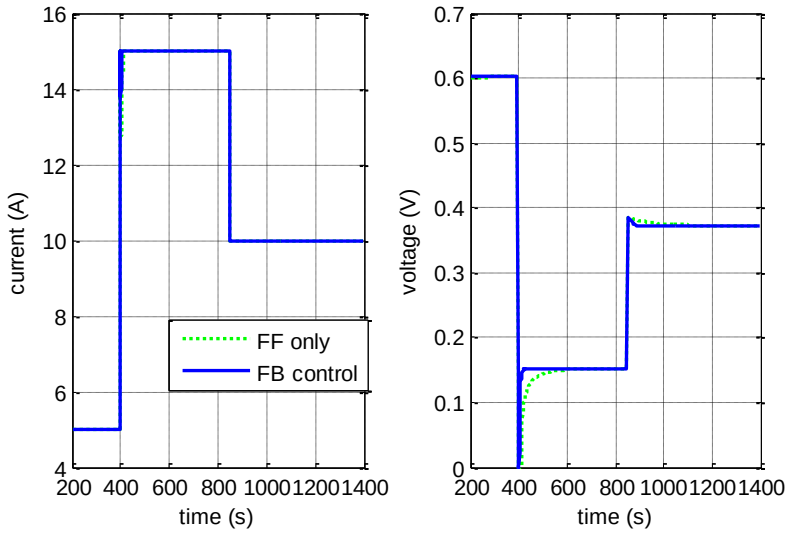


(a) (b)

Figure 3-16 The current load used in the simulation and the voltage response

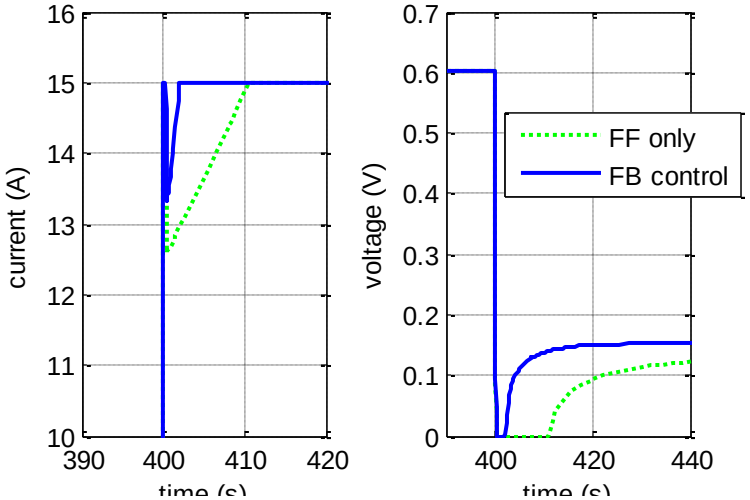


Figure 3-17 A close-up of Figure 3-16

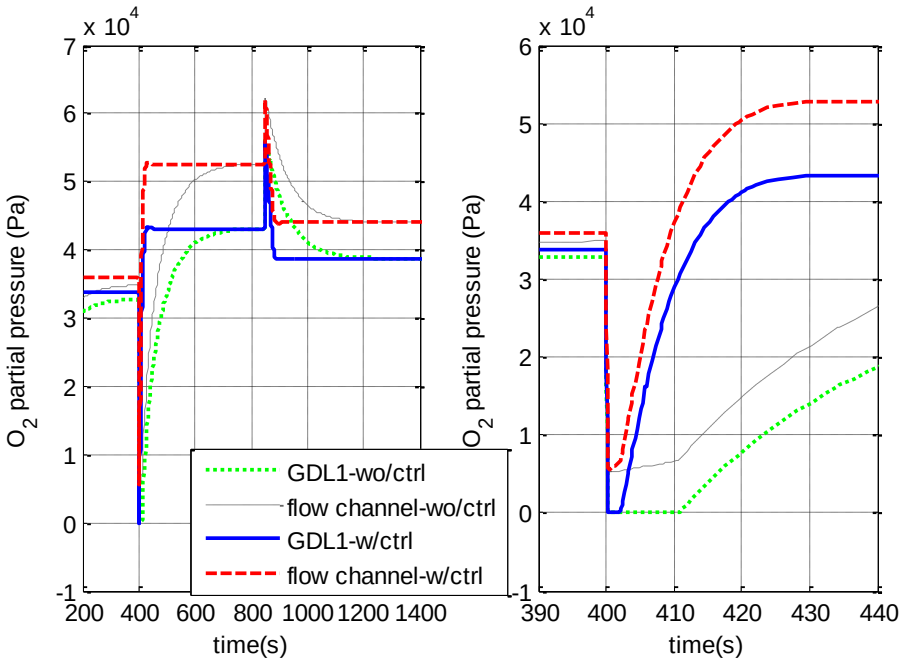


Figure 3-18 The oxygen partial pressures near the catalyst layer and in the flow channel during the full system simulation (the plot in the right is a close-up of the one in the left)

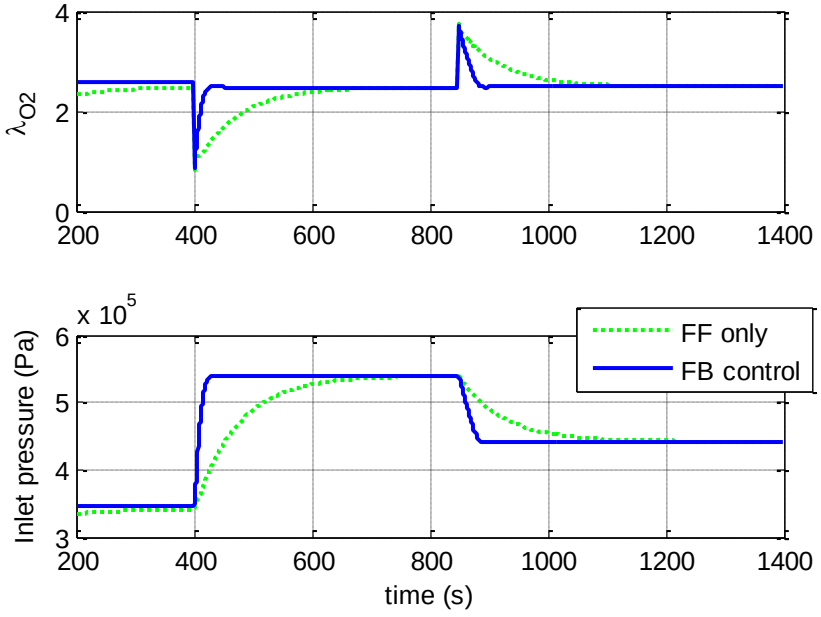


Figure 3-19 The oxygen excess ratio and the cathode inlet pressure in the full system simulation

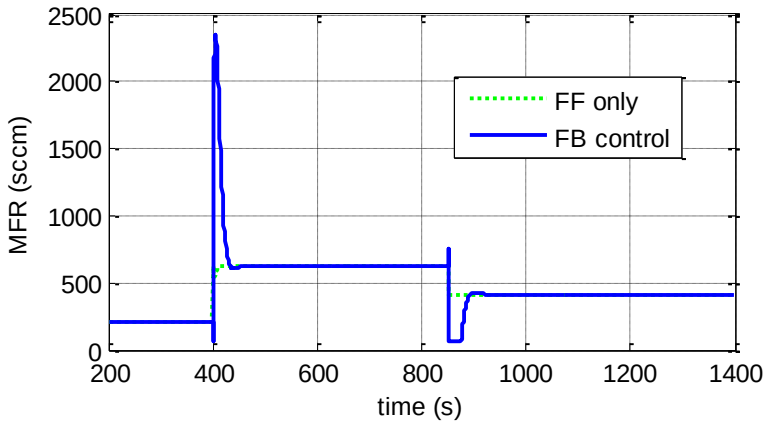


Figure 3-20 The control input (the mass flow rate at the mass flow controller) in the full system simulation

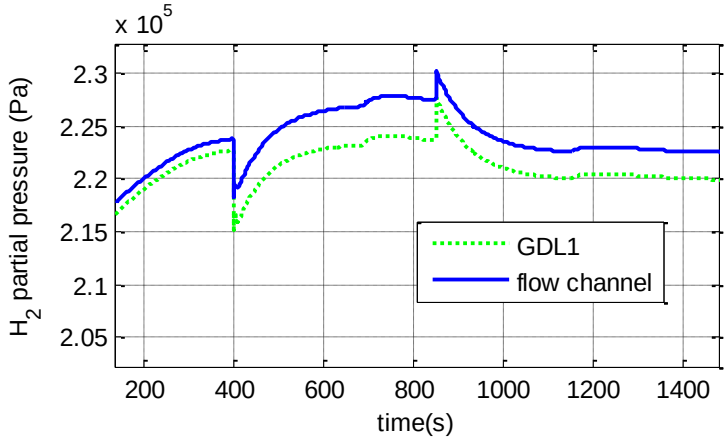


Figure 3-21 The hydrogen partial pressures near the catalyst layer and in the flow channel during the full system simulation

## 3.3 CATHODE CHANNEL FLOODING DIAGNOSTICS

As introduced in Section 2.4, the channel flooding is caused by accumulation of excess liquid water in the flow field, which can be either transported through the GDL under capillary pressure gradient, or formed by water vapor condensation in the channel. The liquid water accumulated in the channel (especially that at the interface of the GDL and the channel) may hinder the reactant transport to the catalyst sites where the electro-

chemical reaction takes place and results in a higher mass concentration loss. In addition, the cross sectional area of the channel is equivalently reduced due to the flow field volume occupation by the flooding water, thus higher flow resistance results and leads to an increased parasitic pressure loss.

While all the types of flooding (and the same with other possible fault such as membrane drying) can result in the cell voltage loss, channel flooding is the only type of faults that can affect the pressure drop between the fuel cell inlet and outlet when the most common flow-through flow field design is used. When a special flow field design, such as interdigitated flow field ([88]), is employed for the bipolar plates, the pressure drop across the cell can be controlled predominantly by the pressure drop caused by the convective gas flow through the porous backing layers. For example, He et al.[88] used the pressure drop between the inlet and outlet channels as a diagnostic signal to monitor the liquid water content in the porous electrodes of a fuel cell with interdigitated flow field. In this dissertation, only the normal flow field with the flow-through design is considered.

The pressure drop has been proved to be an effective and widely accepted diagnostic indicator for flooding detection. Barbir et al. [52] diagnose flooding and drying conditions inside a stack by monitoring pressure drop and cell resistance respectively in an operational fuel cell stack. General Motors patented a method and apparatus that was based on pressure drop monitoring for detecting and correcting water flooding in an air-breathing PEM fuel cell [53] by comparing the measured pressure drop across flow field of a fuel cell stack to acceptable pressure drops (in a lookup table)

determined empirically from a substantially identical, unflooded stack at various electrical discharge rates. Pei et al.[89] showed that the hydrogen pressure drop is strongly affected by liquid water content in the flow channel of fuel cells, and it is not in normal relation with flow rate when the stoichiometric ratio is varied (expand this sentence). The total pressure drop can be calculated by a frictional pressure loss formula accurately, relating with mixture viscosity, stack temperature, operating pressure, stoichiometric ratio and stack current.

In the following, the dynamics model of the reactant supply system as expressed in(3.1)(3.2) is exploited for the diagnosis of channel flooding. By including the water volume in the channel in the state variables, we expand the model of the reactant supply system and construct an EKF-based diagnostic scheme based on the modified nonlinear model.

### *3.3.1 Problem Formulation*

In model (3.1) and (3.2), the inlet pressure $p_{ch,in}$ (equivalently the pressure drop, since the fuel cell back pressure $p_{bpr}$ is assumed to be a constant) is modeled as the subsystem's output. The impact of the channel flooding on this output variable is embodied by the term $k_{ch} = \dfrac{32\mu(T)RT}{D_h^2 \cdot A_{ch} \cdot M \cdot p_{ch}}$, which represents the friction in unit length against the gas flow in the channel. When water accumulates in the flow field, the channel cross sectional area $A_{ch}$ and the hydraulic diameter $D_h$ are equivalently reduced, resulting in an increased friction parameter $k_{ch}$, which in turn leads to a higher pressure

drop. The formula above also reveals that $k_{ch}$ is inversely proportional to the square of the cross sectional area $A_{ch}$, since $D_h^2$ is proportional to $A_{ch}$.

To obtain a direct relationship between the friction parameter $k_{ch}$ and the amount of water accumulated in the channel (described by the water volume $V_{l,ch}$), the channel cross sectional area $A_{ch}$ is written as $A_{ch} = A_{ch}^{nom} - \frac{V_{l,ch}}{L} = A_{ch}^{nom}\left(1 - \frac{V_{l,ch}}{L \cdot A_{ch}^{nom}}\right)$, where $A_{ch}^{nom}$ is the nominal value of the cross sectional area of the channel when no liquid water exists. This formula is based on the simplified assumption that the liquid water inside the channel is evenly spread along the length of the flow field. Note $D_h^2$ is proportional to $A_{ch}$, we then have $D_h^2 A_{ch} = \left(D_h^{nom}\right)^2 A_{ch}^{nom}\left(1 - \frac{V_{l,ch}}{L \cdot A_{ch}^{nom}}\right)^2 = \frac{\left(D_h^{nom}\right)^2 A_{ch}^{nom}}{\left(V_{ch}^{nom}\right)^2}\left(V_{ch}\right)^2$. Therefore, the term $\frac{k_{ch}L}{2}$ can be written as

$$\frac{k_{ch}L}{2} = \frac{16\mu(T)RTL\left(V_{ch}^{nom}\right)^2}{M \cdot \left(D_h^{nom}\right)^2 A_{ch}^{nom}} \frac{1}{p_{ch}\left(V_{ch}\right)^2} = \frac{\kappa_\beta}{p_{ch}\left(V_{ch}\right)^2} \tag{3.5}$$

By substituting (3.5) in (3.1) and (3.2), and also taking the derivative of $V_{ch}$, the model equations for the air supply system can now be rewritten as in (3.6) and (3.7).

State Equations

$$\begin{cases} \dfrac{MV_{sm}}{RT}\dot{p}_{sm} = \left(\dot{m}_{in}^{a} + \dot{m}_{hm}^{v}\right) - \dfrac{p_{sm} - p_{ch}}{K_{sm,out} + K_{ch,in} + \dfrac{\kappa_{\beta}}{p_{ch}\left(V_{ch}\right)^{2}}} \\ \dfrac{MV_{ch}}{RT}\dot{p}_{ch} = \dfrac{p_{sm} - p_{ch}}{K_{sm,out} + K_{ch,in} + \dfrac{\kappa_{\beta}}{p_{ch}\left(V_{ch}\right)^{2}}} - \dfrac{p_{ch} - p_{rm}}{\dfrac{\kappa_{\beta}}{p_{ch}\left(V_{ch}\right)^{2}} + K_{ch,out} + K_{rm,in}} \\ \qquad -\dot{m}_{rct}^{O_2} - \dfrac{Mp_{ch}}{RT}\dot{V}_{ch} \\ \dfrac{MV_{rm}}{RT}\dot{p}_{rm} = \dfrac{p_{ch} - p_{rm}}{\dfrac{\kappa_{\beta}}{p_{ch}\left(V_{ch}\right)^{2}} + K_{ch,out} + K_{rm,in}} - \dfrac{p_{rm} - p_{bpr}}{K_{rm,out}} \end{cases} \tag{3.6}$$

Output Equation

$$p_{ch,in} = p_{ch} + \left( \frac{p_{sm} - p_{ch}}{K_{sm,out} + K_{ch,in} + \dfrac{\kappa_{\beta}}{p_{ch}\left(V_{ch}\right)^{2}}} - \dot{m}_{rct}^{O_2} \right) \times \left( K_{ch,in} + \frac{\kappa_{\beta}}{p_{ch}\left(V_{ch}\right)^{2}} \right) \tag{3.7}$$

The problem of the channel flooding diagnosis can then be stated as: *Based on model (3.6) and (3.7), construct a diagnostic scheme that utilizes the measurable input and output of the air supply system to generate a signal (residual) that can effectively indicate the existence and magnitude of the system fault, i.e., water flooding inside the flow field*.

The problem above is essentially an estimation problem for the water volume $V_{l,ch}$, or equivalently the channel volume $V_{ch}$, since $V_{ch} = L \cdot A_{ch}^{nom} - V_{l,ch} = V_{ch}^{nom} - V_{l,ch}$. While $V_{ch}$ appears in the state space equations as a varying parameter, it can be constructed as an observer problem simultaneously estimating the system state variables

and parameters. To address this problem, we propose an EKF-based diagnostic scheme, which is described in the next subsection.

### *3.3.2 EKF design*

The channel flooding water removal model given in (2.19) completes the description of the liquid water dynamics in the channel (characterized by the water volume $V_{l,ch}$, or equivalently $V_{ch}$) given in (2.15). As much as this modeling approach facilitates simulation validations of controllers and diagnostic systems that deal with the channel flooding fault, it is unable to capture the stochastic nature of the liquid water dynamics. Therefore it is hard to utilize the model in an observer-based diagnostic scheme design.

Here, the liquid water in the channel is considered as an unknown disturbance and its derivative is modeled as a process noise, i.e., $\dot{V}_{l,ch} = w_{l.ch}$. Since $V_{ch}$ is used as the parameter in (3.6) and (3.7), we obtain its derivative as $\dot{V}_{ch} = -\dot{V}_{l,ch} = -w_{l.ch} = w_{ch}$.

To standardize the state-space model notation, let the states to be defined as $\begin{bmatrix} p_{sm} & p_{ch} & p_{rm} & V_{ch} \end{bmatrix}^T = \begin{bmatrix} x_1 & x_2 & x_3 & x_4 \end{bmatrix}^T$, and the $O_2$ reaction rate considered as a known disturbance $\dot{m}_{rct}^{O_2} = d_{rct}$. Also note the total inlet air mass flow rate is $\dot{m}_{in}^a + \dot{m}_{hm}^v = \dot{m}_{in}^a \left(1 - x_{amb}^v\right) \frac{1}{\overline{x}^a}$. As a consequence, we define this term as the control input, i.e., $\dot{m}_{in}^a + \dot{m}_{hm}^v = \left(1 - x_{amb}^v\right) \frac{1}{\overline{x}^a} \dot{m}_{in}^a \triangleq b_{hm} \cdot u_{\mathrm{MF}}$, where $b_{hm} \triangleq \left(1 - x_{amb}^v\right) \frac{1}{\overline{x}^a}$ is a constant

coefficient that only depends on the component of the ambient air and $u_{\mathrm{MF}} \triangleq \dot{m}_{in}^{a}$ is the mass flow rate at the controller (MFC).

By substituting the above defined terms and the new state equation for the channel volume $\dot{V}_{ch} = w_{ch}$, equations (3.6) and (3.7) are now modified to be (3.8) and (3.9)

$$\text{State Equations} \quad \begin{cases} \dot{x}_1 = -\alpha_{sm} \dfrac{x_1 - x_2}{K_{n1} + \dfrac{\kappa_\beta}{x_2 x_4^2}} + \alpha_{sm} b_{hm} \cdot u_{\mathrm{MF}} \\ \dot{x}_2 = \dfrac{\theta_{Mix}}{x_4} \dfrac{x_1 - x_2}{K_{n1} + \dfrac{\kappa_\beta}{x_2 x_4^2}} - \dfrac{x_2 - x_3}{K_{n2} + \dfrac{\kappa_\beta}{x_2 x_4^2}} - \dfrac{\theta_{Mix}}{x_4} d_{rct} - \dfrac{x_2}{x_4} w_{ch} \\ \dot{x}_3 = \alpha_{rm} \dfrac{x_2 - x_3}{K_{n2} + \dfrac{\kappa_\beta}{x_2 x_4^2}} - \alpha_{rm} \dfrac{x_3 - p_{bpr}}{K_3} \\ \dot{x}_4 = w_{ch} \end{cases} \tag{3.8}$$

$$\text{Output Equation} \qquad y = x_2 + \left( \frac{x_1 - x_2}{K_{n1} + \dfrac{\kappa_\beta}{x_2 x_4^2}} - d_{rct} \right) \times \left( K_{ch,in} + \frac{\kappa_\beta}{x_2 x_4^2} \right) + v_m \tag{3.9}$$

where $\alpha_{sm} = \dfrac{RT}{MV_{sm}}$, $\alpha_{rm} = \dfrac{RT}{MV_{rm}}$, and $\theta_{Mix} = \dfrac{RT}{M}$. $v_m$ is the measurement noise assumed to be white.

To apply the discrete EKF approach, the system needs to be discretized first. Using the forward Euler method and sampling time $\Delta T$, we obtain the following discrete state space equations as given in (3.10)~(3.14).

$$x_{1,k+1} = x_{1,k} - \Delta T \cdot \alpha_{sm} \frac{x_{1,k} - x_{2,k}}{K_{n1} + \dfrac{\kappa_\beta}{x_{2,k} x_{4,k}^2}} + \Delta T \cdot \alpha_{sm} b_{hm} \cdot u_{\mathrm{MF},k} \tag{3.10}$$

$$x_{2,k+1} = x_{2,k} + \Delta T \cdot \frac{\theta_{Mix}}{x_{4,k}} \frac{x_{1,k} - x_{2,k}}{K_{n1} + \dfrac{\kappa_\beta}{x_{2,k} x_{4,k}^2}} - \Delta T \cdot \frac{x_{2,k} - x_{3,k}}{K_{n2,k} + \dfrac{\kappa_\beta}{x_{2,k} x_{4,k}^2}} - \Delta T \cdot \frac{\theta_{Mix}}{x_{4,k}} d_{rct,k} - \Delta T \cdot \frac{x_2}{x_4} w_{ch,k} \tag{3.11}$$

$$x_{3,k+1} = x_{3,k} + \Delta T \cdot \alpha_{rm} \frac{x_{2,k} - x_{3,k}}{K_{n2,k} + \dfrac{\kappa_\beta}{x_{2,k} x_{4,k}^2}} - \Delta T \cdot \alpha_{rm} \frac{x_{3,k} - p_{bpr}}{K_3} \tag{3.12}$$

$$x_{4,k+1} = x_{4,k} + \Delta T \cdot w_{ch,k} \tag{3.13}$$

$$y_k = x_{2,k} + \left( \frac{x_{1,k} - x_{2,k}}{K_{n1} + \dfrac{\kappa_\beta}{x_{2,k} x_{4,k}^2}} - d_{rct,k} \right) \times \left( K_{ch,in} + \frac{\kappa_\beta}{x_{2,k} x_{4,k}^2} \right) + v_{m,k} \tag{3.14}$$

The standard EKF procedure can then be applied to estimate the state vector $\begin{bmatrix} x_{1,k} & x_{2,k} & x_{3,k} & x_{4,k} \end{bmatrix}^T$ in the above discrete system.

### *3.3.3 Simulation results*

The simulation is carried out under constant voltage mode. The voltage profile for this simulation and the corresponding current response is shown in Figure 3-22. The dictated channel volume follows a zigzag-like profile (Figure 3-23), emulating the sudden purge and the gradual accumulating process of the liquid water in the channel.

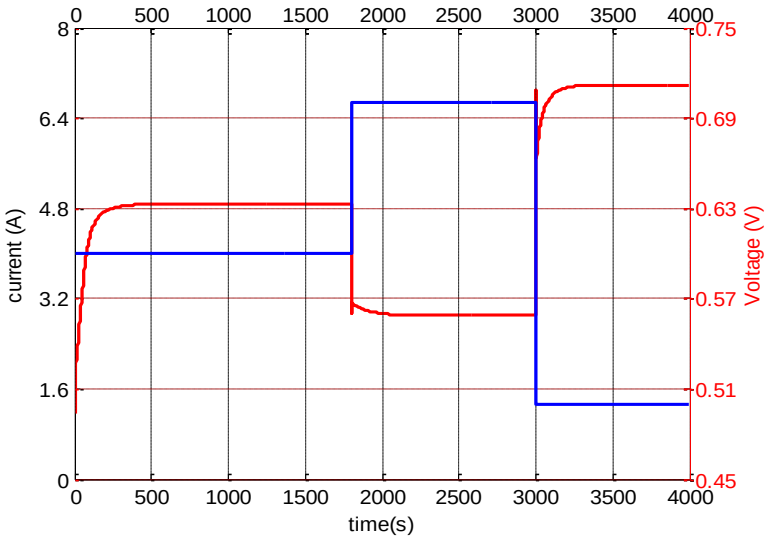


Figure 3-22 The system voltage input and current response

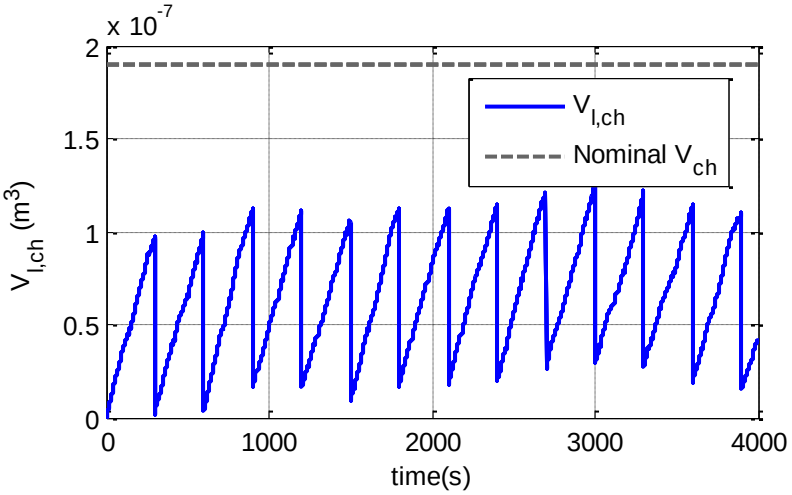


Figure 3-23 The dictated water volume inside the channel

The simulation results are presented in Figure 3-24. It can be seen that, by appropriately choosing the EKF parameters (mainly including the discrete time step length, the covariance matrices for process and measurement noises), successful tracking of the liquid water volume in the channel, along with estimation of total pressures in the fuel cell system, can be achieved.

Figure 3-25 is a close-up of Figure 3-24 for clearer view. The estimation error is seen to be the largest at the moment of sudden purge.

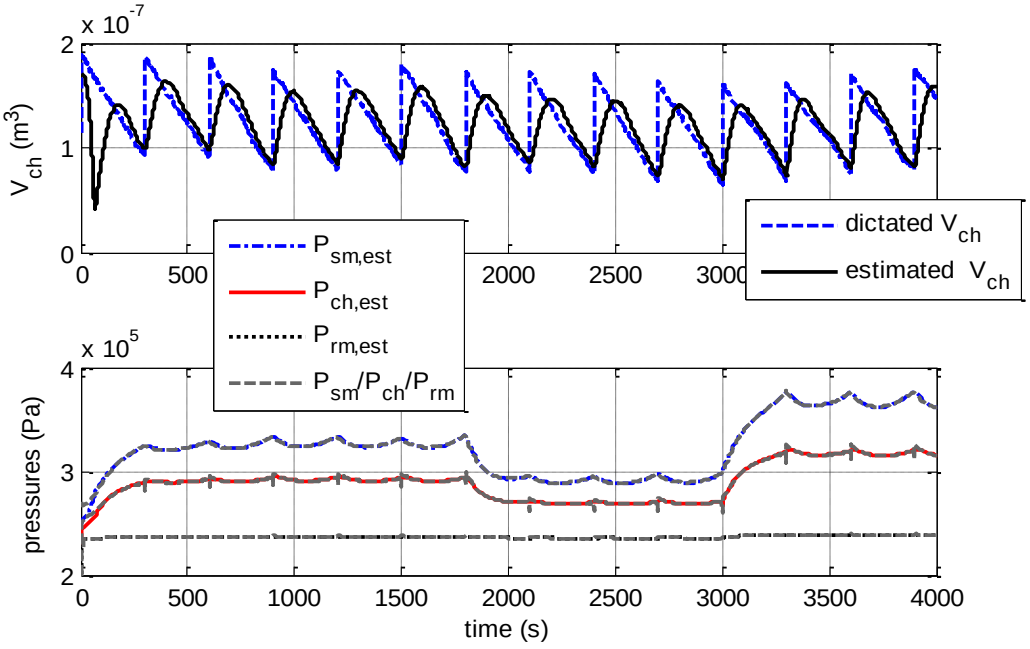


Figure 3-24 Simulation results of on-line fuel cell diagnosis scheme based on the EKF

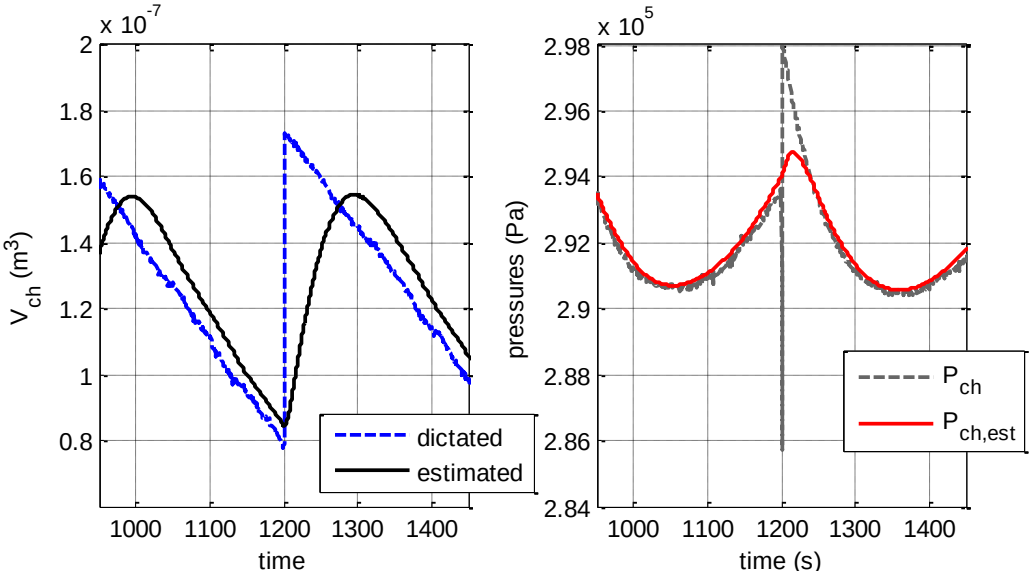


Figure 3-25 A close-up of Figure 3-24

## 3.4 CHAPTER SUMMERY

A diagnostic based control design for the air supply of the fuel cell system is proposed in this chapter. This concept allows selection of the most suitable controller in a controller bank that delivers the best performance under specific operating conditions and that mitigates the faulty condition based on the feedback of the diagnosis results. The control problem is reformulated as an H-infinity robust control problem, the objective of which is to minimize the difference between the desired and actual excess $O_2$ ratio, thus preventing and minimizing the oxidant starvation at the cathode. A model-based on-line diagnostics system is developed for fuel cell flooding diagnosis thanks to the incorporation of the fault effect in the fuel cell model. The channel flooding diagnostic problem is decoupled from the GDL flooding and membrane drying diagnostic problem, and is formed as a simultaneous state and parameter estimation problem. Extended Kalman Filter technique is then applied to solve the problem. Simulation results show that with the designed $H\infty$ feedback controller, a much shorter reactant starvation interval (the sudden drop in the GDL $O_2$ partial pressure after the current demand rise is inevitable) can be achieved, greatly improving the fuel cell operating conditions. The proposed EKF-based on-line diagnostic system is also demonstrated to be able to track the liquid water present in the cathode channel with acceptable accuracy when filter parameters are properly tuned.

# CHAPTER FOUR

# EXPERIMENTAL STUDY OF FUEL CELL AGING PROCESS

Prognostics demands aging model(s) that represent the understanding of a particular fault to failure progression rate[90], or the damage variables evolution rate (Damage variables are internal parameters or external variables of the fuel cell unit system that undergo a noticeable change during the aging process in the fuel cell's life span). To obtain this model, it is first necessary to identify and experimentally validate damage variables.

In this chapter, aging process of the PEM fuel cell is studied experimentally as a preliminary step for building the demanded prognostic-oriented degradation model for health monitoring and prognostic purpose. Various in-situ diagnostic tools are explored for the damage tracking for the health state of the fuel cell during its durability test. We discuss the criteria for choosing valid aging indicator for the fuel cell and compare several candidate damage variables. Experimental results of the evolution of these damage variables are presented and analyzed.

## 4.1 EXPERIMENTAL SETUP

The experimental platform in the Fuel Cell and Diagnostics Lab at Oak Ridge National Laboratory (ORNL) was composed of a fuel cell test stand and a tested PEM fuel cell unit, which are respectively described in this section.

### *4.1.1 Fuel Cell Test Stand*

Fuel cell test stand serves as the auxiliary system, or balance of plant, in a functionally integrated fuel cell system. In this research, a commercially available and fully automated fuel cell test stand (Figure 4-1) at ORNL is employed, equipped with an electronic load bank (AMREL PLA800-60-300), and a frequency response analyzer (AMREL INSC-II Frequency Response Analyzer) to create load variations. Figure 4-2 depicts a schematic of the integrated fuel cell system for better illustration of the connection between the fuel cell, the auxiliary system and the electronic load.

The ORNL fuel cell test stand uses mass flow controllers (MKS Instruments, Inc.) to meter bottled gas to the fuel cell and manually adjustable back pressure regulators (Swagelok KCB1A0C5EP11) to operate the fuel cell at the specified pressure. Reactant gas humidity was controlled by a stand-alone Dew Point Humidifier System from Arbin Instruments, while the fuel cell temperature is controlled with an environmental chamber (Sigma Systems 170MMC-3) that is capable of maintaining operating temperatures of -40 to +200 ℃. Also, for fuel cell inlet pressure measurement, the pipelines immediately in front of the fuel cell inlets were customized for the installation of two pressure sensors at both anode and cathode sides of the fuel cell.

In Figure 4-2, NI Device represents the device from National Instrument used for signal acquisition and signal exchange between the mass flow controllers (MFC) and the main control computer where customized code is used for MFC commanding and data monitoring/recording. The main control computer can also control the electronic load bank (eLOAD) through GPIB link under its remote control mode.

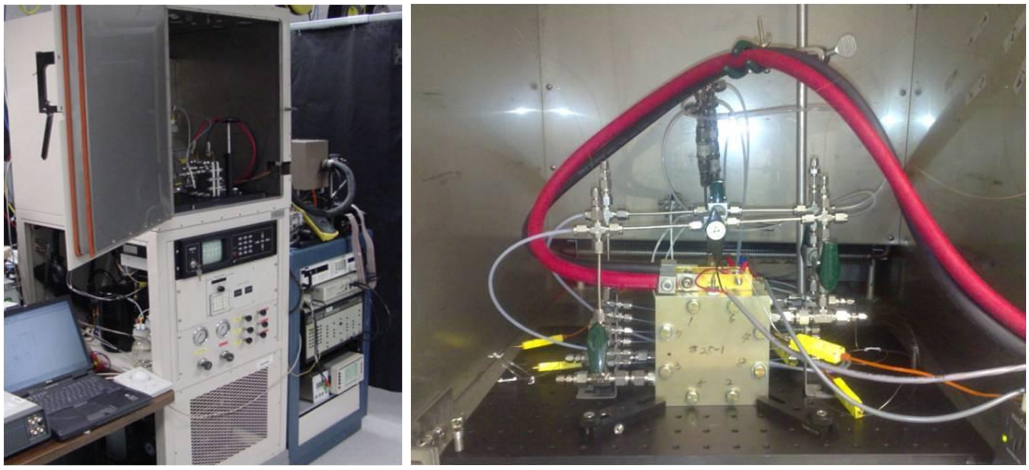

Figure 4-1 Photo of the Fuel Cell Test Stand

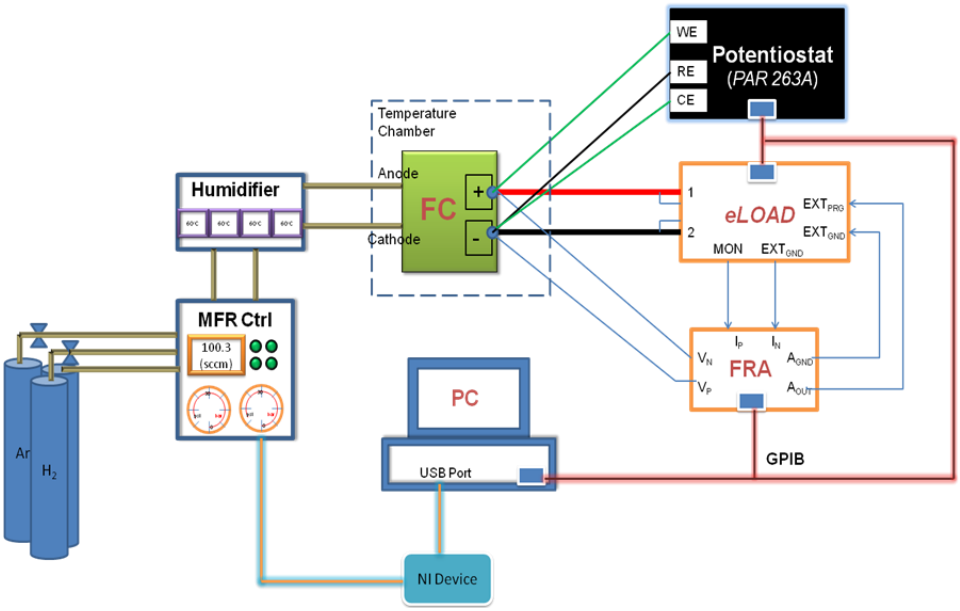


Figure 4-2 Schematic of the Experimental Setup

### *4.1.2 Fuel Cell*

A homemade unit fuel cell with 15 $cm^2$ active area is used in this research. Various fuel cell components are designed in ORNL and manufactured by outsource companies and eventually assembled in the lab.

The Nafion-117 membrane was employed to ensure membrane integrity for the 1000 hours durability evaluation. Electrochem Inc. manufactured the MEAs to the specification using 180μm thick Nafion-117. The 0.5 mg Pt/ $cm^2$ electrode was confined to the center of the MEA and an outer frame of the polymer was available for sealing with gaskets. An un-integrated 380μm gas diffusion layer (GDL) was employed with a micro-porous carbon layer on the MEA side.

Bipolar plates of two different materials were employed for current collection and to create a flow field amenable to fuel cell applications. For FC with metal bipolar plate, a specially designed alloy with optimal nitrating characteristics, Fe20Cr4V was manufactured (by ATI Allegheny Ludlum) and employed in the metallic foils. To create a flow field in the foils amenable to fuel cell applications the foils were mechanically stamped with a single channel serpentine flow field. The 50 micron thick foils were all stamped using the same force and resulted in a reproducible 1.6 mm channel as shown in Figure 4-3. For FC with graphite bipolar plate, the industry standard, polished fuel cell-grade graphite plates (6.5 mm thick from ElectroChem) were obtained and cut to the same areal dimensions. The engraved flow-channel dimensions were chosen to replicate the single-serpentine pathway in the stamped alloy foils and are depicted in Figure 4-3.

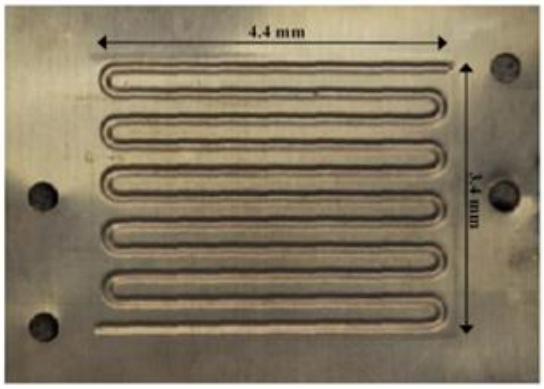


Figure 4-3 Stamped foil showing serpentine flow field of cathode side

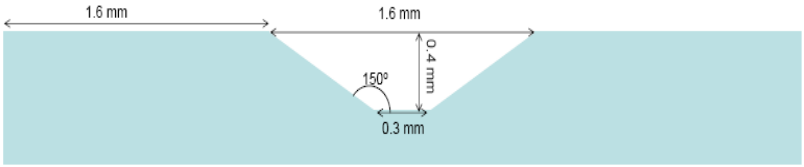


Figure 4-4 Flow channel geometry

To seal the fuel cell from leaks, ensure good electrical contact, and channel flow to the serpentine pathway, a series of gaskets was employed. Gasketing materials were either 250 micron Viton or 50-130 micron FEP (fluorinated ethylene propylene).

### *4.1.3 Experiment Design*

The flow chart of the experimental procedure is given in Figure 4-5.

To evaluate the fuel cell aging rate under different operating conditions, a test operating condition must first be designed and controlled to maintain throughout the durability test. After the tested unit fuel cell has been prepared and broken in (explained in Section 4.2), the durability test is then initiated under the designed operating conditions to induce the controlled aging.

For every 1/10$^{th}$ of the nominal fuel cell life (about 80 ~ 100 h), the durability test has to be interrupted in order to perform a set of fuel cell characterization using various in-situ diagnostic techniques to obtain the damage variables of interest. The characterization techniques employed in the research include polarization curves, Electrochemical Impedance Spectroscopy (EIS), Cyclic Voltammetry (CV) test and Linear Sweep Voltammetry (LSV), where CV and LSV tests require that fuel cell be operated under some specific conditions that are completely different than the normal aging operating conditions.

After each interrupted damage test, the fuel cell is reinstated to the durability test operating conditions for continued aging test. Because of the waiting time between different test condition for the fuel cell to reach steady state, the in-situ diagnosis for the fuel cell damage characterization would usually cost a total time from 6~12 hours.

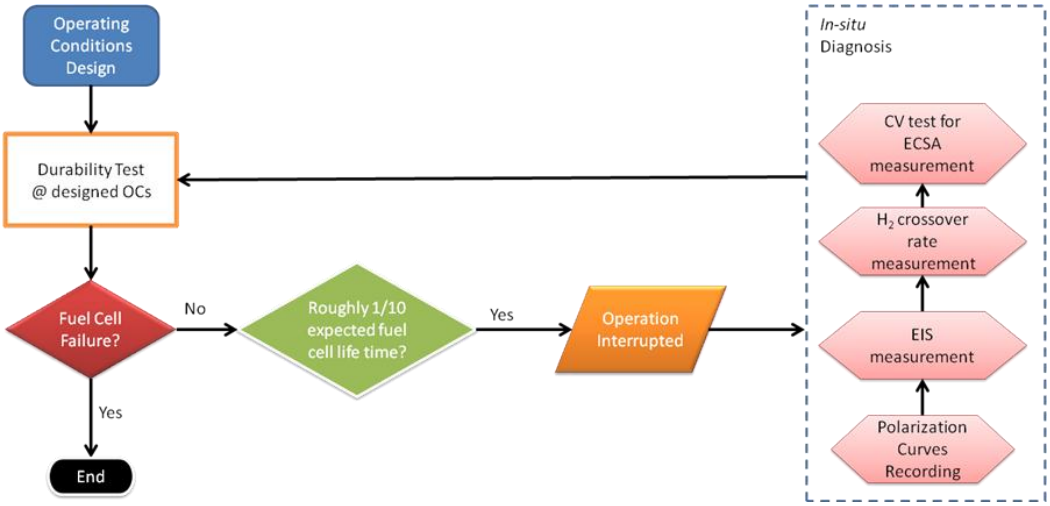


Figure 4-5 Experiment procedure flow chart

## 4.2 DURABILITY TEST

Before the durability test starts, the fuel cell needs to be prepared. Once fully assembled, the cells were compressed using eight 6-32 bolts and applying 10 in-lbs of torque. Using a friction coefficient of 0.36 (based on dry threads) this corresponds to a pressure of 22 atm on the $32\,cm^2$ collector plates. After the initial compression the cell was mounted into the test stand and leak checked using an inert gas. Following the USFCC (United States Fuel Cell Council) guidelines, crossover was investigated at 2.5 psig, and a total system leak rate was measured to be less than 1.0 psi after 10 minutes, using an initial pressure of 25 psig. Once these guidelines had been satisfied, 99.999% pure H2 and compressed air were introduced to the fuel cell and the system was heated to 80℃ and pressurized to 25.5 psig on the cathode and 25 psig on the anode. While heating and pressurizing the fuel cell, the system was operated at a constant voltage of 0.6V while flowing 200 $cm^3$/min (standard temperature and pressure – STP) (sccm) of both H2 and air. The gases were fully humidified to 78℃ and the gas supply lines were heated to 79℃. Once the fuel cell system achieved desired operating temperatures and pressures, the membranes were broken-in by using the following cycle: 0.6V for 30min, 0.4V for 30min, and open circuit voltage (OCV) for 1min. This procedure was repeated 16 times while flowing 2.5 times the stoichiometrically required O2 and 1.25 excess H2 with a minimum flow rate of 100 and 50 sccm, respectively.

Finally, voltage cycling was initiated for the long term durability test controlled at the designed operating conditions. In this research, the fuel cell is operated under fully humidified conditions of both hydrogen and air with stoichiometric coefficients of 1.5 for

H2 and 2.2 for O2 at a controlled fuel cell temperature of 80 ℃ using the following cycle: 0.6V for 30min, 0.7V for 20min, 0.5V for 20min, and OCV for 1min. Throughout this entire sequence the fuel cell was periodically re-tightened using 10 in-lb of torque. The 1hr 11min profile is shown in Figure 4-6, and the operating conditions are tabled in Table 4-1.

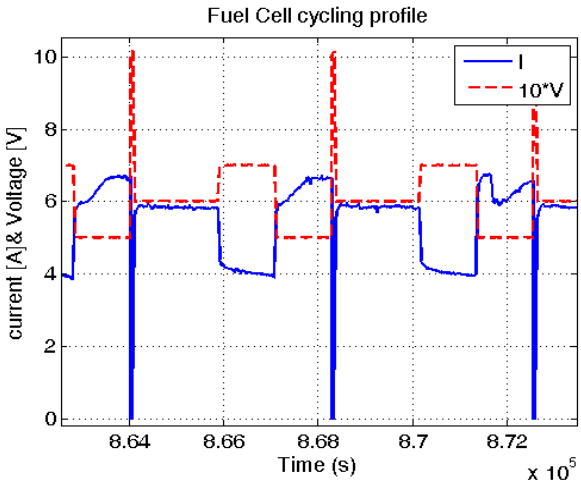


Figure 4-6 The cycling potential and resulting current profile for the durability test

Table 4-1 Operating conditions used in the durability test

| **Controlled Variable** | **Control Method** | **Controlled value during durability test** |
|---|---|---|
| Hydrogen Mass Flow (Anode) | Mass Flow Controller (MFC) | 1.5 stoichiometry (minimum: 50 sccm) |
| Air Mass Flow (Cathode) | MFC | 2.2 stoichiometry (minimum: 100 sccm) |
| Back Pressure | Return Manifold Pressure Control | 25 psi (relative to 1 atm) |
| FC temperature | Heating Tape | 80 ℃ |
| Humidifier Dew Point Temperature (DPT) | Dew Point Humidifier | 78 ℃ (Both sides) |
| Gas Temperature | Heating Tape | 79 ℃ (Both sides) |

## 4.3 IN-SITU DIAGNOSTIC TOOLS FOR FUEL CELL DAMAGE TRACKING

### *4.3.1 Electrochemical Impedance Spectroscopy (EIS)*

Electrochemical impedance spectroscopy (EIS), a diagnostic tool that has been widely employed in the studies of electrochemical systems such as battery, has been utilized by an increasing number of researchers in PEM fuel cell studies in recent years[47]. While static polarization curves are usually used to characterize the fuel cells' overall performance, the information contained in the polarization curves is insufficient to separate various sources of fuel cell losses. EIS, on the other hand, is capable of distinguishing between ohmic, activation and concentration losses ([77]).

The EIS technique is used to obtain the fuel cell impedance around some steady state operating point as a function of frequency by applying a small sinusoidal AC potential (or current) as a perturbation signal to the fuel cell and measuring the current (or potential) response[47]. The results can be best interpreted using an equivalent electrical circuit model, as depicted in Figure 4-7 ([77]).

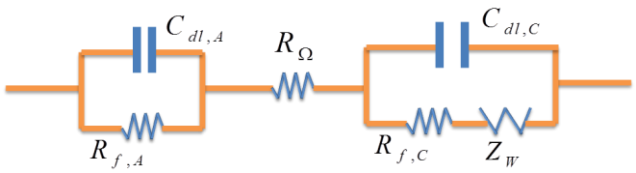


Figure 4-7 A simple fuel cell equivalent electrical circuit model

In the above figure, $R_\Omega$ is the total Ohmic resistance, $R_{f,A}, R_{f,C}$ represent the Faradic resistances at the anode and the cathode, respectively, $C_{dl,A}, C_{dl,C}$ the double layer capacitances at the electrolyte/electrode interfaces, and $Z_w$ the Warbug impedance

element accounting for the mass transport loss at the cathode side. The total impedance can thus be expressed as

$$Z = R_{ohm} + \frac{1}{1/R_{f,A} + j\omega C_{dl,A}} + \frac{1}{1/\left(R_{f,C} + Z_w\right) + j\omega C_{dl,C}} \tag{4.1}$$

Since the activation loss at the anode side is significantly smaller than that at the cathode side for hydrogen PEMFC, the anode impedance is neglected for simplicity, i.e., we take $R_{f,A} = 0$. Also, when the EIS curves are recorded at small current load, mass transport loss effect is considered small and can be neglected ( $Z_w = 0$ ) as well. The impedance of the fuel cell is then simplified to:

$$Z = R_{ohm} + \frac{1}{1/R_{f,C} + j\omega C_{dl,C}} \tag{4.2}$$

The model expressed in (4.2) is the common Randles cell model, with a plane double layer capacitor. However, when applied to the fuel cell EIS data fitting, this model is not entirely satisfactory in explaining the impedance behavior in the interested frequency range. This leads to the substitution of the plain capacitor with a constant phase element (CPE) [39], and model (4.2) is modified to be

$$Z = R_{ohm} + \frac{1}{1/R_{f,C} + \left(j\omega\right)^{\alpha} Q_C} \tag{4.3}$$

where $Q_C$ and $\alpha$ are CPE parameters to be identified. The result of the data fitting using the Randles cell model with a CPE is shown in Figure 4-8.

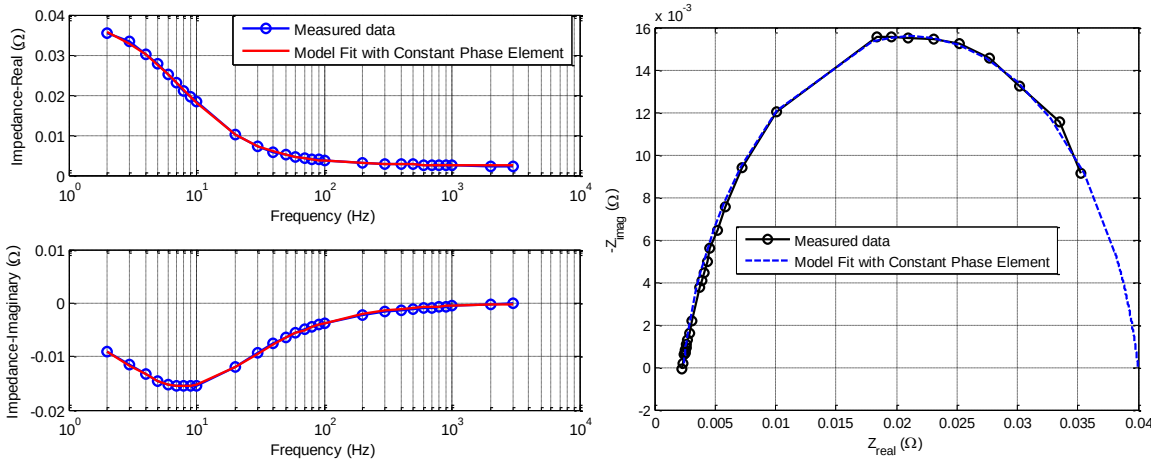


Figure 4-8 Bode plot (left) and Nyquist plot (right) of the EIS (recorded at 1A) and data fitting using Randle cell model with a CPE

In the Nyquist plot of the EIS curve in Figure 4-8, the high frequency intercept of *x*-axis can be interpreted as the total ohmic resistance of the fuel cell, i.e. $R_{ohm}$. This parameter can be acquired with relative ease and may indicate the state of the membrane. Theoretically, the EIS curve has another intersection with the *x*-axis at zero frequency (the low frequency part that is below 1Hz of the EIS curve cannot be recorded due to equipment limitation). The distance between the two intercepts can be interpreted as the Faradic resistance $R_{f,C}$ that accounts for the activation loss (mainly cathode activation loss).

The *x*-axis intercept of the EIS curve at zero frequency, defined here as $Z_R$, can be understood by revisiting the voltage-current equation in(2.53), which is rewritten as follows

$$V_{\text{cell}} = 1.229 - 0.85\times10^{-3}\left(T_{fc} - 298.15\right) + \frac{RT_{fc}}{2F}\ln\left[\frac{p^*_{H_2}\left(p^*_{O_2}\right)^{\frac{1}{2}}}{p_{H_2O}}\right] - \frac{RT}{4(1-\alpha)F}\ln\left[\frac{\left(i+i_{leak}\right)}{i_0^{\text{ref}}\Big|_{t=0}}\times\frac{1}{\xi_{\text{cat}}}\times\left(\frac{p_{O_2}^{\text{ref}*}}{p^*_{O_2}}\right)^{\alpha}\right] - i\cdot A_{\text{fc}}\cdot R_{ohm} \quad (4.4)$$

By substituting $I = i\cdot A_{\text{fc}}$ , and $p^*_{O_2} = p^{ch}_{O_2} - \frac{I\cdot\delta_{GDL}}{D_{\text{eff}}RT4FA_{fc}}$ , the above equation becomes

$$V_{\text{cell}} = \bar{E}_0 - \frac{RT}{4(1-\alpha)F}\ln\left(I + I_{leak}\right) + \frac{RT}{4(1-\alpha)F}\ln\left(p^{ch}_{O_2} - \frac{I\cdot\delta_{GDL}}{D_{\text{eff}}RT4FA_{fc}}\right) - I\cdot R_{ohm} \quad (4.5)$$

where $\bar{E}_0 = 1.229 - 0.85\times10^{-3}\left(T_{fc} - 298.15\right) + \frac{RT_{fc}}{2F}\ln\left(p^*_{H_2}\right) + \frac{RT}{4(1-\alpha)F}\ln\left(\xi_{\text{cat}}\right)$

$+\frac{RT}{4(1-\alpha)F}\ln\left(A_{\text{fc}}\cdot i_0^{\text{ref}}\Big|_{t=0}\right) - \frac{\alpha RT}{4(1-\alpha)F}\ln\left(p_{O_2}^{\text{ref}*}\right)$, is the sum of all the terms that are not affected by the current *I*.

$Z_R$ (around steady state current $I_0$) can now be obtained by differentiating (4.5) with respect to *I*:

$$Z_R = -\frac{dV_{\text{cell}}}{dI}\Big|_{I_o} = R_{ohm} + \frac{RT}{4(1-\alpha)F}\frac{1}{I_0 + I_{leak}} + \frac{RT}{4(1-\alpha)F}\frac{1}{p^{ch}_{O_2}\frac{D_{\text{eff}}RT4FA_{fc}}{\delta_{GDL}} - I_0} \quad (4.6)$$

The three terms at the right hand side of equation (4.6) correspond to Ohmic resistance, Faradic resistance and mass transport resistance, respectively. Define Faradic resistance $R_{f,C} = \frac{RT}{4(1-\alpha)F}\frac{1}{I_0 + I_{leak}}$, and $R_{conc} = \frac{RT}{4(1-\alpha)F}\frac{1}{p^{ch}_{O_2}\frac{D_{\text{eff}}RT4FA_{fc}}{\delta_{GDL}} - I_0}$ as the

mass transport resistance. It can been seen that, when $I_0$ is small, $p_{O_2}^{ch}$ is large (abundant O2 in the channel), and $D_{\text{eff}}$ is high (fast diffusion through GDL), $R_{conc}$ is small compared to the Faradic resistance $R_{f,C}$ and can be neglected. Thus, the distance between the two intercepts in Figure 4-8, i.e., $Z_R - R_{ohm}$, can be characterized mainly by the Faradic resistance $R_{f,C}$.

In this research, EIS is employed to track the equivalent electrical circuit parameters of the fuel cell by fitting the EIS curves using the Randles cell model with a CPE throughout the aging process under the operation conditions (OCs) given in Table 4-2.

Table 4-2 Operating conditions (OCs) under which the EIS curves are recorded

| **Operating Conditions** | **Values or Controlling Manner of OCs** |
|---|---|
| Hydrogen Mass Flow Rate | 1.3 stoichiometry (minimum: 50 sccm) |
| Air Mass Flow Rate | 2.0 stoichiometry (minimum: 50 sccm) |
| Back Pressure | 25 psi (w.r.t 1 atm) |
| FC temperature | 62 ℃ ~ 64 ℃ (variation due to the control an environmental chamber) |
| Humidifier Dew Point Temperature (DPT) | 58 ℃ ~ 59 ℃ (Both sides) |
| Gas Temperature | 60 ℃ (Both sides) |
| Steady State Voltage | 0.85V (constant) |

The OCs under which the EIS test is performed needs to be maintained the same at every interrupted in-situ diagnosis for the results to be comparable.

Constant voltage is chosen over constant current here to include the aging effect of catalyst surface area on the equivalent circuit parameter $R_{f,C}$. As can be seen in the

expression $R_{f,C} = \frac{RT}{4(1-\alpha)F}\frac{1}{I_0 + I_{leak}}$, $R_{f,C}$ is only sensitive to $I_{leak}$ under the same steady state current $I_0$. As $I_{leak}$ is supposed to remain at the same small and negligible level until serious crossover occurred near the end of the fuel cell life, $R_{f,C}$ contains no useful information on the fuel cell aging during the majority of its lifetime. $R_{f,C}$ obtained at a constant voltage, however, is theoretically affected by the aging for that $I_0$ drifts due to the catalyst surface area decrease.

On the other hand, high voltage (0.85V) is chosen to exclude the effect of mass transport loss (corresponding $I_0$ is very small).

### *4.3.2 Cyclic Voltammetry (CV)*

A cyclic voltammetry test is the most effective and direct tool to evaluate the electro-chemical area of the electrodes. The typical process involves potentially charging the cell between two voltage limits cyclically while feeding inertia gas to the working electrode (WE, electrode of interest) and hydrogen to the counter electrode (CE) ([91]). The resulting current, the plot of which called a cyclic voltammogram, is then analyzed for the ECSA calculation.

The relevant reactions taking place at the WE are the hydrogen adsorption / desorption (HAD): $Pt - H_{ads} \xleftrightarrow[reverse]{forward} Pt + H^+ + e^-$. A sample cyclic voltammogram is shown in Figure 4-9, where the *x*-axis represents the potential (V) and the *y*-axis the current (A) with the negative axis being on the top. A positive current in a voltammetry test is defined as cathodic, i.e., when reduction reaction occurs at the WE, or electrons

flows into the WE; and a negative current is defined as anodic, denoting oxidization reaction at the WE.

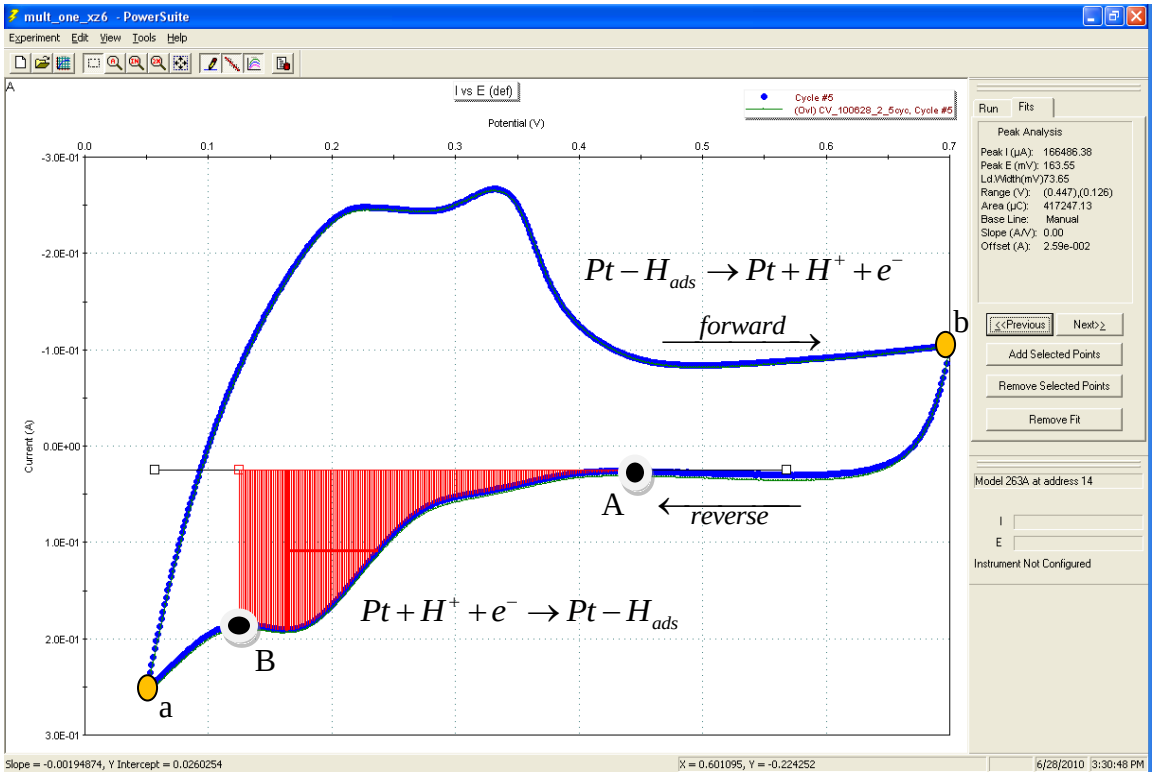


Figure 4-9 Cyclic voltammogram of PEM fuel cell catalyst layer for ECSA analysis taken on two days (snapshot of PowerCV interface). Conditions as in Table 4-3.

A full cycle of the cyclic voltammogram is composed of two segments of curves. The upper part of the voltammogram (segment a→b) is generated when the potential is scanned forward from 50mV to 700mV, during which the hydrogen adsorbed on the WE (crossed over through membrane from CE) is oxidized with the increasing potential (strictly after potential exceeds 100mV, which is the cell's OCV under the CV test conditions), resulting in an anodic current. The lower part of the voltammogram (segment b→a) is obtained when the voltage sweeps back from 700mV to 50mV. Starting from some point (typically around 400mV), the protons and electrons combine to form

hydrogen molecules which then adsorb to the catalyst sites. In both forward and reverse scans, the baseline current at potentials between 0.4 and 0.6 V is the sum of the non-faradic capacitive current due to charging/discharging of the electrical double layer (positive on the forward scan and negative on the reverse scan) and the transport limited H2 crossover current ([92]).

The process of interest is the electro-reduction of protons and adsorption of hydrogen onto the catalyst surface, that is, HAD reaction in the reverse direction. The hydrogen adsorption charge density $q$Pt (Coulombs/cm$^2$) due to this reaction determined from the CV experiment is used to calculate the ECSA of the fuel cell electrode. According to this principle, it is then critical to determine the timing of two events, namely, 1) The time when $H^+$ and $e^-$ start to combine to form H2; and 2) The time when the catalyst surface is just saturated by adsorbed H2.

The starting point of the $H^+$ reduction is usually taken as point A in Figure 4-9, where the absolute value of the steady reverse capacitance charging current begins to increase. Cooper pointed out in [92] that "The voltammogram exhibits multiple peaks associated with both the oxidation and reduction reactions. Each peak is indicative of the adsorption onto or desorption from a particular crystal index of platinum, e.g., 100 and 110 indices". Therefore, the catalyst sites saturation point is taken as the peak point B in Figure 4-9.

The electro-chemical surface area (ECSA) is determined by first calculating the area under the hydrogen adsorption peaks minus the area under the baseline (background) current, i.e., the red shaded area (V·A) in Figure 4-9, and converting this area using the

scan rate (mV/s) to the total charge that adsorbed on the surface (A s, i.e., Coulombs)., The result is then divided by the coefficient 210 $\mu C/cm^2$ (for a platinum electrode) to obtain the final catalytic surface area in $cm^2$. In Figure 4-9, the hydrogen adsorption charge is calculated to be 0.417 C, which corresponds to an active catalyst area coefficient (ECSA/nominal FC area) of 79.4.

The theory of selecting the saturation point (point B) is supported by the later experiments where different potential scan rates are tried to obtain cyclic voltammograms with different sizes; in these experiments, the hydrogen adsorption charges are the same under all scan rates when the above criteria for selecting point A and B are used.

The CV tests are performed under the testing conditions given in Table 4-3.

Table 4-3 Experimental conditions of CV tests for PEMFC cathode ECSA analysis

| **Testing Conditions** | **Conditions Values** |
|---|---|
| Anode Mass Flow Rate | $H_2$ : 50 sccm |
| Cathode Mass Flow Rate | Ar : 20 sccm ([92]) |
| DPT/GST | 35 ℃ /35 ℃ (Both sides) |
| FCT | 35 ℃ |
| Back Pressure | 0 (w.r.t 1atm) ([92]) |
| Connection to Potentiostat (WE/CE/RE) | Cathode/Anode/Anode |
| Cycled Cell Voltage (unit cell) | 50mV - 700mV ([91]) |
| Scan Rate | 50mV/s |

In Table 4-3, WE/CE/RE stand for Working Electrode / Counter Electrode / Reference Electrode. For CV tests, the working electrode is the electrode of interest; since we are only interested in the cathode ECSA, the WE would always be the cathode

throughout the experiments. The anode of the fuel cell, which approximates a standard hydrogen electrode (SHE), would serve as the RE and as well as CE. To minimize the impact of the diagnostic test on the fuel cell's "normal" aging, an upper limit of the cycled potential of 700mV is chosen, since driving the fuel cell above 0.8V could incur irreversible damage to the fuel cell's electrode.

### *4.3.3 Linear Sweep Voltammetry (LSV)*

A linear sweep voltammetry is used to characterize the reactant crossover through the membrane. The test conditions for fuel cell crossover evaluation are akin to those used for in situ ECSA evaluation by CV presented in the last section.

In an LSV test, the working electrode of the fuel cell is scanned from the open circuit potential (~ 0.1 V) to ~ 0.7 V V.S. CE/RE. As with the CV test, driving the WE to potentials > 1.0 V can lead to irreversible damage of the fuel cell electrode due to carbon corrosion. The scan rate is typically in the range of 1~4 mV/sec, which is much slower than that used in the CV test to minimized the non-faradic capacitive current due to charging/discharging of the electrical double layer.

Figure 4-10 shows a typical linear sweep voltammogram when the WE is scanned from 0.1V to 0.7V. It is seen that the current reached an almost steady state around 0.4V. The small linearly increasing trend with the increasing potential is considered to be caused by an internal electrical shorting of the membrane. The crossover current is chosen as the minimal point in between 0.4 and 0.6 V (red dot in the figure).

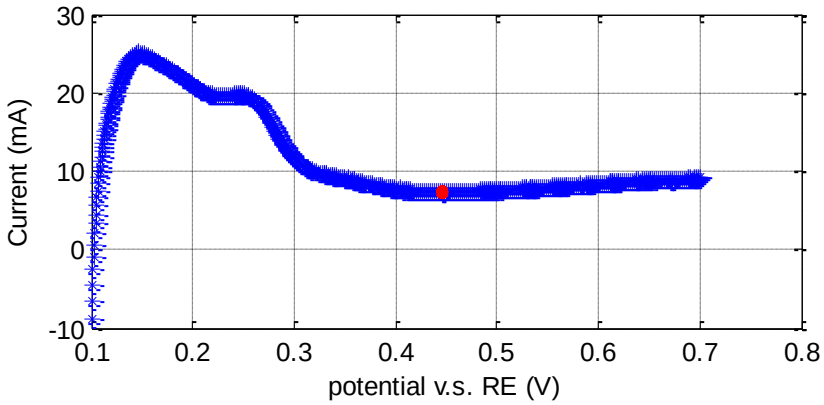


Figure 4-10 Current evolution when the WE potential is swept from 0.1 to 0.7 V

## 4.4 EXPERIMENT RESULTS

### *4.4.1 Voltage and Current Data*

For a fuel cell operated under the cycling voltage durability test conditions as described in section 4.2, its performance can be well characterized by the steady state currents at each voltage level (in our case, 0.6V, 0.7V and 0.5V respectively) and the OCV as well. A typical evolution of these performance indices of a fuel cell with a thin membrane (N212) is shown in Figure 4-11. The performance degradation can be clearly seen as the steady state currents and the OCV gradually decrease with the aging time.

Since the thin membrane is used here, the expected fuel cell life under normal operating conditions is only about 100 hours. The decreasing rate of the various performance indices are seen to accelerate after 70h of aging, supposedly because of the exacerbation of the membrane crossover, which finally led to the failure of the test cell.

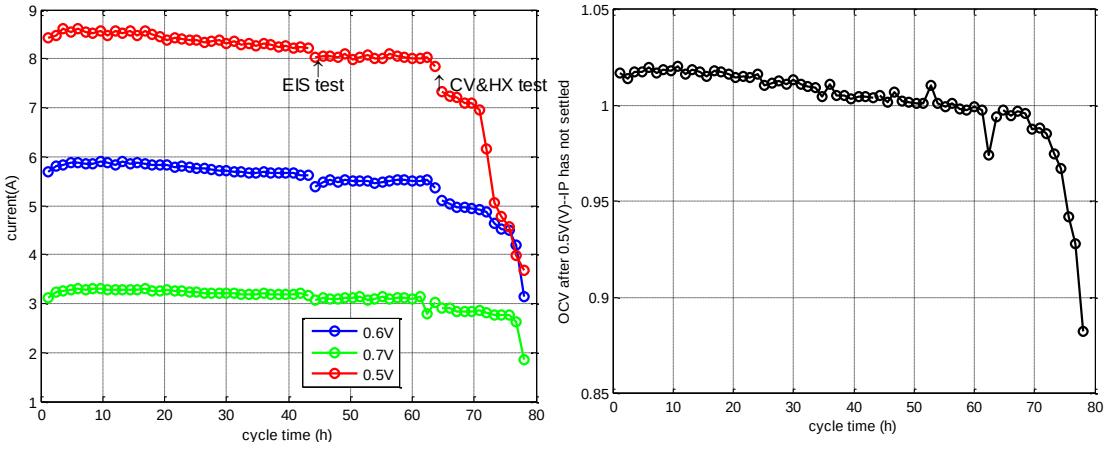


Figure 4-11 Evolution of the steady state currents at different voltage levels and the OCV with aging (Data of a fuel cell with N212 membrane)

### *4.4.2 EIS test*

The EIS curves (around 0.85V) recorded at different phases of the fuel cell life for the fuel cell with graphite plates and N117 membrane are plotted in Figure 4-12. The most remarkable trend seen in this plot is the EIS curve's overall shift towards right during the aging process, indicating the increase of the fuel cell's Ohmic resistance with the aging. The evolution of the fitted parameters of the fuel cell equivalent electrical circuit is depicted in Figure 4-13.

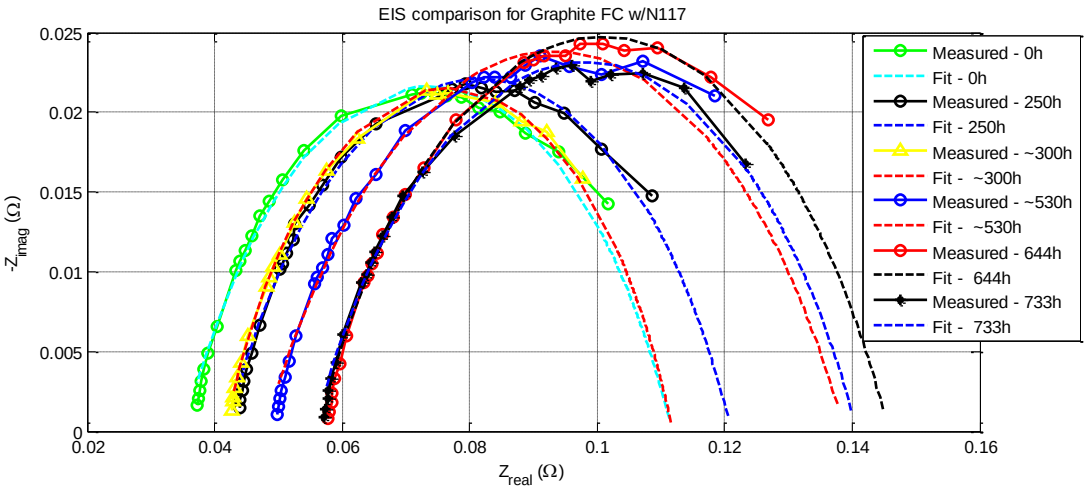

Figure 4-12 EIS curves recorded at different phases of the fuel cell (Graphite FC w/ N117 membrane) life

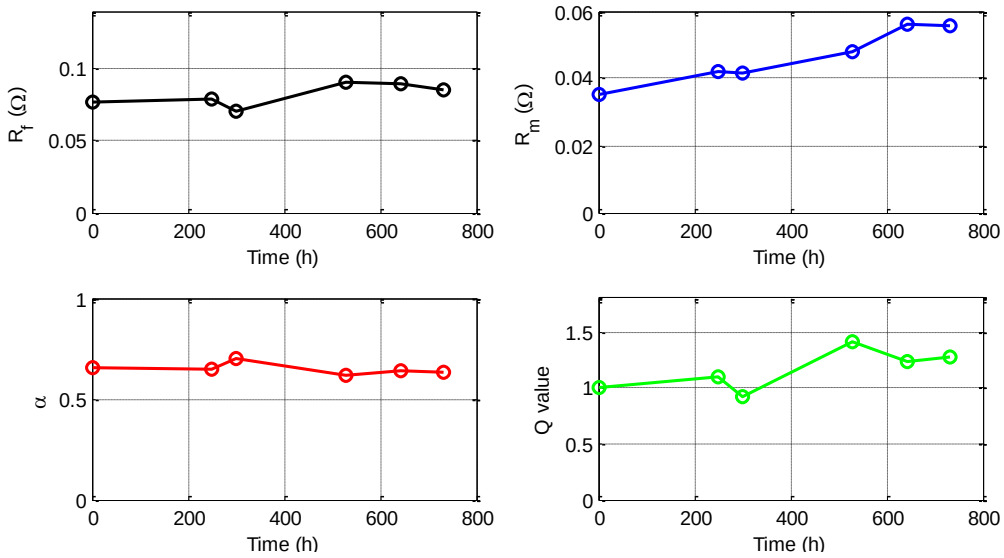


Figure 4-13 Evolution of the fitted parameters of the fuel cell equivalent circuit

In the above figure, the high frequency resistance $R_m$ exhibits the most noticeable growth among the four tracked fitted parameters during aging, with an increase of about 50% at the last test recording compared to its original value. This is also consistent with the observation from the EIS curves in Figure 4-12. The seemingly linear trend shown in this subplot, however, is not repeatedly seen in other experiment results. In fact, due to its various components(2.50), each of which governed by a different aging law, it is difficult to find one aging model to characterize the evolution of $R_m$. The CPE parameter $\alpha$ (refer to (4.3)) appears to be steady during the whole aging process, and can be thought of as a constant that is determined only by the fuel cell type and insensitive to the fuel cell aging. Another CPE parameter $Q$ does exhibit some growing trend with the aging, however, the interpretation of this parameter and its connection with the fuel cell's instantaneous performance are not clear at this point. Finally, the Faradic resistance $R_f$ shows some

slight increase with the aging. However, the magnitude of the increase is much less than expected (at least in this case) and does not qualify $R_f$ as an effective aging parameter. More experiment data are needed to evaluate the connection between the fuel cell aging and the evolution of $R_f$.

### *4.4.3 CV test*

The cyclic voltammograms recorded at different phases of the fuel cell life are plotted in Figure 4-14. Due to possible errors in the experiment procedures, the first three test results are annulled and the data are not included here. The calculated ECSAs with respect to the aging time are also shown, with data fitting using a log function.

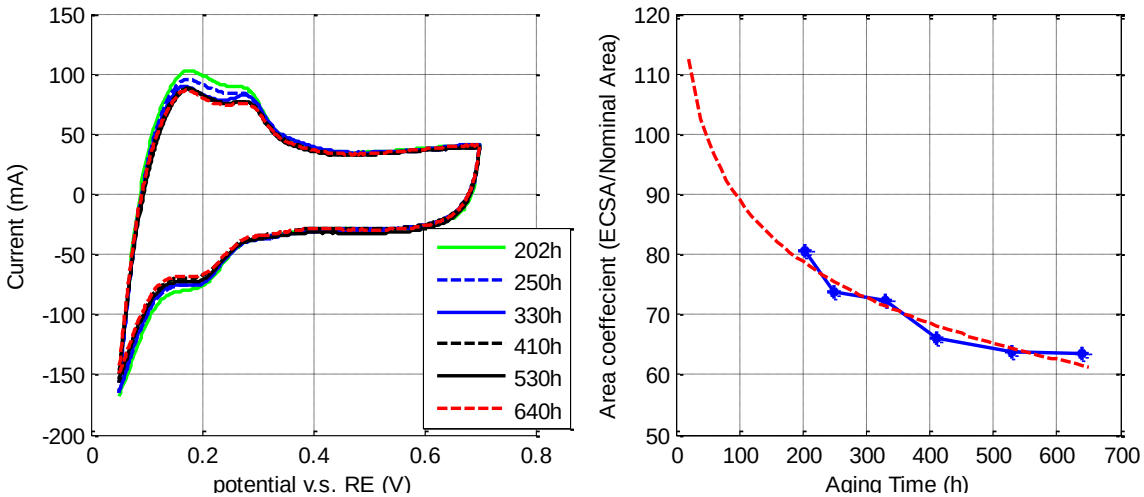


Figure 4-14 Cyclic voltammograms recorded at different phases of the fuel cell life (left) and the evolution of the calculated ECSA with aging (right)

A close-up of the cyclic voltammograms is presented in Figure 4-15. It can be seen that, for all cyclic voltammograms, the process of electro-reduction of protons and adsorption of hydrogen on the catalyst surface ( $Pt + H^+ + e^- \rightarrow Pt - H_{ads}$ ) starts at

around 0.4V, and the catalyst sites saturation occurred at about 0.15V. Since the saturation point exhibit an obvious trend of moving upward and a much larger variation compared to that of the starting point, it is clear that the area under the hydrogen adsorption peaks minus the area under the baseline current is decreasing with the aging time.

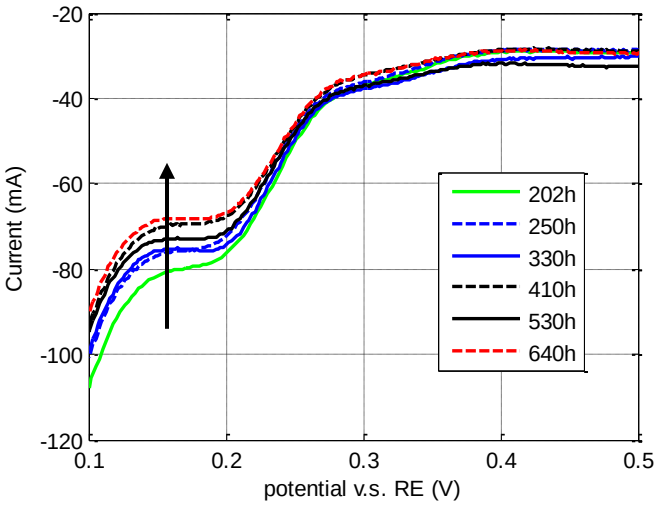


Figure 4-15 Close-up of the cyclic voltammograms in Figure 4-14

### *4.4.4 LSV test*

In Figure 4-16, the voltammograms of the LSV test recorded at different phases of the fuel cell life and the evolution of the measured H2 crossover rate with aging are plotted. It can be seen that the crossover current had only some minor variation below 1 $mA/cm^2$ (note, however, the LSV test was conducted under the temperature 35˚C and the actual crossover current at the durability test conditions is supposed to be higher), which is negligible when the fuel cell is operated under normal operating conditions where the load current is much greater than the leak current. The leak current, or equivalently the

crossover current, is supposed to have increased sharply after 700h and led to the final fail of the fuel cell. Unfortunately, this final fast growth was not captured here due to the abrupt breakdown of the fuel cell before the last LSV test could be arranged.

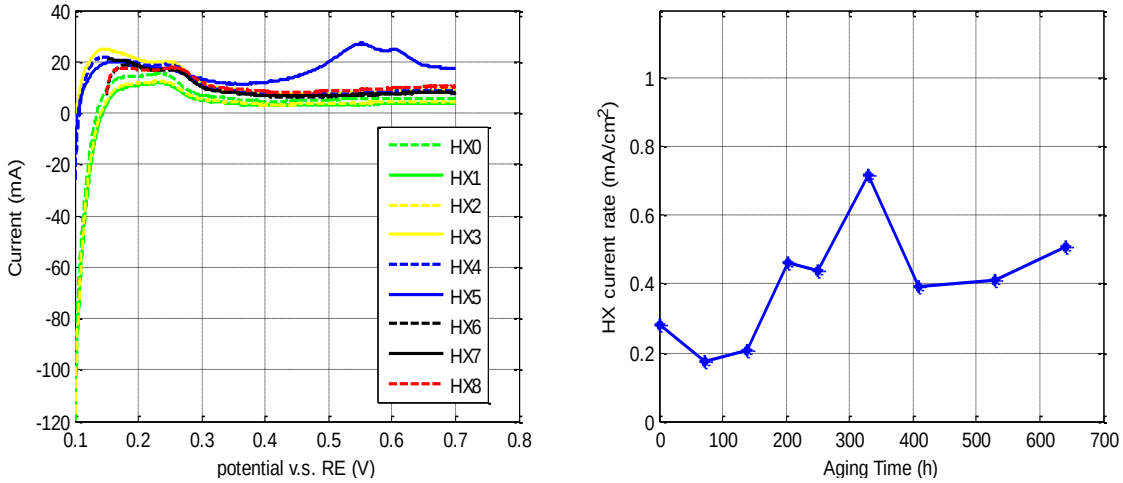


Figure 4-16 Voltammograms of the LSV test recorded at different phases of the fuel cell life (left) and the evolution of the measured $H_2$ crossover rate with aging (right)

## 4.5 CHAPTER SUMMARY

In this chapter, various in-situ diagnostic tools (EIS, CV and HX tests) are explored for PEM fuel cell aging study and to identify the appropriate aging parameters that best characterized the degradation process of the tested fuel cell. Test procedures are designed for the damage tracking of the fuel cell's health state during the durability test utilizing these in-situ diagnostic tools.

The main conclusions that can be drawn from the experiment results are as follows:

i). Damage tracking experiment of fuel cell with membrane N212 suggested that thicker membrane has to be employed for the purpose of accurate tracking of the damage variables;

ii). Remarkable ECSA decreases were observed in all the durability tests with N117 membrane. The ECSA has an exponential type of decay during the aging process;

iii). No remarkable HX rate increase was observed for the fuel cells tested, with different end plates, due to early termination of the durability test before any serious gas crossover occurs;

iv). Remarkable high frequency resistance growth (pure Ohmic resistance) is observed in the graphite fuel cell durability test; while the evolution trends of other fitted parameters in the equivalent electrical circuit are still unclear due to limited experiment data.

From the above conclusions, it is clear that ECSA qualifies as a good indicator for the fuel cell degradation process, while $H_2$ crossover rate does not exhibit distinguishable increase until near the end-of-life of the fuel cell. On the other hand, although phenomenal growth has been observed for the Ohmic resistance, it is difficult to attribute this damage variable to a single fuel cell component since the resistance growth can result from multiple factors such as membrane degradation and carbon corrosion. For health monitoring and prognostic problems, the high frequency resistance needs to be measured or estimated to eliminate its effect on the system's output feature, i.e., cell voltage.

# CHAPTER FIVE

# PROGNOSTIC-ORIENTED FUEL CELL AGING MODELING

From last chapter, we see that the fuel cell durability test is extremely time consuming. The data-driven modeling approach based on the analysis of a large amount of data is thus considered impractical for building the fuel cell aging model; instead, underlying physics principles of its degradation processes have to be explored for that purpose.

In this chapter, physics-based, prognostic-oriented fuel cell degradation models are developed to characterize the damage variables selected in Chapter 4, with the focus on the catalyst degradation model, which establishes the relationship between the operating conditions and the degradation rate of the ECSA. The model complexity is kept minimal for on-line prognostic purpose. A simple degradation model to describe the membrane micro-crack propagation is also briefly discussed.

## 5.1 AGING MODELING FOR CATALYST DEGRADATION CHARACTERIZATION

### *5.1.1 Catalyst Degradation Mechanisms*

The degradation mechanisms for the catalyst have been introduced in Chapter 1; here we briefly recap those mechanisms by decomposing the degradation process to separate steps with further explanations and corresponding electro-chemical or chemical reactions. For the degradation model developed in this section, we focus on the quasi-Ostwald ripening process, which can be roughly divided to three steps.

The first step of this process is Pt dissolution/oxidation, where Pt atoms are either oxidized to Pt ions and dissolve into the ionomer phase in the catalyst layer, or form an

oxide film on the surface of the Pt particles. Platinum dissolution is described by reaction (5.1) in the forward direction.

$$Pt \rightleftharpoons Pt^{2+} + 2e^{-} \tag{5.1}$$

$Pt^{2+}$ is assumed to be the only ionic platinum species present in significant amounts, while other ionic species with higher oxidation states are not expected to be important in the region of interest [32].

Platinum oxide film formation and the subsequent dissolution of this film are described by (5.2) and (5.3) respectively.

$$Pt + 2H_2O \rightleftharpoons PtO + 2H^{+} + 2e^{-} \tag{5.2}$$

$$PtO + 2H^{+} \rightleftharpoons Pt^{2+} + H_2O \tag{5.3}$$

When exposed to high voltage, the formation of the oxide layer actually serves to protect the Pt particles from accelerated dissolution through (5.1) due to elevated potential across the interface of the electrolyte and the cathode. Although it is thermodynamically possible for the PtO to be further chemically dissolved through reaction (5.3), the kinetic rate of this reaction is considered to be extremely slow. Therefore, (5.3) is neglected in our degradation model.

The second step of the quasi-Ostwald process is the migration of Pt ions, where the dissolved Pt ions ($Pt^{2+}$) migrate to nearby Pt particles, with a distance of a few nanometers [7]. The ions can also migrate into the PEM and precipitate there by reduction of $Pt^{2+}$ by crossover $H_2$ from anode, as described by (5.4).

$$Pt^{2+} + H_2 \rightleftharpoons Pt + 2H^{+} \tag{5.4}$$

This reaction results in the absolute mass loss of the effective catalyst and the forming of a Pt "band" in the membrane [14]. The Pt band is actually observed by electron probe microanalysis (EPMA) inside the electrolyte membrane of the used MEA at a location near the cathode catalyst layer [15]. However, the authors in [15] also reported that the amount of Pt inside the electrolyte membrane was markedly smaller than the Pt loading of the cathode catalyst layer. Another evidence of the negligibility of the Pt precipitation in the membrane can be found in[35], where the surface area loss in both catalyst types appears to be primarily by agglomeration. Based on these results, reaction (5.4) is not considered in here.

The third step of the process is the Pt ions reduction and redeposition on the Pt particle surface, which is described by reaction (5.1) in the reverse direction. $Pt^{2+}$ ions tend to redeposit on larger Pt particles that have lower surface energy. This can be seen in the kinetic rate equation for the Pt dissolution/deposition to be presented later.

Since the key kinetic reactions involved in this process, i.e., (5.1) and (5.2), are both electro-chemical reactions, it becomes obvious that potential load is the main driving force for the quasi-Ostwald ripening. In fact, during the potential rise, Pt dissolution, along with the Pt oxidation, is facilitated due to favored electro-chemical environment, with the smaller Pt particle dissolving in a faster rate; while when potential drops, Pt ion reduction is facilitated and tends to redeposit on larger Pt particle due to its lower surface energy. Repeated cycling of the potential therefore results in larger catalyst particles getting larger while smaller catalyst particles getting even smaller. The consequence is then Pt agglomeration, which in turn causes decreased ECSA.

The quasi-Ostwald ripening mechanism explains why the high potential and the load cycling are the main aging factors for catalyst degradation. There is, however, another mechanism for catalyst degradation – particle migration and coalescence – that is not driven by the potential. But due to the fact that the role of this mechanism in the Pt surface area loss at low-temperature fuel cells is still uncertain, and there still lacks unique experiment evidence in support of crystal migration and coalescence [13], it is not considered in the catalyst degradation modeling here.

### *5.1.2 N-Group Catalyst Degradation Model*

In this subsection, we establish a detailed catalyst degradation model based on the platinum dissolution kinetic model proposed by Darling and Meyers in [32], [33]. The main assumptions for this model are as follows:

1) The model is spatially lumped that treats a single, porous platinum electrode and the ionomeric solution that fills the pores of the electrode [32], concentration gradient of the Pt ion across the catalyst layer is neglected;
2) Pt precipitation in the membrane is neglected;
3) The cathode includes Pt/C solid phase uniformly mixed with Nafion electrolyte and gas pore phase. The polymer (and/or ionomer) volume fractions were assumed to be 30% in the cathode and 100% in Nafion membrane. [14]

4) There are $N$ groups of Pt particles. All particles in each group have a unique and identical initial radius at the fresh state of the MEA, and they are uniformly distributed across the cathode;
5) The particle can grow and shrink during the aging process, but the particle number in each group remains the same; also, the sizes of all the particles in one group are equal all the time;
6) When the radius of one group of Pt particles reached the Pt atom radius, that group of Pt particles is considered to be dissolved completely into the inomer phase.
7) PtO grows as a film of uniform thickness, on the surface of the platinum crystallites.

Now, for particles in group $i$, we can obtain the dynamics of the characteristic variable, i.e., the radius $r_i$ and the PtO coverage $\theta_{\mathrm{PtO}}^{(i)}$, by material balance, which are given in (5.5) ([32])

$$\begin{cases} \dfrac{dr_i}{dt} = -\dfrac{M_{\mathrm{Pt}}}{\rho_{\mathrm{Pt}}} v_1^{(i)} \\ \dfrac{d\theta_{\mathrm{PtO}}^{(i)}}{dt} = \dfrac{v_2^{(i)}}{\Gamma_{\max}} - \dfrac{2\theta_{\mathrm{PtO}}^{(i)}}{r_i}\dfrac{dr_i}{dt} \end{cases} \tag{5.5}$$

where $M_{\mathrm{Pt}}$ and $\rho_{\mathrm{Pt}}$ are the molecular weight and density of platinum, respectively. $v_1$ and $v_2$ refer to the reaction rates of (5.1) and (5.2), in moles per second per square centimeter of Pt surface area. $\Gamma_{\max}$ is the number of moles of active sites per unit of platinum area. This number is taken to be constant[32] and is calculated assuming a

specific charge of 220 μC/cm$^2$ in the hydrogen adsorption region. This equation indicates that PtO grows as a film of uniform thickness, on the surface of the platinum crystallites.

The reaction rate $v_1$, the Pt dissolution rate ( $\mathrm{Pt} \rightleftharpoons \mathrm{Pt}^{2+} + 2\mathrm{e}^-$ ) is expressed in (5.6)

$$v_1^{(i)} = k_1 \theta_{\mathrm{vac}}^{(i)} \left\{ \begin{array}{l} \exp\left[ \dfrac{F}{RT} \left( \Delta\phi_c - U_1^{\theta} + \dfrac{\alpha_1}{r_i} \right) \right] \\ -\left( C_{\mathrm{Pt}^{2+}} \Big/ C_{\mathrm{Pt}^{2+}}^{\mathrm{ref}} \right) \cdot \exp\left[ -\dfrac{F}{RT} \left( \Delta\phi_c - U_1^{\theta} + \dfrac{\alpha_1}{r_i} \right) \right] \end{array} \right\} \tag{5.6}$$

where $\Delta\phi_c$ is the phase potential difference between the electrolyte phase and the cathode phase; $U_1^{\theta}$ is the standard equilibrium potential of Reaction (5.1) for bulk platinum; $\alpha_1 = 1.14 \times 10^{-10}$; $\theta_{\mathrm{vac}}^{(i)}$ is the fraction of the platinum surface that is not covered by oxides, and $\theta_{\mathrm{vac}}^{(i)} = \max\left(0, 1 - \theta_{\mathrm{PtO}}^{(i)}\right)$, due to the fact that the PtO film can grow beyond one layer. $C_{\mathrm{Pt}^{2+}}$ and $C_{\mathrm{Pt}^{2+}}^{\mathrm{ref}}$ are the actual and reference concentration for $\mathrm{Pt}^{2+}$, $C_{\mathrm{Pt}^{2+}}^{\mathrm{ref}}$ is chosen to be 1mol/L in this work, while $C_{\mathrm{Pt}^{2+}}$ can be written as (5.7) using mass balance.

$$\frac{dC_{\mathrm{Pt}^{2+}}}{dt} = \frac{\sum_i 4\pi r_i^2 N_i v_1^{(i)}}{A_{\mathrm{fc}} \cdot \delta_{\mathrm{CL}}} \tag{5.7}$$

where $N_i$ is the particle number in the *i*-th group. $A_{\mathrm{fc}}$ and $\delta_{\mathrm{CL}}$ are the nominal fuel cell area and catalyst layer.

The reaction rate $v_2$, the Pt oxidization rate ( $\mathrm{Pt} + 2\mathrm{H_2O} \rightleftharpoons \mathrm{PtO} + 2\mathrm{H}^+ + 2\mathrm{e}^-$ )is expressed in (5.8)

$$v_2^{(i)} = k_2 \left\{ \begin{array}{l} \exp\left( -\dfrac{\omega\theta_{\mathrm{PtO}}}{RT} \right) \exp\left[ \dfrac{0.7F}{RT} \left( \Delta\phi_c - \tilde{U}_2^{\theta} + \dfrac{\alpha_2}{r_i} \right) \right] \\ -\theta_{\mathrm{PtO}} \left( C_{\mathrm{H^+}} \Big/ C_{\mathrm{H^+}}^{\mathrm{ref}} \right)^2 \cdot \exp\left[ -\dfrac{0.3F}{RT} \left( \Delta\phi_c - \tilde{U}_2^{\theta} + \dfrac{\alpha_2}{r_i} \right) \right] \end{array} \right\} \tag{5.8}$$

From the kinetic rate equations presented above, it now becomes clear that particles with smaller radius $r_i$ tend to have higher dissolution rate $v_1$ and oxidation rate $v_2$ under the same potential load.

It should be noted that, instead of the cell voltage measured across the fuel cell terminals, the aging process is actually driven by the phase potential difference between the electrolyte phase and the electrode phase, i.e., $\Delta\phi_{\mathrm{c}} = \phi_{\mathrm{c}} - \phi_{\mathrm{e}}$ in the case of cathode, where $\phi_{\mathrm{e}}$ is the electrical potential of the electrolyte, and $\phi_{\mathrm{c}}$ is the electrical potential at the cathode. As the cell voltage can be expressed as $V_{\mathrm{cell}} = \Delta\phi_{\mathrm{c}} + \Delta\phi_{\mathrm{a}} - i \cdot A_{fc} \cdot R_{ohm}$, and the anode phase potential difference $\Delta\phi_{\mathrm{a}} = \phi_{\mathrm{e}} - \phi_{\mathrm{a}}$ can be neglected, the potential load can be obtained as $\Delta\phi_{\mathrm{c}} = V_{\mathrm{cell}} + i \cdot A_{fc} \cdot R_{ohm}$, i.e., the so called "iR free voltage", and is available from our dynamic model developed in Chapter 2.

For the simplicity of notation, we define $\exp\left( \dfrac{F}{RT} \Delta\phi_c \right) = u_c$, $\exp\left( \dfrac{F}{RT} U_1^{\theta} \right) = u^{\theta}$, and $\exp\left( \dfrac{F}{RT} \dfrac{\alpha_1}{r_i} \right) = f_1(r_i)$. It then follows that:

$$v_1^{(i)} = k_1 \theta_{\mathrm{vac}}^{(i)} \left\{ \frac{u_c}{u^{\theta}} \cdot f_1(r_i) - \left( C_{\mathrm{Pt^{2+}}} \Big/ C_{\mathrm{Pt^{2+}}}^{\mathrm{ref}} \right) \cdot \frac{u^{\theta}}{u_c f_1(r_i)} \right\} \tag{5.9}$$

Also, we define $A_{\text{geo}} = \sum_i 4\pi r_i^2 N_i$ to be the geometric surface area of the catalyst, which is calculated by totalizing the surface area of all particle groups. Note that $A_{\text{geo}}$ does not equal to the ECSA, the two area values can be thought to be proportional to each other, with ECSA/ $A_{\text{geo}}$ =0.63 ([34]).

To study the model behavior, we now implement the degradation model in the Simulink. As a first step, we assume that only 2 particle groups are present in the cathode. The concept of the bimodal particle size distribution is also proposed in [33].

For reaction rate coefficient, we choose $k_1$ = $10^{-10}$ mol/cm$^2$/s, $k_2$ = $3\times10^{-10}$ mol/cm$^2$/s, these rate parameters will be used throughout this section unless otherwise specified. Simulation result for the 2-group case with a constant potential load $\Delta\phi_c = 0.97\text{V}$ is shown in Figure 5-1. The ratio of ECA over nominal fuel cell area ECSA/ $A_{fc}$ is termed as catalyst magnifying coefficient here.

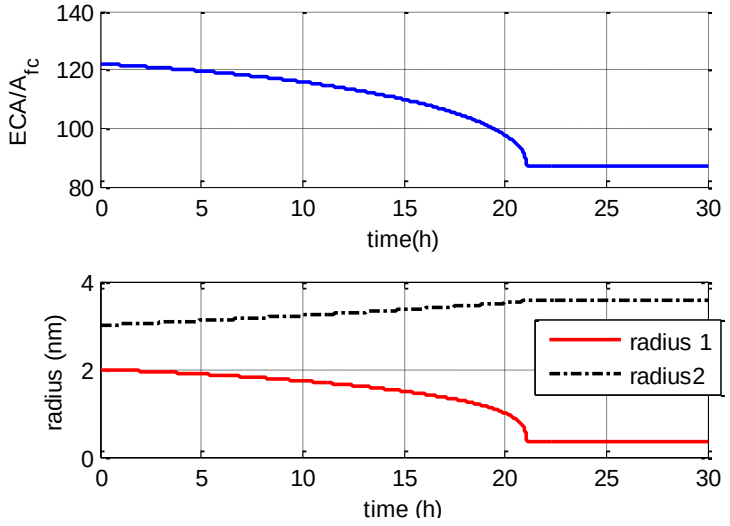


Figure 5-1. Evolution of the catalyst magnifying coefficient and the two radius with time (constant 0.97V)

As seen from the figure above, with the 2-particle group model, the catalyst magnifying coefficient (or equivalently the ECSA) decreases, due to the underlying ripening/agglomeration mechanism. But unfortunately, the model fails to capture the exponential-like shape of the ECSA decay. In fact, instead of having a degradation rate that gradually slows down, the modeled degradation rate in Figure 5-1 is accelerating throughout the decay process, and after about 21h, the ECSA reached a stagnant state.

Next, we assume that there are 64 particle groups in the cathode. Generally speaking, more particle groups would result in better model accuracy, but bigger computational burden at the same time. The number of 64 is chosen here to balance both the accuracy and the computational cost.

A normal distribution for the particle size is assumed in the initial state, the bell shaped distribution plot is shown in the following. The simulation is carried out with the same constant potential load $\Delta\phi_c = 0.97\text{V}$. Simulation results are presented in Figure 5-3 ~ Figure 5-5.

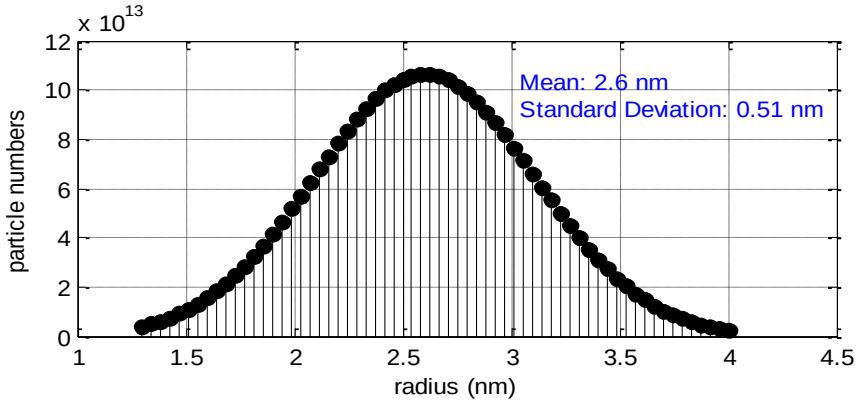


Figure 5-2. Particle size distribution in the initial state

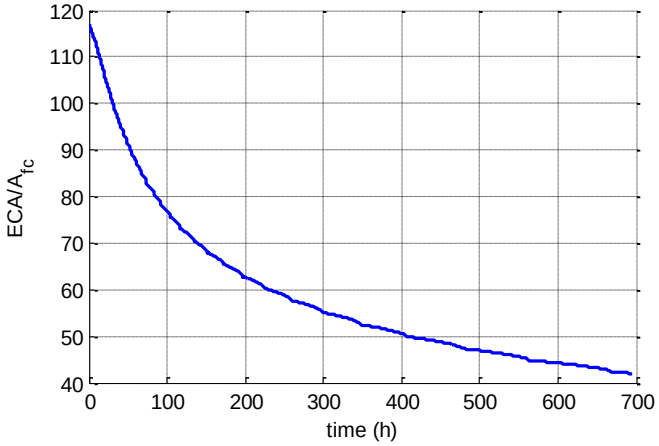


Figure 5-3. The evolution of the catalyst magnifying coefficient for 64-particle model (constant 0.97V)

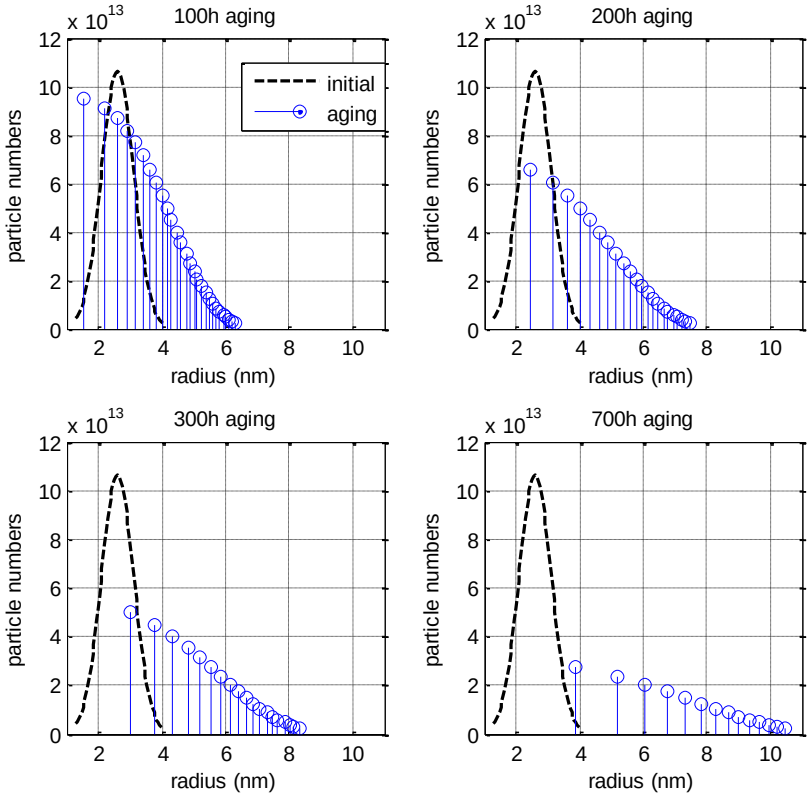


Figure 5-4. Evolution of the particles size distribution during aging (constant 0.97V)

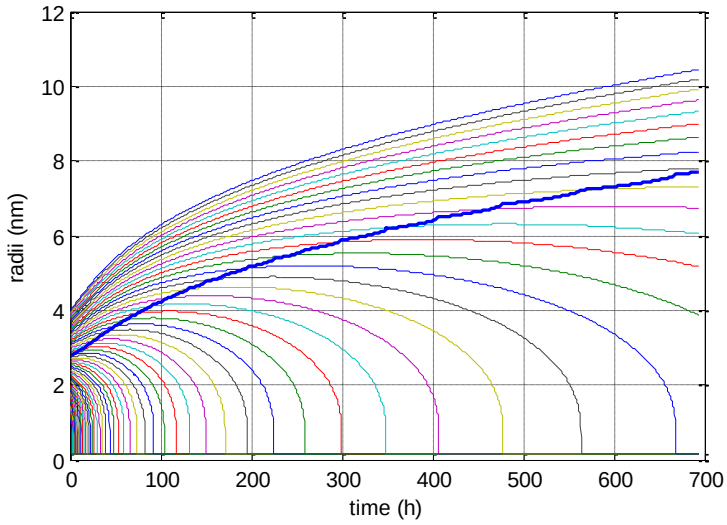


Figure 5-5. Radius evolution of all particle groups with time (constant 0.97V)

In Figure 5-3, it can be seen that the 64-particle-size model has now successfully captured the exponential trend of the ECSA decay that is observed in the PEM fuel cell aging test. Figure 5-4 shows the evolution of the particles size distribution during aging at 100h, 200h, 300h, and 700h respectively. The plots qualitatively reflect the trend of the particle size distribution to spread more widely and shift to larger particle size region. Figure 5-5 depicts the radius evolution of all particle groups with aging, with the mean radius plotted in bold blue line. It can be seen that the smaller groups dissolve and disappear one by one (indicated by crossing the green horizontal line that represents the Pt atom radius), while the larger particles grow at the cost of these small particle size groups.

### *5.1.3 Model Simplification for Prognostic Purpose*

Before deriving the simplified degradation model, we analyze 2-particle-size model in more details. Simulation is carried out using a cycling potential load with 0.8V-

1V square profile, as shown in the Figure 5-6. Simulation results are presented in Figure 5-7~Figure 5-9.

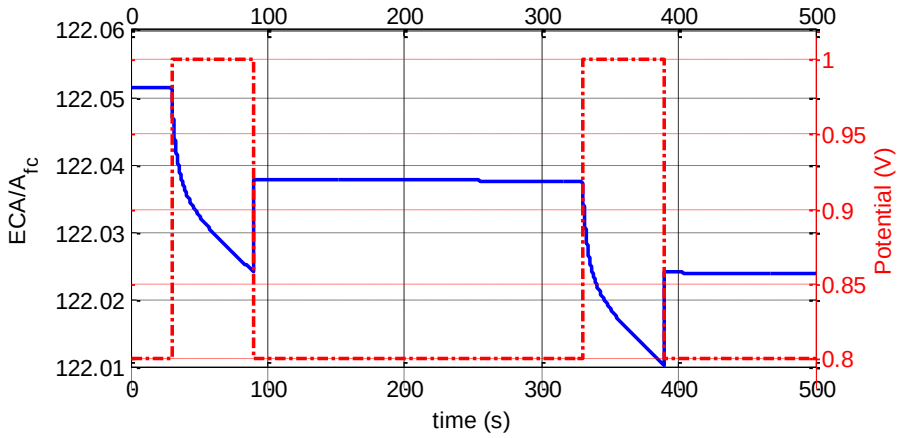


Figure 5-6. The evolution of the catalyst magnifying coefficient for 2-particle-size model (cycling potential with square profile, 0.8V-1V)

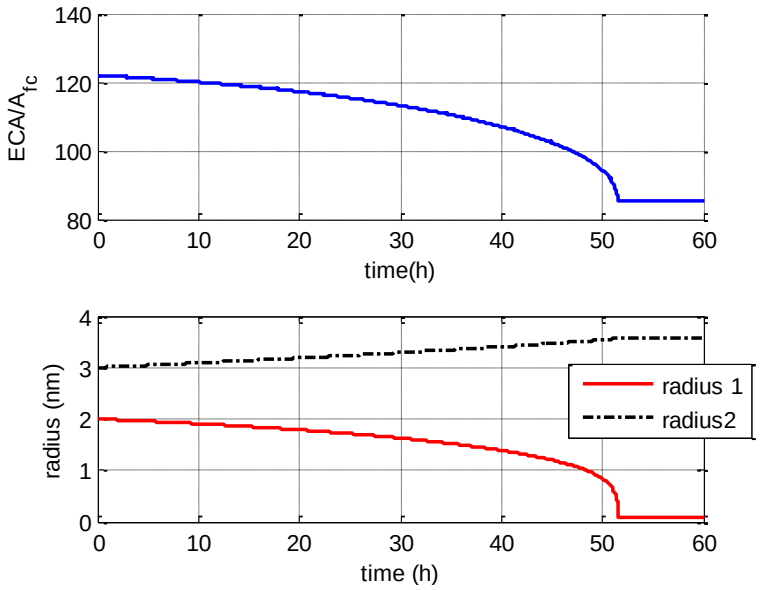


Figure 5-7. Evolution of the catalyst magnifying coefficient and the two radius with time (cycling potential with square profile, 0.8V-1V)

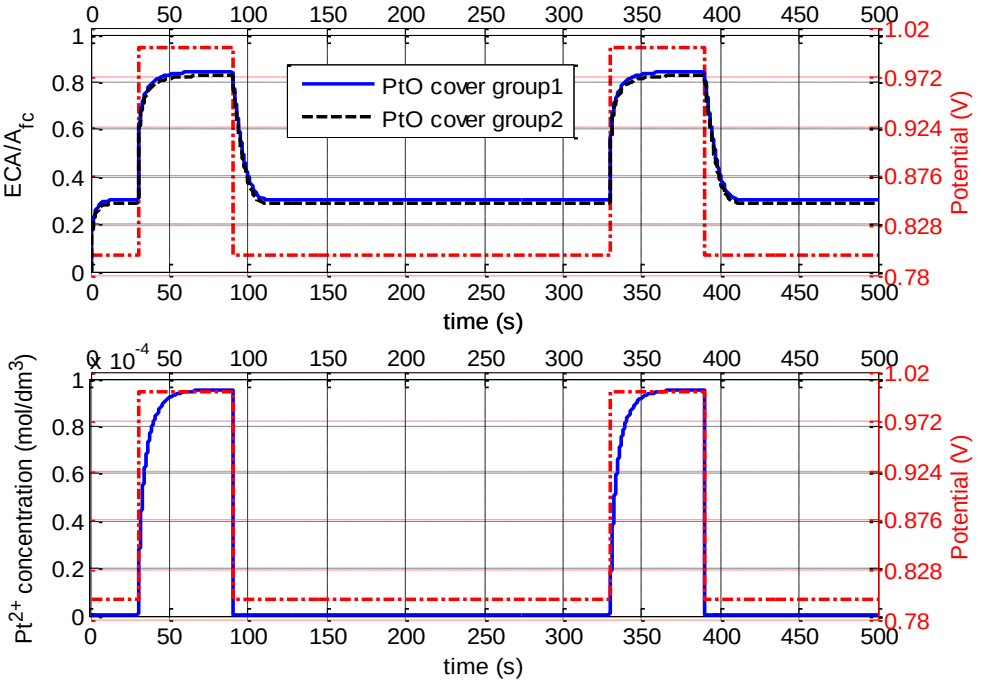


Figure 5-8. PtO coverage of the two groups and the Pt ion concentration with time (cycling potential with square profile, 0.8V-1V)

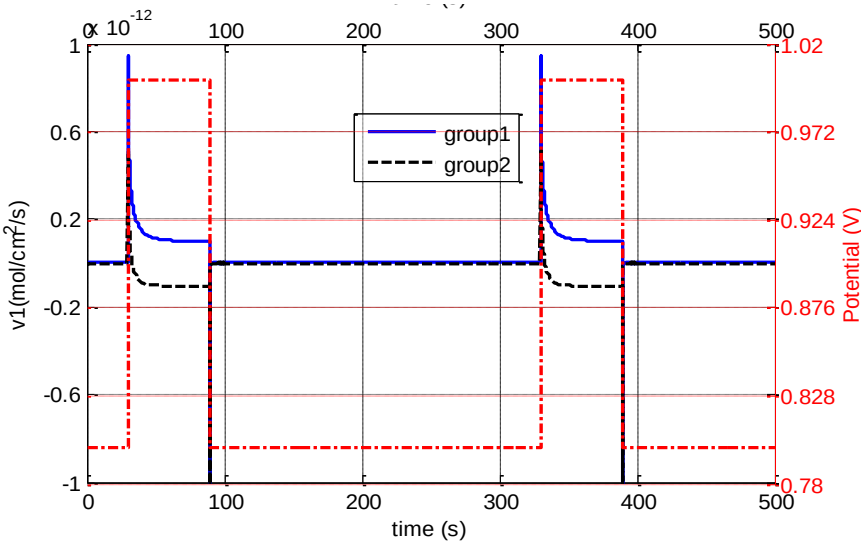


Figure 5-9 Dissolution rate for the two groups with time (cycling potential with square profile, 0.8V-1V)

In Figure 5-7, ECSA (equivalent to the catalyst magnifying coefficient) is seen to have a much greater degradation rate at high potential, i.e., 1V hold, in contrast to the

0.8V hold. This can be better illustrated by Figure 5-9, where it is seen that, during the 1V hold, Pt particles with smaller size (group 1) has a positive dissolution rate while Pt particles with larger size (group 2) has a negative dissolution rate. Meaning the Pt dissolution and Pt ion redeposition are actually occurring at the same time even the potential load is hold constant.

From Figure 5-8, we can see the Pt ion concentration reaches its steady state about 20s after the potential rise. The steady state is possible only when the number of dissolving Pt atom per unit time equals the number of redepositing Pt ion per unit time. By refering to the Pt ion dynamics in (5.7), we have at steady state that:

$$\frac{dC_{\mathrm{Pt}^{2+}}}{dt} = \frac{\sum_i 4\pi r_i^2 N_i v_1^{(i)}}{A_{\mathrm{fc}} \cdot \delta_{\mathrm{CL}}} = 0 \Rightarrow \sum_i r_i^2 N_i v_1^{(i)} = 0$$

$$\Rightarrow \sum_i r_i^2 N_i k_1 \theta_{\mathrm{vac}}^{(i)} \left\{ \frac{u_c}{u^\theta} \cdot f_1(r_i) - \left( C_{\mathrm{Pt}^{2+}} \Big/ C_{\mathrm{Pt}^{2+}}^{\mathrm{ref}} \right) \cdot \frac{u^\theta}{u_c f_1(r_i)} \right\} = 0$$

$$\Rightarrow k_1 \left\{ \frac{u_c}{u^\theta} \sum_i r_i^2 N_i \theta_{\mathrm{vac}}^{(i)} \cdot f_1(r_i) - \left( C_{\mathrm{Pt}^{2+}} \Big/ C_{\mathrm{Pt}^{2+}}^{\mathrm{ref}} \right) \frac{u^\theta}{u_c} \sum_i r_i^2 N_i \theta_{\mathrm{vac}}^{(i)} \cdot \frac{1}{f_1(r_i)} \right\} = 0$$

From the above equation, we then get the steady state of the Pt ion concentration corresponding to the equivalent potential input $u_c$.

$$\left( C_{\mathrm{Pt}^{2+}} \Big/ C_{\mathrm{Pt}^{2+}}^{\mathrm{ref}} \right) = \left( \frac{u_c}{u^\theta} \right)^2 \frac{\sum_i r_i^2 N_i \theta_{\mathrm{vac}}^{(i)} \cdot f_1(r_i)}{\sum_i r_i^2 N_i \theta_{\mathrm{vac}}^{(i)} \cdot \frac{1}{f_1(r_i)}} = \left( \frac{u_c}{u^\theta} \right)^2 \frac{\sum_i r_i^2 N_i \theta_{\mathrm{vac}}^{(i)} \cdot \frac{1}{f_1(r_i)} \cdot \left[ f_1(r_i) \right]^2}{\sum_i r_i^2 N_i \theta_{\mathrm{vac}}^{(i)} \cdot \frac{1}{f_1(r_i)}} \tag{5.10}$$

$$\triangleq \left( \frac{u_c}{u^\theta} \right)^2 \left[ f_1(r_{\mathrm{avg}}) \right]^2$$

where $r_{avg}$ is the equivalent average radius defined by the above equation. Note that the steady state Pt ion concentration is independent with the kinetic reaction rate $k_1$, while a function of the potential load and the average radius of the Pt particles.

Now revisit the dissolution rate $v_1^{(i)} = k_1 \theta_{vac}^{(i)} \left\{ \frac{u_c}{u^\theta} \cdot f_1(r_i) - \left( C_{Pt^{2+}} \Big/ C_{Pt^{2+}}^{ref} \right) \cdot \frac{u^\theta}{u_c f_1(r_i)} \right\}$, and note that $f_1(r_i) = \exp\left( \frac{F}{RT} \frac{\alpha_1}{r_i} \right)$ is a decreasing function. It then becomes obvious that, at a certain level of Pt ion concentration, the smaller particles have higher dissolution rates. In fact, there theoretically exists a radius such that the dissolution rate $v_1$=0, i.e. the particles with this radius would neither dissolve nor be redeposited by the Pt ions. The radius, which is defined by us as balanced radius and denoted as $r_{bal}$, satisfies the following equation:

$$k_1 \theta_{vac}^{(i)} \left\{ \frac{u_c}{u^\theta} \cdot f_1(r_{bal}) - \left( C_{Pt^{2+}} \Big/ C_{Pt^{2+}}^{ref} \right) \cdot \frac{u^\theta}{u_c f_1(r_{bal})} \right\} = 0 \Rightarrow$$

$$\left( C_{Pt^{2+}} \Big/ C_{Pt^{2+}}^{ref} \right) = \left( \frac{u_c}{u^\theta} \right)^2 \left[ f_1(r_{bal}) \right]^2 \tag{5.11}$$

By comparing the above equation to (5.10), it is clear that, $r_{bal}$ and $r_{avg}$ are equivalent with each other in the sense of Pt ion concentration balance. All the particles with smaller radius than the balanced radius have positive dissolution rate and shrink in size, while the other particles larger than the balanced radius have negative dissolution rate (redeposition) and grow.

Now, by taking the derivative of the geometric catalytic surface area $A_{\text{geo}} = \sum_i 4\pi r_i^2 N_i$ with respect to time, we have

$$\begin{aligned}\frac{dA_{\text{geo}}}{dt} &= \sum_i \frac{d}{dt}\left(4\pi r_i^2 N_i\right) = \sum_i 4\pi \cdot 2r_i \cdot \dot{r}_i \cdot N_i = \sum_i 4\pi \cdot 2r_i \cdot \left(-\frac{M_{\text{Pt}}}{\rho_{\text{Pt}}} v_1^{(i)}\right) \cdot N_i \\ &= -8\pi \cdot \frac{M_{\text{Pt}}}{\rho_{\text{Pt}}} \sum_i r_i \cdot v_1^{(i)} \cdot N_i\end{aligned} \tag{5.12}$$

Substituting (5.9) and (5.10) into the above equation, we get

$$\begin{aligned}\frac{dA_{\text{geo}}}{dt} &= -8\pi \cdot \frac{M_{\text{Pt}}}{\rho_{\text{Pt}}} \sum_i r_i \cdot v_1^{(i)} \cdot N_i \\ &= -8\pi \cdot \frac{M_{\text{Pt}}}{\rho_{\text{Pt}}} \sum_i r_i N_i k_1 \theta_{\text{vac}}^{(i)} \left\{ \frac{u_c}{u^\theta} \cdot f_1(r_i) - \left( C_{\text{Pt}^{2+}} \Big/ C_{\text{Pt}^{2+}}^{\text{ref}} \right) \cdot \frac{u^\theta}{u_c f_1(r_i)} \right\} \\ &= -8\pi \cdot \frac{M_{\text{Pt}}}{\rho_{\text{Pt}}} \sum_i r_i N_i k_1 \theta_{\text{vac}}^{(i)} \left\{ \frac{u_c}{u^\theta} \cdot f_1(r_i) - \left( \frac{u_c}{u^\theta} \right)^2 \left[ f_1(r_{\text{avg}}) \right]^2 \cdot \frac{u^\theta}{u_c f_1(r_i)} \right\} \Rightarrow\end{aligned}$$

$$\frac{dA_{\text{geo}}}{dt} = -8\pi \cdot \frac{M_{\text{Pt}}}{\rho_{\text{Pt}}} \cdot k_1 \frac{u_c}{u^\theta} \sum_i r_i N_i \theta_{\text{vac}}^{(i)} \left\{ f_1(r_i) - \frac{\left[ f_1(r_{\text{avg}}) \right]^2}{f_1(r_i)} \right\} \tag{5.13}$$

To establish a connection between the catalytic area $A_{\text{geo}}$ and the average particle radius $r_{\text{avg}}$, the following approximation is made

$$r_{\text{avg}} \approx \bar{r}_{\text{a}} = \frac{3 \cdot V_{\text{Pt}}}{A_{\text{geo}}} \tag{5.14}$$

where $\bar{r}_{\text{a}}$ is the average radius in the sense of particle geometry, and is the mean radius plotted in Figure 5-5.

Now, to further simplify the degradation rate equation as expressed in (5.13), we make the following *Assumptions*:

1) At any time during the aging process, there are two fictitious Pt particle groups with radius $r_1$ and $r_2$ that can represent the averaged effect of the Pt particles with smaller and larger radius than $\bar{r}_a$ , respectively ($r_1 < \bar{r}_a$ and $r_2 > \bar{r}_a$);

2) The sum of the areas of the two fictitious Pt particle groups equals to the total catalytic area, $a_1 + a_2 = A_{geo}$;

3) By defining the difference between the averaged and the fictitious radius as $\Delta r_1 = \bar{r}_a - r_1$, and $\Delta r_2 = r_2 - \bar{r}_a$, we assume that $\frac{\Delta r_1}{\bar{r}_a}$ and $\frac{\Delta r_2}{\bar{r}_a}$ are constant throughout the aging process.

Assumption 3) is made by observation from Figure 5-5 and is consistent with the fact that the particle size distribution is spreading wider during the aging process. By making this assumption the modeling process is greatly simplified, and the simulation results show that it is a valid approximation.

According to Assumption 1) and also note that the values of $\theta_{vac}^{(i)}$ for particle groups with different radii are very close to each other (which can be seen in Figure 5-8) and take $\theta_{vac}^{(i)} = \theta_{vac}$ for $i$=1,2, (5.13) can be written as

$$\frac{dA_{geo}}{dt} = -8\pi \cdot \frac{M_{Pt}}{\rho_{Pt}} \cdot k_1 \frac{u_c}{u^{\theta}} \cdot \theta_{vac} \sum_{i=1,2} r_i N_i \left\{ f_1(r_i) - \frac{\left[ f_1(\bar{r}_a) \right]^2}{f_1(r_i)} \right\} \tag{5.15}$$

From the assumption that $Cpt^{2+}$ is at steady state, we have

$$\frac{dC_{Pt^{2+}}}{dt}=0\Rightarrow\sum_i r_i^2N_i\left\{f_1(r_i)-\frac{\left[f_1(\bar{r}_a)\right]^2}{f_1(r_i)}\right\}=0 \tag{5.16}$$

Substitute the total surface area for the particles in the *i*-th group $a_i=4\pi r_i^2N_i$ (*i* = 1, 2), the above equation becomes

$$\sum_i r_i^2N_i\left\{f_1(r_i)-\frac{\left[f_1(\bar{r}_a)\right]^2}{f_1(r_i)}\right\}=0\Rightarrow\sum_i a_i\left\{f_1(r_i)-\frac{\left[f_1(\bar{r}_a)\right]^2}{f_1(r_i)}\right\}=0$$

$$\Rightarrow\frac{a_1}{a_2}=\frac{\dfrac{\left[f_1(\bar{r}_a)\right]^2}{f_1(r_2)}-f_1(r_2)}{f_1(r_1)-\dfrac{\left[f_1(\bar{r}_a)\right]^2}{f_1(r_1)}}=\frac{\dfrac{f_1(\bar{r}_a)}{f_1(r_2)}-\dfrac{f_1(r_2)}{f_1(\bar{r}_a)}}{\dfrac{f_1(r_1)}{f_1(\bar{r}_a)}-\dfrac{f_1(\bar{r}_a)}{f_1(r_1)}}$$

$$\Rightarrow\frac{a_1}{a_2}=\frac{\exp\left[\dfrac{F\alpha_1}{RT}\left(\dfrac{1}{\bar{r}_a}-\dfrac{1}{r_2}\right)\right]-\exp\left[-\dfrac{F\alpha_1}{RT}\left(\dfrac{1}{\bar{r}_a}-\dfrac{1}{r_2}\right)\right]}{\exp\left[\dfrac{F\alpha_1}{RT}\left(\dfrac{1}{r_1}-\dfrac{1}{\bar{r}_a}\right)\right]-\exp\left[-\dfrac{F\alpha_1}{RT}\left(\dfrac{1}{r_1}-\dfrac{1}{\bar{r}_a}\right)\right]}\Rightarrow$$

$$\frac{a_1}{a_2}=\frac{\exp\left[\dfrac{F\alpha_1}{RT}\left(\dfrac{\Delta r_2}{\bar{r}_a r_2}\right)\right]-\exp\left[-\dfrac{F\alpha_1}{RT}\left(\dfrac{\Delta r_2}{\bar{r}_a r_2}\right)\right]}{\exp\left[\dfrac{F\alpha_1}{RT}\left(\dfrac{\Delta r_1}{\bar{r}_a r_1}\right)\right]-\exp\left[-\dfrac{F\alpha_1}{RT}\left(\dfrac{\Delta r_1}{\bar{r}_a r_1}\right)\right]} \tag{5.17}$$

when $\frac{\Delta r_1}{r_1},\frac{\Delta r_2}{r_2}$ are small, $\frac{F\alpha_1}{RT}\left(\frac{\Delta r_1}{\bar{r}_a r_1}\right),\frac{F\alpha_1}{RT}\left(\frac{\Delta r_2}{\bar{r}_a r_2}\right)$ is also small, we can then make the following approximation by utilizing the Taylor expansion of the exponential function:

$$\exp\left[\frac{F\alpha_1}{RT}\left(\frac{\Delta r_i}{\bar{r}_a r_i}\right)\right]-\exp\left[-\frac{F\alpha_1}{RT}\left(\frac{\Delta r_i}{\bar{r}_a r_i}\right)\right]\approx 2\cdot\frac{F\alpha_1}{RT}\left(\frac{\Delta r_i}{\bar{r}_a r_i}\right) \tag{5.18}$$

Substitute (5.18) into (5.17), we have

$$\frac{a_1}{a_2} \approx \frac{\Delta r_2}{r_2} \Big/ \frac{\Delta r_1}{r_1} \tag{5.19}$$

Note that $a_1 + a_2 = A_{\text{geo}}$, then the total catalyst area in each group can be written as

$$\begin{cases} a_1 \approx A_{\text{geo}} \cdot \dfrac{\Delta r_2}{r_2} \Big/ \left( \dfrac{\Delta r_1}{r_1} + \dfrac{\Delta r_2}{r_2} \right) \\ a_2 \approx A_{\text{geo}} \cdot \dfrac{\Delta r_1}{r_1} \Big/ \left( \dfrac{\Delta r_1}{r_1} + \dfrac{\Delta r_2}{r_2} \right) \end{cases} \tag{5.20}$$

We already have from (5.15)

$$\begin{aligned} \frac{dA_{\text{geo}}}{dt} &= -8\pi \cdot \frac{M_{\text{Pt}}}{\rho_{\text{Pt}}} \cdot k_1 \frac{u_c}{u^\theta} \cdot \theta_{\text{vac}} \sum_{i=1,2} \frac{a_i}{4\pi r_i} f_1(\bar{r}_{\text{a}}) \left\{ \frac{f_1(r_i)}{f_1(\bar{r}_{\text{a}})} - \frac{f_1(\bar{r}_{\text{a}})}{f_1(r_i)} \right\} \\ &= -8\pi \cdot \frac{M_{\text{Pt}}}{\rho_{\text{Pt}}} \cdot k_1 \frac{u_c}{u^\theta} \cdot \theta_{\text{vac}} f_1(\bar{r}_{\text{a}}) \frac{1}{4\pi} \sum_{i=1,2} \frac{a_i}{r_i} \left\{ \frac{f_1(r_i)}{f_1(\bar{r}_{\text{a}})} - \frac{f_1(\bar{r}_{\text{a}})}{f_1(r_i)} \right\} \end{aligned}$$

By substituting (5.20), the following approximation is obtained:

$$\frac{dA_{\text{geo}}}{dt} \approx -8\pi \cdot \frac{M_{\text{Pt}}}{\rho_{\text{Pt}}} \cdot k_1 \frac{u_c}{u^\theta} \cdot \theta_{\text{vac}} f_1\left( \frac{3 \cdot V_{\text{Pt}}}{A_{\text{geo}}} \right) \frac{1}{4\pi} \left\{ \begin{array}{l} \dfrac{a_1}{r_1} \left[ 2 \cdot \dfrac{F\alpha_1}{RT} \left( \dfrac{\Delta r_1}{\bar{r}_{\text{a}} r_1} \right) \right] \\ -\dfrac{a_2}{r_2} \left[ 2 \cdot \dfrac{F\alpha_1}{RT} \left( \dfrac{\Delta r_2}{\bar{r}_{\text{a}} r_2} \right) \right] \end{array} \right\} \Rightarrow$$

$$\frac{dA_{\text{geo}}}{dt} = -4k_1 \cdot \frac{u_c}{u^\theta} \cdot \theta_{\text{vac}} \cdot \frac{M_{\text{Pt}}}{\rho_{\text{Pt}}} \cdot \frac{F\alpha_1}{RT} \cdot f_1\left( \frac{3 \cdot V_{\text{Pt}}}{A_{\text{geo}}} \right) \cdot \frac{A_{\text{geo}}}{3V_{\text{Pt}}} \left\{ \frac{a_1}{r_1} \left( \frac{\Delta r_1}{r_1} \right) - \frac{a_2}{r_2} \left( \frac{\Delta r_2}{r_2} \right) \right\} \tag{5.21}$$

Define $\dfrac{\Delta r_2}{\bar{r}_{\text{a}}} = \beta_r, \Delta r_1 = \alpha_r \Delta r_2$, the simplified aging model can finally be expressed as

$$\begin{cases} \dfrac{dA_{\text{geo}}}{dt} = -4k_1 \cdot \dfrac{u_c}{u^{\theta}} \cdot \theta_{\text{vac}} \cdot \dfrac{M_{\text{Pt}}}{\rho_{\text{Pt}}} \cdot \dfrac{F\alpha_1}{RT} \cdot \exp\left( \dfrac{F\alpha_1}{RT} \dfrac{A_{\text{geo}}}{3V_{\text{Pt}}} \right) \cdot \dfrac{A_{\text{geo}}^3}{9V_{\text{Pt}}^2} \dfrac{\alpha_r \beta_r^2}{\left(1+\beta_r\right)\left(1-\alpha_r\beta_r\right)} \\ \dfrac{d\theta_{\text{PtO}}}{dt} = \dfrac{v_2}{\Gamma_{\max}} - \dfrac{2\theta_{\text{PtO}}}{\bar{r}_{\text{a}}} \dfrac{d\bar{r}_{\text{a}}}{dt} \end{cases} \tag{5.22}$$

where $\theta_{\text{vac}} = \max\left(0, 1-\theta_{\text{PtO}}\right)$. The degradation model is now simplified to a second-order system with the catalyst surface area ($A_{\text{geo}}$) and the PtO coverage as the state variables. Also, in terms of factorability, the expression for degradation rate of $A_{\text{geo}}$ is in good shape since it can be factorized in the form of a product of a function of the current amount of damage $\text{g}_2\left(A_{\text{geo}}\right)$ times a function of the excitation amplitude $\text{g}_1\left(\Delta\phi_c\right)$, as shown in (5.23)

$$\frac{dA_{\text{geo}}}{dt} = \varepsilon\, \text{g}_1\left(\Delta\phi_c\right) \cdot \text{g}_2\left(A_{\text{geo}}\right) \tag{5.23}$$

The advantage of the degradation rate expression meeting condition (5.23) is that the Palmgren-Miner rule can now be tied to the damage accumulation equation. Basically, the Palmgren-Miner rule [93] is about an "additivity" property that implies it is possible to approximate the damage development under variable excitation amplitude by considering steps of constant amplitude and by summing the aging effects. This approach is used, for example, in [20], [94] to track damage evolution in machinery.

Simulations are carried out for the model validation by comparing the simple model output with the detailed one. The results are shown below in Figure 5-10 and Figure 5-11. Respectively, a constant 0.97V and a cycling potential profile from 0.8V ~ 0.97V are used as the input potential loads to emulate the OCV aging condition and a

normal fuel cell operating condition. In both cases, the model parameters are chosen to be $\alpha_r = 1.1$, and $\beta_r = 0.038$. It can be seen that, by tuning the model parameters, high goodness of fit can be achieved. The right plots of the figures show the evolution of the average radius $\bar{r}_a$ and the two fictitious radii $r_1$ and $r_2$

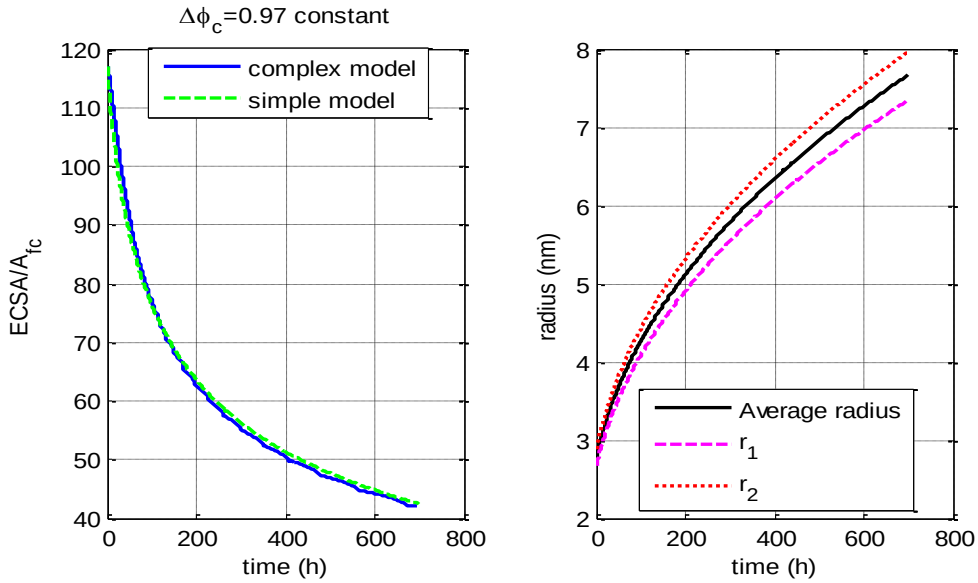


Figure 5-10. Comparison between the catalyst magnifying coefficient evolution for 64-particle model (constant 0.97V)

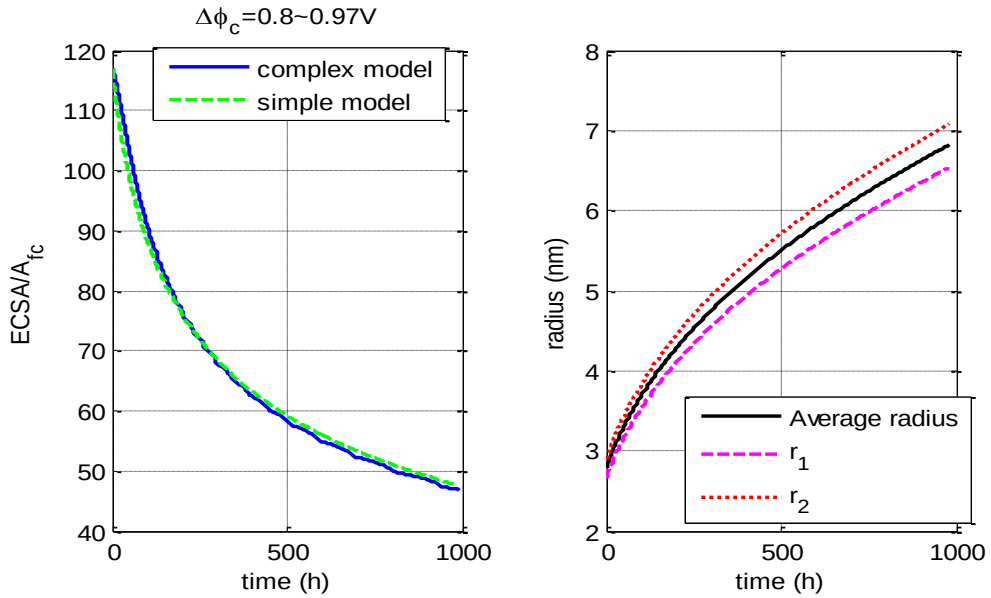


Figure 5-11 Model comparison (cycling potential 0.8V ~ 0.97V)

## 5.2 A SIMPLE AGING MODEL FOR POLYMER MEMBRANE

One important limiting factor to the fuel cell durability is the ability of the membrane to resist the mechanical breach. In contrast to the gradual performance loss brought by the ECSA decrease, the mechanical breach typically lead to a "quick death" of the fuel cell after its formation due to the subsequent massive gas crossover.

As introduced in Chapter 1, the degradation mechanisms for the fuel cell membrane can be roughly categorized as mechanical degradation and chemical degradation. Under the influence of both mechanisms, the physical, chemical, and mechanical properties of the membrane experience gradual degradations throughout the fuel cell lifetime. For example, the chemical decomposition of the membrane directly leads to membrane thinning and loss of proton conductivity (the decomposition of the membrane does not necessarily reduce the mechanical toughness). It also has effect on the mechanical weakening. The strain-to-failure, an indicator of the membrane

mechanical strength, is reduced during the chemical degradation process. On the other hand, mechanical stress that exists in the MEA as a combination of built-in stresses, assembly stresses, and operation stresses [19] can affect the mechanical strength of the membrane in a similar way that fatigue stresses affect the structural components.

While the chemical degradation results in a gradual loss of proton conductivity (growing membrane resistance) that can be observed at the system output, i.e., the voltage or the current, the gradual strength loss of the membrane caused by chemical and mechanical factors during the long term operation is basically "unobservable". In [19], it is reported that "Our evidence has also shown that defects generated and propagated during RH cycling condition do not contribute much to the gas crossover before the occurrence of the final mechanical breach". Similar evidence is also provided in Chapter 4, where experiment results are presented showing an almost constant $H_2$ crossover rate through the membrane in most of the fuel cell lifetime.

In terms of prognostics application, we suggest the membrane aging model focus on modeling of the rapid degradation process after massive gas crossover occurs rather than the preceding slow degradation process for the following reasons: First, the degradation mechanisms for the loss of mechanical strength of the membrane are complicated and coupled with each other, thus very difficult to describe; Second, the gradual loss of mechanical strength does not affect the fuel cell performance, and there is no available system feedback for the measurement correction to the model prediction, which is very important in the prognostics; and third, although the gradual mechanical

strength finally lead to the massive gas crossover, the initiation of the mechanical breach is rather stochastic and hard to capture in a model.

Once the mechanical breach forms in the membrane due to the accumulated defects and massive gas crossover initiates, the degradation process is analogous to the crack propagation process, i.e., the fatigue process in the structural materials under cyclic stresses. In this chapter, we present a simple membrane degradation model that depicts the micro-crack propagation in the membrane based on the semi-empirical fatigue crack propagation model used widely in structural components.

Newman presented a deterministic model of fatigue crack growth in [95] based on the principle of short crack growth. This model represents the mean value of the fatigue crack growth process down to micro-cracks of the order of material defect size and has the following form:

$$\begin{aligned} \frac{d\mu_c}{dt} &= C\left(\Delta K_{\text{eff}}\right)^m \\ \Delta K_{\text{eff}} &= \left(S_{\max} - S_0\right)\sqrt{\pi\mu_c}F \end{aligned} \tag{5.24}$$

where $\mu_c(t) = E\left[c(\omega,t)\big|_{c(\omega,t_0)=\mu_{c0}}\right]$ is the expected value of the time-dependent crack length process $c(\omega,t)$ conditioned on the initial crack length $c(\omega,t_0)$; a sample of the stressed component is indicated by $\omega$; the time $t$ is expressed in units of number of cycles and $t_0$ is the initial time; $\Delta K_{\text{eff}}$ is the effective stress intensity factor range; $C$ and $m$ are the material-dependent constant. $S_{\max}$ is the maximum applied remote stress; $S_0$ is the crack opening stress; and $F$ is correction factor for geometrical configuration.

By making analogy to the process of crack growth/propagation and considering the stochastic in the form of additive noise, the following aging model to characterize the increase of the leak current density is proposed.

$$\frac{di_{\text{leak}}^{\text{ref}}}{dt} = C\left[\Delta K_{\text{stress}} + \omega_{\text{mem1}}(t)\right]^{m_1}\left(i_{\text{leak}}^{\text{ref}}\right)^{m_2} + \omega_{\text{mem2}}(t) \tag{5.25}$$

where $C$ and $m_i$ are the material-dependent constant; $\omega_{\text{mem}i}(t)$ is the process noise, which can be considered Gaussian; $\Delta K_{\text{stress}}$ is the effective stress intensity factor range, and is a function of the membrane water content fluctuation and temperature variation. It has been observed that larger dimensional change accelerates the microcrack fracture[11]. For example, the density of the microcracks in Nafion at the 80-120% RH cycling conditions was higher than that at the 30-80% RH cycling conditions because the changes in water content in the Nafion membrane under 80-120% RH cycling are much greater than those under 30-80% RH cycling conditions. Here, we assume that the $\Delta K_{\text{stress}}$ can be expressed in the following factorable form as the product of the water content and temperature variation range:

$$\Delta K_{\text{stress}} = \Delta\lambda_m \cdot \Delta T_{\text{fc}} \tag{5.26}$$

where $\lambda_m$ is the membrane water constant, and $\Delta T_{\text{fc}}$ is the fuel cell temperature.

Simulated model outputs with different model parameters are presented in Figure 5-12 for comparison. The exponential growing trend exhibited by this model is consistent with the experimental results that can be found in the literature.

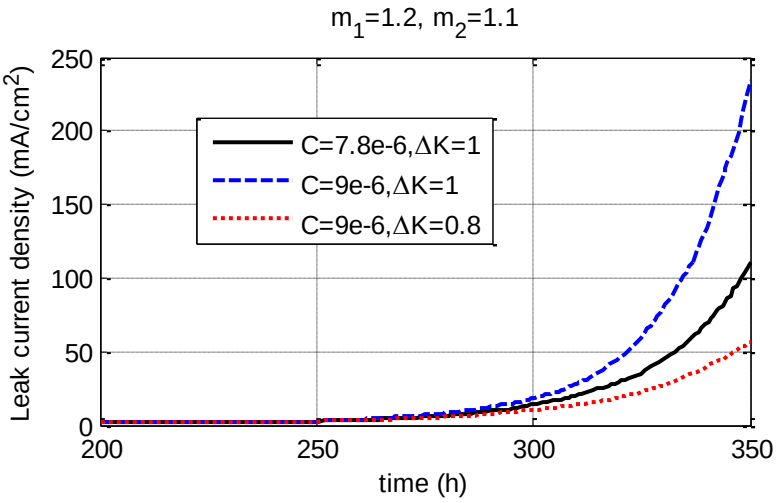


Figure 5-12 Simulation for the membrane degradation model with different parameters

The above model (5.25) is a semi-empirical model that only provides a hypothetic model structure. Model validation and parameters identification for this model require a large amount of ex-situ experimental data.

## 5.3 CHAPTER SUMMERY

In this chapter, prognostic-oriented aging models are created to describe the slowly-varying dynamics in the fuel cell that characterize the degradation process of the MEA of the fuel cell. The ECSA and the membrane gas crossover are chosen as aging parameters based on the experiment results presented in the last chapter. The focus of this chapter is the development a prognostic-oriented catalyst degradation model. Physics principles of the potential driven Ostwald ripening process are explored to establish a first-step detailed catalyst aging model. Model analysis is then conducted on this model to provide insight as for further simplification of the model for prognostic purpose.

The modeling approach employed to build the degradation model for the catalyst can be extended for other materials.

# CHAPTER SIX

# INTEGRATED ON-LINE DIAGNOSTICS AND PROGNOSTICS FOR THE FUEL CELL

In this chapter, we present an UKF-based diagnostic and prognostic scheme. Cathode GDL flooding and membrane drying diagnosis problem is considered and formulated as simultaneous state and parameter estimation problem similar to that of channel flooding. The health monitoring and prognostic scheme employs the degradation model developed in Chapter 5 for damage tracking and life prediction of the fuel cell. The proposed UKF framework is then applied to solve the diagnostic and prognostic problems, with simulation results presented for algorithm validation.

## 6.1 INTRODUCTION TO PROGNOSTICS

The oldest and most common maintenance and repair strategy is "fix it when it breaks." The problems with this approach include the occurrence of unscheduled downtime at times that may be inconvenient [2], especially in the case of critical missions. The only way to minimize both maintenance and repair costs and probability of failure is to perform ongoing assessment of machine health and ongoing prediction of future failures based on current health and operating and maintenance history. This is the motivation for prognostics: minimize repair and maintenance costs and associated operational disruptions, while also minimizing the risk of unscheduled downtime. Improving reliability and reducing unscheduled downtime by monitoring and predicting machine health.

Prognosis may be essentially understood as the generation of long-term predictions for a fault indicator, made with the purpose of estimating the RUL of a failing component[59]. Generally speaking, there are two types of prognostics in terms of the time for the initiation of the prognostics algorithm. The first type activates the prognostics only after fault(s) being detected and isolated by the diagnostics system; the triggered prognostics algorithm should start making RUL predictions shortly after the fault was detected as soon as enough data has been collected; the second type of prognostics, on the other hand, start life prediction shortly after the time of birth of the system, for which there may not be an explicit declaration of fault detection, e.g., applications like battery health management, where prognosis is carried out on a decay process. In this case, we expect to trigger prognosis as soon as enough data has been collected [96].

## 6.2 UKF FRAMEWORK FOR JOINT ESTIMATION

We first consider a general joint estimation problem based on the following discrete system.

$$\begin{aligned} \mathbf{x}_{k+1} &= \mathbf{F}\left(\mathbf{x}_k, \mathbf{u}_k, \mathbf{v}_k, \mathbf{w}\right) \\ \mathbf{y}_k &= \mathbf{H}\left(\mathbf{x}_k, \mathbf{u}_k, \mathbf{n}_k, \mathbf{w}\right) \end{aligned} \tag{6.1}$$

where $\mathbf{x}_k$ represent the sates of the system, $\mathbf{y}_k$ the outputs, $\mathbf{u}_k$ the inputs , $\mathbf{v}_k, \mathbf{n}_k$ the process and measurement noises, respectively, and $\mathbf{w}$ the time-varying system parameters.

Since the parameters $\mathbf{w}$ are unknown and time-varying, the state and parameter must be simultaneously/jointly estimated based on the noisy measured output. On the other hand, the dynamics of the time-varying system parameters are usually hard to

describe, i.e., there is a lack of descriptive dynamic equation to characterize the parameters. A commonly used method to address this issue is to treat the parameter as a stochastic signal driven by a white noise ( $\mathbf{r_k}$ )

$$\mathbf{w_{k+1}} = \mathbf{w_k} + \mathbf{r_k} \tag{6.2}$$

Then, by concatenating the state and parameter to form an augmented state vector $\mathbf{x_k^a} = \begin{bmatrix} \mathbf{x_k^T} & \mathbf{w_k^T} \end{bmatrix}^T$, joint state space equations [17] (assuming additive noises) can be obtained as follows

$$\begin{aligned} \begin{bmatrix} \mathbf{x_{k+1}} \\ \mathbf{w_{k+1}} \end{bmatrix} &= \begin{bmatrix} \mathbf{F}(\mathbf{x_k}, \mathbf{u_k}, \mathbf{w}) \\ \mathbf{I} \cdot \mathbf{w_k} \end{bmatrix} + \begin{bmatrix} \mathbf{B} \cdot \mathbf{v_k} \\ \mathbf{r_k} \end{bmatrix} \\ \mathbf{y_k} &= \mathbf{H}(\mathbf{x_k}, \mathbf{u_k}, \mathbf{w}) + \mathbf{n_k} \end{aligned} \tag{6.3}$$

The joint estimation problem of states and parameters based on observation can be formulated in an optimal recursive estimation framework as given in the following equation

$$\hat{\mathbf{x}}_\mathbf{k}^a = E\left[\hat{\mathbf{x}}_\mathbf{k}^a \middle| \mathbf{Y_k}\right] = E\left[\hat{\mathbf{x}}_\mathbf{k}^a \middle| \mathbf{y_0}, \mathbf{y_1}, \ldots \mathbf{y_k}\right] \tag{6.4}$$

Two step process (recursively) are involved, the first is the measurement correction

$$p\left(\hat{\mathbf{x}}_\mathbf{k}^a \middle| \mathbf{Y_k}\right) = \frac{p\left(\hat{\mathbf{x}}_\mathbf{k}^a \middle| \mathbf{Y_{k-1}}\right) p\left(\mathbf{y_k} \middle| \mathbf{x_k}\right)}{p\left(\mathbf{y_k} \middle| \mathbf{Y_{k-1}}\right)} \tag{6.5}$$

And the second is the one-step prediction

$$p\left(\hat{\mathbf{x}}_{\mathbf{k}+1}^a \middle| \mathbf{Y_k}\right) = \int p\left(\mathbf{x_{k+1}} \middle| \mathbf{x_k}\right) p\left(\mathbf{x_k} \middle| \mathbf{Y_k}\right) d\mathbf{x_k} \tag{6.6}$$

Various filtering techniques can be implemented in this general recursive estimation framework, including the most widely used extended Kalman filter, particle

filtering, and unscented Kalman filter. EKF is difficult to tune, and the Jacobian is usually hard to derive, and it can only handle limited amount of nonlinearity, while PF can handle arbitrary distributions and nonlinearities but is computationally very complex. In this Chapter, we focus on UKF since it gives a nice tradeoff between PF and EKF.

## 6.3 PROBLEM FORMULATION

In Chapter 5, we have already established a prognostic-oriented fuel cell aging model to describe the catalyst degradation process. The model is a second order system with simple structure. For simplicity of demonstration, we further simplify that model to a first order dynamic model, as shown in (6.7), by neglecting the dynamics of the platinum oxide coverage during the load cycling.

$$\frac{dA_{\text{geo}}}{dt} \approx -\frac{4k_1}{9V_{\text{Pt}}^2}\cdot\frac{u_c}{u^{\theta}}\cdot\theta_{\text{vac}}\cdot\frac{M_{\text{Pt}}}{\rho_{\text{Pt}}}\cdot\frac{F\alpha_1}{RT}\cdot\exp\left(\frac{F\alpha_1}{RT}\frac{A_{\text{geo}}}{3V_{\text{Pt}}}\right)\cdot A_{\text{geo}}^3\alpha_r\beta_r^2 \tag{6.7}$$

Let $\alpha_r = 1.1$, we assume it to be a constant parameter that remains unchanged in the whole degradation process.

Since $k_1$ is extremely small in value, we can scale the above equation in time with a scaling coefficient $\varepsilon$ to denote its slowness explicitly. Also note that $k_1$ is an implicit function of the temperature T, we can write the degradation rate of the catalytic surface area as a function of the catalytic surface area itself, input potential load

$$\frac{dA_{\text{geo}}}{dt} = \varepsilon\cdot\mathbf{g}\left(A_{\text{geo}}, \Delta\phi_c, \beta_r, T\right) \tag{6.8}$$

As we mentioned above, dynamics of the platinum oxide coverage is neglected in this first order system. Thus the platinum oxide coverage is considered as a static

function of the equivalent load input: $\theta_{\text{vac}} = \text{map}(u_c)$. Now, by taking into account the uncertain factors as additive process noises, the following stochastic degradation model can be obtained

$$\begin{aligned} \frac{dA_{\text{geo}}}{dt} &= \varepsilon \cdot \mathbf{g}\left(A_{\text{geo}}, \Delta\phi_c, \beta_r, T\right) + w_1(t) \\ \dot{\beta}_r &= w_2(t) \end{aligned} \tag{6.9}$$

where the unknown time-varying parameter $\beta_r$ is taken as a state variable, and its derivative as a process noise.

For diagnostic purpose, the fast dynamics for the oxygen partial pressure in GDL is given in (6.10), the GDL flooding fault is incorporated by considering the effective oxygen diffusion coefficient in the GDL as a function of the liquid water volume, i.e., $D_{\text{eff}}\left(V_{GDL}^{l}\right)$. For simplicity, we assume the oxygen partial pressure in channel $p_{ch}^{O_2}$ is available by some independent observer design, and $p_{ch}^{O_2} = \hat{p}_{ch}^{O_2} + w_3(t)$ to account for the estimation error. The noise $w_3(t)$ is assumed to be a white noise.

$$\begin{aligned} V_{GDL}^{pore}\, \dot{p}_{GDL}^{O_2} &= D_{\text{eff}}\left(V_{GDL}^{l}\right) \cdot \frac{\left(\hat{p}_{ch}^{O_2} + w_3(t)\right) - p_{GDL}^{O_2}}{\delta_{GDL}/2} \cdot A_{\text{fc}} - \frac{\dot{m}_{rct}^{O_2}}{M_{O_2}} RT + w_4(t) \\ \dot{V}_{GDL}^{l} &= w_5(t) \end{aligned} \tag{6.10}$$

In the above equation, $w_4(t)$ and $w_5(t)$ are additive process noises which are also considered white.

Both the fast dynamics (6.10) and the slow dynamics (6.9) share the same output equation, i.e, the voltage-current equation as shown below.

$$V_{cell} = E_0\left(T_{\text{fc}}\right) - \frac{RT_{\text{fc}}}{4\left(1-\alpha\right)F}\ln\left[\frac{\left(p_{O_2}^{\text{ref}*}\right)^{\alpha}}{i_0^{\text{ref}}\big|_{t=0}}\right] - \frac{RT_{\text{fc}}}{4\left(1-\alpha\right)F}\ln\left(i+i_{leak}\right) + \frac{RT_{\text{fc}}}{2F}\ln p_{H_2}^{*} + \frac{RT_{\text{fc}}}{4\left(1-\alpha\right)F}\ln p_{O_2}^{*} + \frac{RT_{\text{fc}}}{4\left(1-\alpha\right)F}\ln\xi_{\text{cat}} - i\cdot A_{\text{fc}}\cdot R_{ohm} \tag{6.11}$$

wher $p^{*O_2} = p_{GDL}^{O_2} - \dot{m}_{rct}^{O_2}\dfrac{\delta_{GDL}/2\cdot RT}{M_{O_2}A_{\text{fc}}D_{\text{eff}}\left(V_{GDL}^{l}\right)}$ is the oxygen partial pressure at catalyst site; and $E_0\left(T_{\text{fc}}\right) = 1.229 - 0.85\times10^{-3}\left(T_{\text{fc}} - 298.15\right)$ is only dependent on the fuel cell temperature.

The cell voltage can be broken down as follows

$$V_{cell} = h_0\left(t\right) + h_1\left(t\right) + h_2\left(t\right) \tag{6.12}$$

where $h_0\left(t\right)$ represents the known terms in the cell expression, $h_1\left(t\right)$ represents terms that can be affected by faulty conditions, and $h_2\left(t\right)$ the terms that are affected by aging parameter. The expressions for the three terms are given as follows:

$$h_0\left(t\right) = E_0\left(T_{\text{fc}}\right) - \frac{RT_{\text{fc}}}{4\left(1-\alpha\right)F}\ln\left[\frac{\left(p_{O_2}^{\text{ref}*}\right)^{\alpha}}{i_0^{\text{ref}}\big|_{t=0}}\right] + \frac{RT_{\text{fc}}}{2F}\ln p_{H_2}^{*} \tag{6.13}$$

$$h_1\left(t\right) = \frac{RT_{\text{fc}}}{4\left(1-\alpha\right)F}\ln p_{O_2}^{*} - i\cdot A_{\text{fc}}\cdot R_{ohm} \tag{6.14}$$

$$h_2\left(t\right) = \frac{RT_{\text{fc}}}{4\left(1-\alpha\right)F}\ln\xi_{\text{cat}} - \frac{RT_{\text{fc}}}{4\left(1-\alpha\right)F}\ln\left(i+i_{leak}\right) \tag{6.15}$$

In this dissertation, we decouple the diagnostic and prognostic problems by exploiting their different time scales. Two separate UKF designs are employed to solve the problems, while the schematic structure and the information exchange between the two UKFs are depicted in Figure 6-1.

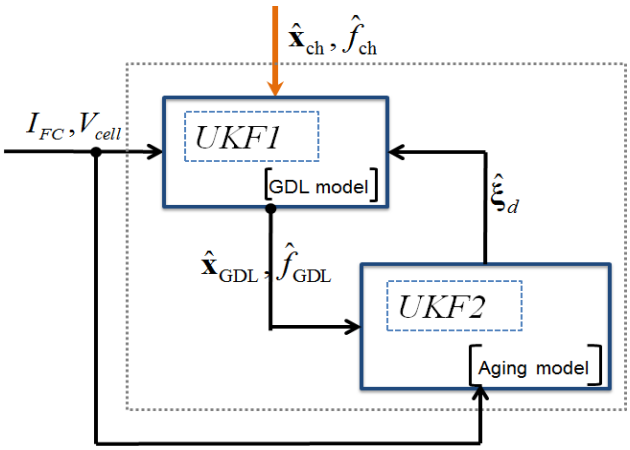


Figure 6-1 Schematic for the two UKF structure

In the next two sections, we describe the two UKFs respectively.

## 6.4 UKF Design for Diagnostics of GDL Flooding

In this section, we apply the UKF-based diagnostic scheme for the diagnosis of GDL flooding and membrane drying. Two cases are discussed, in the first case, we assume the Ohmic resistance of the fuel cell, i.e., the EIS high frequency information is available; in the second case, the high frequency resistance is assumed unknown, but other auxiliary features, such as variance of voltage signal that can be used to distinguish

*Case 1: Known HFR*

To apply the discrete UKF diagnostic framework, we now discretize the fast dynamics system equations as follows

State equations:

$$p_{GDL,k+1}^{O_2} = p_{GDL,k}^{O_2} + \Delta T \cdot \frac{D_{\text{eff}}\left(V_{GDL,k}^{l}\right)}{V_{GDL}^{pore}} \cdot \frac{\left(\hat{p}_{ch,k}^{O_2} + w_3(t)\right) - p_{GDL,k}^{O_2}}{\delta_{GDL}/2} \cdot A_{\text{fc}}$$
$$-\Delta T \cdot \frac{RT}{V_{GDL}^{pore}} \frac{\dot{m}_{rct,k}^{O_2}}{M_{O_2}} + \Delta T \cdot w_{4,k} \tag{6.16}$$
$$V_{GDL,k+1}^{l} = V_{GDL,k}^{l} + \Delta T \cdot w_{5,k}$$

Output equation

$$z_{1,k} = \frac{RT_{\text{fc}}}{4(1-\alpha)F} \ln p_{O_2}^{*} - i \cdot A_{\text{fc}} \cdot R_{ohm} + n_{\text{UKFI},k} \tag{6.17}$$

where $R_{ohm}$ is assumed to be known, and $n_{\text{UKFI},k}$ accounts for the measurement noise. The measurement signal $z_{1,k}$ can be obtained as

$$z_{1,k} = \hat{h}_{1,k} = V_{\text{cell},k} - h_{0,k} - \hat{h}_{2,k} \tag{6.18}$$

where $\hat{h}_2(t) = \frac{RT_{\text{fc}}}{4(1-\alpha)F} \ln \hat{\xi}_{\text{cat}} - \frac{RT_{\text{fc}}}{4(1-\alpha)F} \ln\left(i + \hat{i}_{leak}\right)$ is the aging terms provided by the health monitoring module.

Simulation validation is carried out with the voltage and current profile as shown in Figure 6-2. The dictated GDL water volume follows a sine wave. The simulation results are presented in Figure 6-3.

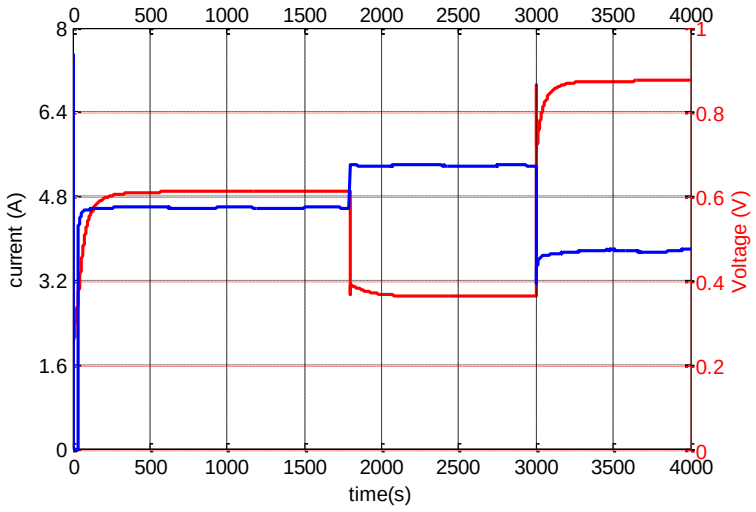


Figure 6-2 The system voltage and current

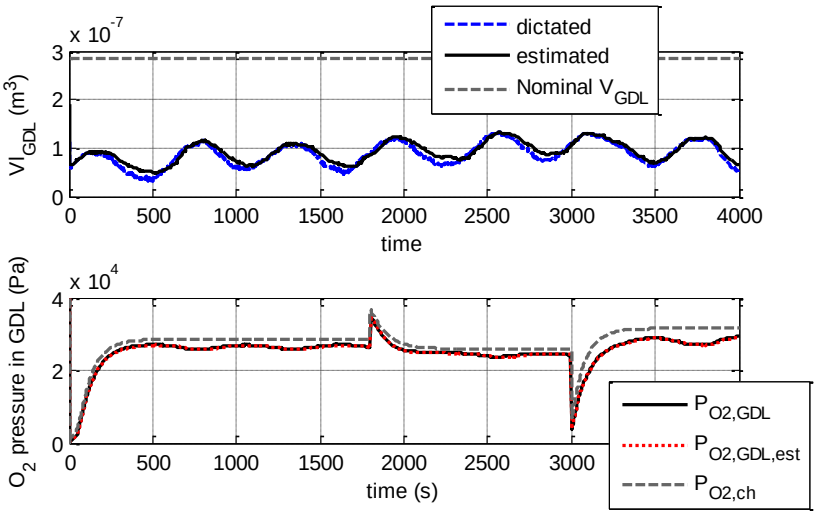


Figure 6-3 UKF estimation results for GDL flooding diagnosis

The simulation results show that the state and parameter estimation is achieved with acceptable accuracy. Under different current density, the arbitrarily dictated GDL flooding water volumes is tracked with a small error, while the actual and estimated state variable almost completely overlap. This can be better illustrated by a close-up of Figure 6-3 shown in Figure 6-4.

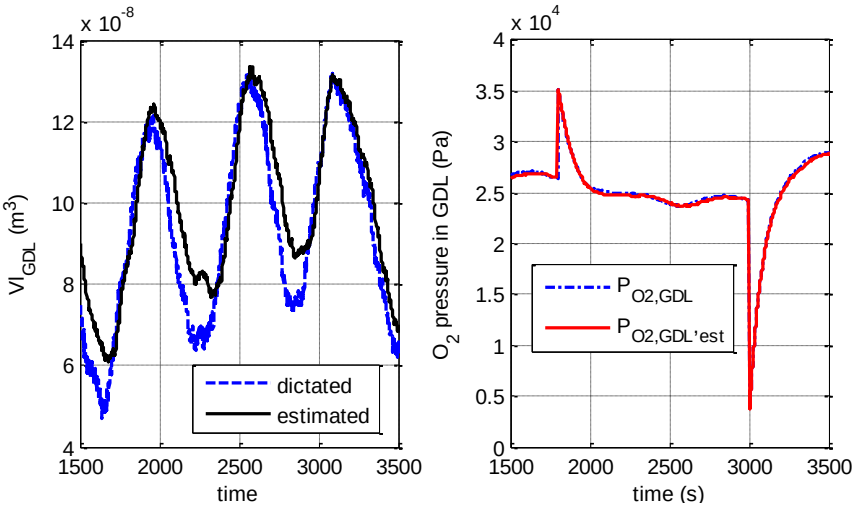


Figure 6-4 A close-up of Figure 6-3

*Case 2 Known feature*

We assume current interrupt method is applicable so that the long term HFR at membrane full hydration state could be tuned.

i. If the qualitative feature indicate possible flooding

State equations:

$$p_{GDL,k+1}^{O_2} = p_{GDL,k}^{O_2} + \Delta T \cdot \frac{D_{\text{eff}}\left(V_{GDL,k}^{l}\right)}{V_{GDL}^{pore}} \cdot \frac{\left(\hat{p}_{ch,k}^{O_2} + w_3(t)\right) - p_{GDL,k}^{O_2}}{\delta_{GDL}/2} \cdot A_{\text{fc}}$$
$$-\Delta T \cdot \frac{RT}{V_{GDL}^{pore}} \frac{\dot{m}_{rct,k}^{O_2}}{M_{O_2}} + \Delta T \cdot w_{4,k} \qquad (6.19)$$
$$V_{GDL,k+1}^{l} = V_{GDL,k}^{l} + \Delta T \cdot w_{5,k}$$

Output equation

$$z_{1,k} = \frac{RT_{\text{fc}}}{4(1-\alpha)F} \ln p_{O_2}^{*} - i \cdot A_{\text{fc}} \cdot R_{ohm} + n_{\text{UKFI},k} \qquad (6.20)$$

ii. otherwise

State equations:

$$p_{GDL,k+1}^{O_2} = p_{GDL,k}^{O_2} + \Delta T \cdot \frac{D_{\text{eff}}}{V_{GDL}^{pore}} \cdot \frac{\left(\hat{p}_{ch,k}^{O_2} + w_3(t)\right) - p_{GDL,k}^{O_2}}{\delta_{GDL}/2} \cdot A_{\text{fc}}$$
$$-\Delta T \cdot \frac{RT}{V_{GDL}^{pore}} \frac{\dot{m}_{rct,k}^{O_2}}{M_{O_2}} + \Delta T \cdot w_{4,k} \tag{6.21}$$
$$R_{ohm,k+1} = R_{ohm,k} + \Delta T \cdot w_{6,k}$$

Output equation

$$z_{1,k} = \frac{RT_{\text{fc}}}{4(1-\alpha)F} \ln p_{O_2}^* - i \cdot A_{\text{fc}} \cdot R_{ohm,k} + n_{\text{UKFI},k} \tag{6.22}$$

Simulation validation is then carried out with the voltage and current profile as shown in Figure 6-5. The dictated GDL water volume follows a sine wave. The simulation results are presented in Figure 6-6 and Figure 6-7.

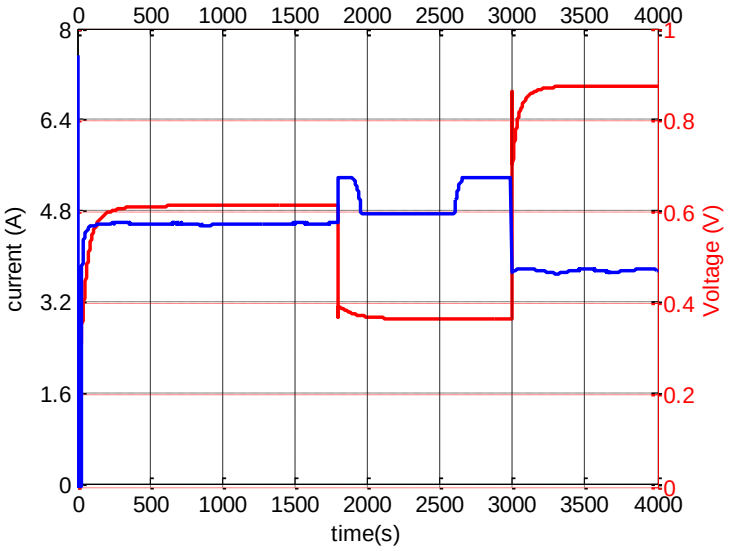


Figure 6-5 The system voltage and current

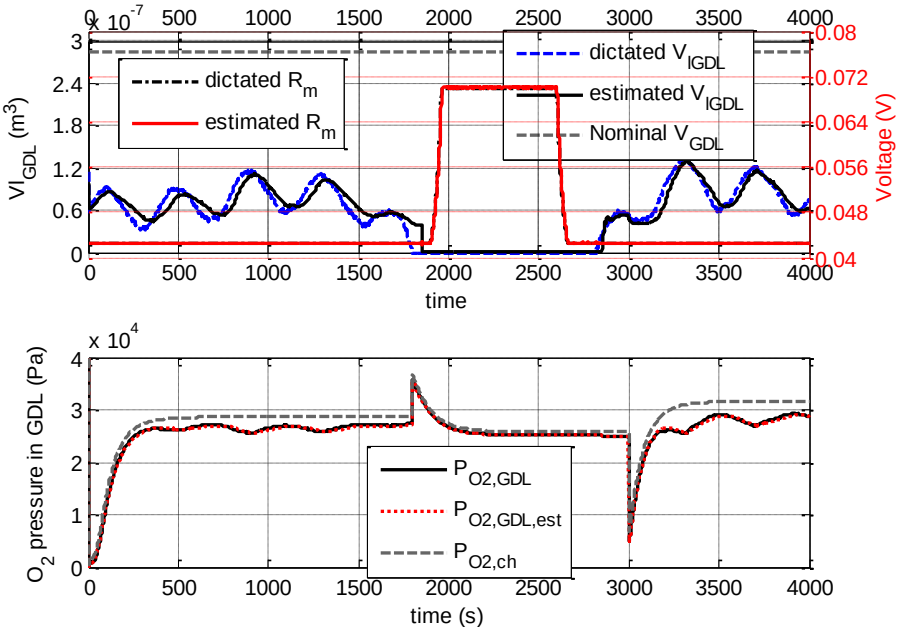


Figure 6-6 UKF estimation results for GDL flooding and membrane drying diagnosis

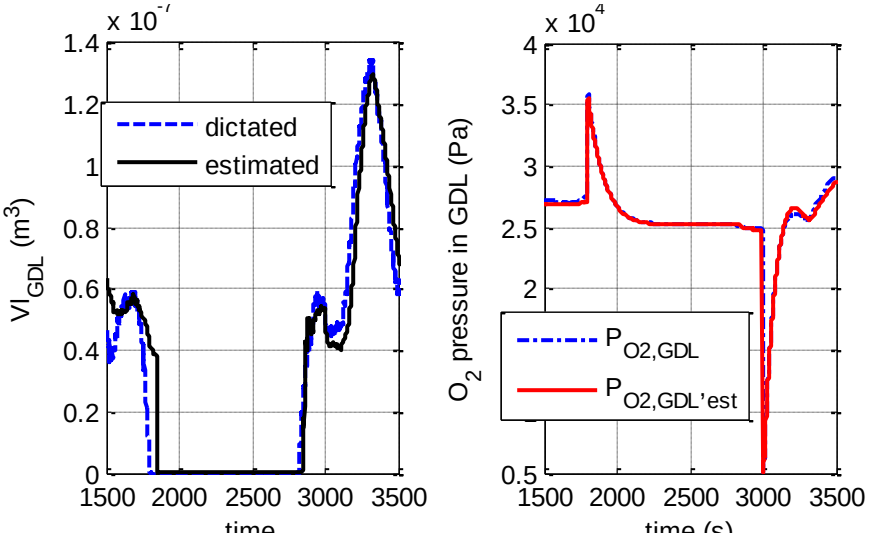


Figure 6-7 A close-up of Figure 6-6

## 6.5 UKF DESIGN FOR HEALTH MONITORING AND PROGNOSTICS

### *6.5.1 Damage Tracking and Prognostics for Catalyst Degradation*

As a first step, we investigate the health monitoring and prognostic problem for the catalyst degradation only. Similarly to the UKF diagnostic scheme, we first discretize the system equations.

State equations:

$$\begin{aligned} A_{\text{geo},k+1} &= \varepsilon \cdot N_{\varepsilon} \cdot \Delta T \cdot \mathbf{g}\left(A_{\text{geo},k}, \Delta\phi_{c,k}, \beta_{r,k}, T_{\text{fc}}\right) + \varepsilon \cdot N_{\varepsilon} \cdot \Delta T \cdot w_{1,k} \\ \beta_{r,k+1} &= \beta_{r,k} + \varepsilon \cdot N_{\varepsilon} \cdot \Delta T \cdot w_{2,k} \end{aligned} \tag{6.23}$$

Output equation

$$z_{2,k} = \frac{RT_{\text{fc}}}{4(1-\alpha)F} \ln \xi_{\text{cat},k} - \frac{RT_{\text{fc}}}{4(1-\alpha)F} \ln\left(i_k + i_{\text{leak},k}\right) + n_{\text{UKFII},k} \tag{6.24}$$

The measured output signal for the system $z_{2,k}$ can be obtained

$$z_{2,k} = \hat{h}_{2,k} = V_{\text{cell},k} - h_{0,k} - \hat{h}_{1,k} \tag{6.25}$$

Figure 6-8 shows the scheme for acquiring the output signal for UKF2.

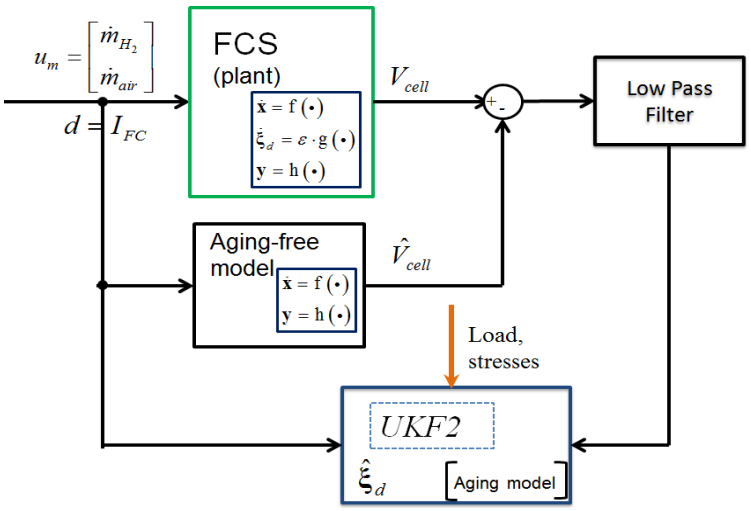


Figure 6-8 Acquisition of the output signal for UKF2

Simulation is carried out where we assume a cyclic load profile as given in Figure 6-9.

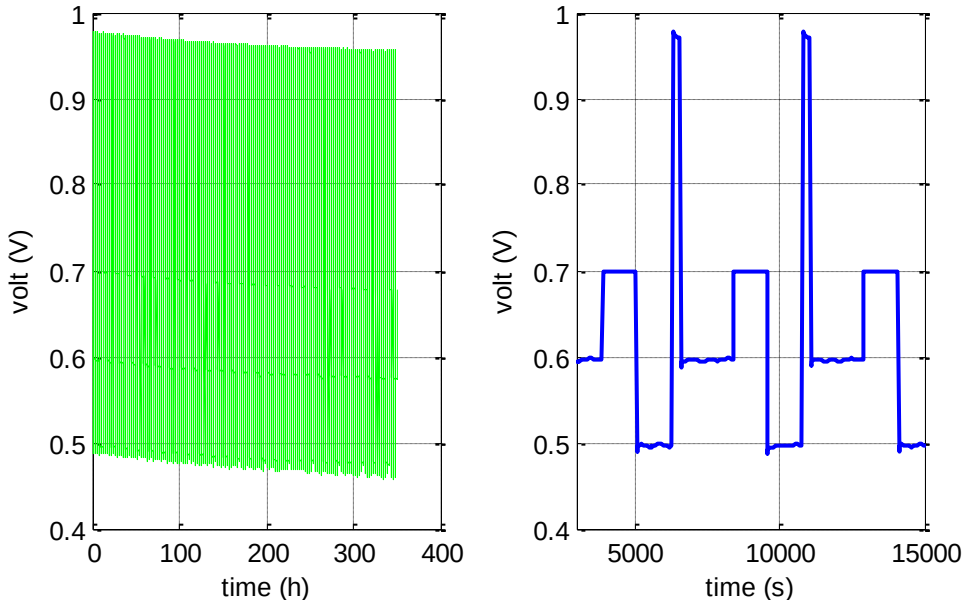


Figure 6-9 Load profile for PHM scheme simulation validation

The simulation result for health monitoring validation is presented in Figure 6-10. It can be seen that the ECSA has been tracked satisfactorily, while $\beta_r$ varies between the range [0.03, 0.04], and gradually settles down after 100h. The result also justifies our previous assumption that $\frac{\Delta r_1}{\bar{r}_a}$ and $\frac{\Delta r_2}{\bar{r}_a}$ are constant during the aging process. In fact, the first 100h can be considered as the necessary phase for parameter identification. After this phase, the parameter $\beta_r$ would stay relatively stable around some constant value. We will see later that this characteristic feature can be exploited to do fault diagnostics for the purpose of early detection of the massive gas crossover.

The parameters used for this simulation are as follows:

Initial state estimate: $\begin{bmatrix} \hat{A}_{Pt}^0 \\ \hat{\beta}_r^0 \end{bmatrix} = \begin{bmatrix} A_{Pt}^0 \times 1.1 \\ 0.035 \end{bmatrix}$

Initial covariance matrix: $P_0 = \begin{bmatrix} (0.02 \times A_{Pt}^0)^2 & 0 \\ 0 & (0.04 \times 0.15)^2 \end{bmatrix}$

Process noise covariance matrix:

$$\begin{bmatrix} Q_1 & 0 \\ 0 & Q_2 \end{bmatrix} = \begin{bmatrix} (A_{Pt}^0 \times 2 \times 10^{-6})^2 & 0 \\ 0 & (0.035 \times 2 \times 10^{-6})^2 \end{bmatrix}$$

Measurement noise covariance matrix: $R = 6.7 \times 10^{-6}$

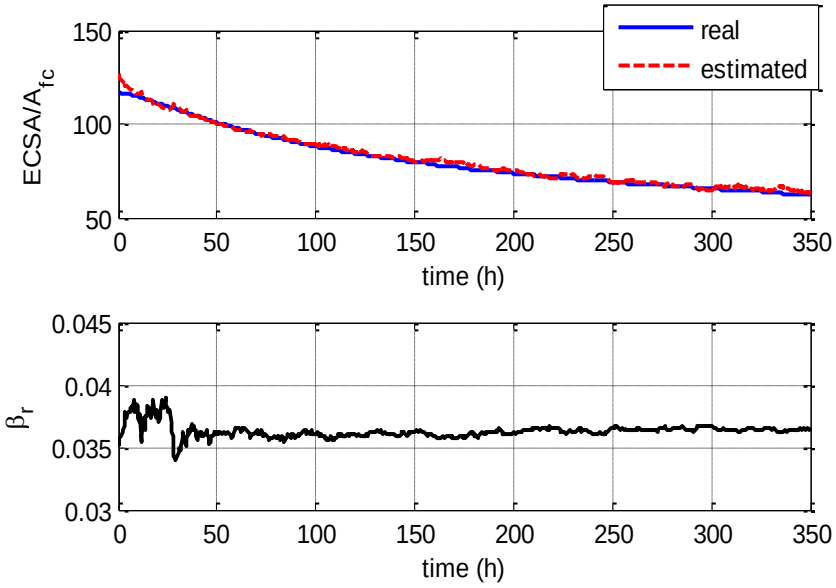


Figure 6-10 Simulation result for health monitoring

The simulation results for prognostic validation are presented in Figure 6-11 and Figure 6-12.

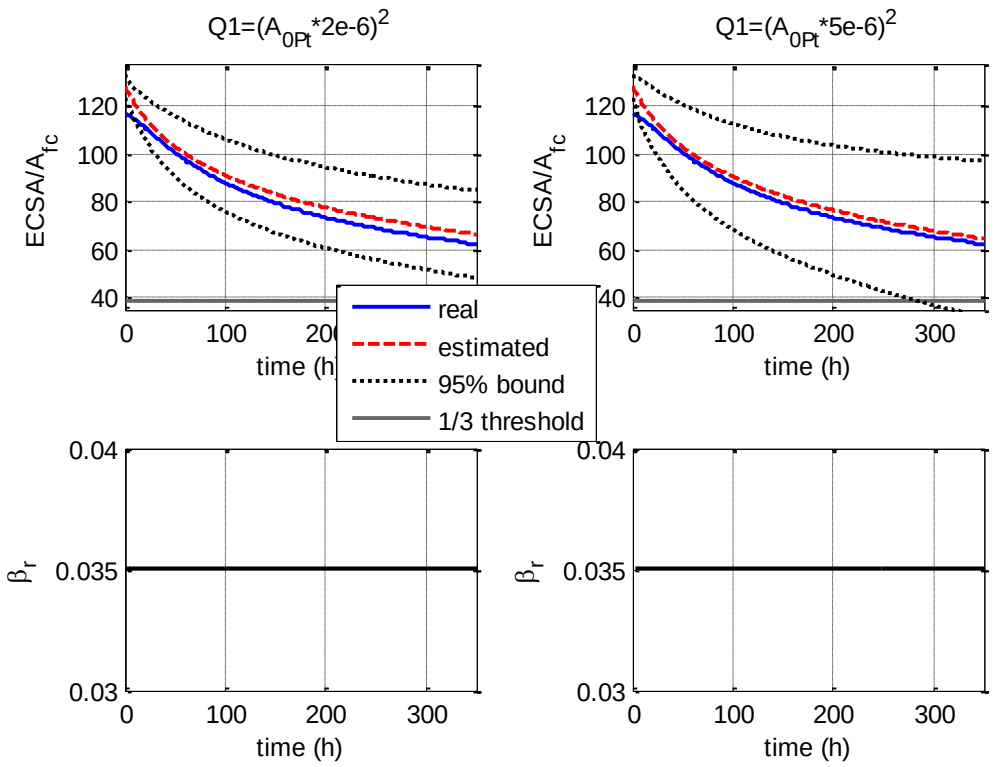


Figure 6-11 Simulation result for prognostics at the beginning of life

In Figure 6-11, prognostic is performed at the very beginning of life of the fuel cell. It can be seen that the 95% error is growing larger with increasing prediction step due to lack of measurement correction. $\beta_r$ is seen to be constant all the time with the same reason. Two values for the process noise $Q_1$ are compared, i.e., $(A_{Pt}^0 \times 2\times 10^{-6})^2$ and $(A_{Pt}^0 \times 5\times 10^{-6})^2$. As expected, the smaller value of the process noise results in a narrower 95% bound, and thus a more accurate prediction.

Figure 6-12 shows the simulation results with prognostic starting from the middle of the durability test, here at 100h. Due to lack of measurement correction, $\beta_r$ stops updating and is taken as a constant with its 100h value during the prediction. The 95%

error is also seen growing larger with increasing prediction step, but much narrower compared to that in Figure 6-11.

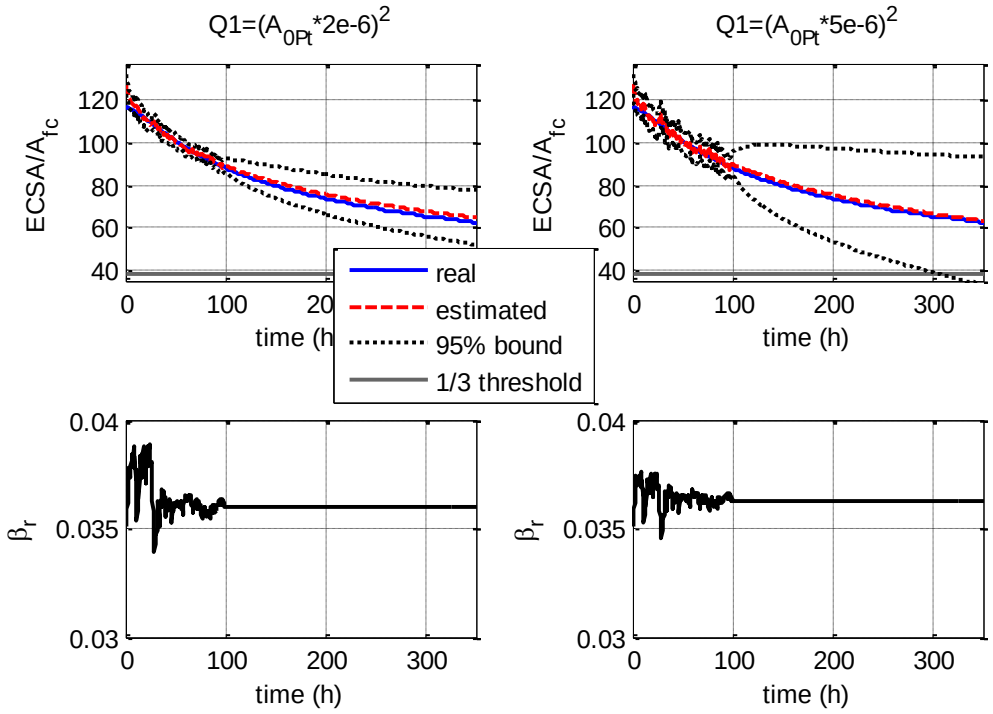


Figure 6-12 Simulation result for Prognostics at 100h

### *6.5.2 Fault Detection of the Initiation of Massive Hydrogen Crossover*

As we discussed before, the initiation of massive gas crossover through the membrane is rather stochastic and can be very difficult to predict. On the other hand, the time of the initiation is also very critical since it indicates the beginning of the end phase of the fuel cell lifetime: the massive gas crossover would accelerate exponentially after its initiation, resulting in a "quick death" of the fuel cell. Therefore, from a prognostic point of view, it is extremely important to be able to detect this initiation time at an early stage. A prognostic scheme for the membrane damage can then be activated after the

fault detection to track the membrane health and predict the remaining useful life of the fuel cell.

To simulate the fault condition of massive gas crossover, the dynamic model developed in Chapter 2 is used. The effect of the gas crossover is included in the fuel cell voltage model (2.53) as leak current density. However, simulation results with this model are shown to be insufficient to reflect the severity of large leak current density. As shown below in Figure 6-13, even with a leak current density as high as 1000mA/cm$^2$, the demanded current can be drawn by the external load and the voltage drop is far less than that observed in the experiment.

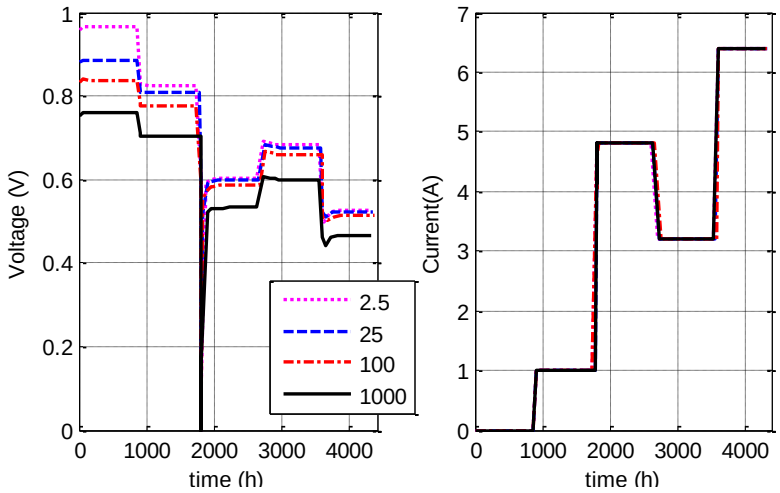


Figure 6-13 Simulation results with different leak current density level using voltage model (2.53)

The cell voltage model (6.11) is only valid when the leak current density is small enough to be neglected. Under large leak rate, the fuel cell model has to be modified for the simulation of this specific fault condition.

Here, we modify the MEA (2.23)~(2.25) to include the effect of the leaking hydrogen from the anode as follows:

$$W_{\text{rct}}^{H_2} = M^{H_2} \frac{I + i_{\text{leak}} \cdot A_{fc}}{2F} \tag{6.26}$$

$$W_{\text{rct}}^{O_2} = M^{O_2} \frac{I + i_{\text{leak}} \cdot A_{fc}}{4F} \tag{6.27}$$

$$W_{\text{gen}}^{H_2O} = M^{H_2O} \frac{I + i_{\text{leak}} \cdot A_{fc}}{2F} \tag{6.28}$$

where $I$ is the current given by $I = i \cdot A_{fc}$.

The simulation results are presented below. It can be seen that, with the modified model, the fuel cell is unable to output effective electrical power when the leak current density is larger than 100mA/cm$^2$, the OCV also drops to below 0.6V, which is more reasonable considering the experimental results.

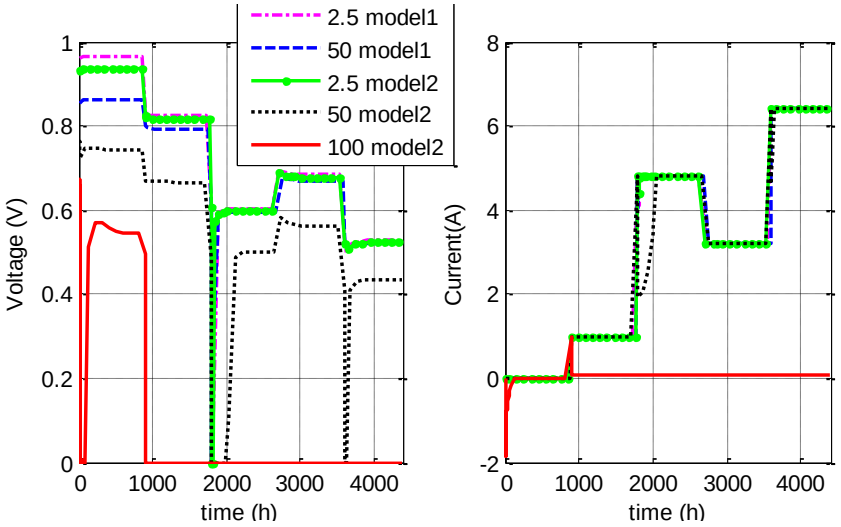


Figure 6-14 Comparison between simulation results with different leak current density level using two fuel cell models

With the modified model, simulation is then carried out with the current load profile presented in Figure 6-15. The corresponding output voltage is presented in Figure 6-16. The gradual performance loss phase from 0~250h and the sharp performance loss phase from 250h~350h can be clearly seen in the figure. Measurement noise covariance matrix: $R = 1 \times 10^{-4}$.

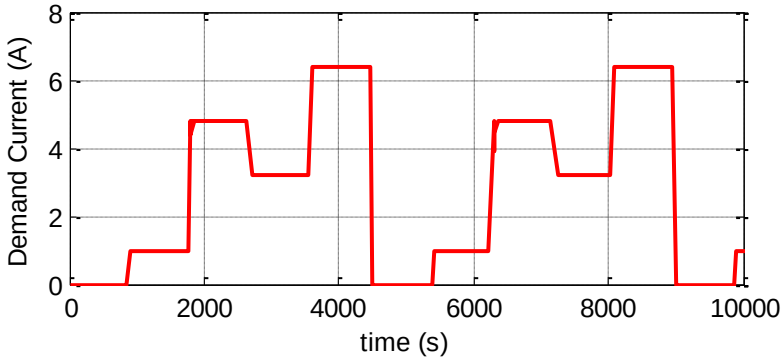


Figure 6-15 Current profile for the aging simulation

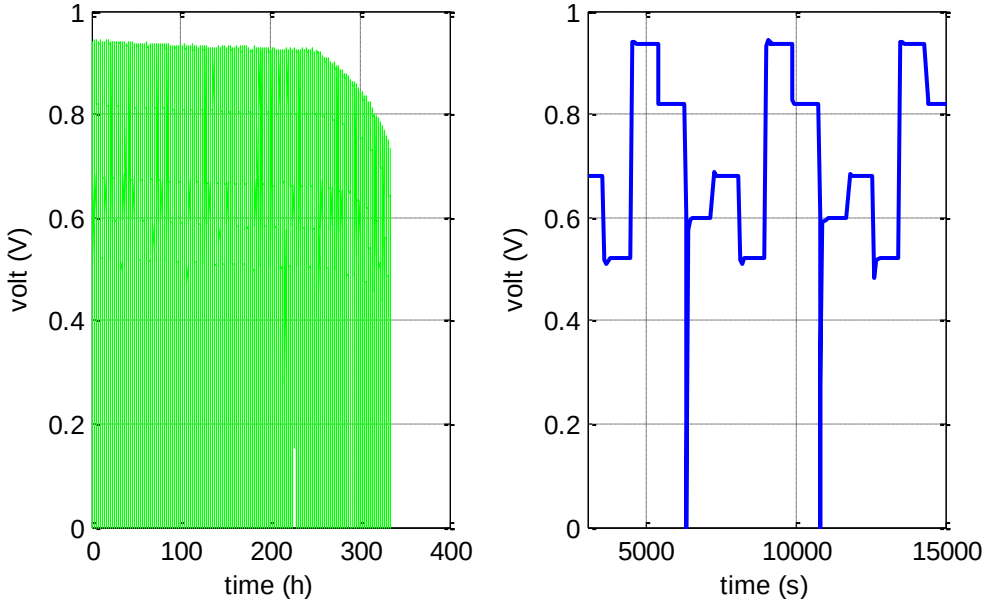


Figure 6-16 Voltage output from the simulated aging test

The simulation results for the damage tracking of ECSA and detection of current leak are shown in Figure 6-17. It can be seen that the parameter $\beta_r$ can be utilized as a good indicator for the early detection of the initiation of massive hydrogen crossover. By appropriately choosing the threshold, the serious current leak can be detected shortly after its initiation, in this case, less than 30h.

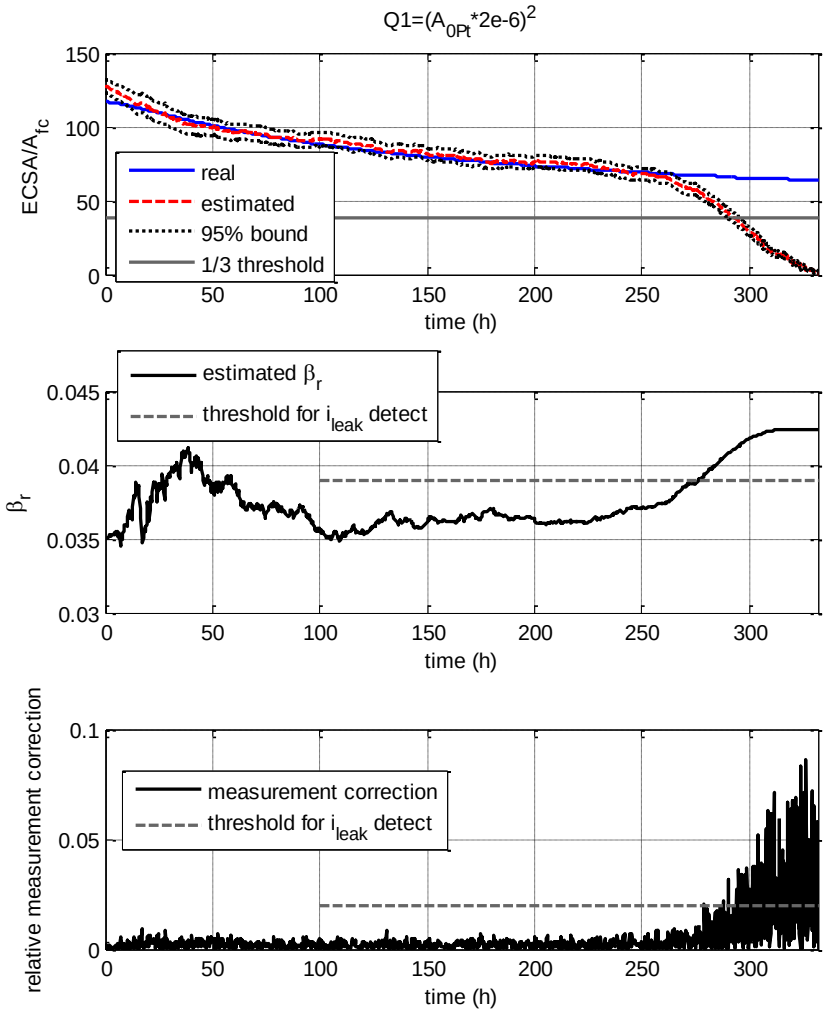


Figure 6-17 Simulation results for the damage tracking of ECSA and detection of current leak

## 6.6 CHAPTER SUMMARY

In this chapter, an integrated diagnostic and prognostic scheme is presented based on the electro-chemical module of the fuel cell. Cathode GDL flooding and membrane drying diagnosis problem, and catalyst damage tracking and life prediction problem are considered, both of which are formulated as simultaneous state and parameter estimation problems. An UKF-based framework is proposed for the diagnostic and prognostic scheme and applied to solve the problems. The outcome of the prognosis scheme provides information about the precision and accuracy of long-term prediction, RUL expectations and 95% confidence intervals. Simulation is carried out for the validation of the proposed scheme. The results show that with measurement correction, the health monitoring system can successfully track the damage variable throughout the degradation process; while at any time during the aging process, the remaining useful life can be predicted with satisfactory accuracy given that future load input information is precisely known.

# CHAPTER SEVEN

# CONCLUSION AND FUTURE WORK

In this dissertation, we proposed a comprehensive on-line supervisory system with the capability of control/diagnostic, health monitoring and prognostic. Correspondingly, control/diagnostic oriented fuel cell dynamic model and prognostic-oriented fuel cell degradation model are developed.

The comprehensive fuel cell dynamic model incorporating fault effects and aging effects (damage variables) is established to be used as the platform for algorithm validation of the control, diagnostic and health monitoring systems. Major improvements of this model compared to the existing fuel cell models are 1) Gas dynamics in the fuel cell channel is modeled to include channel water flooding effect; 2) Channel water dynamic model is incorporated, which is capable of describing the removal of the liquid water in the fuel cell channel; 3) The dynamics of reactants transportation in the GDL is considered as a function of the liquid water present in the GDL; 4) The effect of the effective catalyst surface area (ECSA) and the gas crossover of the membrane is incorporated in the electro-chemical submodel.

Prognostic-oriented aging models are created to describe the slowly-varying dynamics in the fuel cell that characterize the degradation process of the MEA of the fuel cell. The aging parameters are chosen based on the experiment results such that they not only exhibit pronounced degradation trend but also distinguishably affect the fuel cell's instantaneous performances.

Based on the control/diagnostic oriented fuel cell model, a model-based on-line diagnostics system is developed for fuel cell flooding and drying diagnosis. The channel flooding diagnostic problem and GDL flooding and membrane drying diagnostic problem are decoupled, both are formed as state and parameter estimation problem. Extended Kalman Filter and Unscented Kalman Filter are proposed correspondingly to solve the problems. A diagnostic based control design for the air supply of the fuel cell system is proposed. This concept allows selection of the most suited controller in a controller bank that delivers the best performance. H-infinity controller is designed to minimize the desired and actual excess O2 ratio.

Finally, an UKF-based health-monitoring and prognostic scheme is proposed for the purpose of damage tracking and remaining useful life (RUL) prediction for the fuel cell. Simulation results show that with measurement correction, the health monitoring system can successfully track the damage variable throughout the degradation process; while at any time during the aging process, the remaining useful life can be predicted with satisfactory accuracy given that future load input information is precisely known.

# APPENDICES

## APPENDIX A

Derivation of Lumped Pipe Model by PDE Discretization

In this section, we give some key intermediate steps in detail for deriving the lumped general pipe model by discretizing the PDEs in(2.3).

First, as shown in Figure A-1, a pipe with arbitrary closed cross sectional area is equally divided into $N$ parts along the channel axis. The pressure in the ($i$+1)th section is denoted as $p_i$, and the mass flow rate flowing across the border of the $i$th and ($i$+1)th section is denoted as $W_i$.

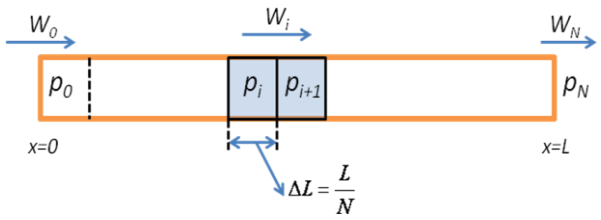


Figure A-1: Discretized general pipe.

By discretizing (2.3), we have for the gas in the ($i$+1)th section of the pipe that

$$\begin{cases} \dfrac{dp_i}{dt} = \dfrac{R \cdot T}{A \cdot M} \cdot \dfrac{W_i - W_{i+1}}{\Delta L} \\ W_{i+1} = \dfrac{p_i - p_{i+1}}{k \cdot \Delta L} \end{cases} \tag{6.29}$$

This results in an $N$th order system of ODEs, which can be put into standard state space form with state vector $\mathbf{p} = \begin{bmatrix} p_0 & p_1 & \cdots & p_i & \cdots & p_{N-1} \end{bmatrix}^T$, and system inputs $W_0$ and $p_N$.

$$\frac{d\mathbf{p}}{dt} = \mathbf{A_p} \cdot \mathbf{p} + \mathbf{B_p} \cdot \begin{bmatrix} W_0 \\ p_N \end{bmatrix} \tag{6.30}$$

where $\mathbf{A_p} = \begin{bmatrix} -a & a & & & & \\ a & -2a & a & & & \\ & a & -2a & a & & \\ & & \ddots & \ddots & \ddots & \\ & & & a & -2a & a \\ & & & & a & -2a \end{bmatrix}_{(N\times N)}$, $a = \dfrac{R\cdot T}{A\cdot M}\dfrac{1}{k\cdot \Delta L^2}$, and

$$\mathbf{B_p} = \begin{bmatrix} \dfrac{R\cdot T}{A\cdot M}\dfrac{1}{\Delta L} & 0 \\ 0 & 0 \\ \vdots & \vdots \\ 0 & 0 \\ 0 & a \end{bmatrix}_{(N\times 2)}$$

For illustration purpose, in this section, we only show the derivation process for the relationship between one of the system outputs $p_0$ and the two system inputs (in terms of transfer functions). The relationship between the other system output $W_N$ and the system inputs can be derived in a similar manner.

Since we only consider $p_0$ as the system output, the $C$ matrix in the output equation is simply $\mathbf{C}_{p_0} = \begin{bmatrix} 1 & 0 & \cdots & 0 \end{bmatrix}_{(1\times N)}$

We then have for the expression of $p_0$ that

$$\begin{aligned} p_0 &= \left[ \mathbf{C}_{p_0} \left( sI - \mathbf{A_p} \right)^{-1} \mathbf{B_p} \right]_{(1\times 2)} \cdot \begin{bmatrix} W_0 \\ p_N \end{bmatrix} \\ &= \begin{bmatrix} 1 & 0 & \cdots & 0 \end{bmatrix}_{(1\times N)} \frac{\begin{bmatrix} R_{1p} & \cdots & R_{2p} \\ \vdots & \cdots & \vdots \\ \cdots & \cdots & \cdots \end{bmatrix}}{\left| sI - \mathbf{A_p} \right|} \begin{bmatrix} \dfrac{R\cdot T}{A\cdot M}\dfrac{1}{\Delta L} & 0 & \cdots & 0 & 0 \\ 0 & 0 & \cdots & 0 & a \end{bmatrix}^T_{(2\times N)} \cdot \begin{bmatrix} W_0 \\ p_N \end{bmatrix} \end{aligned} \tag{6.31}$$

Let $D_N = \left|sI - \mathbf{A_p}\right| = \det\left(sI - \mathbf{A_p}\right)_{(N\times N)}$ in the above equation, it can be shown that, due to the specific structure of matrix $\mathbf{A_p}$, the iteration $D_N = (s+2a)D_{N-1} - a^2 D_{N-2}$ stands.

It is clear that the model to be developed is also of *N*-th order. However, it is observed from the experimental data (and also from simulation results using reasonable model parameters) that the system's behavior is characteristic of a first order system, implying negligible higher order dynamics. Thus in the following deduction, we only focus on the first and second order terms. Mathematical explanation to justify the first order system approximation is also given at the end of this section.

To obtain the transfer functions from $\begin{bmatrix} W_0 & p_N \end{bmatrix}^T$ to $p_0$, only $D_N$, $R_{1p}$, $R_{2p}$ in (9) need to be computed. Utilizing the iteration above and neglecting the higher order (third order and above) terms, we first obtain

$$D_N \approx a^{N-2}N^4\left[\frac{d_N}{N^4}s^2 + \frac{1+1/N}{2}\frac{R\cdot T}{A\cdot M}\frac{1}{kL^2}s + \left(\frac{R\cdot T}{A\cdot M}\frac{1}{kL^2}\right)^2\right] \tag{6.32}$$

where $\lim_{N\to\infty}\frac{d_N}{N^4} = 1/24$. Similarly, we get

$$R_{1p} \approx a^{N-2}N^3\left(\frac{\bar{d}_{N-1}}{N^3}s + \frac{R\cdot T}{A\cdot M}\frac{1}{kL^2}\right) \tag{6.33}$$

where $\lim_{N\to\infty}\frac{\bar{d}_{N-1}}{N^3} = 1/6$. And $R_{2p} = a^{N-1}$.

Substituting $D_N$, $R_{1p}$, $R_{2p}$ into (9), then, as *N* goes to infinity, we have the following second-order model in frequency domain

$$\lim_{N\to\infty} p_0 \simeq \frac{\left[\frac{1}{6}\frac{A\cdot M}{R\cdot T}k^2L^3s + kL \quad 1\right]}{\frac{1}{24}\left(\frac{A\cdot M}{R\cdot T}kL^2\right)^2 s^2 + \frac{1}{2}\frac{A\cdot M}{R\cdot T}kL^2 s + 1}\cdot\begin{bmatrix} W_0 \\ p_N \end{bmatrix} \tag{6.34}$$

From $k = \frac{2\chi\cdot\mu(T)\cdot R\cdot T}{D_h^2\cdot A\cdot M\cdot p}$ , which is given before, it is easy to show that $\frac{A\cdot M}{R\cdot T}kL^2 = \frac{2\chi\cdot\mu\cdot L^2}{D_h^2\cdot p}$. For a general circular pipe with length $L$ = 1m and hydraulic diameter $D_h$ = 1mm (which is a long and thin pipe), when flowing air at a pressure about 1bar, $\frac{A\cdot M}{R\cdot T}kL^2 = \frac{2\chi\cdot\mu\cdot L^2}{D_h^2\cdot p} \approx \frac{2\times16\times17\times10^{-6}\times10^6}{10^5} \approx 0.55\times10^{-2}$ , which is a very small number. For pipes that have a smaller ratio of $L/D_h$, the number would be even smaller, i.e., $\frac{A\cdot M}{R\cdot T}kL^2 \ll 1$. Since the coefficient of the second order term is $\left(\frac{A\cdot M}{R\cdot T}kL^2\right)^2$, we neglect the second order dynamics and simplify the model to the following first order system.

$$p_0 = \frac{\left[kL \quad 1\right]}{\frac{1}{2}\frac{A\cdot M}{R\cdot T}kL^2 s + 1}\cdot\begin{bmatrix} W_0 \\ p_N \end{bmatrix} \tag{6.35}$$

## REFERENCE


[1] "DOE Fuel Cells Technology Validation Plan." 2007.

[2] R. Kothamasu, S. H. Huang, and W. H. VerDuin, "System health monitoring and prognostics—a review of current paradigms and practices," *The International Journal of Advanced Manufacturing Technology*, vol. 28, no. 9, pp. 1012–1024, 2006.

[3] J. Larminie and A. Dicks, *Fuel Cell Systems Explained*, 2nd ed. Wiley, 2003.

[4] B. A. McCain, A. G. Stefanopoulou, and I. V. Kolmanovsky, "On the dynamics and control of through-plane water distributions in PEM fuel cells," *Chemical Engineering Science*, vol. 63, no. 17, pp. 4418–4432, 2008.

[5] W. Schmittinger and A. Vahidi, "A review of the main parameters influencing long-term performance and durability of PEM fuel cells," *Journal of Power Sources*, vol. 180, no. 1, pp. 1–14, May 2008.

[6] T. Okada, "Effect of Ionic contaminants," in *Handbook of Fuel Cells – Fundamentals, Technology and Applications*, Wiley & Sons, 2003, pp. 627–646.

[7] Shengsheng Zhang, Xiaozi Yuan, Haijiang Wang, W. Merida, Hong Zhu, Jun Shen, Shaohong Wu, and Jiujun Zhang, "A review of accelerated stress tests of MEA durability in PEM fuel cells," *International Journal of Hydrogen Energy*, vol. 34, no. 1, pp. 388–404, Jan. 2009.

[8] S. Zhang, X.-Z. Yuan, J. N. C. Hin, H. Wang, K. A. Friedrich, and M. Schulze, "A review of platinum-based catalyst layer degradation in proton exchange membrane fuel cells," *Journal of Power Sources*, vol. 194, no. 2, pp. 588–600, 2009.

[9] N. Yousfi-Steiner, P. Moçotéguy, D. Candusso, and D. Hissel, "A review on polymer electrolyte membrane fuel cell catalyst degradation and starvation issues: Causes, consequences and diagnostic for mitigation," *Journal of Power Sources*, vol. 194, no. 1, pp. 130–145, Oct. 2009.

[10] F. A. de Bruijn, V. A. T. Dam, and G. J. M. Janssen, "Review: Durability and Degradation Issues of PEM Fuel Cell Components," *Fuel Cells*, vol. 8, no. 1, pp. 3–22, Feb. 2008.

[11] R. Borup, J. Meyers, B. Pivovar, Y. S. Kim, R. Mukundan, N. Garland, D. Myers, M. Wilson, F. Garzon, D. Wood, P. Zelenay, K. More, K. Stroh, T. Zawodzinski, J. Boncella, J. E. McGrath, M. Inaba, K. Miyatake, M. Hori, K. Ota, Z. Ogumi, S. Miyata, A. Nishikata, Z. Siroma, Y. Uchimoto, K. Yasuda, K.-I. Kimijima, and N. Iwashita, "Scientific aspects of polymer electrolyte fuel cell durability and degradation," *Chemical Reviews*, vol. 107, no. 10, pp. 3904–3951, 2007.

[12] W. Bi, Q. Sun, Y. Deng, and T. F. Fuller, "The effect of humidity and oxygen partial pressure on degradation of Pt/C catalyst in PEM fuel cell," *Electrochimica Acta*, vol. 54, no. 6, pp. 1826–1833, 2009.

[13] Y. Shao-Horn, W. C. Sheng, S. Chen, P. J. Ferreira, E. F. Holby, and D. Morgan, "Instability of Supported Platinum Nanoparticles in Low-Temperature Fuel Cells," *Topics in Catalysis*, vol. 46, no. 3–4, pp. 285–305, Nov. 2007.

[14] W. Bi and T. F. Fuller, "Modeling of PEM fuel cell Pt/C catalyst degradation," *Journal of Power Sources*, vol. 178, no. 1, pp. 188–196, Mar. 2008.

[15] R. Shimoi, T. Aoyama, and A. Iiyama, "Development of Fuel Cell Stack Durability based on Actual Vehicle Test Data: Current Status and Future Work," SAE International, Warrendale, PA, 2009-01-1014, Apr. 2009.

[16] Y. Shao, G. Yin, and Y. Gao, "Understanding and approaches for the durability issues of Pt-based catalysts for PEM fuel cell," *Journal of Power Sources*, vol. 171, no. 2, pp. 558–566, 2007.

[17] J. P. Meyers and R. M. Darling, "Model of Carbon Corrosion in PEM Fuel Cells," *Journal of The Electrochemical Society*, vol. 153, no. 8, p. A1432, 2006.

[18] D. E. Curtin, R. D. Lousenberg, T. J. Henry, P. C. Tangeman, and M. E. Tisack, "Advanced materials for improved PEMFC performance and life," in *8th Grove Fuel Cell Symposium, 24-26 Sept. 2003*, Switzerland, 2004, vol. 131, pp. 41–8.

[19] U. Pasaogullari and C.-Y. Wang, Eds., *Modeling and Diagnostics of Polymer Electrolyte Fuel Cells: 49*, 1st ed. Springer, 2010.

[20] D. Chelidze, J. P. Cusumano, and A. Chatterjee, "A Dynamical Systems Approach to Damage Evolution Tracking, Part 1: Description and Experimental Application," *Journal of Vibration and Acoustics*, vol. 124, no. 2, p. 250, 2002.

[21] A. Miotti, A. Di Domenico, Y. G. Guezennec, and S. Rajagopalan, "Control-oriented model for an automotive PEM fuel cell system with imbedded 1+1D membrane water transport," in *2005 IEEE Vehicle Power and Propulsion Conference, VPPC, September 7, 2005 - September 9, 2005*, Chicago, IL, United states, 2005, vol. 2005, pp. 611–618.

[22] J. T. Pukrushpan, H. Peng, and A. G. Stefanopoulou, "Control-Oriented Modeling and Analysis for Automotive Fuel Cell Systems," *J. Dyn. Sys., Meas., Control*, vol. 126, no. 1, p. 14, 2004.

[23] J. Alejandro, A. Arce, and C. Bordons, "Development and experimental validation of a PEM fuel cell dynamic model," *Journal of Power Sources*, vol. 173, pp. 310–324, 2007.

[24] M. Soltani and S. M. T. Bathaee, "Development of an empirical dynamic model for a Nexa PEM fuel cell power module," *Energy Conversion and Management*, vol. 51, no. 12, pp. 2492–500, Dec. 2010.

[25] M. A. Danzer, J. Wilhelm, H. Aschemann, and E. P. Hofer, "Model-based control of cathode pressure and oxygen excess ratio of a PEM fuel cell system," *Journal of Power Sources*, vol. 176, no. 2, pp. 515–522, 2008.

[26] M. W. Fowler, R. F. Mann, J. C. Amphlett, B. A. Peppley, and P. R. Roberge, "Incorporation of voltage degradation into a generalised steady state electrochemical model for a PEM fuel cell," *Journal of Power Sources*, vol. 106, no. 1–2, pp. 274–283, 2002.

[27] A. A. Franco and M. Tembely, "Transient multiscale modeling of aging mechanisms in a PEFC cathode," *Journal of the Electrochemical Society*, vol. 154, p. B712, 2007.

[28] A. A. Franco, P. Schott, C. Jallut, and B. Maschke, "A Multi-Scale Dynamic Mechanistic Model for the Transient Analysis of PEFCs," *Fuel Cells*, vol. 7, no. 2, pp. 99–117, Apr. 2007.

[29] A. A. Franco, M. Gerard, M. Guinard, B. Barthe, and O. Lemaire, "Carbon Catalyst-Support Corrosion in Polymer Electrolyte Fuel Cells: Mechanistic Insights," 2008, pp. 35–55.

[30] A. A. Franco and M. Gerard, “Multiscale Model of Carbon Corrosion in a PEFC: Coupling with Electrocatalysis and Impact on Performance Degradation,” *Journal of The Electrochemical Society*, vol. 155, no. 4, p. B367, 2008.

[31] A. A. Franco, R. Coulon, R. Ferreira de Morais, S. K. Cheah, A. Kachmar, and M. A. Gabriel, “Multi-scale Modeling-based Prediction of PEM Fuel Cells MEA Durability under Automotive Operating Conditions,” 2009, pp. 65–79.

[32] R. M. Darling and J. P. Meyers, “Kinetic model of platinum dissolution in PEMFCs,” *Journal of the Electrochemical Society*, vol. 150, no. 11, pp. 1523–7, Nov. 2003.

[33] R. M. Darling and J. P. Meyers, “Mathematical model of platinum movement in PEM fuel cells,” *Journal of the Electrochemical Society*, vol. 152, no. 1, pp. A242–A247, 2005.

[34] E. F. Holby, W. Sheng, Y. Shao-Horn, and D. Morgan, “Pt nanoparticle stability in PEM fuel cells: Influence of particle size distribution and crossover hydrogen,” *Energy and Environmental Science*, vol. 2, no. 8, pp. 865–871, 2009.

[35] M. K. Debe, A. K. Schmoeckel, G. D. Vernstrom, and R. Atanasoski, “High voltage stability of nanostructured thin film catalysts for PEM fuel cells,” *Journal of Power Sources*, vol. 161, no. 2, pp. 1002–1011, 2006.

[36] E. F. Holby, Y. Shao-Horn, W. C. Sheng, and D. Morgan, “New understanding of Pt surface area loss in PEMFC’s: Temperature effects,” in *10th Polymer Electrolyte Fuel Cell Symposium, PEFC 10 - 218th ECS Meeting, October 10, 2010 - October 15, 2010*, Las Vegas, NV, United states, 2010, vol. 33, pp. 369–377.

[37] A. Gebregergis, P. Pillay, and R. Rengaswamy, “PEMFC fault diagnosis, modeling, and mitigation,” 445 Hoes Lane / P.O. Box 1331, Piscataway, NJ 08855-1331, United States, 2010, vol. 46, pp. 295–303.

[38] J.-M. Le Canut, R. M. Abouatallah, and D. A. Harrington, “Detection of Membrane Drying, Fuel Cell Flooding, and Anode Catalyst Poisoning on PEMFC Stacks by Electrochemical Impedance Spectroscopy,” *Journal of The Electrochemical Society*, vol. 153, no. 5, p. A857, 2006.

[39] N. Fouquet, C. Doulet, C. Nouillant, G. Dauphin-Tanguy, and B. Ould-Bouamama, “Model based PEM fuel cell state-of-health monitoring via ac impedance measurements,” *Journal of Power Sources*, vol. 159, no. 2, pp. 905–13, Sep. 2006.

[40] J. Gazzarri, M. Eikerling, Qianpu Wang, and Zhong-Sheng Liu, “Estimation of Local Relative Humidity in Cathode Catalyst Layers of PEFC,” *Electrochemical and Solid-State Letters*, vol. 13, no. 6, pp. 58–62, Jun. 2010.

[41] R. Makharia, M. F. Mathias, and D. R. Baker, “Measurement of Catalyst Layer Electrolyte Resistance in PEFCs Using Electrochemical Impedance Spectroscopy,” *Journal of The Electrochemical Society*, vol. 152, no. 5, p. A970, 2005.

[42] X. Yuan, J. C. Sun, H. Wang, and J. Zhang, “AC impedance diagnosis of a 500 W PEM fuel cell stack. Part II: Individual cell impedance,” *Journal of Power Sources*, vol. 161, no. 2, pp. 929–937, 2006.

[43] T. Hoshiko, H. Nakajima, T. Konomi, T. Kitahara, and S. Kita, “Estimation of Water Layer Thickness Adjacent to the Cathode Catalyst Layer of a PEFC (Analysis Using Electrochemical Impedance Spectroscopy),” 2008, vol. 16, pp. 2117–2123.

[44] S. Wasterlain, F. Harel, D. Candusso, D. Hissel, and X. Francois, “First results obtained with an impedance meter developed for the diagnosis of large Proton-Exchange-Membrane Fuel-Cell stacks,” in *Advanced Electromechanical Motion Systems & Electric Drives Joint Symposium, 2009. ELECTROMOTION 2009. 8th International Symposium on*, 2009, pp. 1–6.

[45] A. Narjiss, D. Depernet, D. Candusso, F. Gustin, and D. Hissel, “Online diagnosis of PEM fuel cell,” in *2008 13th International Power Electronics and Motion Control Conference, EPE-PEMC 2008, September 1, 2008 - September 3, 2008*, Poznan, Poland, 2008, pp. 734–739.

[46] T. Kadyk, R. Hanke-Rauschenbach, and K. Sundmacher, “Nonlinear frequency response analysis of PEM fuel cells for diagnosis of dehydration, flooding and CO-poisoning,” *Journal of Electroanalytical Chemistry*, vol. 630, no. 1–2, pp. 19–27, 2009.

[47] Xiaozi Yuan, Haijiang Wang, Jian Colin Sun, and Jiujun Zhang, “AC impedance technique in PEM fuel cell diagnosis - a review,” *International Journal of Hydrogen Energy*, vol. 32, no. 17, pp. 4365–80, Dec. 2007.

[48] J. Wu, X. Z. Yuan, H. Wang, M. Blanco, J. J. Martin, and J. Zhang, “Diagnostic tools in PEM fuel cell research: Part I Electrochemical techniques,” *International journal of hydrogen energy*, vol. 33, no. 6, pp. 1735–1746, 2008.

[49] N. Y. Steiner, D. Hissel, P. Mocoteguy, and D. Candusso, “Non intrusive diagnosis of polymer electrolyte fuel cells by wavelet packet transform,” *International Journal of Hydrogen Energy*, vol. 36, no. 1, pp. 740–6, Jan. 2011.

[50] A. M. Niroumand, W. Merida, and M. Saif, “PEM fuel cell low flow FDI,” *Journal of Process Control*, vol. 21, no. 4, pp. 602–612, 2011.

[51] J. Chen and B. Zhou, “Diagnosis of PEM fuel cell stack dynamic behaviors,” *Journal of Power Sources*, vol. 177, no. 1, pp. 83–95, 2008.

[52] F. Barbir, H. Gorgun, and X. Wang, “Relationship between pressure drop and cell resistance as a diagnostic tool for PEM fuel cells,” *Journal of Power Sources*, vol. 141, no. 1, pp. 96–101, 2005.

[53] A. D. Bosco and M. H. Fronk, “Fuel cell flooding detection and correction,” U.S. Patent 6,103,409,2000.

[54] D. Hissel, M. Péra, and J. Kauffmann, “Diagnosis of automotive fuel cell power generators,” *Journal of Power sources*, vol. 128, no. 2, pp. 239–246, 2004.

[55] N. Y. Steiner, D. Candusso, D. Hissel, and P. Mooteguy, “Model-based diagnosis for proton exchange membrane fuel cells,” P.O. Box 211, Amsterdam, 1000 AE, Netherlands, 2010, vol. 81, pp. 158–170.

[56] M. Schwabacher, “A survey of data-driven prognostics,” in *Proceedings of the AIAA Infotech@ Aerospace Conference*, 2005.

[57] M. Orchard, B. Wu, and G. Vachtsevanos, “A particle filtering framework for failure prognosis,” in *2005 World Tribology Congress III, September 12, 2005 - September 16, 2005*, Washington, D.C., United states, 2005, pp. 883–884.

[58] M. E. Orchard and G. J. Vachtsevanos, “A particle filtering-based framework for real-time fault diagnosis and failure prognosis in a turbine engine,” in *2007 Mediterranean Conference on Control and Automation, MED, July 27, 2007 - July 29, 2007*, Athens, Greece, 2007.

[59] M. E. Orchard and G. J. Vachtsevanos, “A particle-filtering approach for on-line fault diagnosis and failure prognosis,” *Transactions of the Institute of Measurement and Control*, vol. 31, no. 3–4, pp. 221–246, 2009.

[60] D. Rakhmatov, S. Vrudhula, and D. A. Wallach, “A model for battery lifetime analysis for organizing applications on a pocket computer,” *IEEE Transactions on Very Large Scale Integration (VLSI) Systems*, vol. 11, no. 6, pp. 1019–1030, Dec. 2003.

[61] D. Haifeng, W. Xuezhe, and S. Zechang, “A new SOH prediction concept for the power lithium-ion battery used on HEVs,” in *Vehicle Power and Propulsion Conference, 2009. VPPC’09. IEEE*, 2009, pp. 1649–1653.

[62] B. Saha, K. Goebel, S. Poll, and J. Christophersen, “An integrated approach to battery health monitoring using bayesian regression and state estimation,” in *Autotestcon, 2007 IEEE*, 2007, pp. 646–653.

[63] T. Yoshida, M. Takahashi, S. Morikawa, C. Ihara, H. Katsukawa, T. Shiratsuchi, and J. Yamaki, “Degradation Mechanism and Life Prediction of Lithium-Ion Batteries,” *Journal of The Electrochemical Society*, vol. 153, no. 3, p. A576, 2006.

[64] R. Hobbs, R. Newnham, D. Karner, and F. Fleming, “Development of predictive techniques for determination of remaining life for lead acid batteries under fast charge,” in *Battery Conference on Applications and Advances, 1999. The Fourteenth Annual*, 1999, pp. 177–188.

[65] F. Rufus, S. Lee, and A. Thakker, “Health monitoring algorithms for space application batteries,” in *Prognostics and Health Management, 2008. PHM 2008. International Conference on*, 2008, pp. 1–8.

[66] S. W. Eom, M. K. Kim, I. J. Kim, S. I. Moon, Y. K. Sun, and H. S. Kim, “Life prediction and reliability assessment of lithium secondary batteries,” *Journal of Power Sources*, vol. 174, no. 2, pp. 954–958, 2007.

[67] E. D. Sexton, R. F. Nelson, and J. B. Olson, “Life prediction for valve regulated lead acid batteries from early current/voltage data,” in *Applications and Advances, 2001. The Sixteenth Annual Battery Conference on*, 2001, p. 193.

[68] H. Wenzl, I. Baring-Gould, R. Kaiser, B. Y. Liaw, P. Lundsager, J. Manwell, A. Ruddell, and V. Svoboda, “Life prediction of batteries for selecting the technically most suitable and cost effective battery,” *Journal of power sources*, vol. 144, no. 2, pp. 373–384, 2005.

[69] M. Safari, M. Morcrette, A. Teyssot, and C. Delacourt, “Life-Prediction Methods for Lithium-Ion Batteries Derived from a Fatigue Approach,” *Journal of The Electrochemical Society*, vol. 157, p. A713, 2010.

[70] M. Safari, M. Morcrette, A. Teyssot, and C. Delacourt, “Multimodal Physics-Based Aging Model for Life Prediction of Li-Ion Batteries,” *Journal of The Electrochemical Society*, vol. 156, no. 3, p. A145, 2009.

[71] D. J. Spiers and A. D. Rasinkoski, “Predicting the service lifetime of lead/acid batteries in photovoltaic systems,” *Journal of power sources*, vol. 53, no. 2, pp. 245–253, 1995.

[72] B. Saha, K. Goebel, S. Poll, and J. Christophersen, “Prognostics Methods for Battery Health Monitoring Using a Bayesian Framework,” *IEEE Trans. Instrum. Meas.*, vol. 58, no. 2, pp. 291–296, Feb. 2009.

[73] E. V. Thomas, I. Bloom, J. P. Christophersen, and V. S. Battaglia, "Statistical methodology for predicting the life of lithium-ion cells via accelerated degradation testing," *Journal of Power Sources*, vol. 184, no. 1, pp. 312–317, 2008.

[74] B. Saha and K. Goebel, "Uncertainty management for diagnostics and prognostics of batteries using Bayesian techniques," in *Aerospace Conference, 2008 IEEE*, 2008, pp. 1–8.

[75] Dinh Vinh Do, C. Forgez, K. El Kadri Benkara, and G. Friedrich, "Impedance Observer for a Li-Ion Battery Using Kalman Filter," *IEEE Transactions on Vehicular Technology*, vol. 58, pp. 3930–3937, Oct. 2009.

[76] J. T. Pukrushpan, A. G. Stefanopoulou, and H. Peng, *Control of Fuel Cell Power Systems: Principles, Modeling, Analysis and Feedback Design*, 1st ed. Springer, 2004.

[77] R. O'Hayre, S.-W. Cha, W. Colella, and F. B. Prinz, *Fuel Cell Fundamentals*, 2nd ed. Wiley, 2009.

[78] E. C. Kumbur, K. V. Sharp, and M. M. Mench, "Liquid droplet behavior and instability in a polymer electrolyte fuel cell flow channel," *Journal of Power Sources*, vol. 161, no. 1, pp. 333–45, Oct. 2006.

[79] J. T. Pukrushpan, H. Peng, and A. G. Stefanopoulou, "Control-oriented modeling and analysis for automotive fuel cell systems," *Journal of Dynamic Systems, Measurement and Control, Transactions of the ASME*, vol. 126, no. 1, pp. 14–25, 2004.

[80] H. M. Zhang, H. P. Ma, J. Hu, Y. H. Cai, and B. L. Yi, "Diagnostic tool to detect liquid water removal in the cathode channels of proton exchange membrane fuel cells," *Journal of Power Sources*, vol. 162, no. 1, pp. 469–73, Nov. 2006.

[81] F. Y. Zhang, X. G. Yang, and C. Y. Wang, "Liquid Water Removal from a Polymer Electrolyte Fuel Cell," *J. Electrochem. Soc.*, vol. 153, no. 2, p. A225, 2006.

[82] T. C. Ransohoff and C. J. Radke, "Laminar flow of a wetting liquid along the corners of a predominantly gas-occupied noncircular pore.," *Journal of Colloid and Interface Science*, vol. 121, no. 2, pp. 392–401, 1988.

[83] D. A. McKay, W. T. Ott, and A. G. Stefanopoulou, "Modeling, parameter identification, and validation of reactant and water dynamics for a fuel cell stack," in *2005 ASME International Mechanical Engineering Congress and Exposition, IMECE 2005, November 5, 2005 - November 11, 2005*, Orlando, FL, United states, 2005, vol. 74 DSC, pp. 1177–1186.

[84] D. A. McKay, J. B. Siegel, W. Ott, and A. G. Stefanopoulou, "Parameterization and prediction of temporal fuel cell voltage behavior during flooding and drying conditions," *Journal of Power Sources*, vol. 178, no. 1, pp. 207–222, 2008.

[85] Y. Shan and S. Y. Choe, "A high dynamic PEM fuel cell model with temperature effects," *Journal of power sources*, vol. 145, no. 1, pp. 30–39, 2005.

[86] P. V. Kokotović, H. K. Khalil, and J. O'Reilly, *Singular perturbation methods in control: analysis and design*. SIAM, 1999.

[87] A. Vahidi, A. Stefanopoulou, and H. Peng, "Model predictive control for starvation prevention in a hybrid fuel cell system," in *Proceedings of the 2004 American Control Conference (AAC), June 30, 2004 - July 2, 2004*, Boston, MA, United states, 2004, vol. 1, pp. 834–839.

[88] W. He, G. Lin, and T. Van Nguyen, "Diagnostic Tool to Detect Electrode Flooding in Proton-Exchange Membrane Fuel Cells," *AIChE Journal*, vol. 49, no. 12, pp. 3221–3228, 2003.

[89] P. Pei, M. Ouyang, W. Feng, L. Lu, H. Huang, and J. Zhang, "Hydrogen pressure drop characteristics in a fuel cell stack," *International Journal of Hydrogen Energy*, vol. 31, no. 3, pp. 371–377, 2006.

[90] G. Vachtsevanos, F. L. Lewis, M. Roemer, A. Hess, and B. Wu, *Intelligent Fault Diagnosis and Prognosis for Engineering Systems*, 1st ed. Wiley, 2006.

[91]"Protocol on Fuel Cell Component Testing." [Online]. Available: http://www.fchea.org/core/import/PDFs/Technical%20Resources/Trans-H2Quality-ContamMatrix-04-010A.pdf.

[92] K. Cooper, "In Situ PEM FC Electrochemical Surface Area And Catalyst Utilization Measurement." [Online]. Available: http://www.scribner.com/component/option,com_quickfaq/Itemid,230/cid,2/id,10/view,items/.

[93] M. T. Todinov, "Necessary and sufficient condition for additivity in the sense of the Palmgren–Miner rule," *Computational materials science*, vol. 21, no. 1, pp. 101–110, 2001.

[94] D. Chelidze and J. P. Cusumano, "A Dynamical Systems Approach to Failure Prognosis," *Journal of Vibration and Acoustics*, vol. 126, no. 1, p. 2, 2004.

[95] J. Newman, "A Crack-Closure Model for Predicting Fatigue Crack Growth under Aircraft Spectrum Loading," in *Methods and Models for Predicting Fatigue Crack Growth Under Random Loading*, J. Chang and C. Hudson, Eds. 100 Barr Harbor Drive, PO Box C700, West Conshohocken, PA 19428-2959: ASTM International, pp. 53–53–32.

[96] A. Saxena, J. Celaya, E. Balaban, K. Goebel, B. Saha, S. Saha, and M. Schwabacher, "Metrics for evaluating performance of prognostic techniques," in *Prognostics and Health Management, 2008. PHM 2008. International Conference on*, 2008, pp. 1–17.